UNIVERSITY OF BIRMINGHAM

BIOSTABILITY OF AN ORTHOPAEDIC DEVICE AND ITS LONG-TERM IMPLANTABLE BIOMATERIALS

by

BERNARD MICHAEL LAWLESS

A thesis submitted to the University of Birmingham for the degree of

DOCTOR OF PHILOSOPHY

Spinal Implant Design (SID) Group,

Biomedical Engineering Research Group,

Department of Mechanical Engineering,

School of Engineering,

University of Birmingham

August 2018

Abstract

The BDyn device is a bilateral posterior dynamic stabilisation spinal implant used to treat degenerative disc disease. The BDyn device consists of a polycarbonate urethane (PCU) component, a silicone component, a mobile titanium alloy rod, a fixed titanium alloy rod and it is fixed to the vertebrae by titanium alloy pedicle screws.

The viscoelastic properties, chemical structure and surface morphological changes of the untreated, *in vitro* degraded and *in vivo* degraded were compared. The macro and micro-scale viscoelastic properties, chemical structure and surface morphology of five long-term implantable PCU biomaterials, which were *in vitro* degraded by four separate degradation methods were also investigated.

No resonant frequencies were reported for the untreated and *in vitro* degraded components and devices however, resonance was detected in the frequency sweep test of BDyn Explant 2 with the sharp increase of the loss stiffness occurred at 4 Hz; this highlights the importance of evaluating orthopaedic devices with frequency dependent mechanical testing techniques. The biomaterials were viscoelastic throughout the frequency range tested and were significantly different at specific frequencies when comparing untreated specimens to specimens degraded by a specific degradation method; this further highlights the need to evaluate elastomeric biomaterials with frequency dependent mechanical testing techniques.

To my father, mother and Christina,

I would never be able to thank you enough.

Acknowledgements

Back in June 2012, I visited Birmingham for the first time with my friends from my undergraduate degree. I was about to start my Master's postgraduate degree in ITT Dublin and we decided to visit their friend Ronan Dorrepaal. Ronan was doing a Master's degree in Chemical Engineering. To be honest, I remember thinking at the time that I wouldn't be too keen on moving to Birmingham... Just under two years later (March 2014), I was coming to the end of my Master's degree in Dublin and I applied for a Marie Curie Early Stage Researcher position in the University of Birmingham and S14 Implants in Bordeaux. My interview with Prof. Duncan Shepherd and Dr. Daniel Espino was really enjoyable and I was given a "lab tour" by Spencer Barnes; I say "lab tour" as we literally went to the Shell Lounge, had a coffee and chatted about rugby for over an hour... A week after my interview, I was snowboarding in Bulgaria and I got an email with the job offer. I was absolutely over the moon and my three years in Birmingham did not let me down.

With that in mind, I would like to thank Prof. Duncan Shepherd and Dr. Daniel Espino for being fantastic supervisors. I am eternally grateful for your support, guidance, flexibility, time and advice. I would also like to thank my postgraduate Master's degree supervisors, Mr. Stephen Tiernan and Dr. Fiona McEvoy, as I carried experiences from my Master's to my PhD. Merci beaucoup de mon superviseur industriel Dr. Johann Robin, chef de projet R&D Mr. Brice Sennequier et CEO Mr. Frederic Fortin chez S14 Implants. I have fond memories of working in S14, the beautiful city of Bordeaux and l'UBB! I wish you all the best in the future.

To my fellow Marie Curie ESRs Carolina, Alba and Alicja, it seems like a lifetime ago that we all met at the Bullring in Birmingham! From discussing research to eating fantastic fish in Marché des Capucins, I've enjoyed every moment and I cannot thank you enough.

To Prof. David Hukins and Mr. Douglas Wardlaw, I would like to thank you for the many constructive conversations we had about research especially at the SID meetings. I would like to thank the European Commission for funding this project (604935) and the Institution of Mechanical Engineers (IMechE) for funding my visit to VU Amsterdam.

To Spencer, Dave, May, Naomi, Feras, Hanna and Hamid from the biomedical engineering lab, I would like to thank you all for all of the chats, the coffee/tea ISO standard and the laughs! I really enjoyed my time in GLX and each one of you contributed to that.

I would like to thank Carl Hingley, Peter Thornton, Lee Gauntlett, Jack Garrod, Kevan Charlesworth, Adam Sheward and Becky Charles from the Department of Mechanical Engineering; Terry Green from the School of Chemistry; Daniel Smith from the School of Chemical Engineering and Frank Biddlestone from the School of Metallurgy and Materials.

I would like to thank Erik Paardekam, Luca Bartolini, Marica Marrese from the Iannuzzi Group, Dr. Georgio Mattei from Optics11 and Prof. Davide Iannuzzi for being so welcoming to me, their time, guidance and help when I was a visiting researcher at VU Amsterdam.

To Dr. Catherine Kelly and Dr. Mike Jenkins, thank you for your time and work in investigating the viscoelastic response of biomaterials with respect to temperature.

To all of my co-authors in various studies (thesis and non-thesis related), thank you for all of your time, work, discussions (work and non-work related) and coffee! I especially would like to thank Megan Cooke, Dr. Sophie Cox and the members from TRAILab.

To come full circle, Ronan ended up leaving Birmingham around May 2015 and is now doing a PhD in the UCD Spectral Imaging Research Group (SIRG). We have published a study in Acta Biomaterialia and we are working on future publications; it's crazy to think a trip to Birmingham to a "friend's friend" has led to scientific publications six years later! With that, I would like to thank Ronan Dorrepaal and his supervisor Assoc. Prof. Aoife Gowen for inviting me and being so welcoming to UCD SIRG to use their state-of-the-art hyperspectral chemical imaging machines and technology.

To Dr. and Mr. H.E. Burton (I couldn't resist, Chris!), thank you for the endless chats, laughs, red wine, Imtiaz, steak rolls, cups of tae, Rocket League, no thesis chat and just being there!

To Auntie Gillian MacKinnon thank you for the email as if it wasn't for you, this thesis would not have happened. To Les, Kate, Rosslyn, Mary, Hector and the rest of the clan, thanks for letting me bore you with my chat about my research.

To Mam, Dad, Jimmy, Fiona and Stephen – thank you for all of your love and support in everything I've done.

Last but not least, to Tina, from proof reading to keeping me in good spirits, thank you for your love and support. Similar to Gillian, this thesis would not have been possible if it wasn't for you.

Academic output

Peer-reviewed publications

Lawless, B.M., Barnes, S.C., Espino, D.M. and Shepherd, D.E., 2016. Viscoelastic properties of a spinal posterior dynamic stabilisation device. *Journal of the Mechanical Behavior of Biomedical Materials*, *59*, pp.519-526

Lawless, B.M., Espino, D.M. and Shepherd, D.E., 2018. *In vitro* oxidative degradation of a spinal posterior dynamic stabilization device. *Journal of Biomedical Materials Research Part B: Applied Biomaterials*, *106*(3), 1237-1244

Dorrepaal, R.M.*, Lawless, B.M.*, Burton, H.E., Espino, D.M., Shepherd, D.E.T., Gowen. A.A. 2018. Hyperspectral chemical imaging reveals spatially varied degradation of polycarbonate urethane (PCU) biomaterials. *Acta Biomaterialia, 73, 81-89*

Podium and poster presentations

B.M. Lawless, S.C. Barnes, R.M. Dorrepaal, A.A. Gowen, D.M. Espino, D.E.T. Shepherd. 2017. Degradation of a posterior dynamic stabilisation device: an in vivo and in vitro comparison. *European Society of Biomechanics Congress, Seville, Spain.* †

B.M. Lawless, S.C. Barnes, D.M. Espino, D.E.T. Shepherd. 2016. Frequency-dependent viscoelastic properties of a posterior dynamic stabilisation device. *European Society of Biomechanics Congress, Lyon, France.* ‡

B.M. Lawless, S.C. Barnes, D.M. Espino, D.E.T. Shepherd. 2016. Viscoelastic properties of a spinal implant. *University of Birmingham Mechanical Engineering Symposium, Birmingham, United Kingdom* †

Co-first author *; Podium Presentation ‡; Poster Presentation †

Table of Contents

List of Figures

List of Tables

List of Abbreviations

AF	annulus fibrosus
AL	aliphatic
Al	aluminium
ANOVA	analysis of variance
ARC	aromatic
ASTM	American society for testing and materials
ATR-FTIR	attenuated total reflectance Fourier transform infra-red
AU	arbitrary unit
BDO	butane diol
BSA	bovine serum albumin
CE	cholesterol esterase
$CoCl_2$	cobalt chloride
DDD	degeneration disc disease
DFT	discrete Fourier transform
DMA	dynamic mechanical analysis
μDMA	micro-dynamic mechanical analysis
DMTA	dynamic mechanical temperature analysis
E^*	complex modulus
E'	storage modulus
E"	loss modulus
ESC	environmental stress cracks
EtO	ethylene oxide
FBGC	foreign body giant cells
FE	finite element
FFT	fast Fourier transform

FTIR	Fourier transform infra-red
H_2O_2	hydrogen peroxide
HCI	hyperspectral chemical imaging
HCM	hyperspectral chemical mapping
HDPE	high density polyethylene
ISO	international organisation for standardisation
IVD	intervertebral disc
k^*	complex stiffness
k'	storage stiffness
k"	loss stiffness
kCl	potassium chloride
LDPE	low density polyethylene
MDI	methylene di(p-phenyl isoctanate)
MIO	metal ion oxidation
MS	mass spectrometry
NaCl	sodium chloride
NMR	nuclear magnetic resonance
NP	nucleus pulposus
OCE	optical coherence elastography
OCT	optical coherence tomography
PBS	phosphate buffer saline
PCU	polycarbonate urethane
PCU-S	polycarbonate urethane based silicone
PDMS	polydimethylsiloxane
PDS	posterior dynamic stabilisation
PEU	polyether urethane

PEU-S	polyether urethane based silicone
PEUU	polyether urethane urea
PEEK	polyetheretherketone
PET	polyethylene terephthalate
PHMO	polyhexamethylene oxide
PIDO	proportional integral derivative offset
PU	polyurethane
SEM	scanning electron microscopy
SG	Savitzky Golay
SPU	segmented polyurethane
tan(δ)	loss factor
Ti	titanium
TPSCU	thermoplastic silicone polycarbonate urethane
TTS	time temperature superposition
UHMWPE	ultra-high molecular weight polyethylene
UNT	untreated
UTS	ultimate tensile strength
V	vanadium

Declaration of Originality

I hereby certify that the material, which I now submit for assessment on the programmes of study leading to the award of Doctor of Philosophy, is entirely my own work unless stated here:

- Chapter 4: Matlab code used to calculate the micro-scale viscoelastic properties, by μDMA, was created by Luca Bartolini and members from VU Amsterdam.
- Chapter 4: The 3% H_2O_2 degradation solution changes were performed by Dr. Hanna E. Burton.
- Chapter 4: Approximately 8 out of 52 weeks of the real-time and accelerated degradation solution changes were performed by Dr. Carolina E. Lavecchia.
- Chapter 4 and Chapter 5: Mr. Ronan Dorrepaal and I performed hyperspectral chemical imaging of all specimens.
- Chapter 4 and Chapter 5: Matlab code used to quantify hyperspectral chemical images was created by Mr. Ronan Dorrepaal and Assoc. Prof. Aoife A. Gowen.
- Chapter 8: Matlab code used to calculate the viscoelastic properties, by DMA, was created in collaboration with Dr. David G. Eckold and Dr. Spencer C. Barnes.

The work in this thesis was carried out in the Biomedical Engineering Research Group, (Department of Mechanical Engineering, University of Birmingham, United Kingdom), S14 Implants (Pessac, France), UCD Spectral Imaging Research Group (UCD School of Biosystems Engineering, University College Dublin, Republic of Ireland) and Iannuzzi Group (Faculty of Science, Vrije Universiteit Amsterdam, The Netherlands) from August 2014 to November 2017. This thesis has been typed by myself and proof read by my supervisors Prof. Duncan E.T. Shepherd and Dr. Daniel M. Espino. This thesis has not been accepted in any previous application for a degree. Some areas of this thesis have been published in peer-reviewed publications (Lawless et al., 2018, 2016) while other sources of information are referenced throughout.

Signed:_____ Date: _____

Bernard Michael Lawless

Chapter 1

Introduction

1 Introduction

Vibration is simply defined as an oscillating motion (Steidel, 1989). One of the earliest studies of oscillating motion is Galileo's work, in 1584, when he created the principle of the isochronous pendulum (Steidel, 1989). The published work of John William Strutt, also known as Lord Rayleigh, relating to vibration helped to develop the theory and the field of mechanical vibration (Steidel, 1989).

Alongside heavy and frequent lifting, long term vibration exposure was stated as a high risk factor of low back pain (Magnusson et al., 1996). Studies have evaluated the *in vivo* response of the spine to sinusoidal vibrations at different frequencies (Panjabi et al., 1986; Wilder et al., 1982). Panjabi et al. (1986) recorded the average *in vivo* lumbar vertebrae resonant frequency at 4.4 Hz for the axial direction with the person in the seated position (sitting upright unsupported). Wilder et al. (1982) recorded the greatest transmissibility (recorded from accelerometers in the seat and the head helmet) in the male and female lumbar spine of 4.9 Hz and 4.75 Hz, respectively; these resonant frequencies are similar to the frequencies recorded by Panjabi et al. (1986). Further, Wilder et al. (1982) recorded second and third resonant frequencies at 9.5 Hz and 12.7 Hz for both genders.

Knowledge and understanding the resonance or natural frequencies of the spine is important in relation to reducing exposure to these potentially harmful frequencies (Panjabi et al., 1986). Further, design and mechanical testing of spinal devices should assess the behaviour of such devices at spinal resonant frequencies. Motion preserving spinal devices have recently emerged as a new treatment of cervical and lumbar degenerative disorders (Kurtz et al., 2009). However, little work has been undertaken to analyse the frequency dependent response of spinal devices and the frequency dependent behaviour of the biomaterials used in such implants; to design structures that function properly, it is imperative that that the mechanical behaviour of a material is understood (Gere and Timoshenko, 1997). Any resonance of the device, at any frequency, is a limitation of the device as the resonance may damage the device and in a worst-case scenario, the device may fail. Further, these materials degraded and assessing the mechanical response of these degraded materials, and the implants they are used in, is lacking.

The aim of this thesis was to investigate the biostability of the BDyn posterior dynamic stabilisation (PDS) orthopaedic (spinal) device elastomeric biomaterials and the biostability of potential replacement polycarbonate urethane (PCU) biomaterials, which could be used, for this PDS device. The specific objectives were:

- To investigate the effect of *in vitro* degradation (oxidation and hydrolysis) on the *in vitro* biostability of five potential replacement PCU biomaterials. The micro-scale and macro-scale viscoelastic properties, the polymer chemical structure and surface morphology were analysed to assess changes due to *in vitro* degradation.
- To assess the biostability of the BDyn PDS device elastomeric biomaterials. The viscoelastic properties, the polymer chemical structure, macro and surface morphology were analysed to assess differences between the control, *in vitro* degraded (oxidation) and *in vivo* degraded BDyn PDS components.

By investigating the *in vitro* biostability of polymers used in orthopaedics, and used in cardiovascular applications, these findings will influence the selection of biomaterials for future implantable devices. Assessing the differences between the untreated, *in vitro* degraded (oxidation) and *in vivo* degraded BDyn PDS components will develop the understanding of the implant's performances in the biological environment and the ability of the *in vitro* oxidative degraded method to replicate changes comparable to *in vivo* degraded specimens. Further, by investigating the failure of the explanted BDyn devices, findings will help biomedical engineers to design and test future spinal implants.

Chapter 2 provides the relevant background information beginning with the mechanics of elastic, viscous and viscoelastic materials. Next, information of the human spinal column and orthopaedic devices used for degenerative diseases is provided. Finally, background of the biostability of polyurethane biomaterials, which includes brief examination of published retrieval studies and information of *in vitro* biodegradation experiments, is provided.

Chapter 3 provides information about the general materials and methods used in this thesis. This chapter focuses generally on the long-term implantable biomaterials, the biomaterials used for a posterior dynamic stabilisation device, *in vitro* oxidative and *in vitro* hydrolytic degradation methods, hyperspectral chemical imaging (HCI) and attenuated total reflectance Fourier transform infra-red (ATR-FTIR) spectroscopy methods, micro-scale (μDMA) and macro-scale dynamic mechanical analysis (DMA) methods, scanning electron microscopy (SEM) and statistical analyses used.

Chapter 4 investigates the *in vitro* biostability of five commercially available, long-term implantable polycarbonate urethane (PCU) biomaterials. This chapter provides study specific materials and methods used and investigates the changes in viscoelasticity (μDMA and DMA), PCU chemical structure (HCI) and surface morphology (SEM).

Chapter 5 compares the viscoelastic response of the BDyn devices and its individual elastomeric components. Further, this chapter compares the viscoelasticity of the untreated, *in vitro* and *in vivo* degraded BDyn components and the BDyn device assembled with degraded components. The chapter provides study specific materials and methods used and investigates the changes in viscoelasticity (DMA), PCU chemical structure (HCI and ATR-FTIR), macro-morphological plastic deformation and surface morphology (SEM). The work in this chapter has been published in the Journal of Mechanical Behaviour of Biomedical Materials (Lawless et al., 2016) and the Journal of Biomedical Materials Research Part B: Applied Biomaterials (Lawless et al., 2018).

Chapter 6 provides an overall discussion, future research necessary to further develop our understanding of the biostability of elastomeric orthopaedic devices and biomaterials and general conclusions of this thesis.

Chapter 2

Background

2 Background

2.1 Introduction

This chapter provides information to understand subsequent chapters in this thesis. This chapter explains the mechanics of materials (section 2.2), the human vertebral column (section 2.3), orthopaedic spinal devices, and more specifically, elastomeric posterior dynamic stabilisation devices (section 2.4), and the biostability of these biomaterials (section 2.5).

2.2 Mechanics of materials

When a force *(F)* is applied to a specimen, the specimen may deform due to this applied force (Figure 2-1). If deformation occurs and the original length *(Lo)* of the specimen alters to a new length *(L)*, this deformation *(ΔL)* can be calculated and the stiffness *(k)* of the structure can be determined from:

$$k = \frac{F}{L_O - L} = \frac{F}{\Delta L} \qquad \text{Equation 2.1}$$

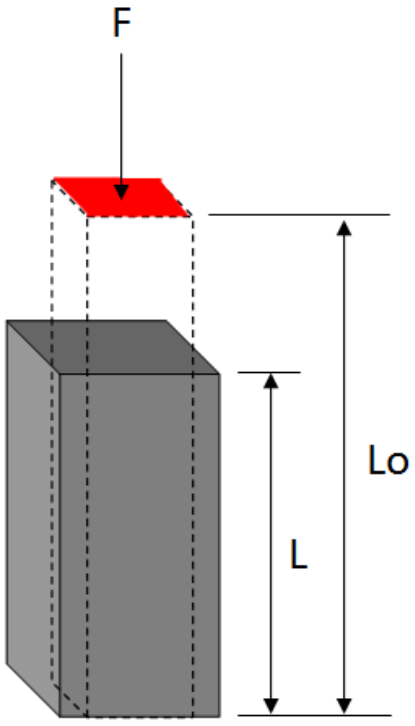

Figure 2-1: Compression of a rectangular cross sectional area piece. Compressive force *(F)*, original length *(Lo)* and length *(L)*, after an applied force, are highlighted.

Further, this deformation *(ΔL)* can be expressed as a function of the initial length *(Lo)*; this is known as strain *(ε)*. A conventional description of strain *(ε)* is commonly known as nominal, engineering or Cauchy strain:

$$\epsilon = \frac{L_O - L}{L_O} = \frac{\Delta L}{L_O} \qquad \text{Equation 2.2}$$

As the ratio is length versus length, strain is a dimensionless parameter.

For the example above (Figure 2-1), the force, *F,* is applied over the entire area, *A*, of the surface (highlighted in Figure 2-1 in red). The applied force, over this area, induces a stress *(σ)* and is described by:

$$\sigma = \frac{F}{A} \qquad \text{Equation 2.3}$$

Stress and strain are two of the most fundamental parameters used to describe the mechanics of materials (Gere and Timoshenko, 1997) and the stress that acts perpendicular to the surface (see Figure 2-1) is known as normal stress. For Figure 2-1, the strain calculated is axial strain. It can be witnessed in Figure 2-1 that the width and depth dimensions, of the squared specimen, have expanded as the specimen was compressed. The negative ratio of the lateral strain *(ϵ_L)* to the axial strain *(ε)* is known as Poisson's ratio (Gere and Timoshenko, 1997).

$$\upsilon = -\frac{\epsilon_L}{\epsilon} \qquad \text{Equation 2.4}$$

The Poisson's ratio of titanium alloys is 0.33 while the Poisson's ratio of rubber ranges between 0.45 and 0.5 (Gere and Timoshenko, 1997). The theoretical upper limit for Poisson's ratio is 0.5 for homogenous, isotropic materials and rubber comes close to this limit (Gere and Timoshenko, 1997). Studies (Briscoe et al., 1998; de Lima et al., 2015; Herbert et al., 2008) have assumed that materials have a specific Poisson's ratio. However, the Poisson's ratio is physically capable of exhibiting time dependent behaviour (Herbert et al., 2008).

2.2.1 Elasticity

Scientist Robert Hooke (1635–1703) was one of the first people to investigate the elastic behaviour of materials (Gere and Timoshenko, 1997). Hooke's description *ut tensio sic vis* (Blatz and Ko, 1962), which translates to "*as the extension, so the force*", established the linear relationship between the applied load and resulting deformation (Gere and Timoshenko, 1997). Hooke's Law holds for linear-elastic materials in the linear-elastic region (see Figure 2-2). From the origin of the stress-strain curve for structural steel (Figure 2-2), the ratio of the stress and strain is linear in behaviour up to the proportional limit (Point A; Figure 2-2); the slope of this straight line is the Young's Modulus *(E)*.

$$E = \frac{\sigma}{\epsilon} \qquad \text{Equation 2.5}$$

Past the proportional limit, the increment of stress per increment of strain reduces and the stress reaches a point where the specimen yields. At this point (Point B), the stress is known as the yield stress of the material. The specimen continues to yield i.e. there is an increase in the strain while there is minimal change in the stress (Point B to Point C).

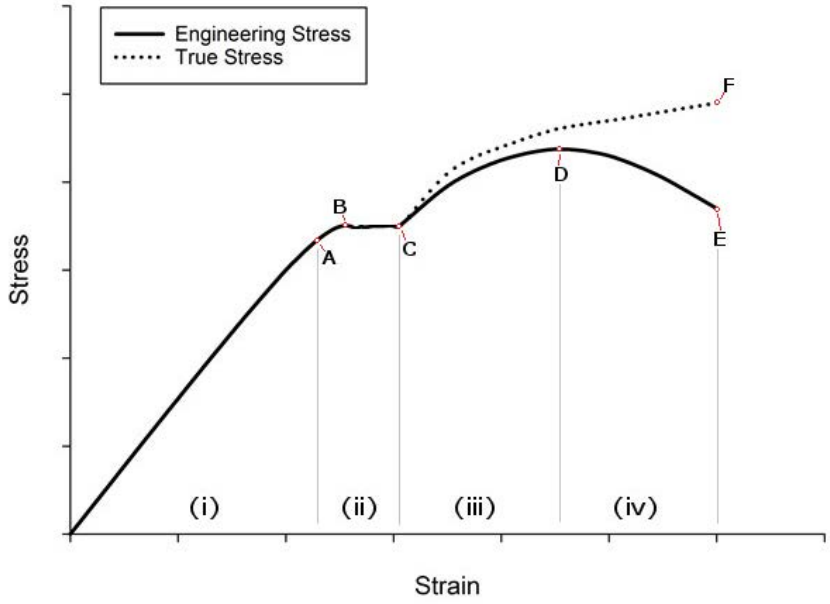

Figure 2-2: Typical stress-strain curve for structural steel. (A) Proportional limit, (B) yield stress (yield strength), (C) beginning of strain harden, (D) ultimate Tensile stress (ultimate strength) and (E) fracture point. The four regions are (i) linear, (ii) yielding, (iii) strain hardening and (iv) necking. Adapted from (Gere and Timoshenko, 1997).

At point C, the steel begins to undergo changes in the crystalline structure and these changes continue until the ultimate tensile stress (Point D); this region (iii) is known as strain hardening. Post the ultimate tensile strength point (Point D), the material begins to neck (region (iv)) and the specimen finally fractures (Point E).

At the beginning of Point C, the cross-sectional area of specimen begins to decrease with increasing strain. If it is possible to measure the actual cross-sectional area and elongation, the true stress and true strain of the material can be calculated and the true stress at fracture (Point F); this stress is different to the engineering stress at fracture (Point E) as the engineering stress uses the cross-sectional area at the beginning of the tension test.

For isotropic materials in the linear elastic region, the shear modulus *(G)* can be calculated from the Young's modulus *(E)* and the Poisson's ratio ***(υ)***:

$$E = 2G(1 + \upsilon) \qquad \text{Equation 2.6}$$

2.2.2 Viscosity

Nine years after Robert Hooke's discovery, Isaac Newton (1643–1727) published *Philosophiae Naturalis Principia Mathematica* (Barnes et al., 1989). Along with Newton's Laws of motion in *Principia*, Newton postulated the idea of a viscous liquid; *"The resistance which arises from the lack of slipperiness of the parts of the liquid, other things being equal, is proportional to the velocity with which the parts of the liquid are separated from one another"* (Barnes et al., 1989). Today, the *"lack of slipperiness"*, or sometimes quoted in earlier translations as "*the want of lubricity*" (Franco and Partal, 2010), is known as viscosity and is a measure of the resistance to flow (Barnes et al., 1989).

With Newton's concept, when a layer of fluid moves with respect to another layer (Figure 2-3), the greater the internal friction, to promote movement, the greater the force and induced stress (Franco and Partal, 2010). In the nineteenth century, Claude-Louis Navier and George Gabriel Stokes independently described the three dimensional theory of the motion of a fluid and this led to the formation of Newton's Law (Barnes et al., 1989; Franco and Partal, 2010). Similar to Hooke's Law, Newton's Law is a linear Law i.e., it assumes proportionality between shear stress *(τ)* and shear rate *($\dot{\gamma}$)* (Barnes et al., 1989). This proportionality between the shear stress and shear rate is the viscosity *(μ)* of the fluid:

$$\tau = \mu \frac{du}{dy}$$ Equation 2.7

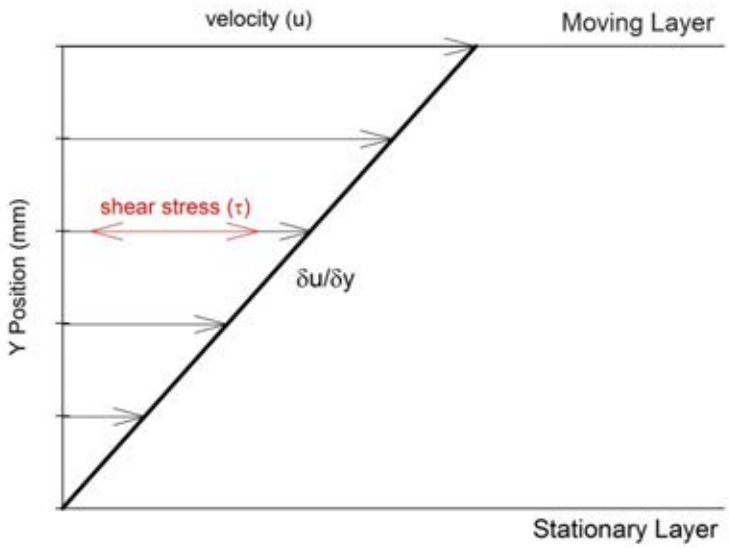

Figure 2-3: Newton's Law of viscosity. The stationary layer, the moving layer, velocity *(u)* of the fluid, the shear stress *(τ)* and y position which is perpendicular to the flow.

Fluids that have a shear stress linearly proportional to the shear rate are known as Newtonian fluids and one example of this is water. However, many fluids are considered non-Newtonian (Figure 2-4); i.e. the fluid does not follow Newton's Law of viscosity. Non-Newtonian fluid behaviour can be characterised into different types:

- Shear thickening (rheopectic); increase in viscosity with increase of shear rate
- Shear thinning (thixotropic); decrease in viscosity with increase of shear rate
- Bingham plastic; the fluid requires a specific shear stress before it begins to flow

Fluids that are non-Newtonian include liquid body armour (shear thickening), paint (shear thinning), blood (shear thinning) and toothpaste (Bingham plastic).

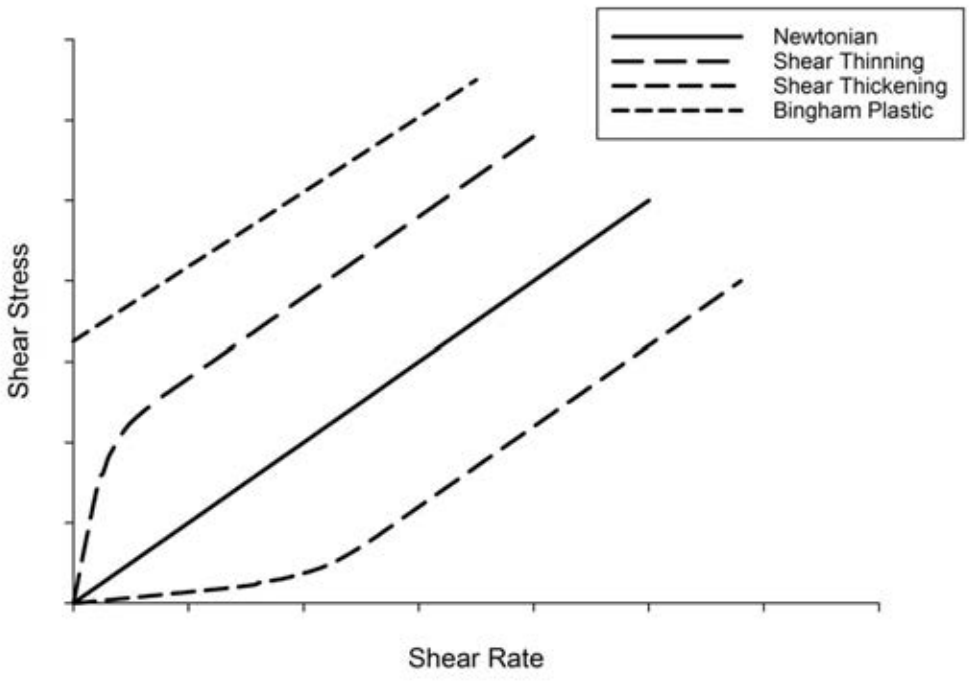

Figure 2-4: Viscosity of a Newtonian fluid and the viscosity three different non-Newtonian fluids (shear thinning, shear thickening and Bingham plastic). Shear stress *(τ)* and shear rate *(γ̇)*.

The behaviour of some materials falls in between the classical Hookean elastic response and Newtonian viscous response; these materials are known as viscoelastic materials and the behaviour of these materials have been described by the term viscoelasticity.

2.2.3 Viscoelasticity

Viscoelastic materials exhibit both elastic and vicious properties (Haddad, 1995). They are characterised by a certain level of rigidity of an elastic body but, at the same time, the same body flows and dissipates energy by frictional losses as a viscous fluid (Haddad, 1995). This flow and dissipation of energy is due to internal mechanisms such as bond breakage, formation and dislocations (Haddad, 1995). A material's viscoelastic properties can be quantified by quasi-statically (creep, stress relaxation) and dynamically (dynamic mechanical analysis).

2.2.3.1 Quasi-static viscoelasticity

Unlike elastic and viscous materials, when a load is applied to a viscoelastic material, a stress is induced and the deformation (ΔL; see Equation 2.2) does not stop at a constant value (Figure 2-5). Instead, the deformation continues or 'creeps' over time until the strain equilibrates at a final displacement.

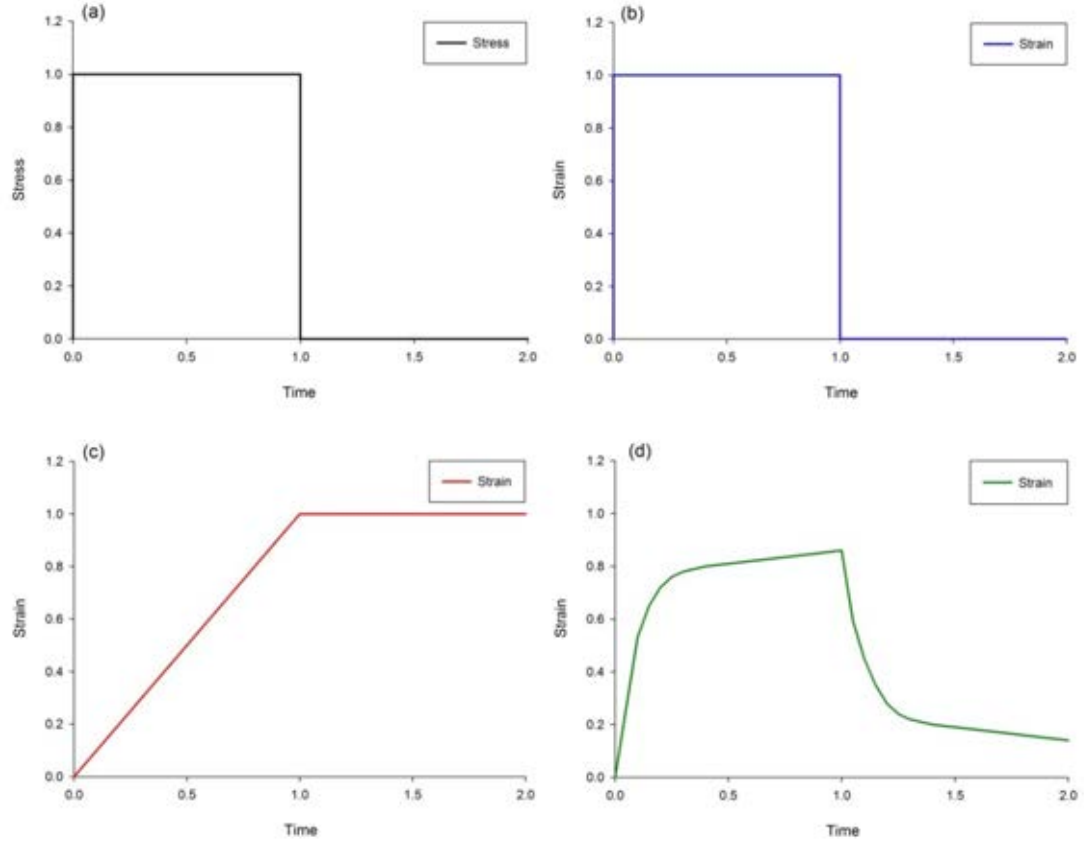

Figure 2-5: Comparison of (a) induced stress versus strain response for (b) an elastic, (c) a viscous and (d) a viscoelastic material. Adapted from (Haddad, 1995)

Once the load is removed, the residual strain reduces over time and it may disappear entirely (Haddad, 1995) thus, creating a hysteresis loop (see Figure 2-6). This hysteresis loops is caused by the viscoelastic nature of polymers (Menard, 2008) as under cyclical loading and unloading, viscoelastic material exhibit a phase lag which leads to a dissipation of mechanical energy (Liu and Qi, 2010). The area within the hysteresis loops represents the dissipated energy per volume, in a viscoelastic material, per cycle (Carbone and Persson, 2005; Li and Xu, 2007; Liu and Qi, 2010).

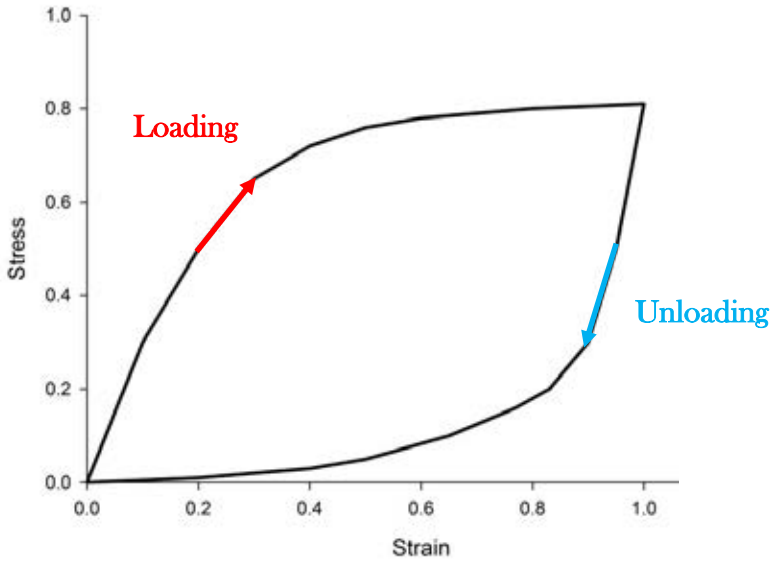

Figure 2-6: Hysteresis loop; Loading (Red) and Unloading (Blue) highlighted

In contrast, when a deformation is applied to a viscoelastic material, the induced stress does not stop at a constant value. Instead, the stress 'relaxes' over time until the stress equilibrates at a final displacement (Figure 2-7). Depending on the vicious property of a viscoelastic material, the induced stress may decay to zero or equilibrate at a finite value (Haddad, 1995).

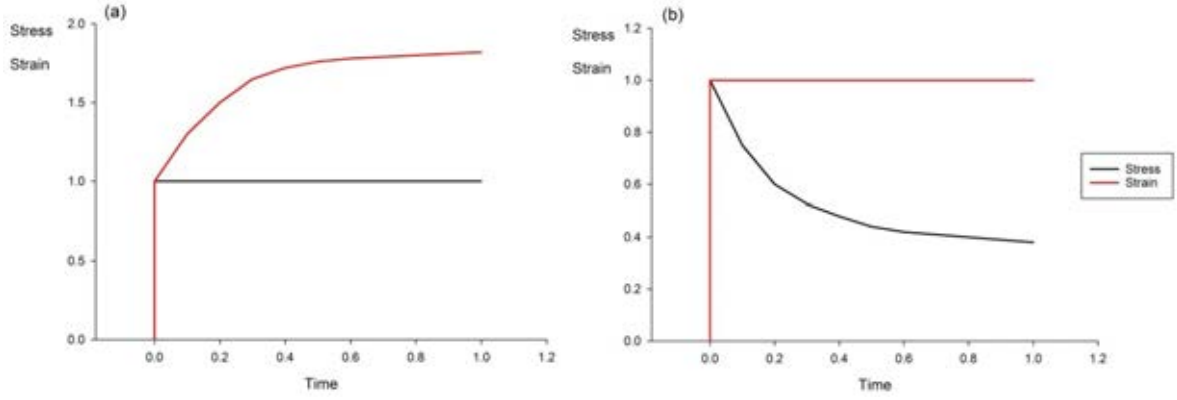

Figure 2-7: (a) creep and (b) stress relaxation. Stress in (a) and the strain in (b) are plotted to a nominal value of '1'.

2.2.3.2 Dynamic Mechanical Analysis (DMA)

Unlike conventional creep and stress relaxation tests, Dynamic Mechanical Analysis (DMA) is a dynamic testing method used to determine the viscoelastic properties of a material or multi-component structure. For DMA, the viscoelastic properties are measured following the application of an oscillating force to a specimen and analysis of the out-of-phase displacement response (Menard, 2008). The sinusoidal load and displacement timed data are recorded (Figure 2-8):

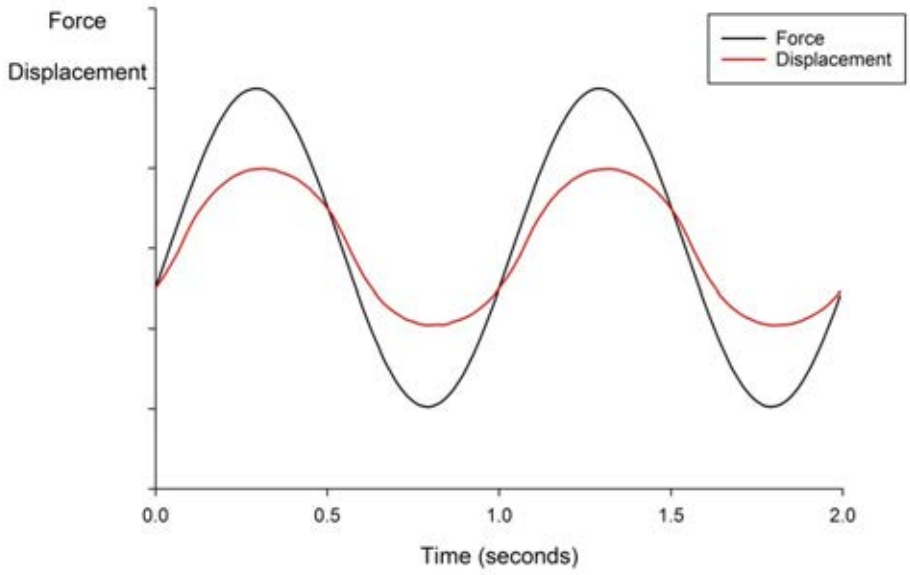

Figure 2-8: Load and displacement sinusoidal waves

Fourier analyses, of the displacement and load sinusoidal waves (Figure 2-8) are performed. From these analyses, the magnitude of the load *(F^*)*, the magnitude of the displacement *(d^*)*, the actual frequency *(f)* and the phase lag *(δ)* are measured. As seen on the plots below (Figure 2-9), the magnitude of the displacement *(d^*)* and the magnitude of the load *(F^*)* are found at the major peak of the displacement and load fast Fourier transform plots (Figure 2-9), respectively. The peaks, in these plots, have been normalised by the dataset length. The actual frequency *(f)* is measured at the position of the major peak. The phase angles of the force and displacement, at the respective major peaks, are calculated and the units are radians. The difference between these phase angles equates the phase lag *(δ)*.

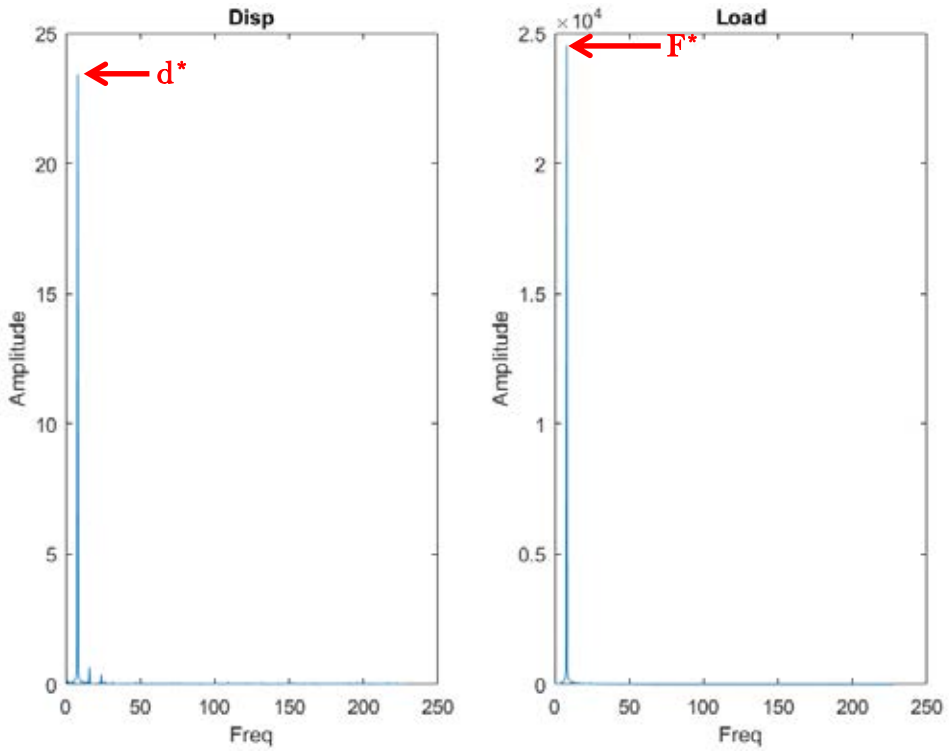

Figure 2-9: Fast Fourier transform plots of (left) displacement and (right) load. The magnitude of the displacement *(d*)* and the magnitude of the load *(F*)* are illustrated.

With the magnitudes of the load *(F*)* and displacement *(d*)*, from the Fourier analyses, the complex (dynamic) stiffness *(k*)* is then calculated:

$$k^* = \frac{F^*}{d^*} \qquad \text{Equation 2.8}$$

A viscoelastic structure can be characterised in terms of storage and loss stiffness. The storage stiffness represents the elastic portion of the viscoelastic structure and it describes the ability of a structure to store (recoverable) energy, while the loss stiffness characterises the ability of the structure to dissipate (irrecoverable) energy through heat and internal motions (Menard, 2008; Placet and Foltête, 2010). Further, the storage stiffness is also referred to as the 'real' portion of *k** while the loss stiffness is referred to as the 'imaginary' portion of *k** (Haddad, 1995). By using the phase lag *(δ)* and the complex (dynamic) stiffness *(k*)*, the storage stiffness *(k')* and loss stiffness *(k")* can be calculated:

$$k' = k^* \cos(\delta) \qquad \text{Equation 2.9}$$

$$k'' = k^* \sin(\delta) \qquad \text{Equation 2.10}$$

A shape factor *(S_F)* is calculated to account for specimen geometry. S_F normalises the load and displacement in terms of cross-sectional area and length, respectively. Therefore, the complex (dynamic) modulus *(E^*)* can be calculated from the complex (dynamic) stiffness, thus, the viscoelastic properties of the specific material, instead of the structure, can be quantified. Further, by dividing the storage and loss stiffness by the shape factor S_F, the storage *(E')* and loss *(E'')* moduli, of the material, can be calculated:

$$E^* = \frac{k^*}{S_F} \qquad \text{Equation 2.11}$$

$$E' = \frac{k'}{S_F} \qquad \text{Equation 2.12}$$

$$E'' = \frac{k''}{S_F} \qquad \text{Equation 2.13}$$

When a viscoelastic material is subjected to a sinusoidal load, the strain response is neither in phase with the induced stress or out of phase by 90° (Ferry, 1980); being in phase the stress or out of phase by 90° would imply a perfectly elastic solid or viscous liquid (Figure 2-10). Thus, as the phase angle increases to 90°, the stored energy becomes negligible compared to the dissipation of energy (Ferry, 1980). The tangent, tan(δ), is a useful parameter to understand the ratio of the dissipation of energy to the storage of energy in a material:

$$\tan(\delta) = \frac{E''}{E'} \qquad \text{Equation 2.14}$$

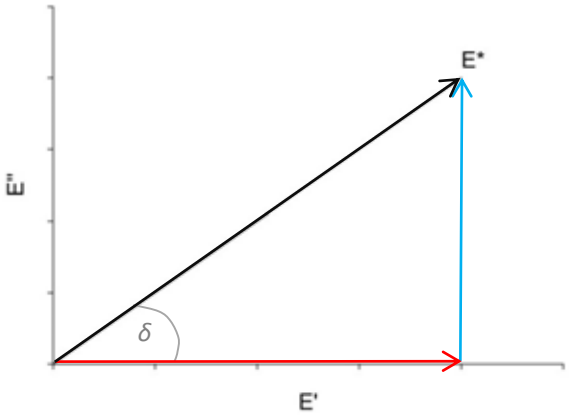

Figure 2-10: Vectorial relationship between the complex *(E^*)*, storage *(E')* and loss *(E'')* moduli. A phase angle (δ) close to 0° implies a more elastic solid material reponse. Adapted from (Ferry, 1980).

Frequency sweep viscoelastic experiments are commonly used to study polymer melt behaviour; however, for other applications, frequency sweep viscoelastic studies are the most neglected experiments (Menard, 2008). By using DMA, many biological materials have been shown to be frequency dependent viscoelastic materials. These materials include bladder (Barnes et al., 2015), bladder tumours (Barnes et al., 2016), articular cartilage (Cooke et al., 2018a, 2018b; Espino et al., 2014; Lawless et al., 2017; Temple et al., 2016), cardiovascular tissue (Burton et al., 2017; Constable et al., 2018) and intervertebral discs (Gadd and Shepherd, 2011; Leahy and Hukins, 2001; Zhou et al., 2014).

2.3 Human Vertebral Column

The human vertebral column is a complex, non-linear structure. The main functions of the vertebral column (Figure 2-11) are to provide support to the head, neck and trunk, to transfer forces to the lower limbs and to protect the spinal cord and cauda equina (Martini et al., 2012). Usually, the vertebral column consists of 33 irregular bones called vertebrae and these vertebrae are divided into five distinct regions: cervical (7), thoracic (12), lumbar (5), sacrum (5) and coccyx (4). The sacral and coccygeal vertebrae are fused while the cervical, thoracic and lumbar vertebrae are known as articulating vertebrae.

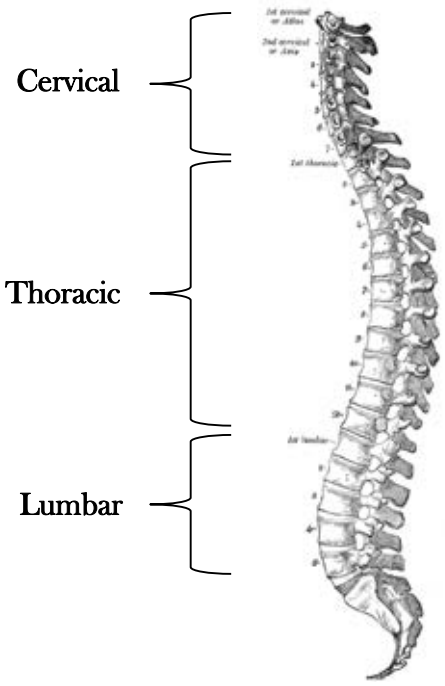

Figure 2-11: Vertebal column. Illustration is in the public domain; plate 111 (Gray, 1918).

Each vertebra (Figure 2-12) consists of three parts: the vertebral body, the vertebral arch and the articular processes. The vertebral body is located anteriorly to the spinal canal and it transfers load along the axis of the vertebral column (Martini et al., 2012). The vertebral body itself comprises mainly of trabecular bone which is surrounded and supported by a thin layer of cortical bone. A thin, porous hyaline cartilage and fibrocartilage endplate is at the cranial and caudal ends of the vertebral body. Posterior to the vertebral body is the vertebral arch. The vertebral arch consists of the pedicles, the laminae, the spinous and transverse processes. The pedicles extend posteriorly from the vertebral body and connect to the laminae to create the vertebral foramina. The vertebral foramen, which begins at the atlas vertebra and ends at the L5 lumbar vertebra, encloses the spinal cord and spinal meninges. Where the laminae meet, the spinous process projects posteriorly while the transverse processes projects laterally from where the pedicles and laminae connect. Also, where the pedicles and the laminae meet, the articular processes are located. Each articular process has a smooth surface, covered in hyaline cartilage, called an articular facet. At the facet joint, the superior articular facet, of the inferior vertebra, articulates with the inferior articular facet, of the superior vertebra (Martini et al., 2012).

Figure 2-12: (left) Lumbar vertebrae and (right) sagittal section of the lumbar vertebra. Illustrations are in the public domain; plates 83 (left) and 92 (right) from (Gray, 1918)

Between the vertebral bodies of the articulating vertebrae lies the intervertebral disc (IVD) (Figure 2-13). In total, there are 23 IVDs. The IVDs keep the vertebral bodies separated and contribute in the movement of the spinal column. The IVD is a frequency dependent viscoelastic structure (Gadd and Shepherd, 2011; Leahy and Hukins, 2001; Zhou et al., 2014) which comprises an annulus fibrosus (AF) and nucleus pulposus (NP) core. The AF is layered with orientated collagen fibre layers and it surrounds the NP. The NP is a gelatinous core consisting of collagen fibrils, proteoglycan and noncollagenous proteins (Kurtz and Edidin, 2006). The NP compresses and displaces to facilitate in the movement of the vertebral column (Martini et al., 2012). The IVD is connected to the vertebral body endplates, called the

symphyseal joint, and the IVD acquires nutrients and fluids through the endplates (Figure 2-13 (A)).

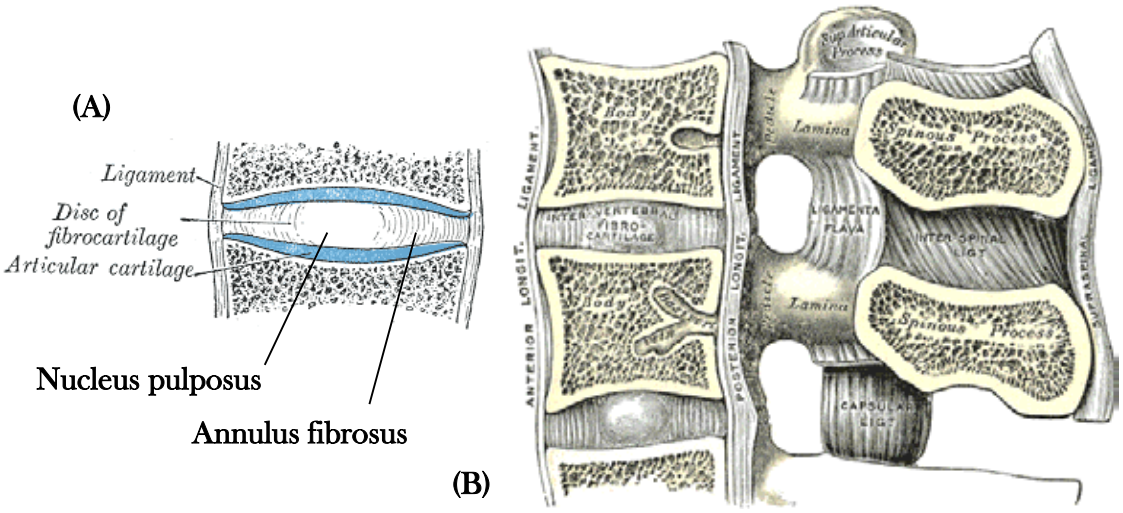

Figure 2-13: Sagittal section views of lumbar vertebrae, intervertebral discs and ligaments. (A) sagittal view of the intervertebral disc and (B) sagittal view of two lumbar vertebrae, ligaments and intervertebral discs. Illustrations are in the public domain; plates 298 (left) and 301 (right) from (Gray, 1918).

In the vertebral column, seven different ligaments connect adjacent vertebrae (Martini et al., 2012); these ligaments are the anterior longitudinal ligament, posterior longitudinal ligament, intertransverse ligaments, ligamentum flavum, facet capsular ligaments, interspinous ligament and supraspinous ligament. Ligaments are uniaxial structures and their functions are to stabilise the vertebral column (Martini et al., 2012), assist in movement and not to allow hyper-movements of the vertebral column. Vertebral column muscles are grouped into three different groups: superficial layer, deep layer and spinal flexors. The purpose of the vertebral column muscles are to contract during vertebral column movements, make delicate adjustments of individual vertebrae and stabilise adjacent vertebrae (Martini et al., 2012).

The spinal cord is part of the central nervous system. Its purpose is to transmit neurological signals from the brain to the peripheries (Martini et al., 2012). The spinal cord is surrounded by the spinal meninges. The spinal meninges are comprised of the dura mater, the arachnoid mater and the pia mater. The spinal meninges protect the neural tissues from the bony structures of the vertebral canal, provide physical stability, protect the blood vessels that deliver nutrients and oxygen to the spinal cord (Martini et al., 2012).

2.4 Orthopaedic Spinal Devices

In England, approximately 80% of the population, at some point in their lives, will seek healthcare advice on spinal pain (NHS England, 2013). Of this 80%, the majority of people can be managed by primary care but approximately 5%, of the population, will endure long-term pain which will affect their quality of life (NHS England, 2013). Low back pain may be caused by one or multiple spinal structures. However, one of the structures commonly associated as a leading cause of low back pain is degeneration of the IVD (Palepu et al., 2012).

The structure and composition of the IVD changes with age (Kurtz and Edidin, 2006) and degeneration of the IVD is part of ageing (Palepu et al., 2012) (Figure 2-14). However, the distinguishing effects of normal ageing and degeneration disc disease (DDD) of the IVD are hard to differentiate (Kurtz and Edidin, 2006). Biochemical changes, that occurs with ageing of the IVD, cause proteoglycans to become fragmented (Adams, 2004) which leads to dehydration of the NP. This results in biomechanical loading changes of the IVD and posterior elements (Pollintine et al., 2004) which can lead to further biochemical and cellular changes that result in the progression of the disc degeneration (Kurtz and Edidin, 2006). The aetiology of DDD is not fully understood (Kurtz and Edidin, 2006), but DDD is linked to multiple factors such as ageing, genetics, occupational factors, accidental back injuries, whole body vibration exposure, smoking and obesity (Battié et al., 2004; Kurtz and Edidin, 2006; Lumoa et al., 1998). Surgical intervention may be required for chronic back pain due to DDD and over 90% of spinal surgery procedures are due to degenerative issues (An et al., 2004; Palepu et al., 2012).

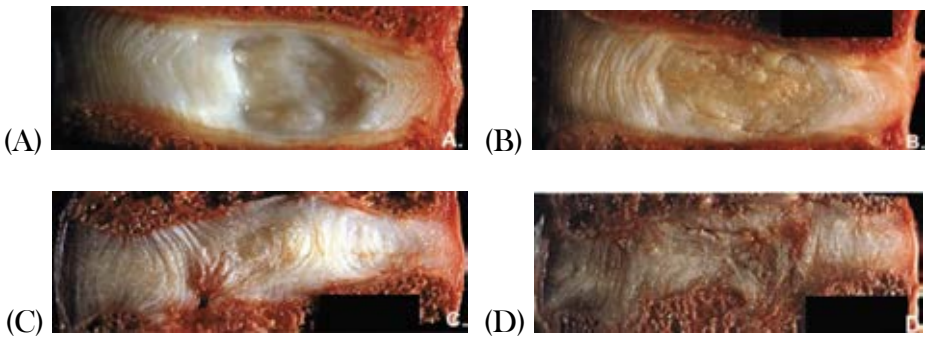

Figure 2-14: IVD degeneration. (A) Healthy, non-degraded IVD, (B) moderately degraded IVD, (C) severely degraded IVD and (D) extremely degraded IVD. Reproduced from Kurtz and Edidin (2006) with a license agreement from Elsevier; this image in Kurtz and Edidin (2006) was adapted from Adams (2002).

2.4.1 Current Devices

Spinal arthrodesis (fusion) is the standard surgical treatment for patients with a variety of degenerative, spinal disorders (Chamoli et al., 2014). In England, 3,559 primary lumbar fusions/disc replacements were performed in 2010-11 (NHS England, 2013) while in the U.S., 488,000 spinal fusions were performed in 2011 (Weiss et al., 2014). Between 1998 and 2008, US hospital charges, for spinal fusion, increased from $4.3 billion to $33.9 billion (Rajaee et al., 2012).

Spinal fusion is the gold standard surgical treatment of low back pain caused by degenerative disorders (Schwarzenbach et al., 2010; Sengupta, 2004; van den Broek et al., 2012b) even though many problems such as prolonged recuperation time, adjacent segment degeneration and pseudarthrosis are associated with it (Serhan et al., 2011). To alleviate these problems, non-fusion techniques have been suggested as an alternative (Cunningham et al., 2010; Serhan et al., 2011). These non-fusion techniques have been developed with the assumption that maintaining biomechanical segment motion is better, for the vertebral column, than eliminating it with fusion (Cunningham et al., 2010). One rapidly evolving non-fusion technique, used for spine surgery, are pedicle screw fixation Posterior Dynamic Stabilisation (PDS) devices (Khoueir et al., 2007; Serhan et al., 2011). Many of these pedicle fixation PDS devices comprise of one or more viscoelastic components: BDyn (S14 Implants, Pessac, France), Dynesys (Zimmer Spine, Warsaw, IN, USA), CD HORIZON BalanC (Medtronic Sofamor Danek, Memphis, TN, USA), Elaspine (Spinelab, Winterthur, Switzerland), NFlex (Synthes Spine Inc., West Chester, PA, USA) and Transition (Globus Medical, Audubon, PA, USA). Even though the main function is similar, i.e. to limit the biomechanical movements of the fixated spinal segment (Palepu et al., 2012), these PDS devices are designed differently, and comprise of different biomaterials, to restrict spinal movement.

2.4.2 BDyn

The BDyn device (S14 Implants, Pessac, France) is a PDS device that provides an alternative to fusion. This bilateral PDS device is designed to preserve intersegmental range of motion, reduce intradiscal pressure and alleviate loading of the facet joints. It can be used in the bridging of one segment level (vertebra-disc-vertebra) or multiple segment levels. The BDyn device consists of two elastomeric components, a mobile titanium alloy rod, a fixed titanium alloy rod, and it is fixed to the vertebrae by titanium alloy pedicle screws (Figure 2-15). The interaction of the mobile rod and the elastomeric components allow partial three-dimensional spinal movement.

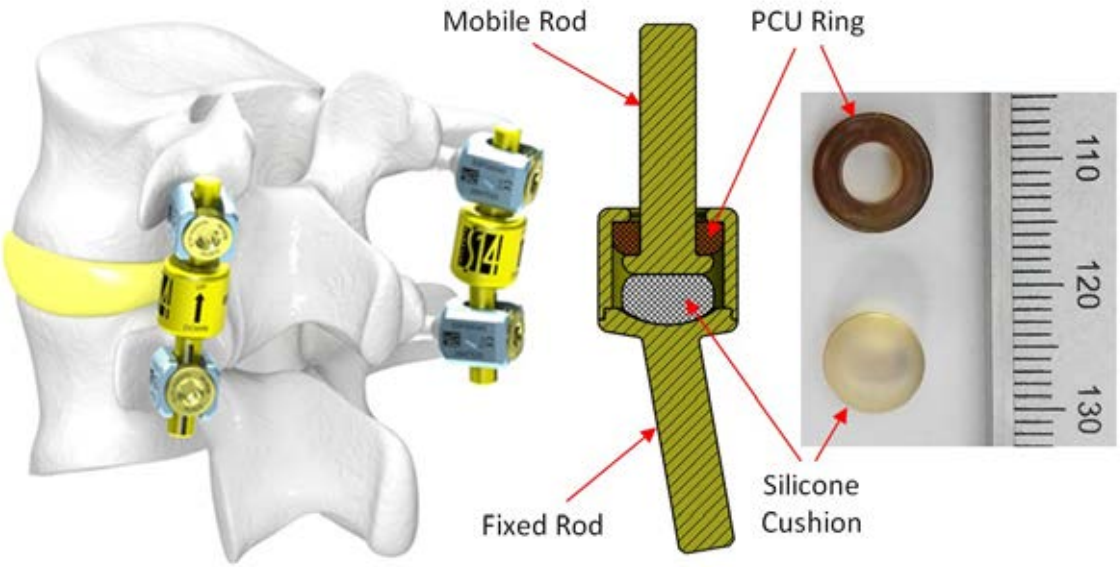

Figure 2-15: BDyn 1 level device fixed to the vertebrae (left) [Reproduced with kind permission from S14 Implants, Pessac, France. © S14 Implants], cross sectional view of the BDyn device (centre) and elastomeric components (right). The polycarbonate urethane (PCU) ring and silicone cushion components, along with the mobile and fixed rods, are highlighted.

The BDyn device has been used in the treatment of degenerative lumbar spondylolisthesis (Gille et al., 2014) and an *in vitro* study has shown that the device can successfully limit the range of motion following a laminectomy of L4-L5 segment (Guerin et al., 2011). To date, it has been implanted in approximately 2,000 patients (S14 Implants, 2017). Recently, the BDyn device was incorporated in a novel dynamic growing rod proposed for use as a surgical treatment of early onset scoliosis (Gonzalez Alvarez et al., 2018).

2.4.3 Other polymeric posterior dynamic stabilisation devices

The Dynesys dynamic stabilisation system (Zimmer Spine, Warsaw, IN, USA) is one of the first dynamic stabilisation systems (Wilke et al., 2009) and one of the most widespread PDS devices used (Schmoelz et al., 2012). In 2011, it was reported that Dynesys had been implanted in more than 42,000 patients (Shen et al., 2011). It comprises of a PCU spacer, a polyethylene terephthalate (PET) cord and titanium alloy pedicle screws (Bothmann et al., 2008; Cunningham et al., 2010; Lee et al., 2008; Welch et al., 2007). The interaction between the PCU spacer and the PET cord allow for restricted spinal movement. Similar to BDyn, Dynesys is a bilateral PDS device that can be instrumented over one or multi-spinal segments.

In 2012, CD HORIZON BalanC (Medtronic Sofamor Danek, Memphis, TN, USA), a dynamic stabilisation system made of and polyetheretherketone (PEEK) and a silicone block, was launched. The silicone block is positioned between the pedicle screws and it is partially surrounded by PEEK. CD HORIZON BalanC is a bilateral system and has been successful used as a hybrid stabilisation system (Formica et al., 2015).

The Elaspine device (Spinelab, Winterthur, Switzerland) comprises pedicle screws and a PCU rod. The PCU rod is connected to the pedicle screws by a locking clip mechanism. Elaspine device was designed to allow relatively homogenous load transmission for all spinal loading directions (Schmoelz et al., 2012).

The NFlex stabilisation system (Synthes Spine Inc., West Chester, PA, USA) comprises titanium alloy pedicle screws and a PCU spacer. The PCU spacer is semi-rigid and in parts, it is surrounded by a titanium ring which the pedicle screws are locked to (Coe et al., 2012). The NFlex device can be used for single level or multiple spinal levels (Coe et al., 2012).

The Transition stabilisation system (Globus Medical, Audubon, PA, USA) is somewhat similar to Dynesys device as it comprises of titanium alloy pedicle screws, PET cord and PCU spacers (Sengupta et al., 2013). The difference with the Dynesys device is that the Transition device consists of two PCU spacers; one spacer at the instrumented level between the pedicle screws while the other spacer is above the superior pedicle screw. The design and positioning of the PCU spacers is to allow a natural compression across the spinal segment and reduce the possibility of screw breakage (Sengupta et al., 2013).

2.5 Biostability

2.5.1 Biostability of polyurethane-based biomaterials

The human body is an aggressive environment for biomaterials (Ramakrishna et al., 2001; Stokes et al., 1995). Once a device is implanted, the human body reacts to the implanted specimen with a foreign body attack and the body's response is to attack and destroy the foreign body (Christenson et al., 2007). At the implantation site, monocytes migrate to the area and differentiate into macrophages (Christenson et al., 2007). The implant is too large to be phagocytosed (the process, the macrophages adhere and fuse to form foreign body giant cells (FBGCs) (Christenson et al., 2007). Adherent macrophages and FBGCs, to the surface of the biomaterial, are known to lead the biodegradation of biomaterials and subsequent clinical device failure (Anderson et al., 2008). At the cell membrane-biomaterial surface interface, the macrophages and FBGCs release degradative agents such as reactive oxygen intermediates (oxygen free radicals), enzymes and acid (Anderson et al., 2008; Christenson et al., 2007; Heiple et al., 1990; Sheikh et al., 2015; Wright and Silverstein, 1983); this has been described as frustrated phagocytosis (Anderson et al., 2008; Henson, 1971a, 1971b). The susceptibility of a biomaterial to degradation, due to these agents at the cell-biomaterial interface, is dictated by the chemical structure of the biomaterial (Anderson et al., 2008; Sheikh et al., 2015).

Since the 1950s, polyurethanes (PUs) have been investigated for numerous biomedical applications (Ghanbari et al., 2009) due to its biocompatibility, biostability, flexibility and toughness (Chandy et al., 2009). The chemical composition of PUs allow it to be tailored to specific requirements (Kanyanta and Ivankovic, 2010) which makes it a suitable material for various types of implantable devices (Chandy et al., 2009). Over the years, numerous hard and soft segment combinations have been utilised for a specific purpose, i.e. increasing the biostability of the biomaterial. The earliest application of PUs was in cardiovascular applications (Akutsu et al., 1959; St John, 2014) and these early PUs utilised a polyester soft segment (Ghanbari et al., 2009; Griesser, 1991). Due to the hydrolytic instability of polyester urethanes, the more stable polyether soft segment was used (Griesser, 1991; Stokes et al., 1987).

Polyether urethanes (PEU) were used in many biomedical applications such as artificial heart valves, pacemaker leads, blood pumps and catheters (Ratner et al., 1988; Thoma and Phillips, 1987; Zhao et al., 1991). Along with increased biostability over polyester urethane, PEU offered high tensile strength and resistance to flex fatigue (Ratner et al., 1988). However, in the late 1980s, PEU pacemaker leads clinically failed (Anderson et al., 2008; Stokes, 1988; Stokes et al.,

1995; Thoma and Phillips, 1987). Explanted PEU leads displayed long term biodegradation with the presence of environmental stress cracks (ESCs) and metal ion oxidation (MIO) (Anderson et al., 2008; Kao et al., 1994; Sheikh et al., 2015; Thoma and Phillips, 1987; Zhao et al., 1993). These ESCs are caused by interaction of macrophages and FBGCs, by frustrated phagocytosis, at the cell-biomaterial interface (Anderson et al., 2008; Christenson et al., 2007; Kao et al., 1994; Zhao et al., 1991, 1993). While MIO of the PEU pacemaker leads was caused by the interaction of the metallic component and oxidation catalysed by corrosion products (Stokes, 1988; Stokes et al., 1995). To increase the biostability, polycarbonate urethanes (PCU) were suggested to provide oxidative and hydrolytic stability (Stokes et al., 1995). Laboratory experiments have demonstrated that PCU is more biostable than PEU (Christenson et al., 2004a; Tanzi et al., 1997; Wiggins et al., 2004). Due to this superiority in biostability, PCU components have been used in cardiovascular (Chandy et al., 2009; Dang et al., 2014; Hartford, 2013) and orthopaedic (Cipriani et al., 2013; Gille et al., 2014; Schmoelz et al., 2003) applications.

2.5.2 Explanted devices and specimens (in vivo degradation)

From the mid-1990s, PCUs have been used in various orthopaedic devices especially in dynamic spinal fixation (Ward and Jones, 2011); see sections 2.4.2 and 2.4.3. As the body breaks down biomaterials by numerous degradation methods, which includes oxidative, hydrolytic and enzymatic, it is important to examine explanted implants by a retrieval analysis. A retrieval analysis gives insight into the implant's performances and investigates whether the implant, and its material components, has been affected from the biological environment (Kurtz et al., 2009).

In relation to polymeric posterior dynamic stabilisation devices, Dynesys has been one of the most investigated devices with regards to retrieval studies (Cipriani et al., 2013; Ianuzzi et al., 2010; Neukamp et al., 2015; Shen et al., 2011; Trommsdorff et al., 2004a, 2004b). By analysing the chemical structure, retrieval studies of explanted Dynesys devices have demonstrated biological oxidative degradation of the PCU components (Cipriani et al., 2013; Ianuzzi et al., 2010; Neukamp et al., 2015). This oxidation of PCU components was not a surprise as Christenson et al. (2006a) demonstrated that PCU is vulnerable to *in vivo* oxidative degradation. To assess the effect of the *in vivo* degradation mechanisms on these biomaterials, studies have attempted to replicate the biodegradation in an *in vitro* set-up.

2.5.3 Biodegradation methods (in vitro degradation)

In vitro biostability studies are useful for relativistic comparisons between implantable biomaterials and to provide directional guidance for *in vivo* studies (Wilkoff et al., 2015); these *in vitro* studies include enzymatic, oxidative and hydrolytic degradation. At the cell/biomaterial interface, adherent macrophages and FBGCs generate localised concentrations of reactive oxygen intermediates (oxygen free radicals), enzymes and acid (Anderson et al., 2008; Christenson et al., 2007; Heiple et al., 1990; Sheikh et al., 2015; Wright and Silverstein, 1983). Studies identified cholesterol esterase (CE) as the most active enzyme in polyurethane degradation (Christenson et al., 2006b; Labow et al., 1999). CE was used to degrade a commercially available PEU (Elasthane 80A) and a PCU (Bionate 80A) and this study concluded that oxidation, rather than enzymatic hydrolysis, is the primary mechanism for the degradation of PEUs and PCUs (Christenson et al., 2006b).

Two common degradation methods, that are used to evaluate polymeric materials of an implantable device, are oxidation and hydrolysis. Oxidative degradation is defined as (ISO, 2010):

"*scission of chemical bonds in a polymer by the attack of one or more oxidising agents*"

Numerous *in vitro* oxidation methods have been described in the literature: Hydrogen peroxide with silver nitrate (Thoma and Phillips, 1987), silver nitrate and lactic acid sodium salt solution (Takahara et al., 1991), hydrogen peroxide and nitric acid (Tanzi et al., 1997), nitric acid (Erdodi et al., 2010; Kang et al., 2010) and mixtures of hydrogen peroxide with cobalt chloride (see Table 2-1).

A popular method of degrading polymers in an *in vitro* scenario is by using hydrogen peroxide (H_2O_2) and cobalt (II) chloride ($CoCl_2$). Over the years, numerous quantities of H_2O_2 and $CoCl_2$ have been examined (see Table 2-1). These methods have used various temperatures, quantities of hydrogen peroxide, cobalt chloride, and time period (Table 2-1).

Table 2-1: Published *in vitro* degradation methods. Number of days per solution changes (days); Mean temperature (Temp). [1] Pre-treated with human plasma (α-macroglobulin) at 37°C for 7 days; [2] Solution was in a spongy glass wool; [3] Stated that the degradation method was based on Zhao et al. (1995) method but degraded for 3 months; [4] Time of experiment read from a graph. Also, changes of solution varied (which is seen from the graph); [5] Specimens were treated with 0.5%, 1%, 2%, 3%, 10%, 20% and 50% H_2O_2; [6] Some specimens were pre-treated with human plasma (α-macroglobulin) at 37°C for 7 days or glass wool.

Lead author	Year	H_2O_2	$CoCl_2$	Time	Days	Temp(°C)
K. Stokes	(1987)	3%	-	6 m	2-3	37
B.D Ratner	(1988)	3%	-	1 d	-	37
B.D Ratner	(1988)	3%	-	7 d	2	37
J.R Frautschi	(1993)	3%	-	180 d	2-3	37
Q.H Zhao [1]	(1993)	10%	0.1 M	10 d	3	50
G.F Meijs	(1993)	25%	-	1 d	-	100
G.F Meijs	(1993)	25%	-	4 & 14 d	2	100
Q.H. Zhao [2]	(1995)	1.63 M	0.05 M	1 m	3-4	37
M.A Schubert [1]	(1995)	10%	0.1 M	9, 12 & 15 d	3	37
M. Tanzi	(1997)	20%	-	21 d	3-4	50
M.A Schubert	(1997)	20%	0.1 M	12 d	3	37
D. Martin [1]	(2001)	10%	0.1 M	10 & 20 d	2-3	50
E.M Christenson	(2004b)	20%	0.1 M	24 d	3	37
I. Khan	(2005a)	3%	-	3 m	7	37
I. Khan [3]	(2005a)	1.63 M	0.05 M	3 m	3-4	37
E.M Christenson	(2005)	20%	0.1 M	36 d	3	37
E.M Christenson	(2006b)	20%	0.1 M	24 d	3	37
B. Ward	(2006)	3%	-	105 & 252 d	2-3	37
D. Sarkar	(2007)	5% 10% 20%	0.1 M	3, 7, 15 & 22 d	7	37
J. McBane	(2007)	20%	-	1 & 3 d	1	37
R. Hernandez	(2008)	20%	0.1 M	24, 48 & 72 d	3	37
T. Chandy	(2009)	20%	0.1 M	1, 3, 5, 7, 10 m	3-4	37
S. Jewrajka	(2009)	20%	0.1 M	40	3-4	50
J. Kang [4]	(2010)	20%	0.1 M	100 d approx.	Varied	37
G.N Arjun	(2012)	20%	0.1 M	90 d	7	45
Y. Andriani	(2013)	20%	0.1 M	28 & 49 d	4	37
N. Arora	(2013)	20%	0.1 M	7 d	-	37
D.K Dempsey	(2014)	3%	-	365 d	7	37
D.K Dempsey	(2014)	20%	0.1 M	36 d	3	37
A. Weems [5]	(2017)	Varied	-	36, 45,140 d	3	37
A. Weems [5]	(2017)	20%	0.1 M	Varied	3	37
G. Gallagher [6]	(2017)	20%	-	72 d	3-4	37
G. Gallagher [6]	(2017)	20%	0.1 M	72 d	3-4	37

The mixture of H_2O_2 and $CoCl_2$ induces a Haber-Weiss reaction that creates hydroxyl radicals. This mixture and creation of these hydroxyl radicals have been deemed sufficient in the *in vitro* degradation of polymer as these radicals are present at the cellular/polymer interface of the biomaterial; this is similar to the oxygen radicals that are present *in vivo* (Christenson et al., 2007).

$$Co^{++} + H_2O_2 \rightarrow Co^{+++} + HO^- + HO\bullet$$

The most popular of these H_2O_2 and $CoCl_2$ methods (Table 2-1) to replicate oxidation is the 20% H_2O_2 and 0.1M $CoCl_2$ solution at 37°C (Andriani et al., 2013; Arora et al., 2013; Chandy et al., 2009; Christenson et al., 2006b, 2005, 2004a; Dempsey et al., 2014; Gallagher et al., 2017; Hernandez et al., 2008; Kang et al., 2010; Sarkar and Lopina, 2007; Schubert et al., 1997; Weems et al., 2017). The reason for this is that the H_2O_2 and $CoCl_2$ method accurately reproduces the *in vivo* effect, after one year, in 24 days (Christenson et al., 2006b). This *in vitro* method has been shown to reproduce chemical and physical degradation similar to *in vivo* oxidative degradation of PEU and PCU after one year in a Sprague-Dawley rat model (Christenson et al., 2006a).

To standardise oxidative degradation of polymeric materials, the International Organisation for Standardisation (ISO) published an *in vitro* oxidative degradation method. A test solution suggested for oxidation is the use of 3% H_2O_2 at 37 ± 1 °C for up to one year (ISO, 2010) and this 3% H_2O_2 method has been used previously (see Table 2-1). A recent study by Dempsey et al. (2014) degraded commercially available PCU and PCU with silicone biomaterials and compared the ISO 3% H_2O_2 method to the 20% H_2O_2 and 0.1 M $CoCl_2$ method. For the degradation of PCU, Dempsey et al. (2014) concluded that the 3% H_2O_2 method does not simulate an oxidative environment and that the 20% H_2O_2 / 0.1 M $CoCl_2$ method should be used for predicting oxidative stability of segmented polyurethanes.

Hydrolytic degradation is defined as (ISO, 2010):

"*scission of chemical bonds in a polymer by the attack of water*"

Water is a very loose term for the definition as it can have a *"neutral, acidic of alkaline pH value and can contain additional chemical compounds or ions"* (ISO, 2010). In ISO 10993-13, there are two hydrolytic degradation methods: Real-time degradation test and accelerated degradation test. The recommended solution for both degradation tests is the same with either (ISO, 2010):

- Grade 2 water for analytical laboratory use in accordance with ISO 3696
- Buffer; see ISO 13781 for examples.

Phosphate buffer saline (PBS) solution is one particular buffer listed in ISO 13781 and this buffer has been used in previous studies in the degradation of segmented polyurethanes (Chaffin et al., 2014, 2012; Khan et al., 2005a; Mishra et al., 2015). However, the difference between the real-time and accelerated degradation tests is the temperature at which the solution should be; real-time solution temperature is 37 ± 1°C while accelerated solution temperature is 70 ± 2°C (ISO, 2010). By utilising a higher temperature, the accelerated method allows the prediction of the effect of ageing. A common method is the assumption that the rate of ageing is increased by a factor (Hukins et al., 2008):

$$f = 2^{\Delta T/10} \qquad \text{Equation 2.15}$$

where,

$$\Delta T = T - T_{ref} \qquad \text{Equation 2.16}$$

For equation 2.16, T refers to the elevated temperature the biomaterial is degraded at while T_{ref} refers to the reference temperature i.e. the temperature of the human body. As an example, for equation 2.15 and 2.16, if a biomaterial is degraded at 70°C for 76 days, this is equivalent to just over 2 years in the body at 37°C.

Studies have used elevated temperatures (T_{ref} > 37°C) to predict properties of hydrolytically degraded biomaterials (Chaffin et al., 2014, 2012; Mahomed et al., 2015; Mishra et al., 2015; Pretsch et al., 2009). However, recently, Padsalgikar et al. (2015) highlighted issues in using the accelerated degradation tests as the predicted long-term *in vitro* performance did not correlate to the *in vivo* performance.

This correlation issue between *in vitro* predictions and *in vivo* assessment was seconded by Wilkoff et al. (2015). Optim (OPT) cardiac lead insulation (St. Jude Medical, USA), which is sometimes referred to as ElastEon 2A (E2A) biomaterial (AorTech, Surrey, UK), is segmented polyurethane with polydimethylsiloxane (PDMS) and polyhexamethylene oxide (PHMO) soft segments. After 4-5 years *in vivo* implantation, Wilkoff et al. (2015) discovered that the molecular weight of OPT decreased by approximately 20% while Chaffin et al. (2012) *in vitro* accelerated treatment, at 85°C approximated to six years at 37°C, of E2A would lose over 50% of its molecular weight. Further, OPT ultimate tensile strength (UTS) decreased by approximately 20-25% after 4-5 years of implantation (Wilkoff et al., 2015) while the accelerated *in vitro* predicted a decrease, in the UTS, by over 50% (Chaffin et al., 2012).

To accurately predict the changes of a biomaterial at 37°C by utilising a higher temperature and a short degradation time period, i.e. applying the Time Temperature Superposition, the biomaterial in question must respond equally to temperature in the temperature range being tested (Han and Kim, 1993; Padsalgikar et al., 2015). Temperature independence can be illustrated with the use of Dynamic Mechanical Temperature Analysis (DMTA) and investigating the linearity of storage *(E')* and loss *(E")* moduli in a log-log plot (Han and Kim, 1993; Padsalgikar et al., 2015).

2.6 Chapter Summary

In summary:

- The human vertebral column is a complex, non-linear, multi-component structure.
- The viscoelastic behaviour of different biological structures, like the intervertebral disc, is frequency dependent.
- Unlike creep and stress relaxation, dynamic mechanical analysis is a dynamic method to quantify the frequency dependent viscoelastic properties of a multi-component structure or material.
- To alleviate problems associated with spinal fusion, the gold standard surgical treatment of low back pain, non-fusion techniques, such as posterior dynamic stabilisation devices, have been suggested as an alternative.
- Some of these posterior dynamic stabilisation devices have elastomeric biomaterial components.
- These elastomeric components have been shown to be susceptible to oxidative and hydrolytic degradation in the human body.
- The understanding of the effect of degradation on the frequency dependent viscoelastic properties of these elastomeric posterior dynamic stabilisation devices, and its biomaterials, is unknown.

Information about the materials and methods used in this thesis is provided in the next chapter.

Chapter 3

Materials and methods

3 Materials and methods

This chapter provides detailed information about the materials (sections 3.1 and 3.2), degradation protocols (sections 3.3 and 3.4), chemical structure characterisation (section 3.5), viscoelastic testing (sections 3.6 and 3.7), surface morphology characterisation (section 3.8) and statistical analyses (section 3.9) methods used in this thesis. Study specific methods are discussed in the materials and methods sections (sections 4.2 and 5.2) in subsequent chapters (Chapters 4 and 5).

3.1 Long-term implantable biomaterials

3.1.1 Biomaterials

Five different commercially available, long-term implantable polycarbonate urethane (PCU) biomaterials were used for testing:

- Bionate II 80A (DSM Biomedical, Exton, PA, USA)
- Quadrathane ARC 80A (Biomerics, Salt Lake City, UT, USA)
- Quadrathane ARC 80A-B20 (Biomerics, Salt Lake City, UT, USA)
- ChronoFlex C 80A (AdvanSource Biomaterials, Wilmington, MA, USA)
- ChronoSil AL 80A 5% (AdvanSource Biomaterials, Wilmington, MA, USA)

Bionate II is an aromatic PCU with a hard segment of methylene di(p-phenyl isocyanate) (MDI) and butane diol (BDO) and a polycarbonate glycol soft segment (Dempsey et al., 2014). Quadrathane and Quadrathane B20 are aromatic PCUs that have an MDI/BDO hard segment and a polycarbonate based soft segment (Mishra et al., 2015). The difference between Quadrathane and Quadrathane B20 is that Quadrathane B20 is compounded with a radiopacifier (20%, by weight, barium sulfate).

ChronoFlex C 80A is an aromatic PCU that has a MDI/BDO hard segment and a polycarbonate based soft segment (Mishra et al., 2015). The only biomaterial, out of the five being analysed in this thesis that is not aromatic is ChronoSil AL 80A 5%. ChronoSil 5% is an aliphatic PCU with a 5% silicone additive; the addition of silicone has been shown to increase the biostability of PCUs (Christenson et al., 2005).

3.1.2 Specimen Manufacturing

All of the biomaterials were purchased in pellet form and they were injection moulded to the specific manufacturer's recommendations at the Warwick Manufacturing Group (University of Warwick, Coventry, UK). The pellets were moulded in 150 mm × 150 mm sized plaques (ISO, 2014) with a thickness of 3 mm ± 0.2 mm. As per implantation protocols, the plaques were sterilised by Ethylene Oxide (EtO) (Steriservices, Bernay, France). The EtO sterilisation process involves 3 cycles with an EtO concentration of 600 mg/L for 4 hours at 43°C. No separate aeration was performed as it is performed in the sterilisation chamber. The plaques were labelled for the oxidation or hydrolysis studies; this was to ensure no batch differences. Next, ASTM D1708 specimen shaped dumbbells were cut (ASTM, 2013) by using a die cutter (Wallace Instruments, Cambridge, UK) on a Wallace Hand Operated Specimen Cutting Press (Wallace Instruments, Cambridge, UK) (Figure 3-1 (A) and (B)). From each plaque, 23 specimens were cut (Figure 3-1 (C)).

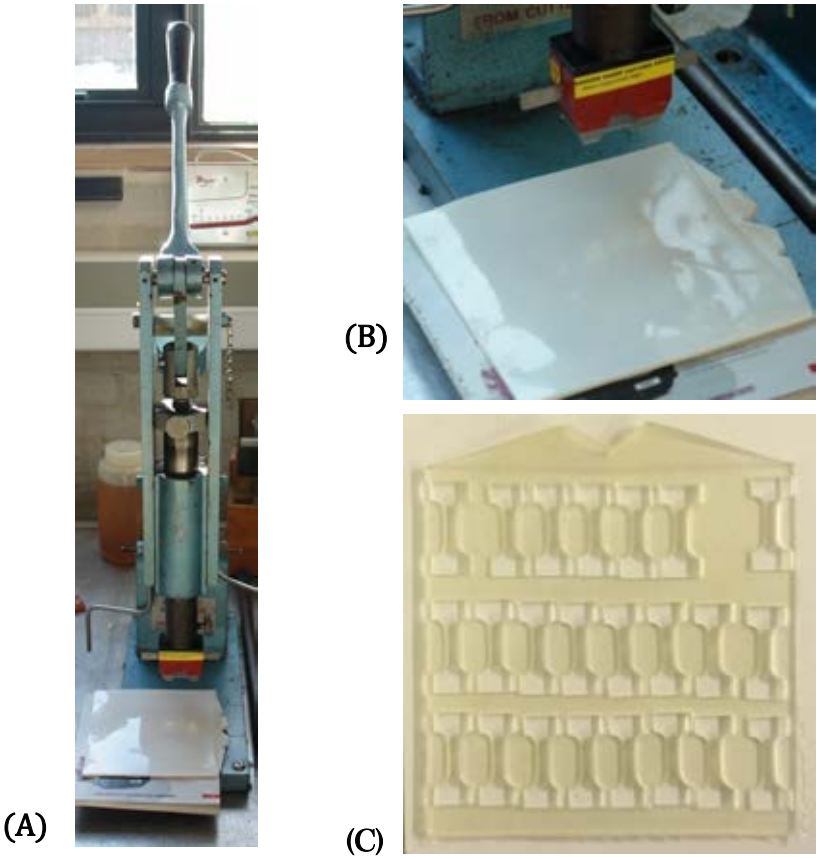

Figure 3-1: (A) Wallace Hand Operated Cutting Press, (B) Quadrathane 80A-B20 before dumbbell specimen cutting and (C) Quadrathane 80A after specimen cutting.

Once a plaque was cut into 23 specimens, the specimens were numbered and an Excel random order generator function (Microsoft, Redmond, Washington, USA) was used to separate the specimens into three groups; Control (n = 6), Degradation Group A (n = 6) and Degradation Group B (n = 6); information on these degradation groups can be found in sections 3.3 and 3.4.

The ASTM D1708 standard specimen shaped dumbbells (see Figure 3-2 and section 8.1 Appendix A) were used for Chapter 4 - Biostability of PCU biomaterials; this specimen shape has been widely used in previous biostability studies (Chaffin et al., 2012; Christenson et al., 2006a; Dempsey et al., 2014; Schubert et al., 1997, 1995; Stokes et al., 1987; Wiggins et al., 2004; Wilkoff et al., 2015).

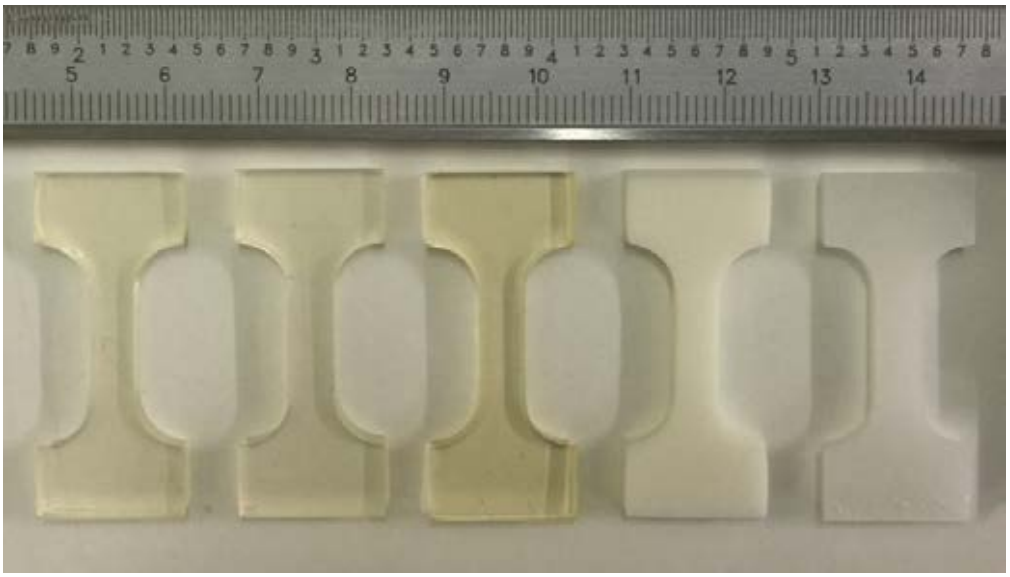

Figure 3-2: Tensile ASTM D1708 dumbbell specimens of the five different long-term implantable biomaterials. From left to right; Quadrathane ARC 80A, ChronoFlex C ARC 80A, Bionate II 80A, Quadrathane ARC 80A-B20 (radiopacifier additive) and ChronoSil AL 80A 5%.

3.2 BDyn

The BDyn posterior dynamic stabilisation device (S14 Implants, Pessac, France) consists of two elastomeric components, a mobile titanium alloy rod, a fixed titanium alloy rod, and it is fixed to the vertebrae by titanium alloy pedicle screws (Figure 2-15). The titanium alloy used for the mobile rod, the fixed rod, the housing is Ti-6Al-4V. The two elastomeric components are a PCU ring (Bionate II 80A, DSM Biomedical, Exton, PA, USA) and a silicone cushion (MED 4770, NuSil Technology LLC, Carpinteria, CA, USA) (Figure 3-3 and section 8.2 Appendix B).

Both elastomeric components are ion treated. This ion treatment has been shown to increase scratch resistance of polymers by increasing the hardness of the surface layer (Kondyurin and Bilek, 2015; Shi et al., 2001) and it has been shown to improve the tribological properties of ultra-high molecular weight polyethylene (UHMWPE), high-density polyethylene (HDPE) and low-density polyethylene (LDPE) used in total joint replacements (Abdul-Kader et al., 2010; Shi et al., 2001; Sze and Tay, 2006). As per implantation protocols, the BDyn device was sterilised by EtO (Steriservices, Bernay, France). Similar to the EtO sterilisation process described in section 3.1.2, the sterilisation process involves 3 cycles with an EtO concentration of 600 mg/L for 4 hours at 43°C. No separate aeration was performed as it is performed in the sterilisation chamber.

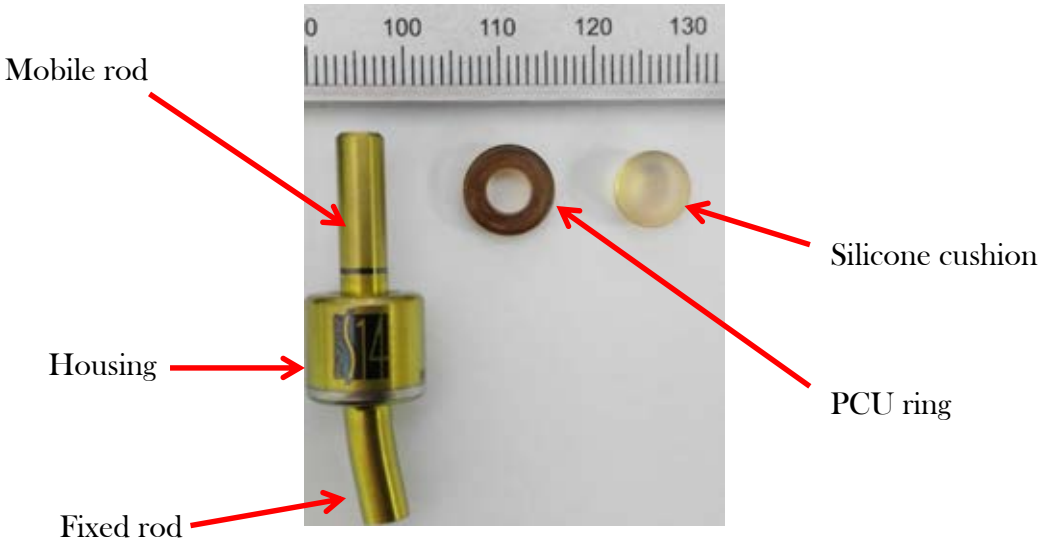

Figure 3-3: From left to right; The BDyn 1 level device, PCU ring (Bionate II 80A) and silicone cushion (MED 4770). The housing, mobile and fixed rods are all titanium alloy (Ti-6Al-4V).

3.3 *In vitro* oxidation

To prepare the oxidative solutions, 30% Hydrogen Peroxide (H_2O_2) (Fisher Scientific, Loughborough, UK) and 0.1 *M* cobalt (II) chloride hexahydrate ($CoCl_2.6H_2O$) ($CoCl_2$) (Sigma Aldrich, Gillingham, Dorset, UK) were used. The 30% H_2O_2 was diluted, using deionised water, to 3% H_2O_2 and 20% H_2O_2 concentration levels. All mass measurements of H_2O_2, deionised water and solution to be added to each tube was measured using an A&D EK-2000i top pan balance (A&D Instruments, Abingdon, Oxfordshire, UK). An Ohaus GA200D analytical balance (Ohaus Corporation, Parsippany, NJ, USA) was used for the mass measurements of $CoCl_2$. The *in vitro* oxidative degradation of all biomaterials and BDyn components were performed in 50 mL medical grade polypropylene tubes (Corning, Wiesbaden, Germany) (Figure 3-4).

For the 3% method, the oxidation of the biomaterials was performed at 37 ± 1°C in a water bath (JB5 Water Bath, Grant Instruments, Cambridgeshire, UK). The solution was changed every 7 days for 52 weeks (Dempsey et al., 2014). The 20% H_2O_2/0.1 *M* $CoCl_2$ accelerated ageing of the biomaterials were performed at 37 ± 1°C in a water bath (JBN18 Water Bath, Grant Instruments, Cambridgeshire, UK). To maintain a relative constant concentration of radicals (Dempsey et al., 2014; Hernandez et al., 2008), the solution was changed every 3 days and the degradation period lasted 24 days. After the 3% (52 weeks) and 20% H_2O_2/0.1 M $CoCl_2$ (24 days) degradation periods, the specimens were rinsed with deionised water and were vacuum dried for 48 hours at room temperature.

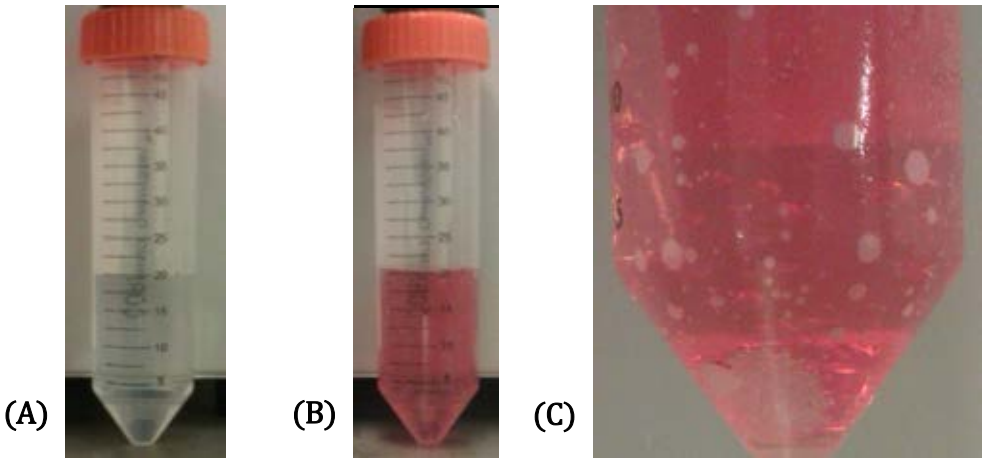

Figure 3-4: (A) 3% H_2O_2 (B) 20% H_2O_2/0.1 *M* $CoCl_2$ and (C) BDyn silicone component in the 20% H_2O_2/0.1 *M* $CoCl_2$ solution.

3.4 *In vitro* hydrolysis

Phosphate buffer saline (PBS) tablets (Sigma Aldrich, Gillingham, Dorset, UK) were used to prepare the hydrolytic solutions. The PBS tablets were diluted, using deionised water, to the appropriate concentration levels; one tablet dissolved in 200 mL of deionised water. This yields a solution of 0.01 M phosphate buffer, 0.0027 M potassium chloride (KCl) and 0.137 M sodium chloride (NaCl) at pH 7.4 which is similar to the buffer solution recommended in ISO 13781:2017 (ISO, 2017); this buffer is suggested for hydrolytic degradation in ISO 10993-13 (ISO, 2010). All mass measurements of the PBS solution, which was individually added to each tube, were measured using either an Ohaus Emerald 500 portable balance (Ohaus Corporation, Parsippany, NJ, USA) or an A&D EK-2000i top pan balance (A&D Instruments, Abingdon, Oxfordshire, UK). Similar to the *in vitro* oxidation experiments (section 3.3), *in vitro* hydrolytic degradation experiments of all biomaterials were performed in 50 mL medical grade polypropylene tubes (Corning, Wiesbaden, Germany) (Figure 3-4).

Both real-time and accelerated degradation tests of the biomaterials were performed in separate JBN18 water baths (JBN18 Water Bath, Grant Instruments, Cambridgeshire, UK) with real-time and accelerated temperatures of 37 ± 1°C and 70 ± 2°C (ISO, 2010), respectively. The solution was changed every 7 days for 52 weeks. After the degradation period the specimens were rinsed with deionised water and were vacuum dried for 48 hours at room temperature.

3.5 Spectroscopy

3.5.1 Infra-red spectroscopy

Infra-red spectroscopy is used to identify and quantify the chemical structure of solids, liquids or gases. The chemical structures of such materials are quantified by the interaction of infra-red radiation with the matter. Alongside mass spectrometry (MS) and nuclear magnetic resonance (NMR) spectroscopy, Fourier transform infra-red (FTIR) spectroscopy is one of the three recommended techniques to quantify the chemical structure of polymers (Dorrepaal et al., 2018; ISO, 2009) and one widely used FTIR technique is attenuated total reflectance Fourier transform infra-red (ATR-FTIR).

3.5.2 Attenuated total reflectance Fourier transform infra-red (ATR-FTIR)

For attenuated total reflectance Fourier transform infra-red (ATR-FTIR) spectroscopy, the infra-red beam passes through the ATR crystal, which is in contact with the surface of the specimen, and reflects off the surface. An evanescent wave is due to the reflection and this wave penetrates into the specimen (approximately 2 μm). The beam exits the ATR crystal and is collected by the detector. ATR-FTIR has been used in characterising degradation of:

- Explanted orthopaedic (spinal) devices (Cipriani et al., 2013; Ianuzzi et al., 2010; Neukamp et al., 2015; Shen et al., 2011; Trommsdorff et al., 2004b);
- Explanted cardiac leads insulation (Wiggins et al., 2001; Wilkoff et al., 2015);
- Explanted biomaterials from animal models (in vivo degradation) (Christenson et al., 2006a, 2004b, Simmons et al., 2008, 2004);
- Degradation of biomaterials from laboratory experiments (in vitro degradation) (Dempsey et al., 2014; Hernandez et al., 2008; Lawless et al., 2018; Mahomed et al., 2010; Padsalgikar et al., 2015; Schubert et al., 1997).

ATR-FTIR point spectroscopy was performed using a Bruker LUMOS spectrometer (Bruker Optics, Billerica, MA, USA). Spectra were recorded in absorbance mode with a Germanium ATR crystal. Twenty spectra, with a spectral resolution of 2 cm^{-1} between 600 and 4000 cm^{-1}, were acquired and mean averaged to obtain each spectrum (Simmons et al., 2004). This point spectroscopy method was utilised for the *in vitro* oxidation of the BDyn components (chapter 5 - Biostability of the BDyn Posterior Dynamic Stabilisation device) and further information of the chemical structure characterisation can be found in section 5.2.2.1. All other chemical structure characterisation was performed with hyperspectral chemical imaging (HCI).

3.5.3 Hyperspectral chemical imaging (HCI)

Hyperspectral chemical imaging (HCI) combines spectroscopy with imaging and it enables the acquisition of spatially localised spectra across the surface of a material (Dorrepaal et al., 2018; Gowen and Dorrepaal, 2016; Mukherjee and Gowen, 2015). HCI is a technique that has been utilised for biochemical processes at the cellular level (Kuimova et al., 2009) and the evaluation of the molecular state of polymer matrices for drug release (Chan and Kazarian, 2006). Recently, a study, in which I am co-first author, demonstrated that ATR-FTIR HCI reveals spatial variations in the degradation of polymer biomaterials (Dorrepaal et al., 2018). Further,

the use of HCI in biodegradation of biomaterials is a more objective technique, than conventional point ATR-FTIR spectroscopy methods (Dorrepaal et al., 2018).

HCI by ATR-FTIR was performed using a Thermo-Scientific Nicolet iN10Mx infra-red microscope (Thermo-Fisher Scientific, Madison, WI, USA). Spectra were recorded in absorbance mode with a slide-on Germanium ATR micro tip crystal. Imaging factors such as, aperture size, spatial resolution, distance between each pixel, etc. are study specific and further information of these parameters are in chapters 4 - Biostability of PCU biomaterials and chapter 5 - Biostability of the BDyn Posterior Dynamic Stabilisation device (sections 4.2.2 and 5.2.2, respectively). The scale bars on all hyperspectral chemical images and hyperspectral chemical maps (HCMs) are arbitrary units (AU).

3.6 Micro-dynamic mechanical analysis (μDMA)

The micro-level viscoelastic properties of all biomaterials, undegraded and degraded by oxidation and hydrolysis, were measured using a customised nano-indenter testing machine (Chavan et al., 2012), with a commercial interferometer (OP1550, Optics11, Amsterdam, The Netherlands) running customised LabVIEW 16.0 software (Figure 3-5); the nano-indenter testing machine used is similar to the PIUMA Nano-indenter (Optics11, Amsterdam, The Netherlands).

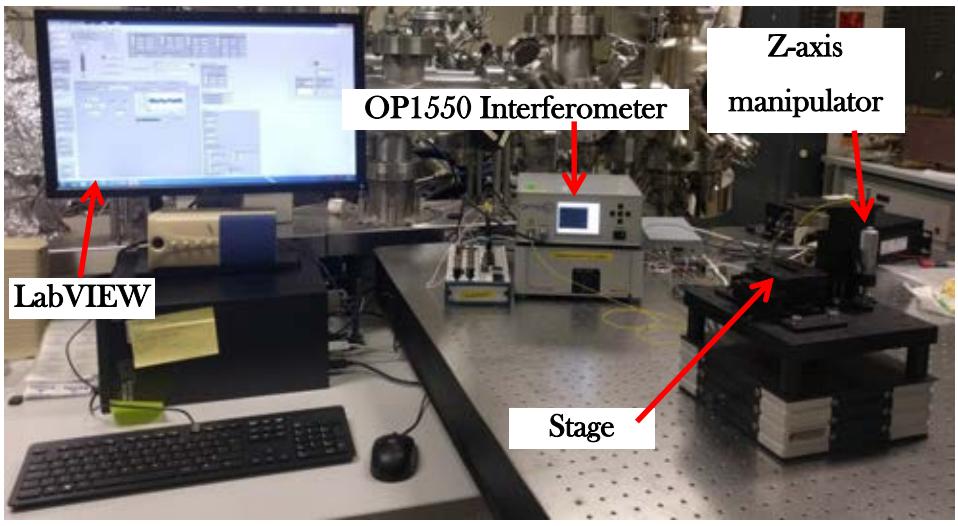

Figure 3-5: Customised nano-indenter testing set-up

Before μDMA testing, a customised probe was manufactured. For the manufacturing of the probe, a 3 mm × 3 mm × 7 mm glass ferrule (VitroCom, Mountain Lakes, New Jersey, USA) (Figure 3-6 (A)) was mounted on a diamond wire cutter and a ridge (500 μm × ~400 μm) was removed (Figure 3-6 (B)). A rectangular glass ribbon 30 μm [thickness] × 300 μm [width] (VitroCom, Mountain Lakes, New Jersey, USA) was sputter coated with a 10 nm thick chromium layer followed by a 100 nm thick gold layer to make it reflective and was subsequently bonded to the glass ferrule (Figure 3-6 (C)).

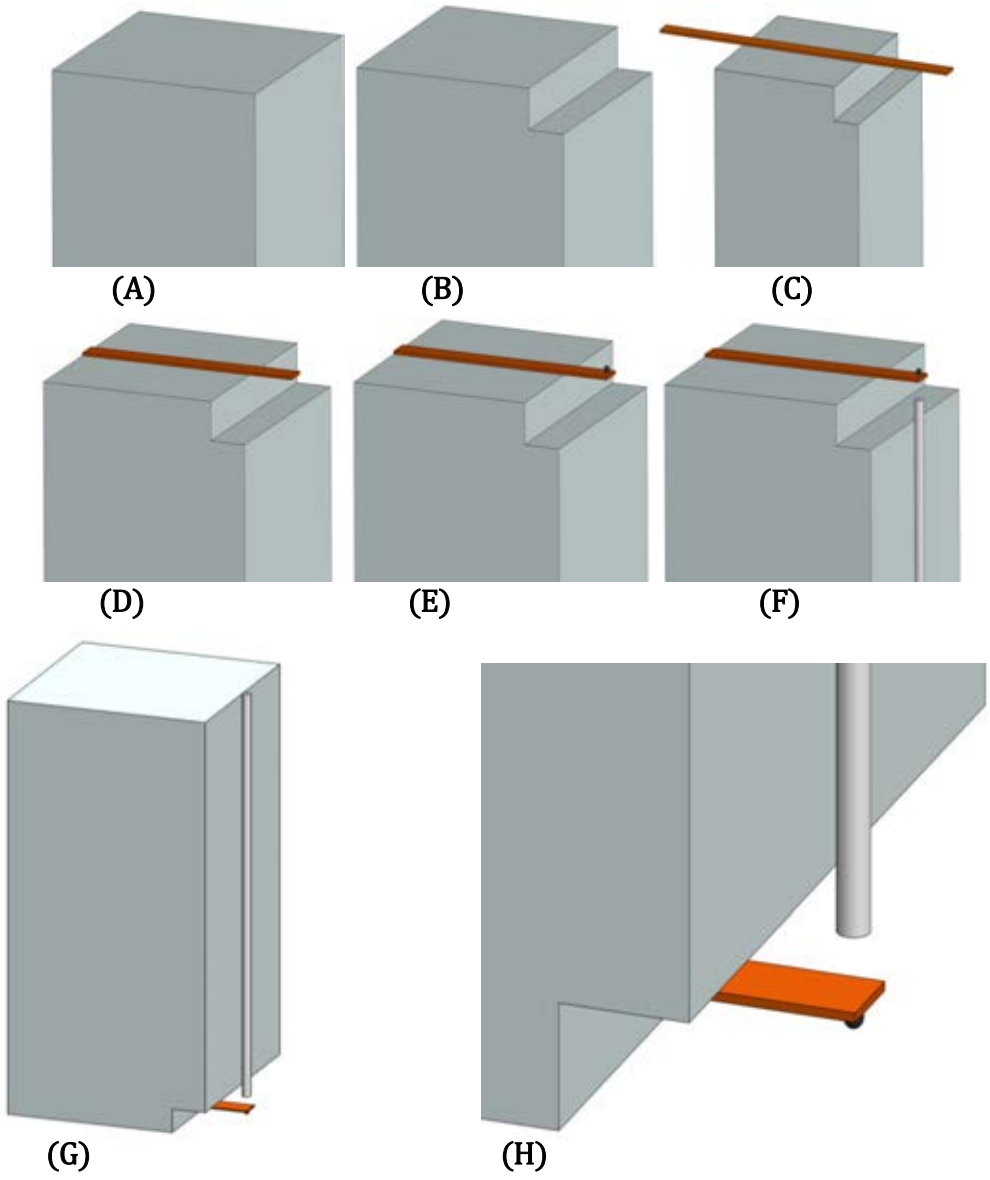

Figure 3-6: (A-F) Manufacturing of the probe, (G) finished probe and (H) zoomed in section of the the indenter. Dimensions of the probe can be found in and section 8.3 Appendix C.

A micrometre precision screw stage was used to accurately set the desired length of the glass ribbon, then, laser ablation was performed to cut off excess ribbon (Figure 3-6 (D)). Next, a borosilicate glass sphere, with a radius of 37 μm (Figure 3-6 (E) and section 8.3 Appendix C), was bonded (Norland 68 Ultra-Violet Curing Adhesive, Norland Products Inc., Cranbury, NJ, USA) to the cantilever tip. Finally, a standard single mode 125 μm optical fibre was cleaved, to create more back reflections which were needed to create one of the two light signals in the interference pattern, and bonded to the ferrule facing the cantilever (Figure 3-6 (F)). The stiffness of the probe was subsequently measured using a custom-built calibration rig; the probe stiffness was 480 ± 13 N/m and further information on the custom-built calibration rig and calibration procedure can be found in Beekmans and Iannuzzi (2015).

Experimental factors such as applied sinusoidal load, investigated frequencies, etc. are study specific and further information of these parameters are detailed in chapter 4 - Biostability of PCU biomaterials (sections 0).

3.7 Dynamic Mechanical Analysis (DMA)

The viscoelastic properties of all components, BDyn implants and biomaterials were measured using a Bose ElectroForce 3200 testing machine running WinTest 4.1 DMA software (Bose Corporation, Electroforce Systems Group, Minnesota, USA; now, TA Instruments, New Castle, DE, USA). The DMA technique, machine and software have been used to quantify the viscoelastic properties of various biological tissues (Barnes et al., 2016; Constable et al., 2018; Cooke et al., 2018a; Fulcher et al., 2009; Lawless et al., 2017; Temple et al., 2016), implantable biomaterials (Mahomed et al., 2009a, 2009b, 2008; Murata et al., 2000), degraded biomaterials (Mahomed et al., 2015, 2010) and mineralised hydrogels (Majumdar et al., 2018; Wands et al., 2008).

All testing was performed in air at 37°C ± 1°C in a custom-built chamber (Figure 3-7 and 8.4 Appendix D) in which water was pumped around the chamber by a Cole Parmer water circulating bath and pump with digital control (Model: 12107-15, Cole Parmer, St Neots, Cambridgeshire, UK). The air temperature was monitored throughout the frequency sweep with a SLS digital thermometer (Scientific Laboratory Supplies (SLS), Wilford, Nottingham, UK) (Figure 3-7).

(A) 

(B) 

Figure 3-7: (A) Bose ElectroForce 3200 testing machine with custom built chamber and water circulating pump and (B) custom built chamber with thermometer.

Other experimental factors such as applied sinusoidal load, requested frequencies (and actual tested frequencies; Table 3-1), machine fixtures used, etc. are study specific and further information of these parameters are detailed in chapter 4 - Biostability of PCU biomaterials and chapter 5 - Biostability of the BDyn Posterior Dynamic Stabilisation device (sections 4.2.4 and 5.2.3, respectively).

Table 3-1: Requested (Hz) and actual (Hz) tested frequencies for a Bose 3200 machine running 4.1 DMA software

Requested (Hz)	Actual (Hz)	Requested (Hz)	Actual (Hz)	Requested (Hz)	Actual (Hz)
0.01	0.01	0.4	0.4	10	10
0.02	0.02	0.5	0.5	15	15
0.03	0.03	0.75	0.75	20	20
0.04	0.04	1	1	25	24
0.05	0.05	2	2	30	29
0.1	0.1	3	3	35	34
0.2	0.2	4	4	40	39
0.3	0.3	5	5	45	44
				50	49

3.8 Scanning Electron Microscopy (SEM)

The surface morphology of all biomaterials and BDyn components investigated in the thesis, was examined using the Hitachi TM3030 Scanning Electron Microscope (SEM) (Chiyoda, Tokyo, Japan). The specimens were examined with back-scatter detector at a 15 kV accelerating voltage.

3.9 Statistical analysis

All statistical analysis was performed using SigmaPlot (Systat Software Inc., San Jose, California, USA). Specific regression analyses, statistical hypotheses tests comparing groups, etc. are study specific and further information of these parameters are detailed in chapter 4 - Biostability of PCU biomaterials and chapter 5 - Biostability of the BDyn Posterior Dynamic Stabilisation device (sections 4.2.6 and 5.2.5, respectively). Statistical results with $p < 0.05$ were considered significant.

3.10 Chapter Summary

In summary, this chapter provided detailed information about the five different commercially available biomaterials, degradation protocols, chemical structure characterisation methods, viscoelastic testing methods, surface morphology characterisation techniques and statistical analyses used in this thesis. Study specific methods are discussed in the materials and methods sections of subsequent chapters (Chapters 4 and 5).

The biostability of the five biomaterials is investigated in the next chapter.

Chapter 4

Biostability of PCU biomaterials

4 Biostability of PCU biomaterials

4.1 Introduction

In 2016, the biomaterials market was worth $70.9 billion (Marketsandmarkets.com, 2016). Broadly, biomaterials fall into four main categories: metallic, ceramic, polymeric and natural (biological) biomaterials. Polymeric biomaterials are commonly used in medical device applications and one of the highest performing medical-grade polymers are polyurethanes (PU) (Khan et al., 2005a). PU biomaterials have a unique combination of suitable mechanical and biological properties, such as durability, elasticity, flexibility, toughness, biocompatibility and biostability (Chandy et al., 2009; Jaganathan et al., 2014; Khan et al., 2005a); a brief background about PU biomaterials and the biostability of PUs can be found in section 2.5.

Due to its increase in biostability over polyester urethanes and polyether urethanes (see section 2.5), PCU has been widely used in cardiovascular (Chandy et al., 2009; Dang et al., 2014; Hartford, 2013) and orthopaedic (Cipriani et al., 2013; Gille et al., 2014; Schmoelz et al., 2003) applications. PCU components have been shown to degrade due to implantation (Cipriani et al., 2013; Ianuzzi et al., 2010; Neukamp et al., 2015) and the degradation mechanism, that PCU components have been susceptible to, is oxidative degradation (Christenson et al., 2006a).

In vitro biostability studies do not fully reproduce degradation that happens *in vivo* (ISO, 2010; Wilkoff et al., 2015). However, *in vitro* biostability studies are useful to provide directional guidance for *in vivo* studies and are useful as a biomaterial screening method (Wilkoff et al., 2015). Numerous studies have evaluated the effect of *in vitro* degradation of PCU biomaterials (Arjun and Ramesh, 2012; Dempsey et al., 2014; Faré et al., 1999; Hernandez et al., 2008; Mishra et al., 2015; Tanzi et al., 1997; Wiggins et al., 2004). To understand how the degradation affects the mechanical behaviour of biomaterials, some studies focussed on quasi-static tensile properties of the *in vitro* degradation specimens (Arjun and Ramesh, 2012; Dempsey et al., 2014; Mishra et al., 2015; Wiggins et al., 2004). While, some studies focussed on the viscoelastic response of these biomaterials by performing a temperature sweep; i.e. performing dynamic mechanical temperature analysis (DMTA) (Arjun and Ramesh, 2012; Hernandez et al., 2008; Wiggins et al., 2004).

As will be shown in this chapter, these biomaterials are frequency dependent viscoelastic materials; the applied strain rate has an effect on the biomaterials response. A detailed assessment of these biomaterials' viscoelasticity, both macro-level and micro-level viscoelastic properties, is currently absent.

The aim of this chapter is to provide a detailed investigation of the effect of *in vitro* biodegradation on the viscoelasticity of five long-term implantable, commercially available, PCU. In total, four degradation protocols, two oxidation and two hydrolytic methods, were used to evaluate the *in vitro* biostability of the five PCU biomaterials. Between the untreated (control) and *in vitro* degraded (oxidation and hydrolysis) specimens, this chapter will:

- Quantify frequency dependent macro viscoelastic properties of the five PCU biomaterials by using DMA;
- Quantify frequency dependent micro viscoelastic properties of the five PCU biomaterials by using μDMA;
- Investigate the effect of four *in vitro* degradation methods on the micro-level and macro-level viscoelasticity of the five biomaterials;
- Compare the chemical structure changes of the untreated (control) and *in vitro* degraded (oxidation and hydrolysis) specimens, for the five biomaterials, by using HCI;
- Compare the macro morphological and surface morphological changes of the untreated (control) and *in vitro* degraded (oxidation and hydrolysis) specimens.

4.2 Materials and Methods

4.2.1 Biomaterials

The five different commercially available, long-term implantable PCU biomaterials (Quadrathane ARC 80A B20, Bionate II 80A, Quadrathane ARC 80A, ChronoFlex C 80A and ChronoSil 80A *5%*; see section 3.1.1) were used to analyse the effect of *in vitro* biodegradation. Further information about the manufacturing of these PCU pellets, ethylene oxide (EtO) sterilisation of these injected moulded ISO plaques and die cutting the plaques into ASTM D1708 shaped specimens can be found in section 3.1.2.

Once the first plaque was die cut into ASTM D1708 shaped specimens, the specimens were numbered and an Excel random order generator (Microsoft, Redmond, Washington, USA) was used to separate the specimens into three groups to assess the effect of *in vitro* oxidative degradation; Control (n = 6), 3% H_2O_2 degraded (n = 6) and 20% H_2O_2 / 0.1 *M* $CoCl_2$ (n = 6) groups. A second plaque was die cut ASTM D1708 shaped specimens and randomly grouped into three groups to assess the effect of *in vitro* hydrolytic degradation; Control (n = 6), real-time degraded (n = 6) and accelerated degraded (n = 6) groups (see Table 4-1). Further information about the *in vitro* oxidative degradation methods (3% H_2O_2 and 20% H_2O_2 / 0.1 *M* $CoCl_2$) can be found in section 3.3 while further information about the *in vitro* hydrolytic degradation methods (real-time [37 ± 1°C] and accelerated [70 ± 2°C]) can be found in section 3.4.

Table 4-1: Biomaterial grouping information. The number of specimens, per biomaterial, that were degraded in the two different studies (Oxidation and Hydrolysis) is stated.

Biomaterials	Plaque 1: Oxidation			Plaque 2: Hydrolysis		
	Control	3%	H_2O_2 / $CoCl_2$	Control	Real-time	Accelerated
Quadrathane B20	Six	Six	Six	Six	Six	Six
Bionate II	Six	Six	Six	Six	Six	Six
Quadrathane	Six	Six	Six	Six	Six	Six
ChronoFlex C	Six	Six	Six	Six	Six	Six
ChronoSil	Six	Six	Six	Six	Six	Six

4.2.2 Spectroscopy - HCI

Attenuated total reflectance Fourier transform infra-red hyperspectral chemical imaging (HCI) was performed on the untreated (control) and *in vitro* degraded (3% H_2O_2, 20% H_2O_2 / 0.1 *M* $CoCl_2$, real-time [37 ± 1°C] and accelerated [70 ± 2°C]) groups. The light aperture size of 200 µm (in the x and y dimension) was selected which implies that the single point detector was 50

μm (a fourfold decrease). For HCI of the *in vitro* biodegraded specimens, a grid of data points was selected and the distance between each pixel was 50 μm; this creates a spatially contiguous image (Dorrepaal et al., 2018).

Twenty spectra with a spectral resolution of 2 cm^{-1} between 675 and 4000 cm^{-1} were acquired and mean averaged to obtain each spectrum (Simmons et al., 2004). The PCU spectra were cut between 750 and 2000 cm^{-1} and spectra of the four aromatic PCU biomaterials were normalised to the internal reference around 819 cm^{-1} peak, the stable aromatic C–H out of plane bending peak (Dorrepaal et al., 2018). Linear baseline correction was performed subsequent to the internal reference normalisation and followed by a baseline shift of one arbitrary unit (Dorrepaal et al., 2018). A secondary normalisation method, the Savitzky Golay (SG) technique (Savitzky and Golay, 1964), was also performed to understand the changes of the wavelengths of the five biomaterials. The SG window size was 31 wave measurements (a buffer size of 15 on either side of the centre point), the fit was a second order polynomial and a second order derivative. Spectral assignments and wavenumbers (cm^{-1}) are listed in Table 4-2.

Table 4-2: Spectral assignment and wavenumber (Christenson et al., 2004a, 2004b; Cipriani et al., 2013; Dorrepaal et al., 2018; Hernandez et al., 2008; Shen et al., 2011; Smith, 1998; B. Ward et al., 2006; R. Ward et al., 2006)

Spectral assignment	Wavenumber (cm^{-1})
C=O stretching vibration of free carbonate	1740-1737
C=O stretching vibration of hydrogen-bonded carbonate	1720
C=O stretching vibration of hydrogen-bonded urethane	1705-1701
NH_2 free aromatic amine	1650
Aromatic C=C stretching vibration	1598-1596
CH_2 bending vibration	1466
O-C-O stretching vibration of carbonate	1254-1246
N–H bending and C–N stretching vibration of urethane	1223-1220
C-C crosslinking (branched ether)	1174
C-O	1110
C-O-C of urethane	1079
C-H bending in plane aromatic ring	1018
O-H bending or bending of aliphatic CO_2H	930-931
C-H bending out of plane aromatic ring	816-819

4.2.3 Micro-Dynamic Mechanical Analysis (μDMA)

Micro-scale viscoelastic response of the untreated and degraded (oxidation and hydrolysis) five biomaterials was measured by using a customised nano-indenter testing machine running customised LabVIEW 16.0 software and customised probe; see section 3.6 and Figure 4-1.

Figure 4-1: Customised probe used in μDMA testing

For μDMA, firstly, double sided tape was placed on the base of the glass petri dish and six specimens were placed on the tape; placing the specimens on double-sided tape prevented specimens from floating. As spherical probes can be adhesive to specimen surfaces (van Hoorn et al., 2016), the specimens were immersed with 5% wt. Bovine Serum Albumin (BSA) (Sigma Aldrich, Dorset, UK) in Dulbecco's PBS solution for 30 minutes at room temperature (van Hoorn et al., 2016). After 30 minutes, the BSA was poured out of the petri dish and the specimens were immersed in Dulbecco's PBS solution. Both the specimens and the probe were fully submerged and allowed to stabilise for 30 minutes (Figure 4-2).

(A) 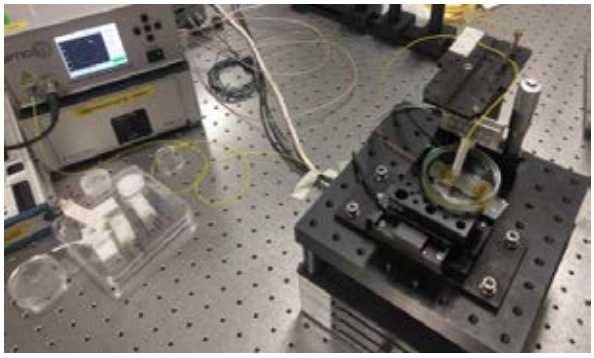 (B) 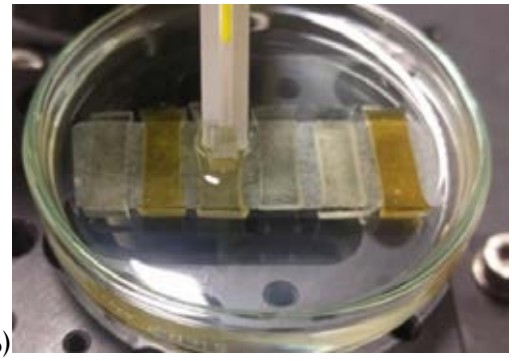

Figure 4-2: (A) Specimens, in a petri dish, on the nano-indentor testing stage and (B) Specimens, held to the base of the petri dish by double side tape, immersed in Dulbecco's PBS solution. All specimens are Bionate II 80A but vary on degradation; (from left to right) control from oxidation plaque, 3% H_2O_2 degraded, 20% H_2O_2 / 0.1 M $CoCl_2$ degraded, control from hydrolysis plaque, real-time degraded and accelerated degraded. For (B), the customised probe is over the B20 specimen.

All tests were performed using indentation control (displacement control). From preliminary testing of control specimens, it was decided that a 5 μm indentation with 100 nm amplitude would be used to characterise the viscoelastic response of the untreated and degraded specimens; this is within the 10 μm depth from the surface which has been stated to be where most of the observed surface changes occur (Cipriani et al., 2013). From the number of specimens degraded per group (Table 4-1), one specimen was randomly selected with the Excel random order generator (Microsoft, Redmond, Washington, USA). In total, six different specimens, of the same biomaterial, were tested per day (see Figure 4-2 (B)) and each specimen was tested at six different locations which were 100 μm apart along the gauge of the specimen; this ensured that the viscoelastic characterisation occurred at a non-contacted location (Mattei et al., 2015).

At each location, the probe was not in contact at the beginning of the test. Once the test was started, a ramp of 5 μm was performed in 2 seconds. Once the probe made contact with the surface, the data acquisition began recording and the probe continued in ramp control until it indented the surface by 5 μm. This 5 μm indentation was held for 60 seconds and allowed the removal of stress-relaxation, which was determined from preliminary testing; it is important to measure the viscoelastic properties on a relaxed sample so enough time should be given to ensure constant indentation depth over time (Beekmans, 2018). The viscoelastic response was measured for five different frequencies between 0.1 and 10 Hz (0.1, 0.316, 1, 3.16 and 10 Hz). Once the frequency sweep was finished, the probe went back to its initial, starting position (not in contact with the biomaterial's surface) and the data acquisition finished. The testing location was moved 100 μm and the μDMA test procedure began again.

All tested locations were performed in Dulbecco's Phosphate Buffer Saline (PBS) solution at room temperature and the stage was enclosed within a custom-built sound proof chamber (Figure 4-3).

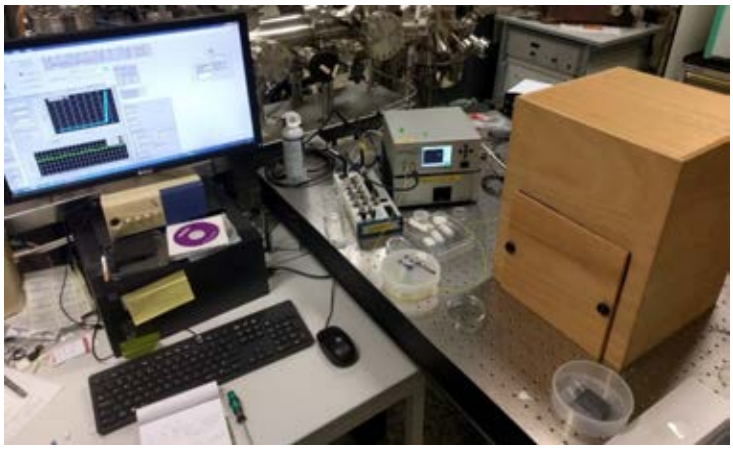

Figure 4-3: Test set-up with sound proof chamber; see Figure 3-5 for test set-up without sound proof chamber

4.2.4 Dynamic Mechanical Analysis (DMA)

To enable macro-viscoelasticity comparisons between specimens, the method used to characterise the viscoelastic properties of control and *in vitro* degraded (oxidation and hydrolysis) ASTM D1708 shaped specimens were kept consistent. The experimental factors such as the applied sinusoidal load, investigated frequencies, machine fixtures used, etc. discussed henceforth were kept consistent unless stated otherwise.

A sinusodially varying tension load of 1 N to 10 N was applied to each specimen (this applied load range was selected from preliminary testing – see 8.10 Appendix J - section 8.10.1) and the storage and loss stiffness were calculated for 25 different frequencies between 49 Hz to 0.01 Hz; see section 2.2.3.2 for more information on how this storage and loss stiffness is calculated by dynamic mechanical analysis (DMA). All devices and components were tested in air at 37°C ± 1°C and the temperature was monitored throughout the frequency sweep (see section 3.7, Figure 3-7, Figure 4-4 and 8.4 Appendix D).

Figure 4-4: Testing of a Quadrathane with a radiopacifier (barium sulfate)

As one specimen was randomly selected with the Excel random order generator (Microsoft, Redmond, Washington, USA) for the micro-dynamic mechanical analysis (see section 0), this left five specimens per degradation group per biomaterial remaining from the initial number of specimens degraded; the number of specimens degraded per group can be found in Table 4-1. For the *in vitro* oxidative degradation groups, all five specimens were used to quantify the macro-viscoelastic properties; Control (n = 5), 3% H_2O_2 degraded (n = 5) and 20% H_2O_2 / 0.1 *M* $CoCl_2$ (n = 5) groups.

For the *in vitro* hydrolytic degradation groups, three specimens were used to quantify the macro-viscoelastic properties; Control (n = 3), 3% H_2O_2 degraded (n = 3) and 20% H_2O_2 / 0.1 *M* $CoCl_2$ (n = 3) groups; these specimens were randomly selected with the Excel random order generator and this sample size (n = 3) is the minimum number of test specimens stated in ISO 10993-13 (ISO, 2010).

DMA of *in vitro* oxidation groups and DMA of the *in vitro* hydrolysis groups were separated; however, the order of specimen testing was randomised by using the Excel Random Function.

4.2.5 Scanning electron microscopy

After DMA, scanning electron micrographs of the control and *in vitro* degraded (oxidation and hydrolysis) were gathered to investigate surface morphological changes due to degradation. By using the ASTM D1708 die cutter (Wallace Instruments, Cambridge, UK), a 5 mm × 5 mm × 3 mm cube was die cut from the ASTM D1708 specimen gauge (Figure 4-5).

(A) 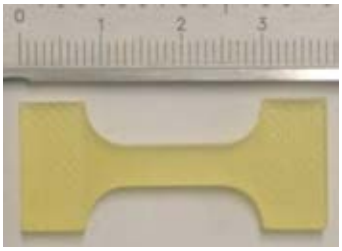 (B) 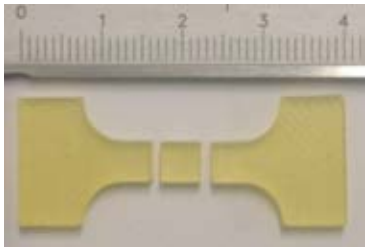 (C) 

Figure 4-5: (A) 3% H_2O_2 degraded ChronoFlex C 80A specimen, (B) isolating the 5 mm × 5 mm × 3 mm cube from the specimen gauge and (C) finished cube.

In total, one specimen was randomly selected per degradation group per biomaterial with the Excel random order generator (Microsoft, Redmond, Washington, USA). These cubed specimens were attached to an SEM stub and each SEM stub contained cubes from the untreated oxidation control, 3% H_2O_2 degraded, 20% H_2O_2 / 0.1 *M* $CoCl_2$ degraded,

untreated hydrolysis control, real-time degraded and accelerated degraded of one specific biomaterial (Figure 4-6 (A)). The stubs, with attached cubed specimens, were sputter coated (Figure 4-6 (B) and (C)) with ~25 nm layer of gold by using an Emscope SC500 sputter coater (Emscope Laboratories, Kent, UK).

(A) 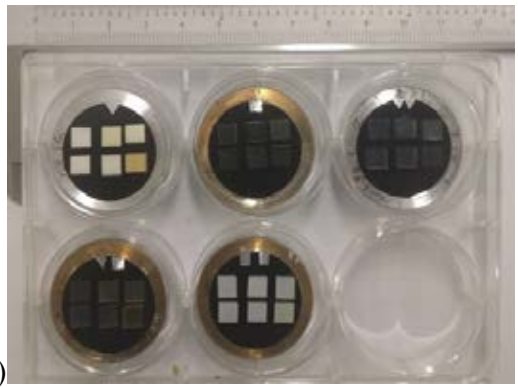 (B) 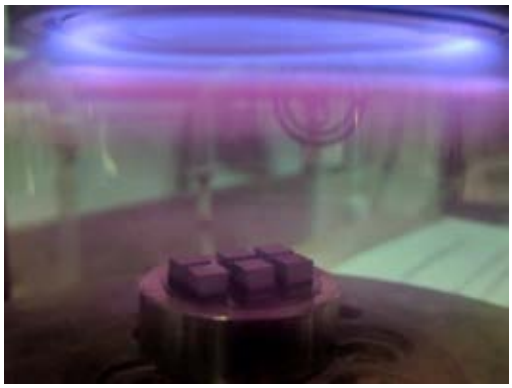

(C) 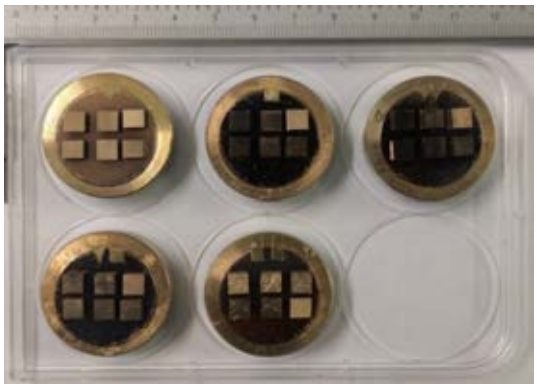

Figure 4-6: (A) Five different biomaterials on five different stubs; (top row, left to right) Quadrathane ARC B20 80A, Bionate II 80A and Quadrathane ARC 80A and (bottom row, left to right) ChronoFlex C 80A and ChronoSil 80A 5%. On each specific stub (top row, left to right) the untreated oxidation control, 3% H_2O_2 degraded, 20% H_2O_2 / 0.1 M $CoCl_2$ degraded and (bottom row, left to right) untreated hydrolysis control, real-time degraded and accelerated degraded. (B) Sputter coating of a SEM stub with attached cubes and (C) sputted coated cubed specimens.

Scanning electron micrographs of the control and degraded specimens were gathered at x1.2k and x2.0k magnification. ImageJ 1.48v (National Institutes of Health, Bethesda, MD, USA) was used to measure surface pits. The scale bar on a specific SEM image was used to calibrate the image. As the pits were irregular in shape, the major diameters, of numerous pits, were recorded and a range of pit sizes, in micrometres, was reported.

4.2.6 Statistical analysis

All statistical analyses were performed using SigmaPlot 13.0 (SYSTAT, San Jose, CA, USA). The median storage and loss stiffness of the untreated (control) and *in vitro* degraded specimens were plotted, with respect to the natural logarithmic frequency, with error bars; the error bars are specified, with the particular sample size, in the figure captions. Further, the median storage and loss stiffness of the untreated biomaterials were plotted in a similar fashion to the comparison of the untreated (control) and in vitro degraded specimens. Regression analyses were performed to evaluate the significance of the curve fit (equation 4.1 and 4.2):

$$k' = A\ln(f) + B \quad \text{for } 0.01 \leq f \leq 49 \qquad \text{Equation 4.1}$$

$$k'' = C\ln(f) + D \quad \text{for } 0.01 \leq f \leq 49 \qquad \text{Equation 4.2}$$

where f is frequency (independent variable), A and C are coefficients and B and D are the constants of the logarithmic regression.

Kruskal-Wallis one-way analysis of variance (ANOVA) on ranks tests were performed to evaluate:

- Micro-level viscoelastic differences among the untreated and degraded biomaterial specimens (n = 6);
- Micro-level viscoelastic differences among the untreated biomaterial specimens (n = 6);
- Macro viscoelastic differences among the untreated biomaterial specimens (n = 5);
- Macro viscoelastic differences among the untreated and oxidative degraded biomaterial specimens (n = 5).
- Macro viscoelastic differences among the untreated and hydrolytic degraded biomaterial specimens (n = 3).

For all Kruskal-Wallis ANOVA tests, if the tests showed significant differences ($p < 0.05$), the multiple comparison Tukey test was used to evaluate significant differences ($p < 0.05$). It must be noted that findings and conclusions made from the micro-level viscoelastic data is limited by statistical pseudo-replication, i.e. multiple observations on the same unit. Thus, findings and conclusions are specific to the surface of the specific biomaterials evaluated so, it may not give a fair representation of a wider comparison of all biomaterials; this limitation is discussed further in section 4.4.

All statistical results with $p < 0.05$ were considered significant.

4.3 Results

4.3.1 Oxidation

Figure 4-7 shows the discolouration between the (A) untreated biomaterials, (B) biomaterials treated for 52 weeks with the ISO 10993-13 3% H_2O_2 degradation protocol and (C) biomaterials treated for 24 days with the 20% H_2O_2 / 0.1 *M* $CoCl_2$ degradation protocol:

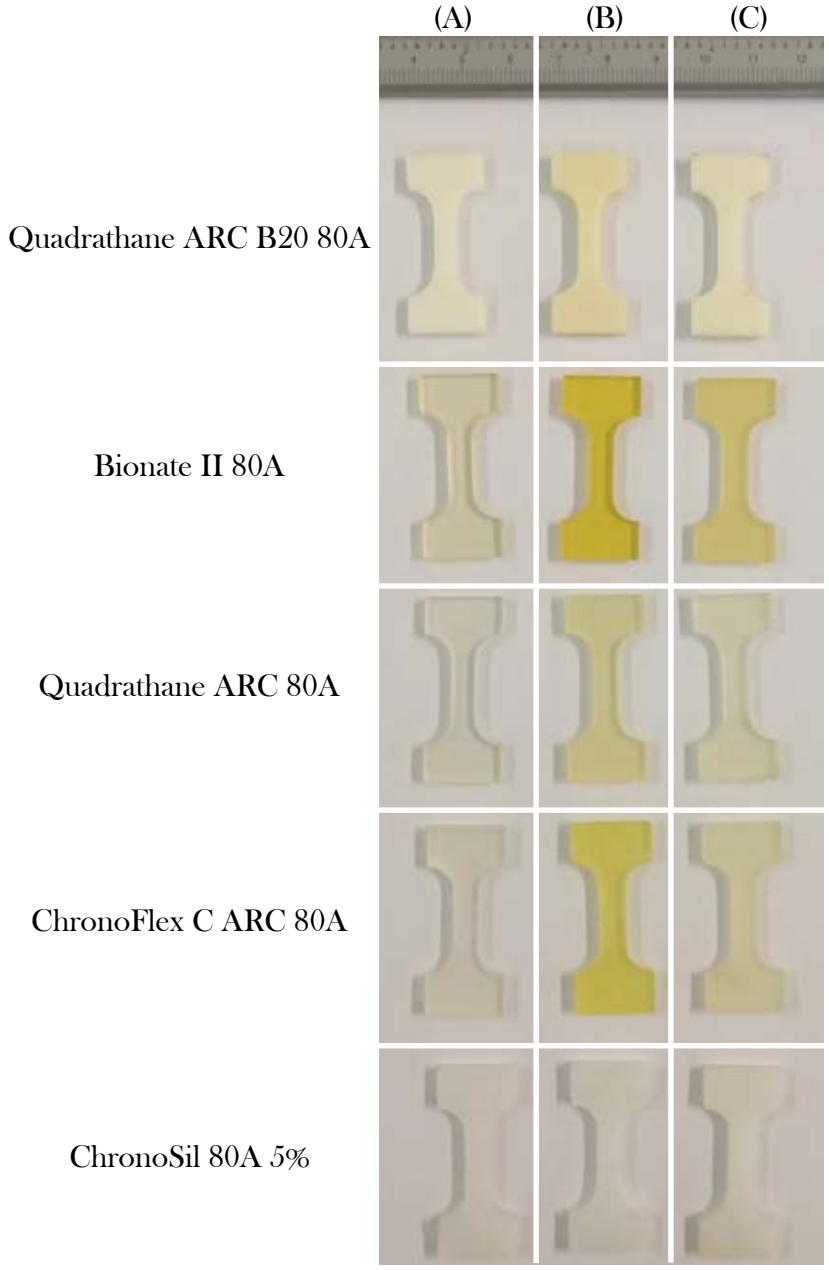

Figure 4-7: The five different biomaterials in three different groups; (A) Untreated (Control), (B) 3% H_2O_2 degraded and (C) 20% H_2O_2 / 0.1 M $CoCl_2$ groups.

4.3.1.1 HCI

The ATR-FTIR spectrum of the untreated and oxidative degraded biomaterials is illustrated in Figure 4-8.

Evidence of PCU oxidative degradation has been established as new absorbance peaks were observed at 930 cm^{-1} (O-H bending or bending of aliphatic CO_2H) and 1174 cm^{-1} (C-C crosslinking) for all *in vitro* $H_2O_2/CoCl_2$ degraded Quadrathane ARC 80A-B20 (with radiopacifier), Bionate II 80A and Quadrathane ARC 80A specimens (6 out of 6 specimens). New absorbance peaks were observed at 930 cm^{-1} and 1174 cm^{-1} for 5 out of 6 *in vitro* $H_2O_2/CoCl_2$ degraded ChronoFlex C 80A. Hyperspectral chemical images (Figure 4-9 and Figure 4-10) demonstrated that the new peaks at 930 cm^{-1} and 1174 cm^{-1}, for the $H_2O_2/CoCl_2$ degraded specimens, varied regionally. The variation of the height of the 1174 cm^{-1} absorbance peak can be analysed by examining the range of the peak height across the specimens; see the scale bar adjacent to HCIs. For example, the variation (approximate range) of the untreated Chronoflex C 80A specimen (Figure 4-10 (J)) is low (1.52-1.67 AU) compared to *in vitro* $H_2O_2/CoCl_2$ degraded specimen (range of Figure 4-10 (L) is approximately 1.6-2.6 AU). HCIs provide further evidence of the PCU oxidative degradation spatial variation as high absorbance peak heights, for the new absorbance peaks at 930 cm^{-1} and 1174 cm^{-1}, is regionalised for the Bionate II 80A and ChronoFlex C 80A $H_2O_2/CoCl_2$ degraded specimens; Figure 4-9 (F) and (L) for variation of 930 cm^{-1} peak height and Figure 4-10 (F) and (L) for variation of 1174 cm^{-1} peak height.

In comparison to the $H_2O_2/CoCl_2$ degraded specimens, no new absorbance peaks were observed at 930 cm^{-1} and 1174 cm^{-1} for the untreated and 3% H_2O_2 degraded specimens (Figure 4-8). Further, no new absorbance peaks at 930 cm^{-1} and 1174 cm^{-1} were observed for the untreated, 3% H_2O_2 degraded and the $H_2O_2/CoCl_2$ degraded Chronosil specimens (Figure 4-8).

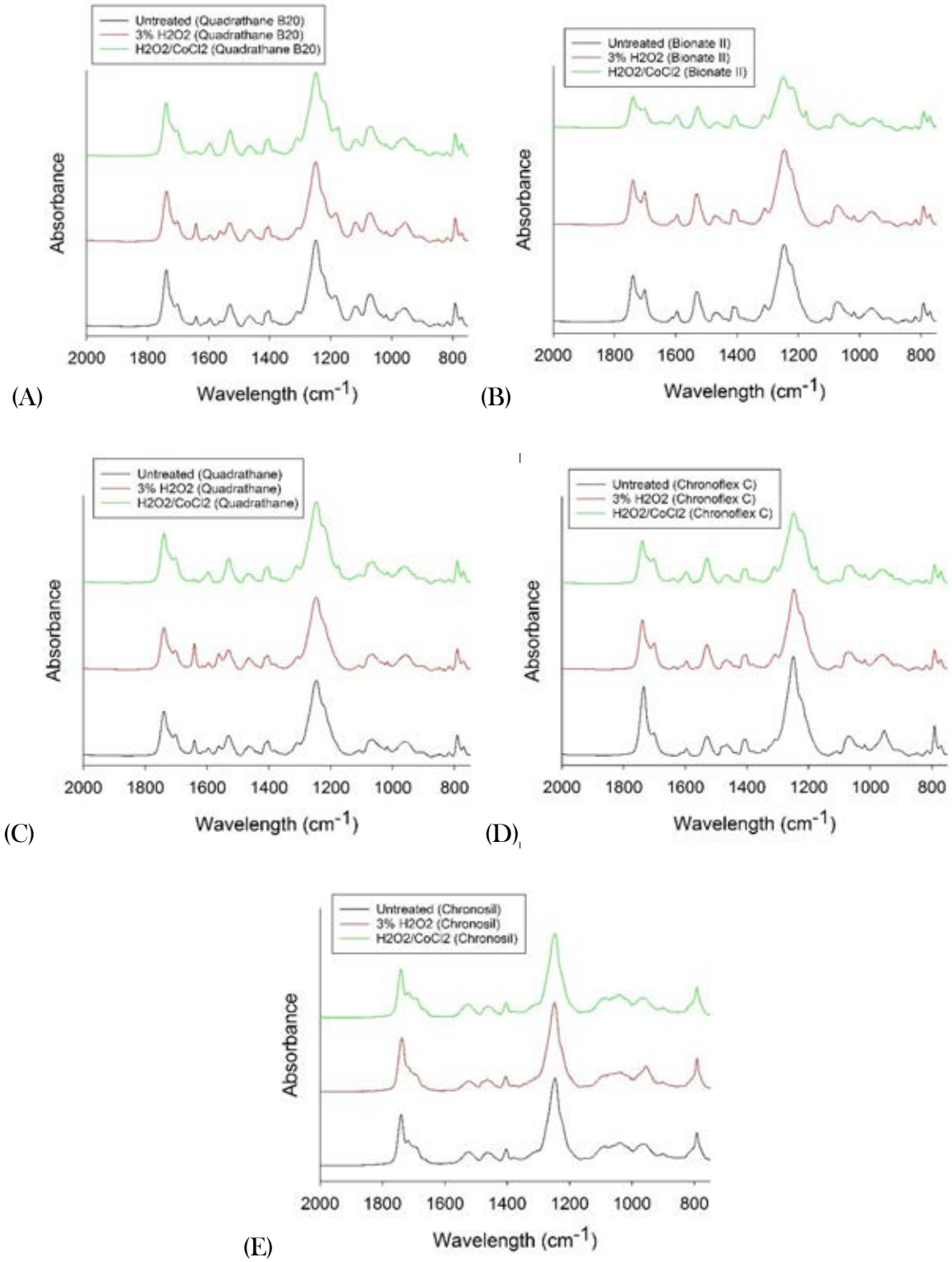

Figure 4-8: Stacked ATR-FTIR spectra of untreated and *in vitro* oxidative degraded five biomaterials; (A) Quadrathane ARC 80A B20, (B) Bionate II 80A, (C) Quadrathane ARC 80A, (D) ChronoFlex C 80A and (E) ChronoSil 80A 5%. Absorbance units are arbitrary units (AU).

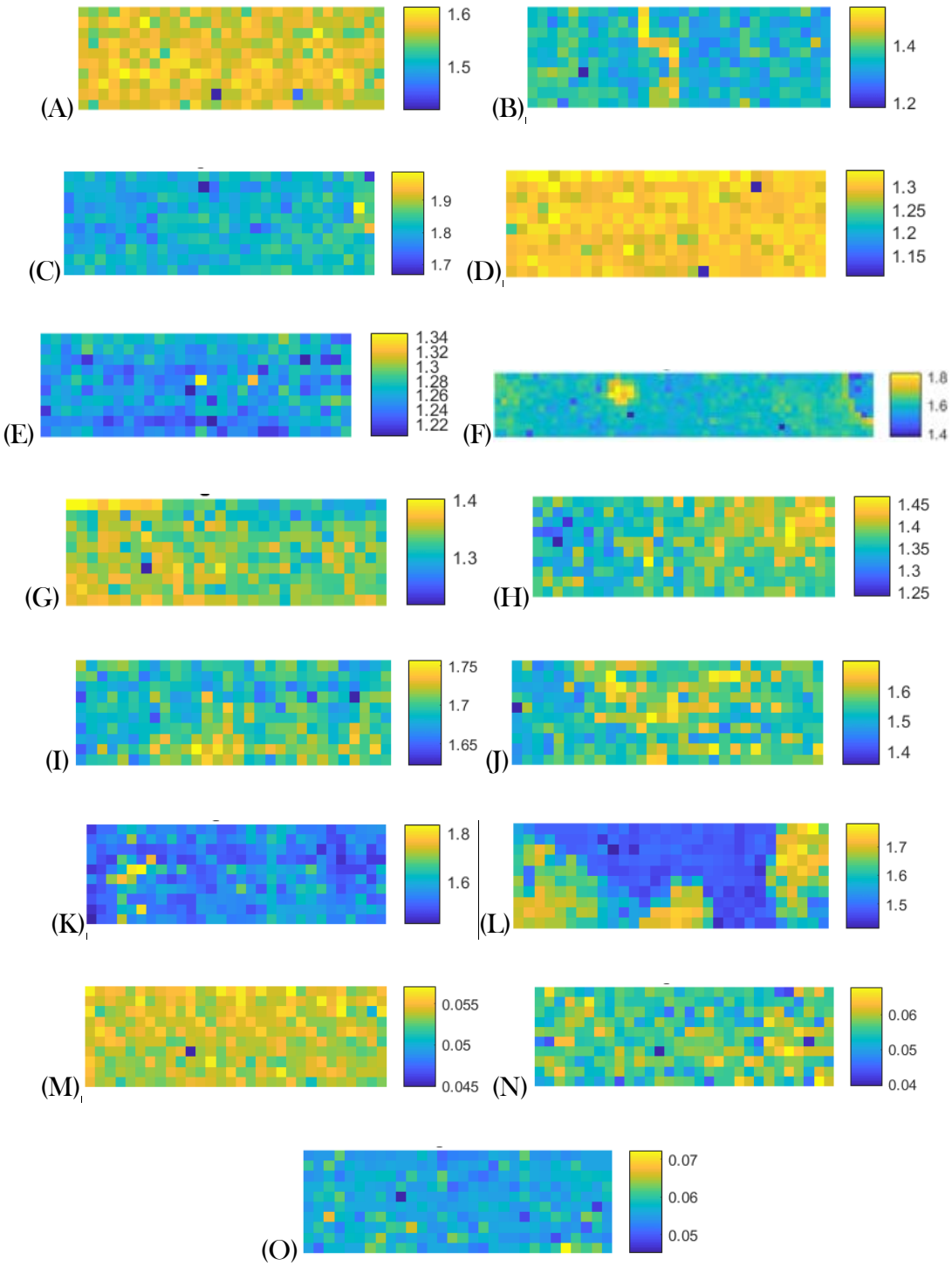

Figure 4-9: Spatial variation of the new peak witnessed at approximately 930 cm^{-1} for the PCU biomaterials; (A, D, G, J, M) untreated, (B, E, H, K, N) *in vitro* oxidative degradation ISO 10993-13 3% H_2O_2 method (3% H_2O_2) and (C, F, I, L, O) *in vitro* accelerated oxidation 20% H_2O_2 and 0.1 M $CoCl_2$ method (H_2O_2/ $CoCl_2$) of the five biomaterials; (A-C) Quadrathane ARC 80A B20, (D-F) Bionate II 80A, (G-I) Quadrathane ARC 80A, (J-L) ChronoFlex C 80A and (M-O) ChronoSil 80A 5%.

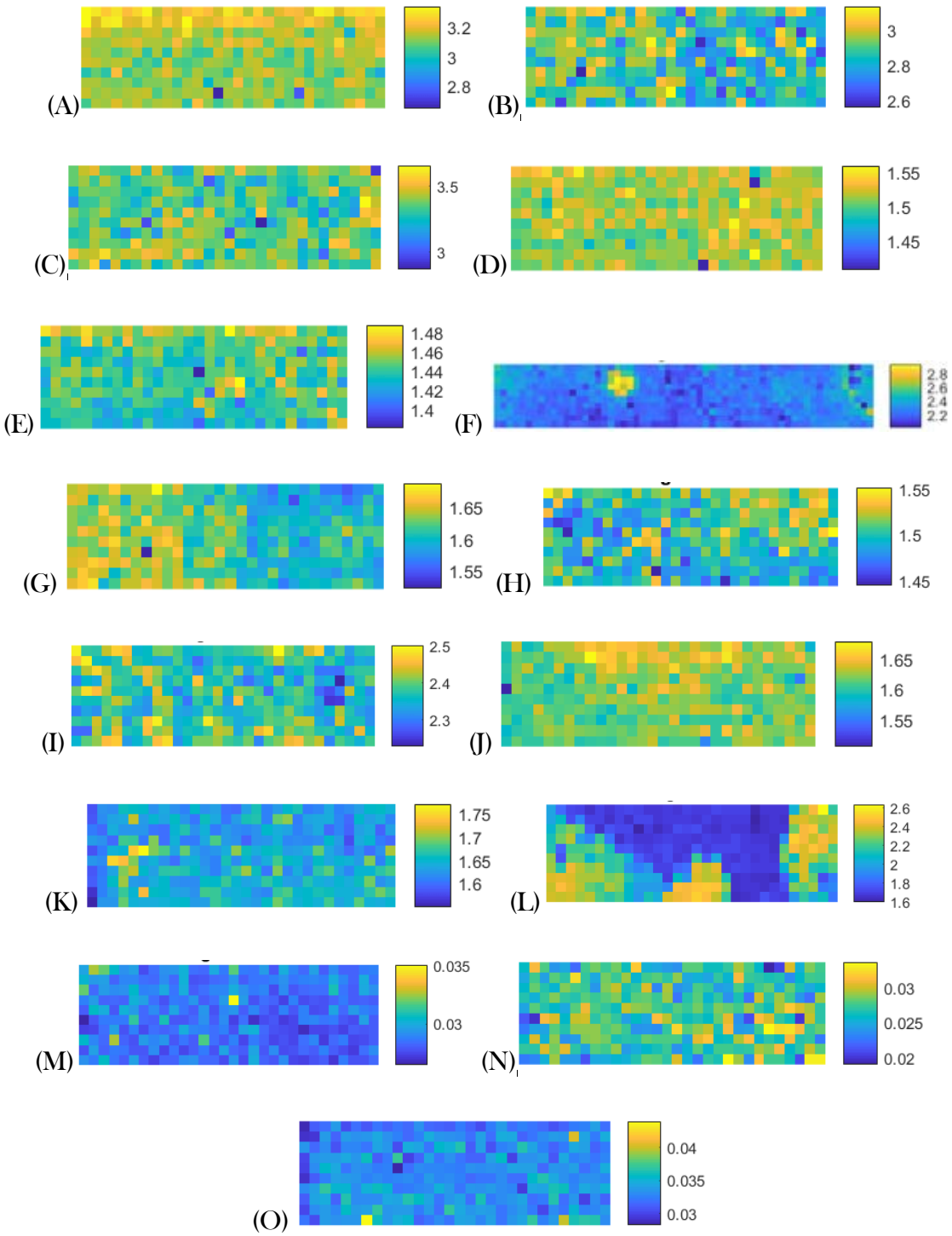

Figure 4-10: Spatial variation of the new peak witnessed at approximately 1174 cm^{-1} for the PCU biomaterials; (A, D, G, J, M) untreated, (B, E, H, K, N) *in vitro* oxidative 3% H_2O_2 method (3% H_2O_2) and (C, F, I, L, O) *in vitro* 20% H_2O_2 and 0.1 M $CoCl_2$ method (H_2O_2/ $CoCl_2$) of the five biomaterials; (A-C) Quadrathane ARC 80A B20, (D-F) Bionate II 80A, (G-I) Quadrathane ARC 80A, (J-L) ChronoFlex C 80A and (M-O) ChronoSil 80A 5%.

From the HCI, a wide spatial variation in absorbance peak intensity around 1248 cm^{-1} was observed (Figure 4-11); this peak is indicative of the O-C-O carbonate bonds (Dorrepaal et al., 2018; Smith, 1998). For Bionate II 80A *in vitro* $H_2O_2/CoCl_2$ degraded specimen (Figure 4-11 (F), a specific region, on the right of the HCI, was highlighted to have a low absorbance peak intensity (1248 cm^{-1}) when compared to the rest of the specimen; this highlights a specific area where the soft segment of this PCU biomaterial has degraded which provides evidence of spatial variation of degradation of a biomaterial.

The new absorbance peak at 1650 cm^{-1} (NH_2 free aromatic amine) has been stated to provide evidence of hard segment chain scission. All six Bionate II 80A *in vitro* $H_2O_2/CoCl_2$ degraded specimens demonstrated a new peak at 1650 cm^{-1}. However, isolated acquisitions of the untreated Bionate II 80A specimens also demonstrated a new peak at 1650 cm^{-1}. Further, 2 (out of 6) Bionate II 80A 3% H_2O_2 degraded specimens demonstrated isolated new peaks at 1650 cm^{-1}. The untreated Quadrathane 80A-B20 and Quadrathane 80A specimens had peaks around 1635-1640 cm^{-1}. Comparing the untreated Quadrathane 80A-B20 and Quadrathane 80A specimens to the $H_2O_2/CoCl_2$ degraded specimens (Figure 4-8), this peak around 1635-1640 cm^{-1} shrunk; this can be further seen with the change of the range of 1650 cm^{-1} absorbance intensity range (comparing range of Figure 4-12 (A) to Figure 4-12 (C) and Figure 4-12 (G) to Figure 4-12 (I)). The ChronoFlex C 80A *in vitro* $H_2O_2/CoCl_2$ degraded HCI (Figure 4-12 (L)) demonstrated a regional variation pattern comparable to the HCI at 930 cm^{-1} (Figure 4-9 (L)) and 1174 cm^{-1} (Figure 4-10 (L)). No new absorbance peaks at 1650 cm^{-1} was observed for the untreated, 3% H_2O_2 degraded and the $H_2O_2/CoCl_2$ degraded Chronosil specimens (Figure 4-8 and Figure 4-12 (M) to Figure 4-12 (O)).

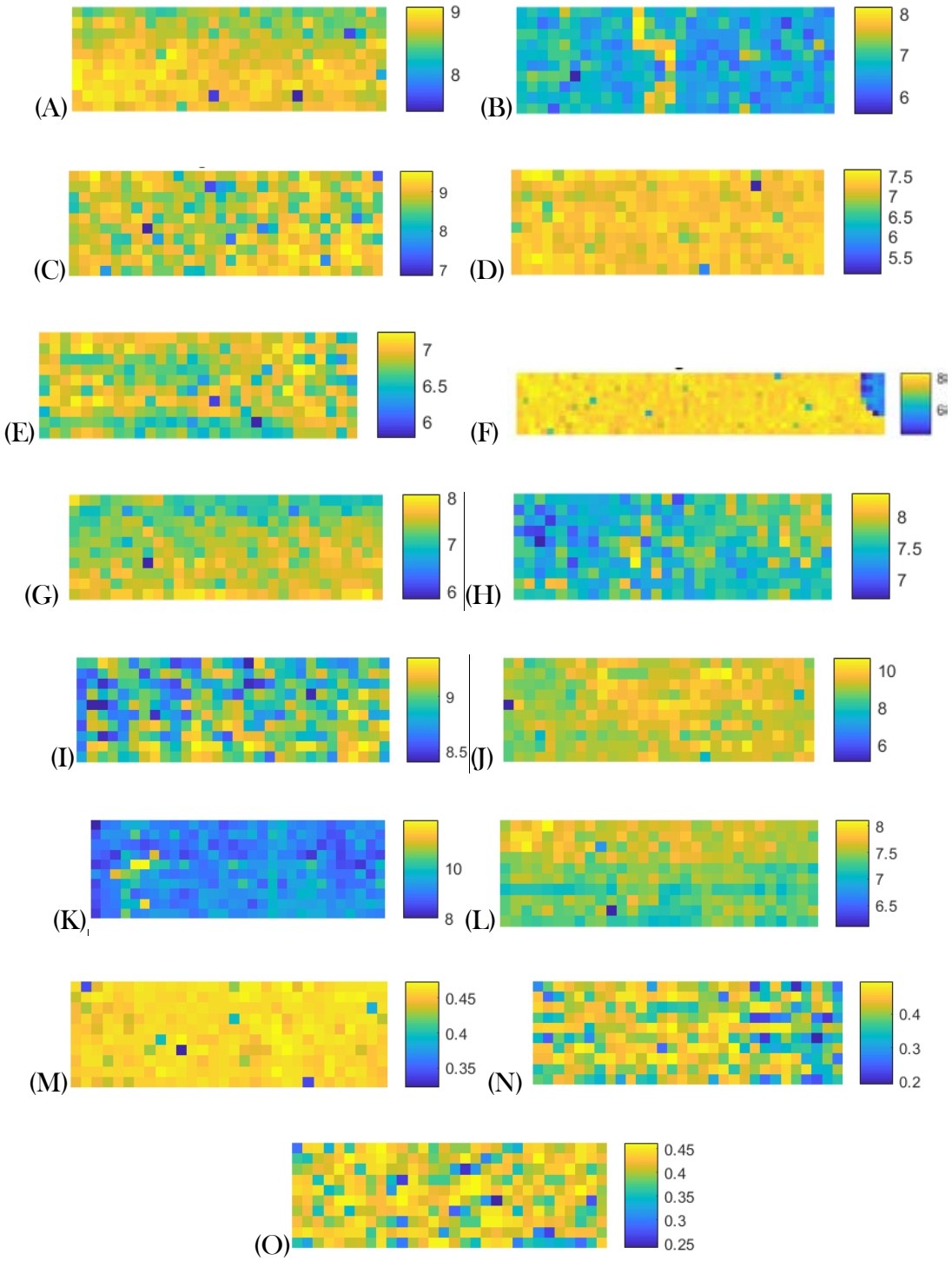

Figure 4-11: Spatial variation of the new peak witnessed at approximately 1248 cm^{-1} for the PCU ; (A, D, G, J, M) untreated, (B, E, H, K, N) *in vitro* oxidative 3% H_2O_2 method (3% H_2O_2) and (C, F, I, L, O) *in vitro* accelerated oxidative 20% H_2O_2 and 0.1 M $CoCl_2$ method (H_2O_2/ $CoCl_2$) of the five biomaterials; (A-C) Quadrathane ARC 80A B20, (D-F) Bionate II 80A, (G-I) Quadrathane ARC 80A, (J-L) ChronoFlex C 80A and (M-O) ChronoSil 80A 5%

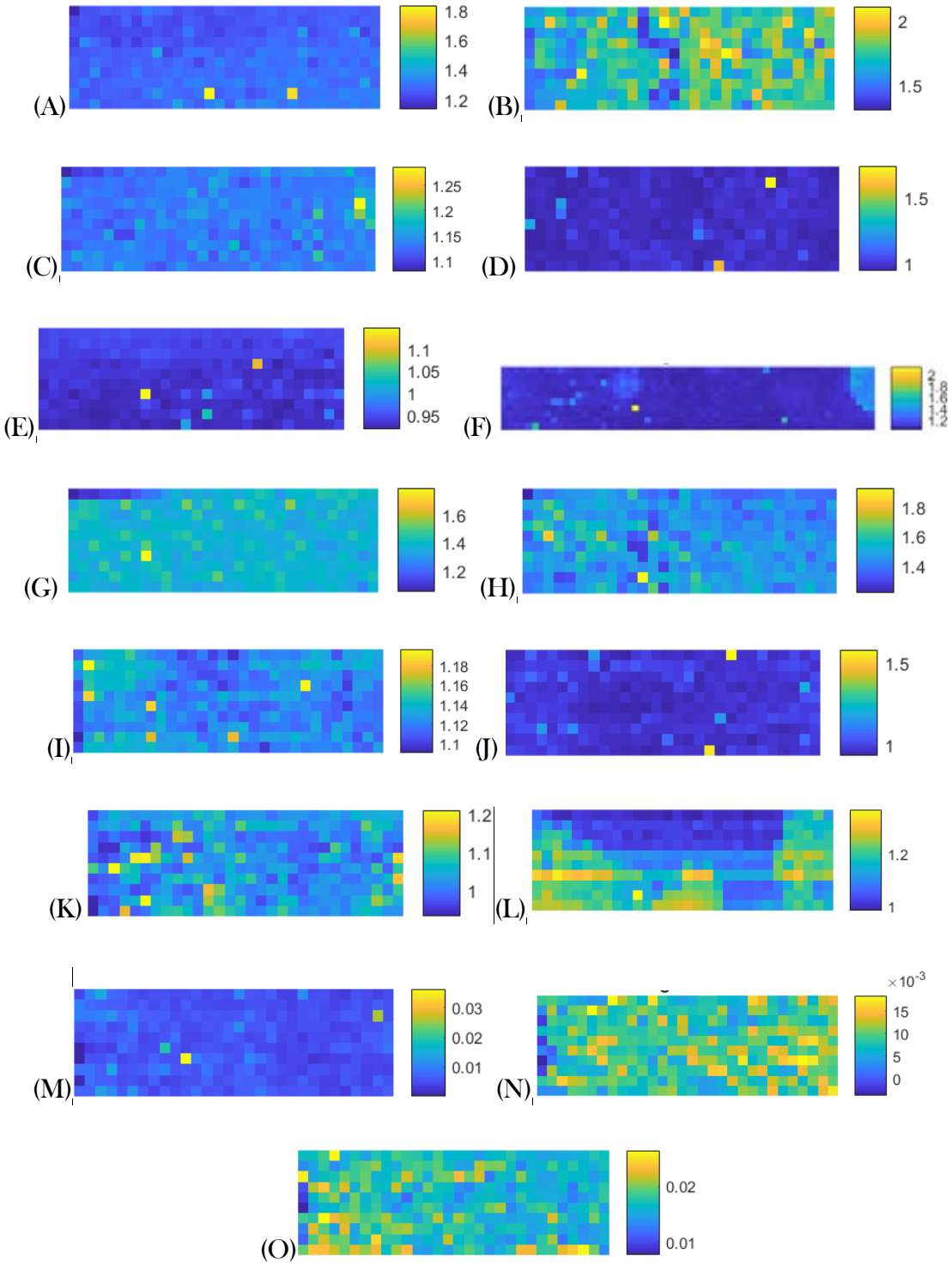

Figure 4-12: Spatial variation of the new peak witnessed at approximately 1650 cm^{-1} for the PCU ; (A, D, G, J, M) untreated, (B, E, H, K, N) *in vitro* oxidative 3% H_2O_2 method (3% H_2O_2) and (C, F, I, L, O) *in vitro* accelerated oxidation 20% H_2O_2 and 0.1 M $CoCl_2$ method (H_2O_2/ $CoCl_2$) of the five biomaterials; (A-C) Quadrathane ARC 80A B20, (D-F) Bionate II 80A, (G-I) Quadrathane ARC 80A, (J-L) ChronoFlex C 80A and (M-O) ChronoSil 80A 5%

4.3.1.2 μDMA

As stated in the materials and methods (section 0), the testing procedure is shown in Figure 4-13. The indenter position was held at 5 μm for 60 seconds to allow the removal of stress-relaxation response (see Load in Figure 4-13) and next, the viscoelastic response was measured for five different frequencies between 0.1 and 10 Hz (0.1, 0.316, 1, 3.16 and 10 Hz).

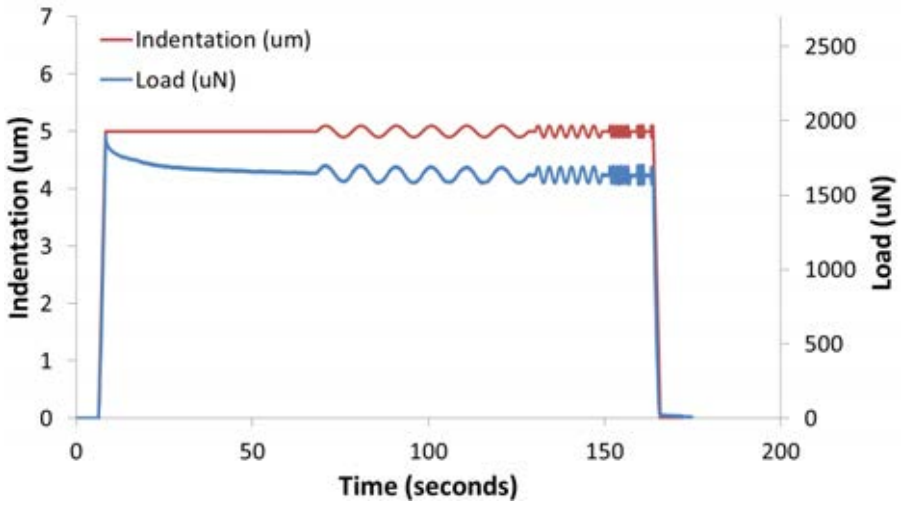

Figure 4-13: Removal of stress relaxation and subsequent frequency sweep. This example is of a measurement of a position on the surface of the Chronoflex C 80A (untreated)

The micro-level viscoelastic frequency dependent trends of the storage and loss stiffness of the five biomaterials are shown in Figure 4-14. For each specific biomaterial, the storage stiffness was larger than the loss stiffness for all frequencies tested.

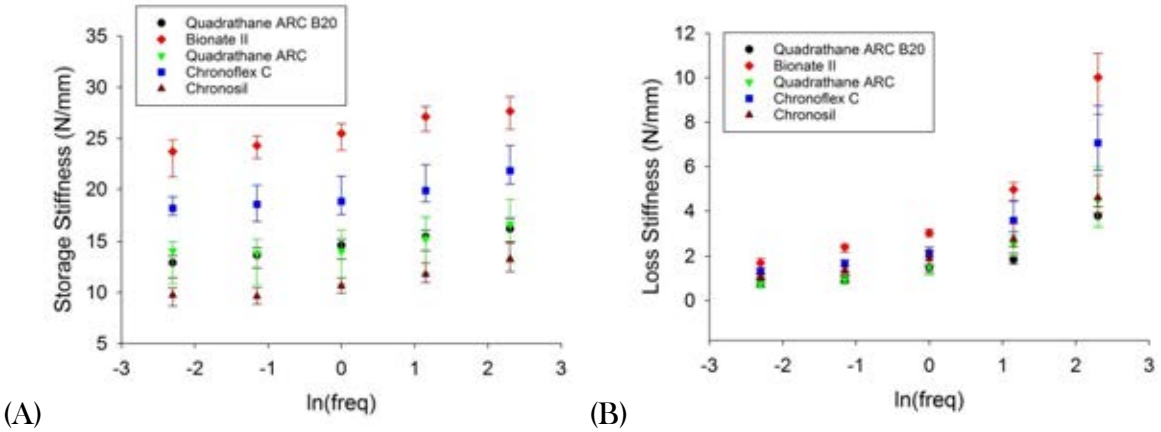

(A) (B)

Figure 4-14: Comparison of the micro-level, surface viscoelastic properties (A) storage stiffness and (B) loss stiffness of the five long-term implantable polymers (untreated) (median ± 95% confidence intervals).

Table 4-3 provides the multiple comparison test results and the frequencies at which the untreated five long-term implantable PCU biomaterials were significantly different. Both, the micro-scale storage and the loss stiffness of the comparison between Quadrathane B20 – Bionate II and Bionate II – Quadrathane were significantly different for all frequencies ($p < 0.05$). There were no significant differences ($p > 0.05$), for the storage stiffness and the loss stiffness, between Quadrathane B20 – Quadrathane, Quadrathane B20 – Chronosil, Bionate II – Chronoflex C and Quadrathane – Chronosil, for all frequencies tested. The micro-level, surface viscoelastic properties for other groupings were significantly different ($p < 0.05$) at specific frequencies (Table 4-3).

Table 4-3: Multiple comparison test results for the micro-level, surface viscoelastic properties of the five long-term implantable, untreated polymers. The frequencies stated indicates that the comparison were significantly different ($p < 0.05$).

Multiple Comparison Test	Storage Stiffness	Loss Stiffness
Quadrathane B20 – Bionate II	0.1 to 10 Hz	0.1 to 10 Hz
Quadrathane B20 – Quadrathane	-	-
Quadrathane B20 – Chronoflex C	-	1 to 10 Hz
Quadrathane B20 - Chronosil	-	-
Bionate II – Quadrathane	0.1 to 10 Hz	0.1 to 10 Hz
Bionate II – Chronoflex C	-	-
Bionate II – Chronosil	0.1 to 10 Hz	10 Hz
Quadrathane – Chronoflex C	-	0.1 to 0.316 Hz
Quadrathane – Chronosil	-	-
Chronoflex C - Chronosil	0.1 to 10 Hz	-

Figure 4-15 and Figure 4-16 presents the storage stiffness and loss stiffness, respectively, of the (A) Quadrathane ARC 80A B20, (B) Bionate II 80A, (C) Quadrathane ARC 80A, (D) Chronoflex C 80A and (E) Chronosil 80A 5%, for normal and the *in vitro* oxidative degraded biomaterials. The majority of storage stiffness trends increased logarithmically in relation to frequency ($p < 0.05$) (equation 4.1, where A is a coefficient and B is a constant, and 8.5 Appendix E- Table 8-1 to Table 8-5). Similarly to the storage stiffness, the majority of the loss stiffness trends increased logarithmically in relation to frequency ($p < 0.05$) (equation 4.2, where C is a coefficient and D is a constant, and 8.5 Appendix E- Table 8-1 to Table 8-5). All six storage stiffness and five (out of six) loss stiffness frequency dependent trends of the Bionate II 80A specimen, degraded with the 3% H_2O_2 method, were not logarithmic in behaviour ($p > 0.05$).

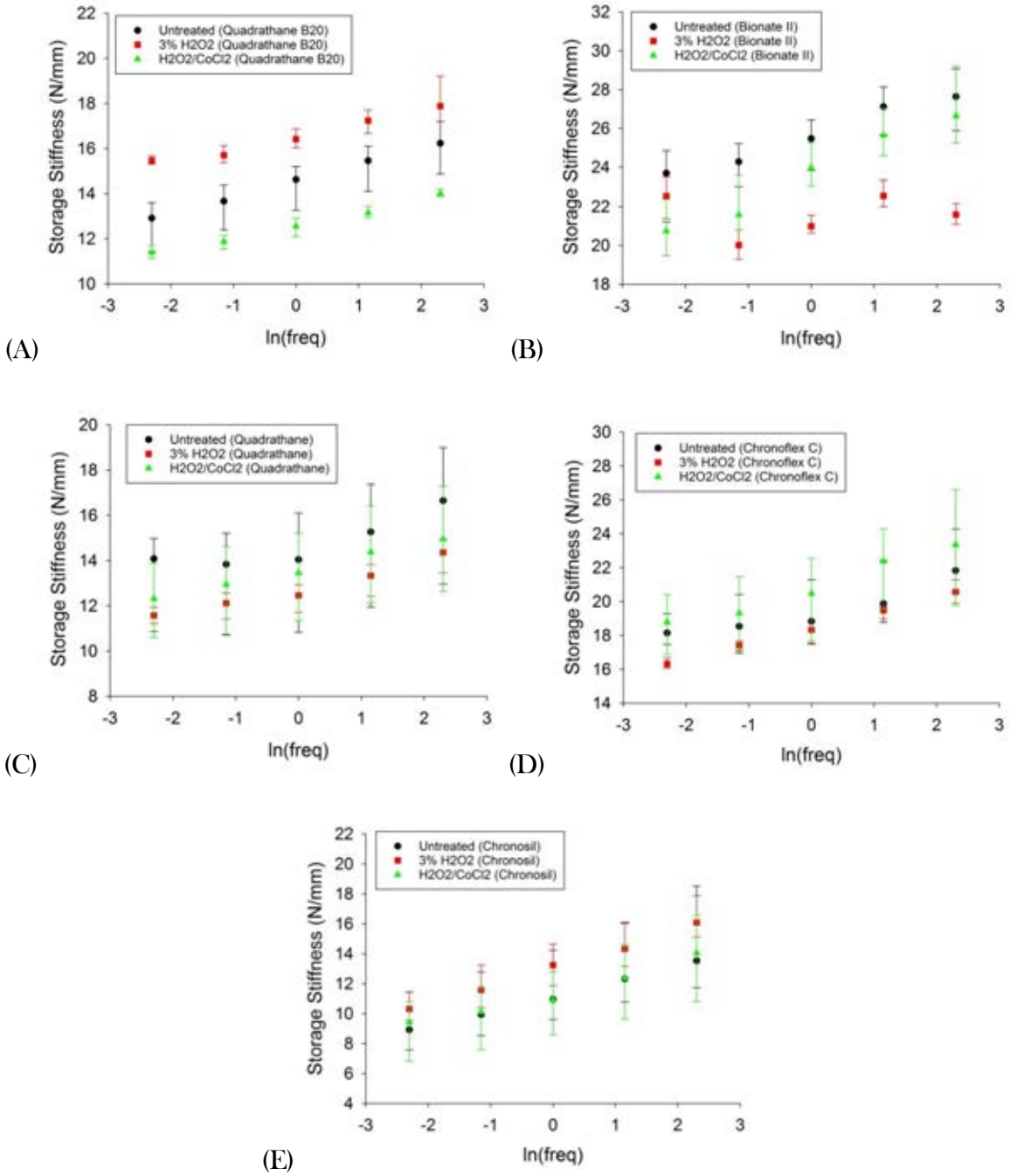

Figure 4-15: Comparison of the micro-level, surface storage stiffness of the untreated, *in vitro* ISO 10993-13 3% H_2O_2 oxidation method (3% H_2O_2) and the *in vitro* accelerated oxidation 20% H_2O_2 and 0.1 M $CoCl_2$ method (H_2O_2/ $CoCl_2$) of the five biomaterials; (A) Quadrathane ARC 80A B20, (B) Bionate II 80A, (C) Quadrathane ARC 80A, (D) ChronoFlex C 80A and (E) ChronoSil 80A 5% (median ± 95% confidence intervals)

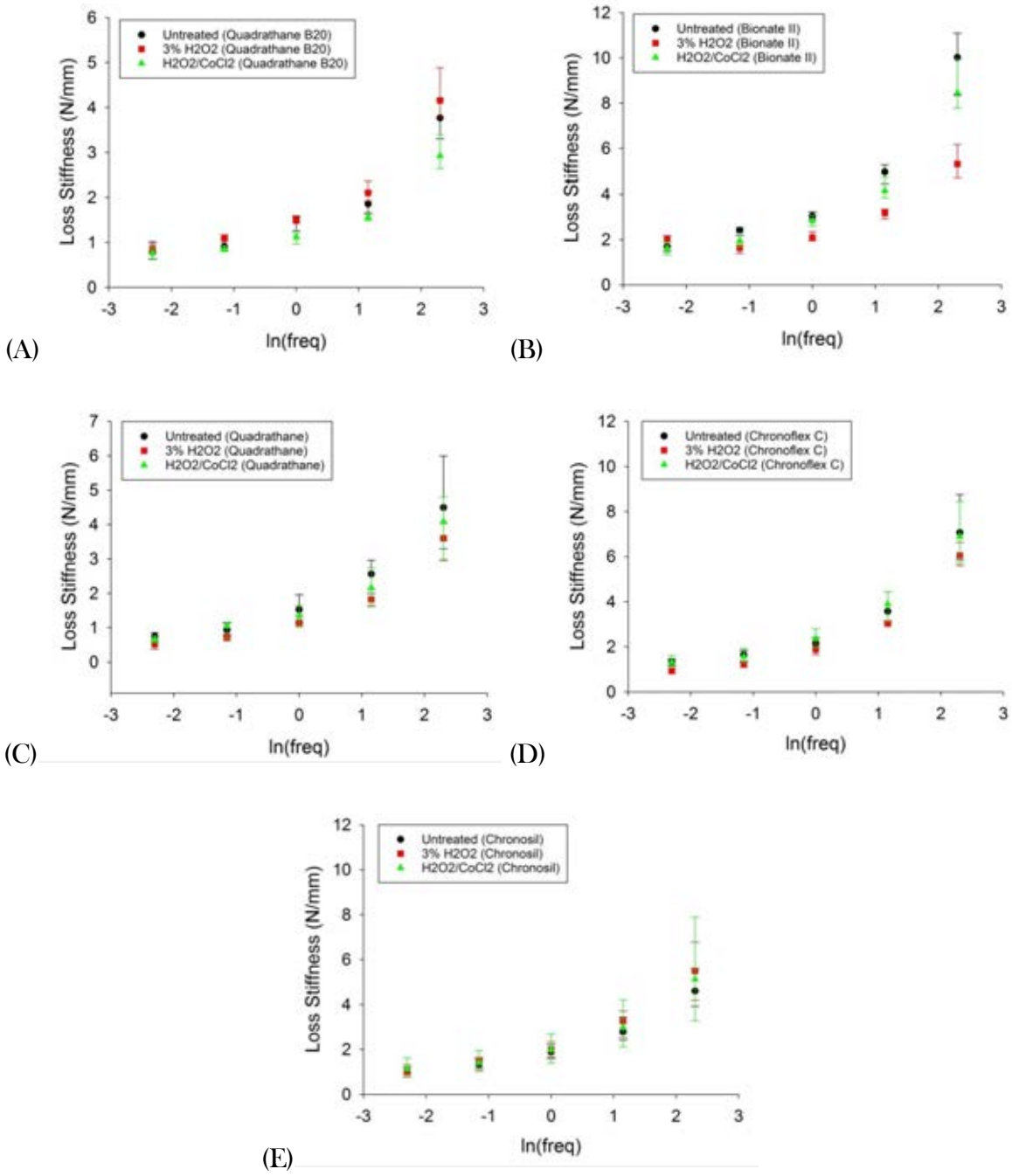

Figure 4-16: Comparison of the micro-level, surface loss stiffness of the untreated, *in vitro* ISO 10993-13 3% H_2O_2 oxidation method (3% H_2O_2) and the *in vitro* accelerated oxidation 20% H_2O_2 and 0.1 M $CoCl_2$ method (H_2O_2/ $CoCl_2$) of the five biomaterials; (A) Quadrathane ARC 80A B20, (B) Bionate II 80A, (C) Quadrathane ARC 80A, (D) ChronoFlex C 80A and (E) ChronoSil 80A 5% (median ± 95% confidence intervals)

The median untreated and *in vitro* degraded storage stiffness (see Figure 4-15) ranged, for the five biomaterials (Table 4-4).

Table 4-4: Median range of storage stiffness (N/mm) values per biomaterial

Biomaterial	Group	Range
Quadrathane B20	UNT	12.91 (0.1 Hz) to 16.23 (10 Hz)
	3% H_2O_2	15.46 (0.1 Hz) to 17.88 (10 Hz)
	$H_2O_2/CoCl_2$	11.39 (0.1 Hz) to 14.01 (10 Hz)
Bionate II	UNT	23.69 (0.1 Hz) to 27.64 (10 Hz)
	3% H_2O_2	20.02 (0.316 Hz) to 22.56 (10 Hz)
	$H_2O_2/CoCl_2$	20.75 (0.1 Hz) to 26.64 (10 Hz)
Quadrathane	UNT	13.84 (0.316 Hz) to 16.65 (10 Hz)
	3% H_2O_2	11.58 (0.1 Hz) to 14.36 (10 Hz)
	$H_2O_2/CoCl_2$	12.32 (0.1 Hz) to 14.95 (10 Hz)
Chronoflex C	UNT	18.15 (0.1 Hz) to 21.83 (10 Hz)
	3% H_2O_2	16.32 (0.1 Hz) to 20.57 (10 Hz)
	$H_2O_2/CoCl_2$	18.78 (0.1 Hz) to 23.36 (10 Hz)
Chronosil	UNT	9.75 (0.1 Hz) to 13.28 (10 Hz)
	3% H_2O_2	10.96 (0.1 Hz) to 15.34 (10 Hz)
	$H_2O_2/CoCl_2$	9.72 (0.1 Hz) to 14.14 (10 Hz)

While, the median untreated and *in vitro* degraded loss stiffness (see Figure 4-16) ranged, for the five biomaterials (Table 4-5).

Table 4-5: Median range of loss stiffness (N/mm) values per biomaterial

Biomaterial	Group	Range
Quadrathane B20	UNT	0.78 (0.1 Hz) to 3.77 (10 Hz)
	3% H_2O_2	0.86 (0.1 Hz) to 4.16 (10 Hz)
	$H_2O_2/CoCl_2$	0.77 (0.1 Hz) to 2.93 (10 Hz)
Bionate II	UNT	1.69 (0.1 Hz) to 10.01 (10 Hz)
	3% H_2O_2	1.63 (0.316 Hz) to 5.31 (10 Hz)
	$H_2O_2/CoCl_2$	1.62 (0.1 Hz) to 8.45 (10 Hz)
Quadrathane	UNT	0.74 (0.1 Hz) to 4.50 (10 Hz)
	3% H_2O_2	0.52 (0.1 Hz) to 3.60 (10 Hz)
	$H_2O_2/CoCl_2$	0.66 (0.1 Hz) to 4.08 (10 Hz)
Chronoflex C	UNT	1.33 (0.1 Hz) to 7.06 (10 Hz)
	3% H_2O_2	0.93 (0.1 Hz) to 6.05 (10 Hz)
	$H_2O_2/CoCl_2$	1.33 (0.1 Hz) to 6.89 (10 Hz)
Chronosil	UNT	1.07 (0.1 Hz) to 4.60 (10 Hz)
	3% H_2O_2	1.00 (0.1 Hz) to 5.49 (10 Hz)
	$H_2O_2/CoCl_2$	1.14 (0.1 Hz) to 5.13 (10 Hz)

The multiple comparison test results, that compared the untreated and *in vitro* oxidative degraded biomaterials, are shown in Table 4-6; the frequencies at which significant differences were detected ($p < 0.05$) are stated. The comparison of micro-scale viscoelastic properties of the untreated group to the $H_2O_2/CoCl_2$, were not significantly different ($p > 0.05$) for all frequencies except for the viscous property (loss stiffness) at 1 Hz for Quadrathane B20. The storage and loss stiffness of the Chronosil groups were not significantly different for all frequencies ($p > 0.05$). Between the untreated and *in vitro* oxidative degraded Quadrathane ARC 80A specimens (Quadrathane in Table 4-6), the loss stiffness at 0.1 Hz was the only comparison that was significantly different ($p < 0.05$). The storage and loss stiffness of Bionate II and Chronoflex C biomaterials were significantly different at specific frequencies ($p < 0.05$).

Table 4-6: Multiple comparison test results for the micro-level, surface viscoelastic properties of the untreated and oxidative degraded long-term implantable polymers. The frequencies stated indicates that the comparison were significantly different ($p < 0.05$) between the untreated, *in vitro* ISO 10993-13 3% H_2O_2 oxidation method (3% H_2O_2) and the *in vitro* accelerated oxidation 20% H_2O_2 and 0.1 M $CoCl_2$ method (H_2O_2/ $CoCl_2$) of the specific biomaterial.

Biomaterial	Multiple Comparison Test	Storage Stiffness	Loss Stiffness
Quadrathane B20	UNT – 3% H_2O_2	-	-
	UNT – $H_2O_2/CoCl_2$	-	1 Hz
	3% H_2O_2 – $H_2O_2/CoCl_2$	0.1 to 10 Hz	0.316 to 10 Hz
Bionate II	UNT – 3% H_2O_2	0.316 to 10 Hz	0.316 to 10 Hz
	UNT – $H_2O_2/CoCl_2$	-	-
	3% H_2O_2 – $H_2O_2/CoCl_2$	1 to 10 Hz	10 Hz
Quadrathane	UNT – 3% H_2O_2	-	0.1 Hz
	UNT – $H_2O_2/CoCl_2$	-	-
	3% H_2O_2 – $H_2O_2/CoCl_2$	-	-
Chronoflex C	UNT – 3% H_2O_2	0.1 Hz	0.1, 0.316 and 3.16 Hz
	UNT – $H_2O_2/CoCl_2$	-	-
	3% H_2O_2 – $H_2O_2/CoCl_2$	0.1 Hz	0.1 to 0.316 Hz
Chronosil	UNT – 3% H_2O_2	-	-
	UNT – $H_2O_2/CoCl_2$	-	-
	3% H_2O_2 – $H_2O_2/CoCl_2$	-	-

4.3.1.3 DMA

The macro viscoelastic frequency dependent trends of the storage and loss stiffness of the five biomaterials are shown in Figure 4-17. Similar to the micro-viscoelastic response of the five biomaterials, the storage stiffness was larger than the loss stiffness, for all frequencies tested, for each specific biomaterial.

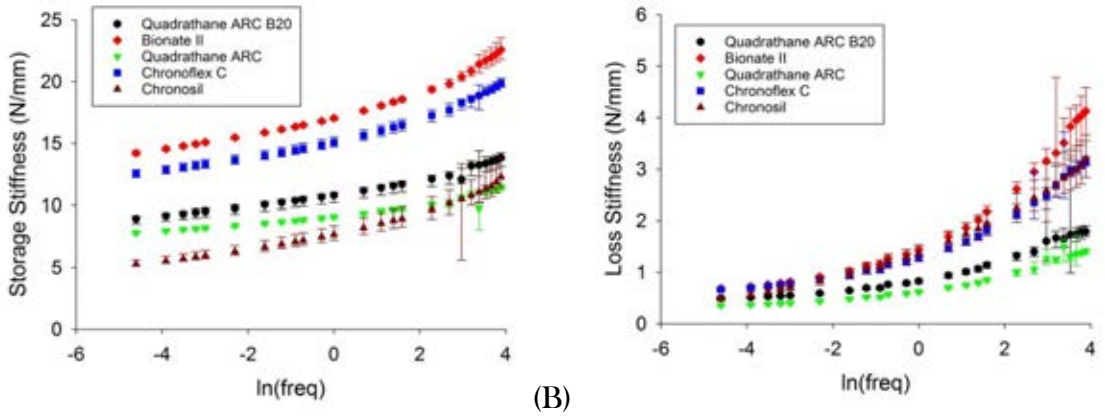

(A) (B)

Figure 4-17: Comparison of the macro viscoelastic properties (A) storage stiffness and (B) loss stiffness of the five long-term implantable polymers (untreated) (median ± 95% confidence intervals).

Table 4-7 provides the multiple comparison test results and the frequencies at which the untreated five long-term implantable PCU biomaterials were significantly different. Similarly to the micro-viscoelastic properties (Table 4-3), both, the storage and the loss stiffness of the comparison between Bionate II – Quadrathane were significantly different for all frequencies ($p < 0.05$).

There were no significant differences ($p > 0.05$), for the storage stiffness and the loss stiffness, between Quadrathane B20 – Quadrathane, Quadrathane B20 – Chronosil and Bionate II – Chronoflex C, across all frequencies tested (Table 4-7); this is similar to the micro-viscoelastic properties (Table 4-3).

Table 4-7: Multiple comparison test results for the macro viscoelastic properties of the five long-term implantable, untreated polymers. The frequencies stated indicates that the comparison were significantly different ($p < 0.05$).

Multiple Comparison Test	Storage Stiffness	Loss Stiffness
Quadrathane B20 – Bionate II	-	0.01 to 29, 39 to 49 Hz
Quadrathane B20 – Quadrathane	-	-
Quadrathane B20 – Chronoflex C	-	-
Quadrathane B20 - Chronosil	-	-
Bionate II – Quadrathane	0.01 to 49 Hz	0.01 to 49 Hz
Bionate II – Chronoflex C	-	-
Bionate II – Chronosil	0.01 to 49 Hz	-
Quadrathane – Chronoflex C	24 to 49 Hz	0.01 to 0.1, 15 and 29 Hz
Quadrathane – Chronosil	-	0.2 to 24 and 49 Hz
Chronoflex C - Chronosil	0.01 to 10 Hz	-

There were no significant differences ($p > 0.05$), for the storage stiffness and the loss stiffness, between Quadrathane B20 – Chronoflex C, for all frequencies tested (Table 4-7). The viscoelastic properties for other groupings were significantly different ($p < 0.05$) at specific frequencies (Table 4-7).

Figure 4-18 and Figure 4-19 presents the macro storage stiffness and loss stiffness, respectively, of the control (untreated) and the *in vitro* oxidative degraded biomaterials; (A) Quadrathane ARC 80A B20, (B) Bionate II 80A, (C) Quadrathane ARC 80A, (D) Chronoflex C 80A and (E) Chronosil 80A 5%. For the frequency range tested, the storage stiffness was larger than the loss stiffness for all frequencies tested for each specific biomaterial tested. Unlike the micro-viscoelastic properties regression analyses, all of the storage stiffness trends increased logarithmically in relation to frequency ($p < 0.05$) for all biomaterials (equation 4.1, where A is a coefficient and B is a constant; see 8.6 Appendix F - Table 8-6 and Table 8-10). Further, all of the frequency dependent loss stiffness trends increased logarithmically with respect to frequency ($p < 0.05$) (equation 4.2, where C is a coefficient and D is a constant; see 8.6 Appendix F - Table 8-6 and Table 8-10).

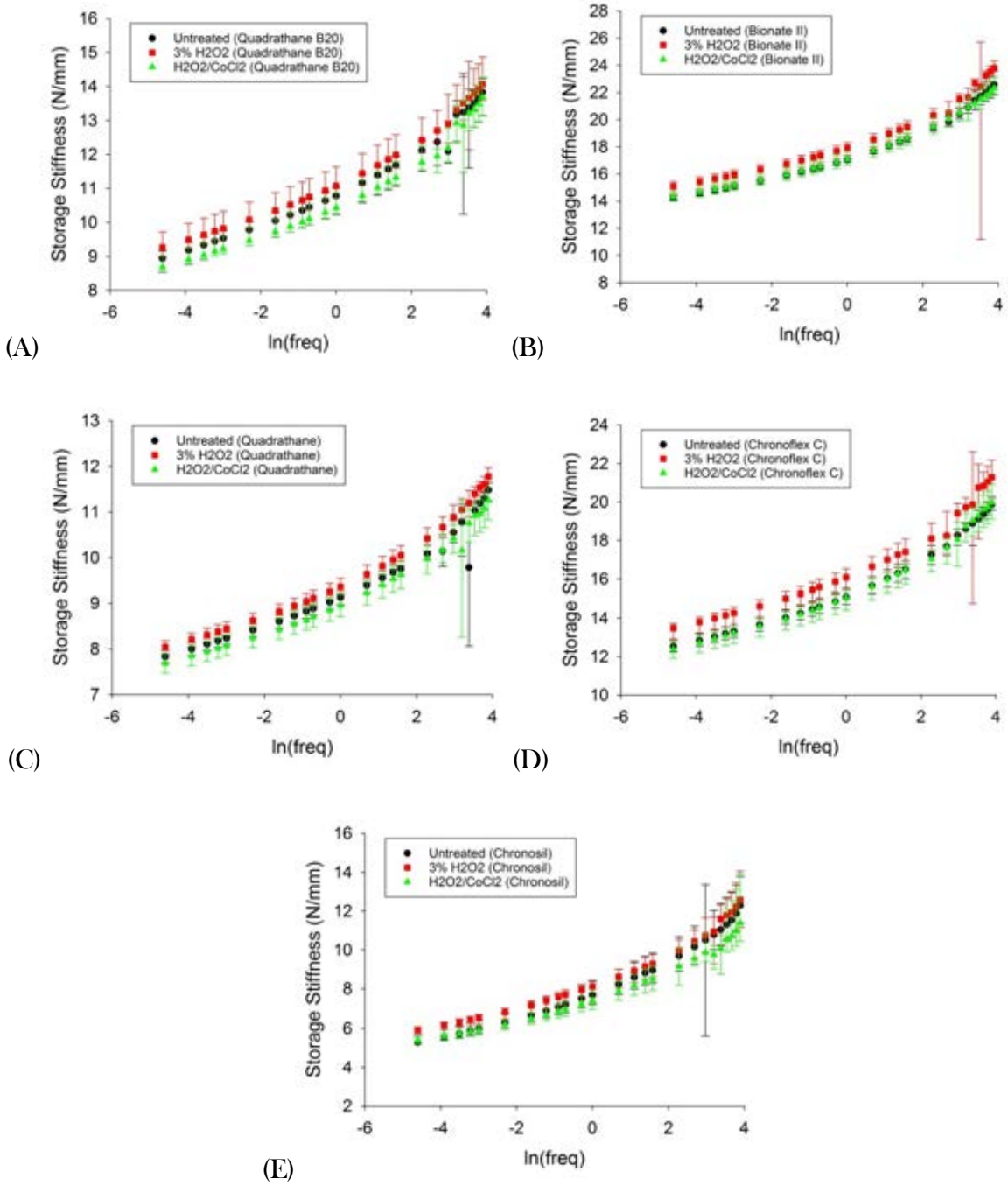

Figure 4-18: Comparison of the macro storage stiffness of the untreated, *in vitro* ISO 10993-13 3% H_2O_2 oxidation method (3% H_2O_2) and the *in vitro* accelerated oxidation 20% H_2O_2 and 0.1 M $CoCl_2$ method (H_2O_2/ $CoCl_2$) of the five biomaterials; (A) Quadrathane ARC 80A B20, (B) Bionate II 80A, (C) Quadrathane ARC 80A, (D) ChronoFlex C 80A and (E) ChronoSil 80A 5% (median ± 95% confidence intervals)

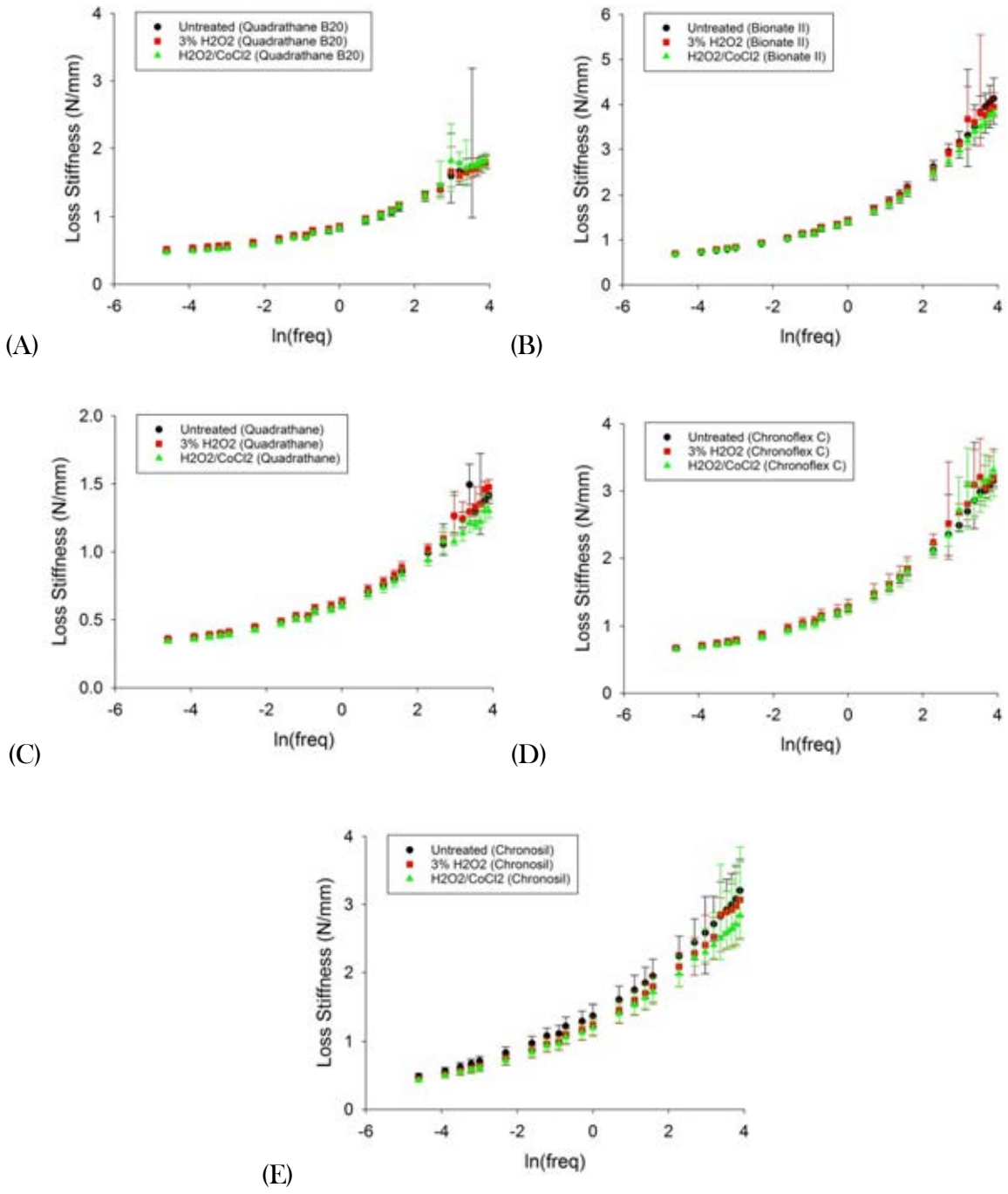

Figure 4-19: Comparison of the macro loss stiffness of the untreated, *in vitro* ISO 10993-13 3% H_2O_2 oxidation method (3% H_2O_2) and the *in vitro* accelerated oxidation 20% H_2O_2 and 0.1 M $CoCl_2$ method (H_2O_2/ $CoCl_2$) of the five biomaterials; (A) Quadrathane ARC 80A B20, (B) Bionate II 80A, (C) Quadrathane ARC 80A, (D) ChronoFlex C 80A and (E) ChronoSil 80A 5% (median ± 95% confidence intervals)

The median untreated and *in vitro* degraded macro storage stiffness (see Figure 4-18) ranged, for the five biomaterials (Table 4-8).

Table 4-8: Median range of storage stiffness (N/mm) values per biomaterial

Biomaterial	Group	Range
Quadrathane B20	UNT	8.94 (0.01 Hz) to 13.83 (49 Hz)
	3% H_2O_2	9.27 (0.01 Hz) to 14.07 (49 Hz)
	$H_2O_2/CoCl_2$	8.68 (0.01 Hz) to 13.69 (49 Hz)
Bionate II	UNT	14.21 (0.01 Hz) to 22.58 (49 Hz)
	3% H_2O_2	15.09 (0.01 Hz) to 23.80 (49 Hz)
	$H_2O_2/CoCl_2$	14.33 (0.01 Hz) to 22.32 (49 Hz)
Quadrathane	UNT	7.83 (0.01 Hz) to 11.48 (49 Hz)
	3% H_2O_2	8.04 (0.01 Hz) to 11.78 (49 Hz)
	$H_2O_2/CoCl_2$	7.69 (0.01 Hz) to 11.26 (49 Hz)
Chronoflex C	UNT	12.53 (0.01 Hz) to 19.87 (49 Hz)
	3% H_2O_2	13.48 (0.01 Hz) to 21.28 (49 Hz)
	$H_2O_2/CoCl_2$	12.38 (0.01 Hz) to 19.97 (49 Hz)
Chronosil	UNT	5.28 (0.01 Hz) to 12.29 (49 Hz)
	3% H_2O_2	5.93 (0.01 Hz) to 12.58 (49 Hz)
	$H_2O_2/CoCl_2$	5.39 (0.01 Hz) to 11.38 (49 Hz)

While, the median untreated and *in vitro* degraded macro loss stiffness (Figure 4-19) ranged, for the five biomaterials (Table 4-9).

Table 4-9: Median range of loss stiffness (N/mm) values per biomaterial

Biomaterial	Group	Range
Quadrathane B20	UNT	0.50 (0.01 Hz) to 1.79 (49 Hz)
	3% H_2O_2	0.52 (0.01 Hz) to 1.80 (49 Hz)
	$H_2O_2/CoCl_2$	0.47 (0.01 Hz) to 1.82 (49 Hz)
Bionate II	UNT	0.68 (0.01 Hz) to 4.13 (49 Hz)
	3% H_2O_2	0.70 (0.01 Hz) to 3.94 (49 Hz)
	$H_2O_2/CoCl_2$	0.68 (0.01 Hz) to 3.81 (49 Hz)
Quadrathane	UNT	0.36 (0.01 Hz) to 1.49 (24 Hz)
	3% H_2O_2	0.36 (0.01 Hz) to 1.48 (49 Hz)
	$H_2O_2/CoCl_2$	0.34 (0.01 Hz) to 1.30 (49 Hz)
Chronoflex C	UNT	0.67 (0.01 Hz) to 3.15 (49 Hz)
	3% H_2O_2	0.68 (0.01 Hz) to 3.20 (29 Hz)
	$H_2O_2/CoCl_2$	0.65 (0.01 Hz) to 3.31 (49 Hz)
Chronosil	UNT	0.49 (0.01 Hz) to 3.20 (49 Hz)
	3% H_2O_2	0.44 (0.01 Hz) to 3.07 (49 Hz)
	$H_2O_2/CoCl_2$	0.43 (0.01 Hz) to 2.84 (49 Hz)

The multiple comparison test results, that compared the macro viscoelastic response of the untreated and *in vitro* oxidative degraded biomaterials, are shown in Table 4-10. The frequencies stated in Table 4-10 imply significant differences were detected ($p < 0.05$) between the stated groups. Similarly to the comparison of micro-scale viscoelastic properties of the untreated group to the $H_2O_2/CoCl_2$, the macro-scale viscoelastic properties of Bionate II and Chronoflex C were not significantly different ($p > 0.05$) for all frequencies for this multiple comparison test. The macro-viscoelastic response (storage and loss stiffness) of the specific groups of Chronosil, Quadrathane B20 and Quadrathane were significantly different at specific frequencies ($p < 0.05$).

Table 4-10: Multiple comparison test results for the macro viscoelastic properties of the untreated and oxidative degraded long-term implantable polymers. The frequencies stated indicates that the comparison were significantly different ($p < 0.05$) between the untreated, *in vitro* ISO 10993-13 3% H_2O_2 oxidation method (3% H_2O_2) and the *in vitro* accelerated oxidation 20% H_2O_2 and 0.1 M $CoCl_2$ method (H_2O_2/ $CoCl_2$) of the specific biomaterial.

Biomaterial	Multiple Comparison Test	Storage Stiffness	Loss Stiffness
Quadrathane B20	UNT – 3% H_2O_2	0.01, 0.75 and 1 Hz	0.03 to 0.1 Hz
	UNT – $H_2O_2/CoCl_2$	-	0.3 Hz
	3% H_2O_2 – $H_2O_2/CoCl_2$	0.01 to 15, 29 Hz	0.01 to 0.2, 0.4 Hz
Bionate II	UNT – 3% H_2O_2	0.01 to 10, 20 and 29 Hz	-
	UNT – $H_2O_2/CoCl_2$	-	-
	3% H_2O_2 – $H_2O_2/CoCl_2$	29, 39 to 49 Hz	-
Quadrathane	UNT – 3% H_2O_2	3 to 15 and 29 Hz	0.5 to 1, 5 Hz
	UNT – $H_2O_2/CoCl_2$	-	20 Hz
	3% H_2O_2 – $H_2O_2/CoCl_2$	0.01 to 10, 20, 24, 34 to 49 Hz	0.01 to 10, 20, 34, 49 Hz
Chronoflex C	UNT – 3% H_2O_2	24 Hz	-
	UNT – $H_2O_2/CoCl_2$	-	-
	3% H_2O_2 – $H_2O_2/CoCl_2$	0.01 to 10 and 20 Hz	0.01 Hz
Chronosil	UNT – 3% H_2O_2	0.01 to 0.03 Hz	-
	UNT – $H_2O_2/CoCl_2$	-	0.01 to 0.5 Hz
	3% H_2O_2 – $H_2O_2/CoCl_2$	0.01 to 0.05 Hz	-

4.3.1.4 SEM

Figure 4-20 to Figure 4-24 shows representative SEM images of the surfaces of the five biomaterials; Quadrathane ARC 80A B20 (Figure 4-20), Bionate II 80A (Figure 4-21), Quadrathane ARC 80A (Figure 4-22), Chronoflex C 80A (Figure 4-23) and Chronosil 80A 5% (Figure 4-24). For all SEM figures (Figure 4-20 to Figure 4-24), images (A), (C) and (E) are recorded at x1.2k magnification while images (B), (D) and (F) are at x2.0k magnification. Further, for all SEM images of the biomaterials' surfaces, (A) and (B) are Untreated biomaterial, (C) and (D) are biomaterials treated with 3% H_2O_2 at 37°C and (E) and (F) are biomaterials treated with 20% H_2O_2/0.1M $CoCl_2$ at 37°C.

There was no evidence of surface pitting, or any other surface morphology changes, between the untreated and 3% H_2O_2 degraded for Quadrathane B20, Bionate II and Chronoflex C. On the surface of the 3% H_2O_2 degraded Quadrathane specimen, one pit was identified (Figure 4-22 (C) and (D)). The surface morphology of Chronosil (Figure 4-24) untreated, 3% H_2O_2 degraded and H_2O_2/$CoCl_2$ degraded was different compared to the visually smooth surface morphology of the untreated and 3% H_2O_2 degraded Quadrathane B20, Bionate II, Quadrathane and Chronoflex C. All five biomaterials that were degraded with H_2O_2/$CoCl_2$, for 24 days, demonstrated various levels of surface pitting.

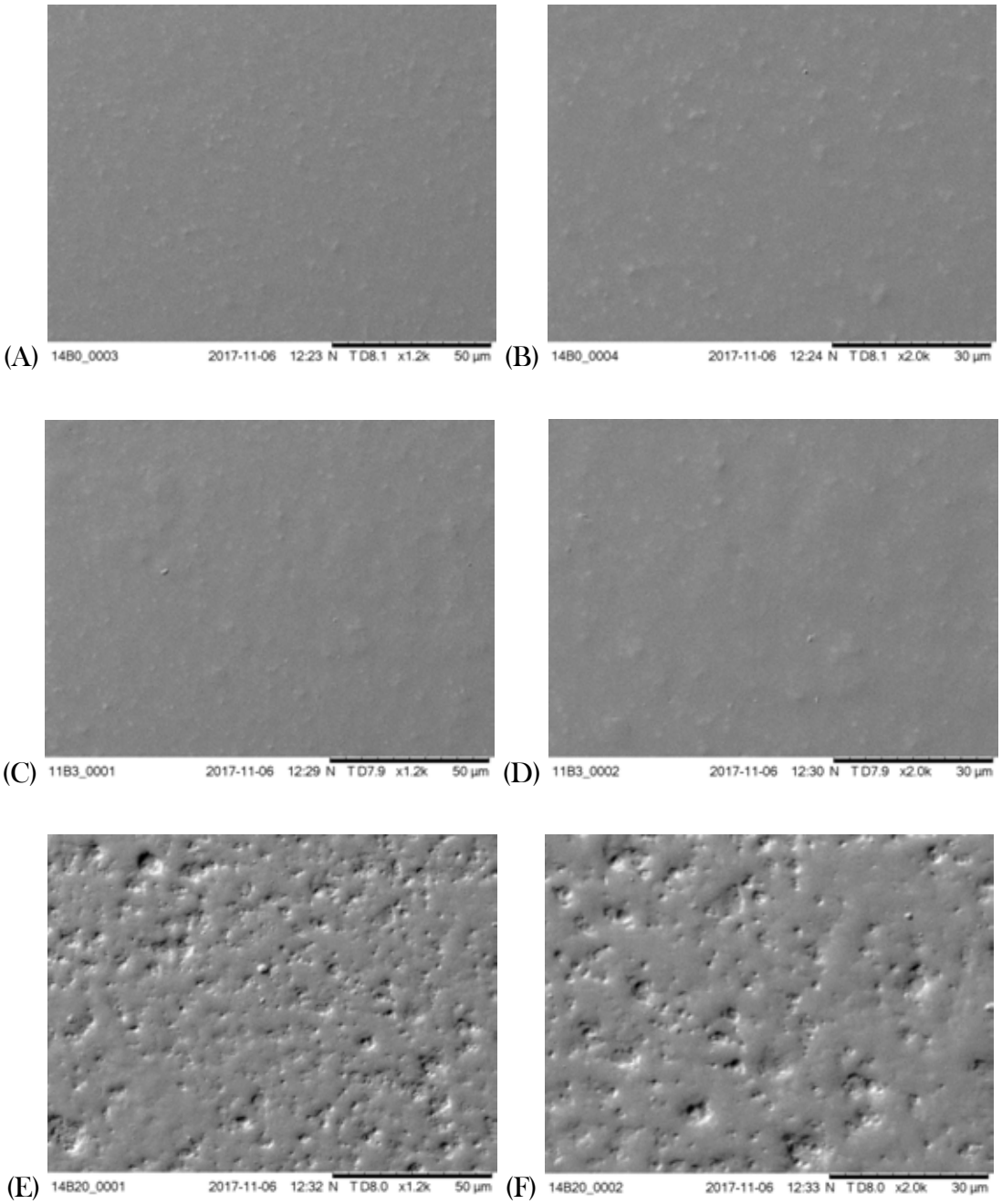

Figure 4-20: Scanning electron micrographs of quadrathane with radiopacifiers (Quad B20) at (A, C, E) x1.2k and (B, D, F) x2.0k. (A & B) Untreated, (C & D) treated with 3% H_2O_2 at 37°C and (E & F) treated with 20% H_2O_2/0.1*M* $CoCl_2$ at 37°C.

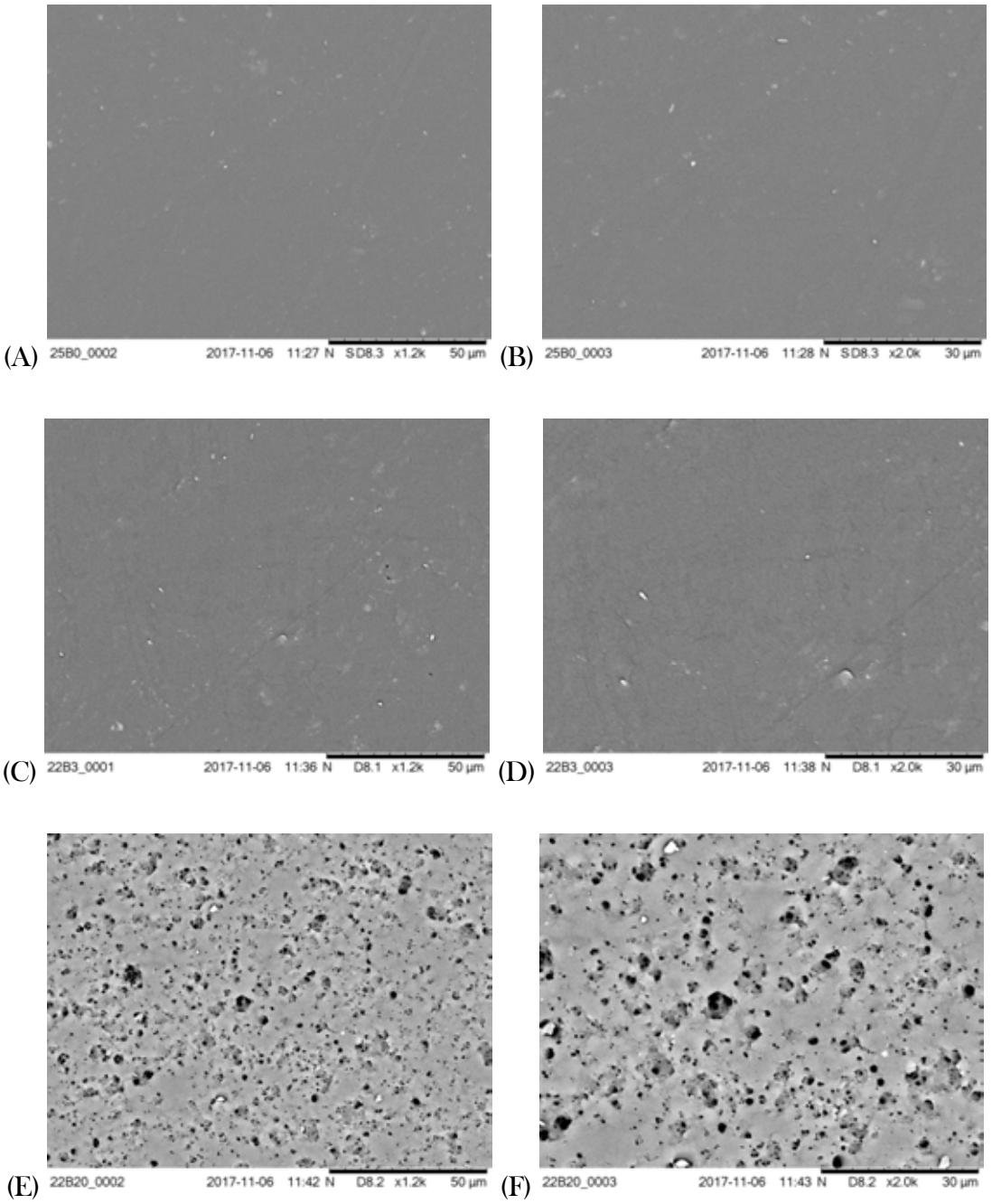

Figure 4-21: Scanning electron micrographs of Bionate II 80A at (A, C, E) x1.2k and (B, D, F) x2.0k. (A & B) Untreated, (C & D) treated with 3% H_2O_2 at 37°C and (E & F) treated with 20% H_2O_2/0.1M $CoCl_2$ at 37°C.

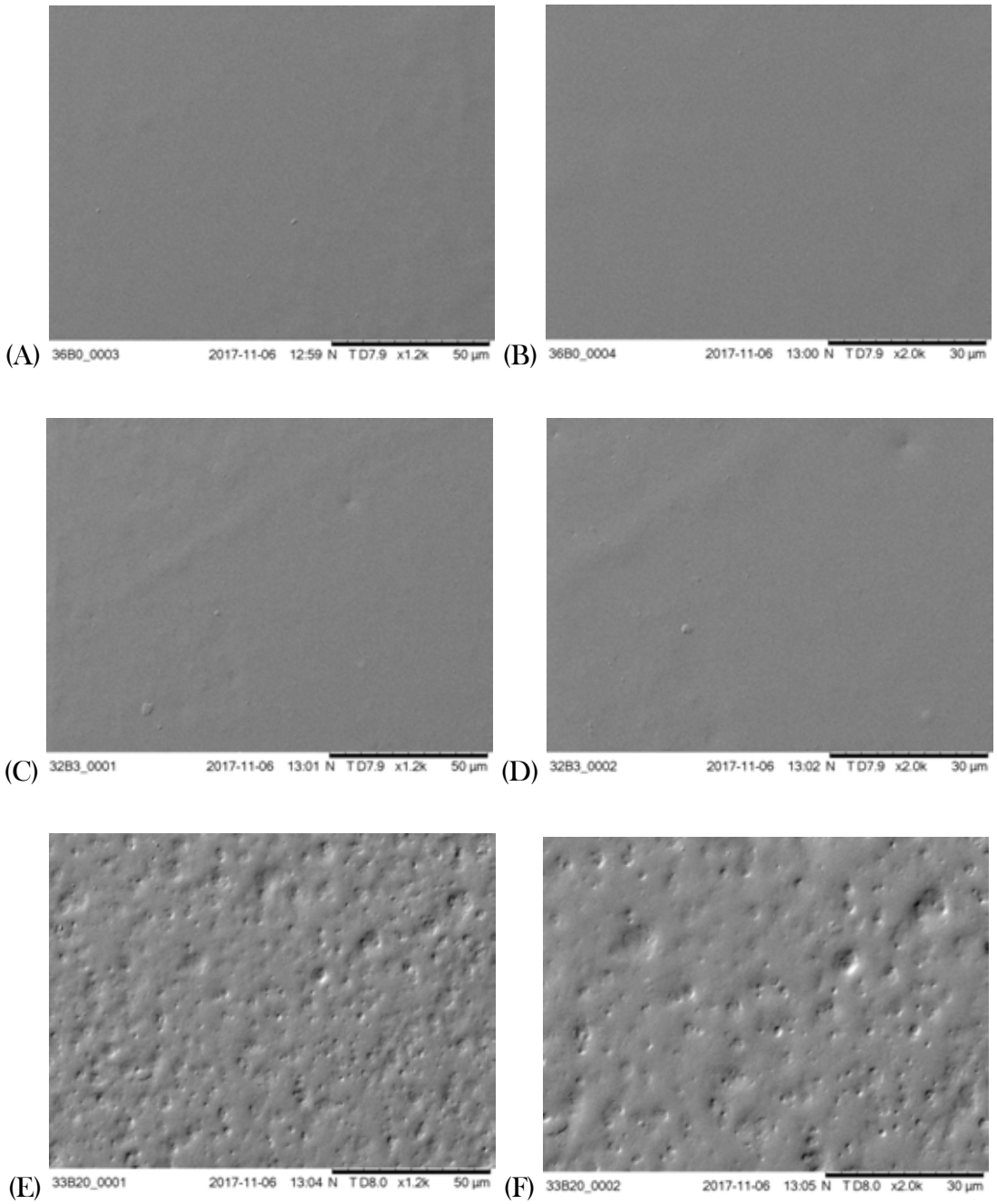

Figure 4-22: Scanning electron micrographs of Quadrathane ARC 80A at (A, C, E) x1.2k and (B, D, F) x2.0k. (A & B) Untreated, (C & D) treated with 3% H_2O_2 at 37°C and (E & F) treated with 20% H_2O_2/0.1M $CoCl_2$ at 37°C.

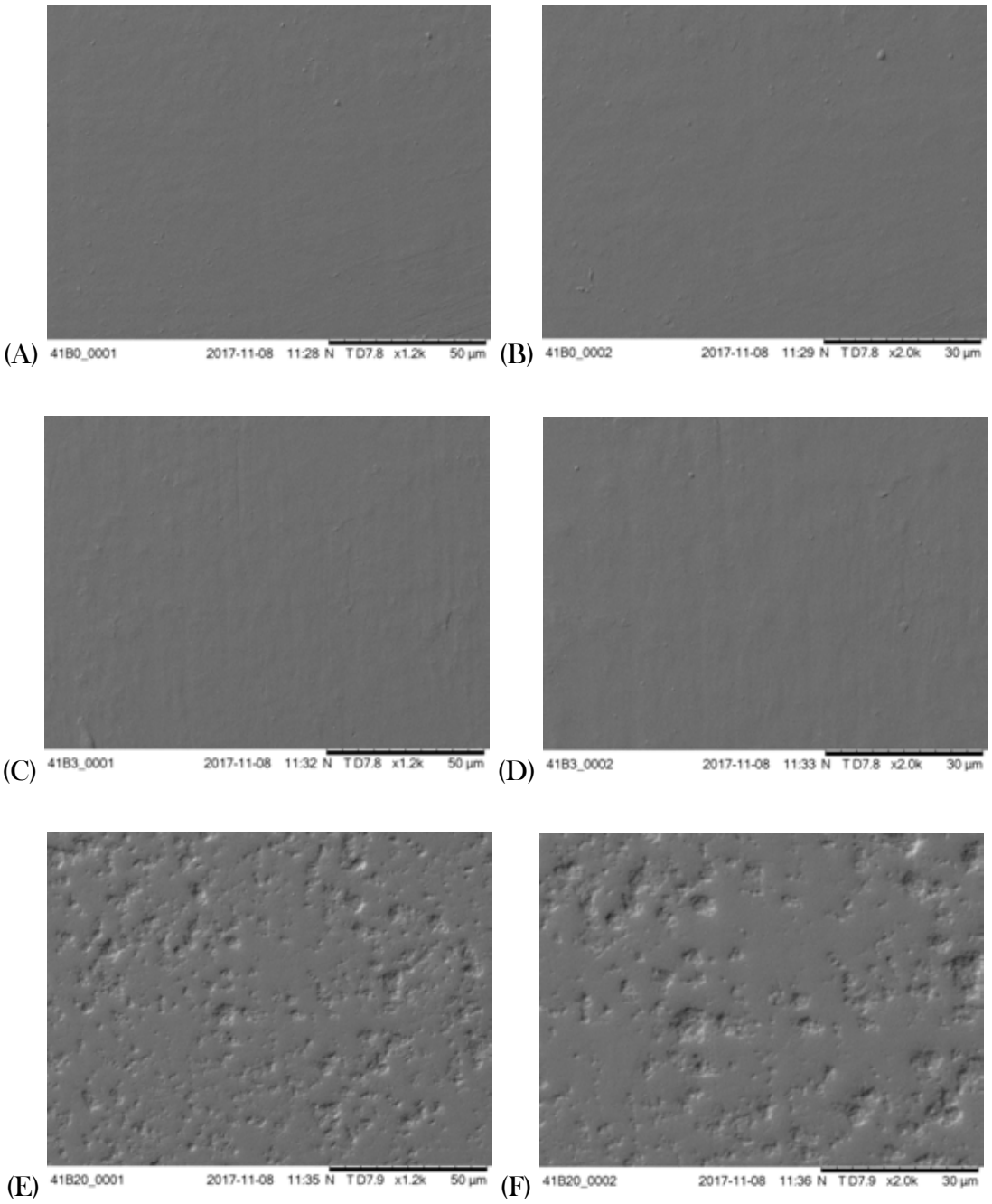

Figure 4-23: Scanning electron micrographs of ChronoFlex C ARC 80A at (A, C, E) x1.2k and (B, D, F) x2.0k. (A & B) Untreated, (C & D) treated with 3% H_2O_2 at 37°C and (E & F) treated with 20% H_2O_2/0.1M $CoCl_2$ at 37°C.

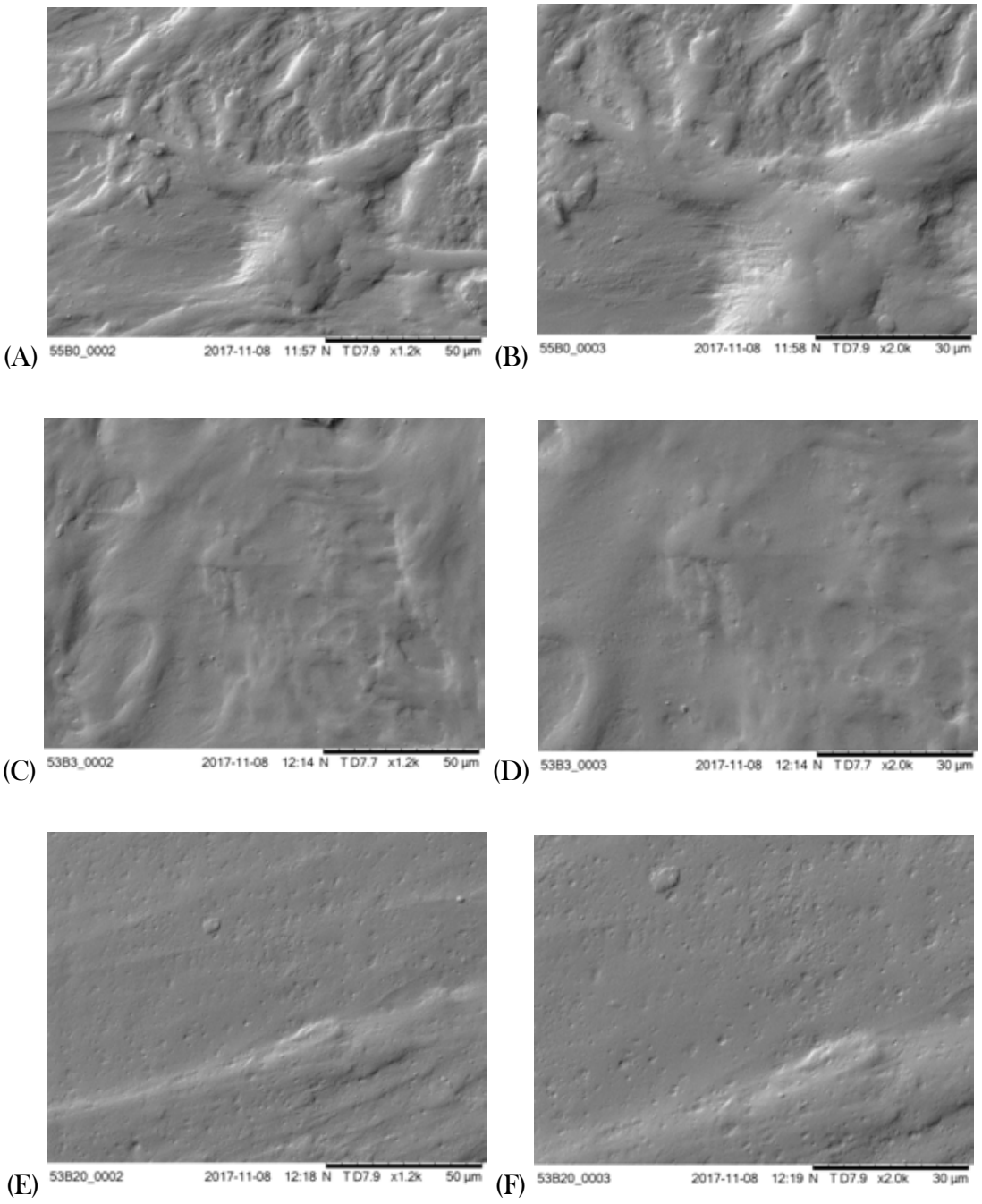

Figure 4-24: Scanning electron micrographs of ChronoSil AL 80A 5% at (A, C, E) x1.2k and (B, D, F) x2.0k. (A & B) Untreated, (C & D) treated with 3% H_2O_2 at 37°C and (E & F) treated with 20% H_2O_2/0.1*M* $CoCl_2$ at 37°C.

As the five biomaterials degraded with $H_2O_2/CoCl_2$, for 24 days, demonstrated various levels of surface pitting, these surface pits were measured using ImageJ; an example of the measurement of the surface pits can be seen in Figure 4-25.

(A) 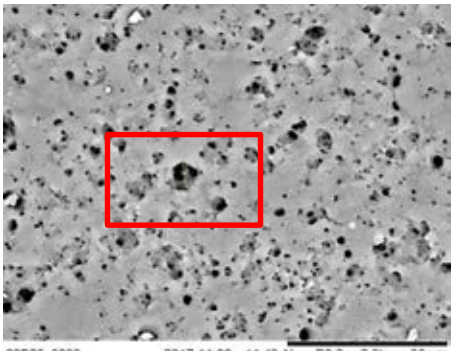

(B) 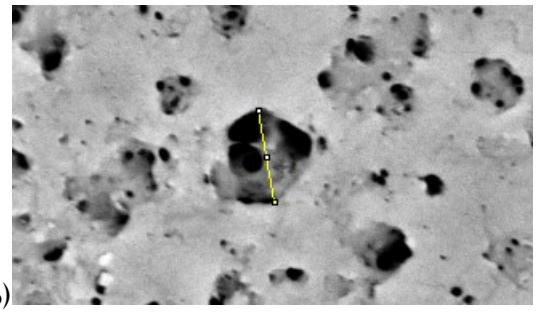

Figure 4-25: (A) SEM image, at x2.0k magnification, of Bionate II 80A treated with 20% H_2O_2/0.1*M* $CoCl_2$ at 37°C; the same micrograph is used in Figure 4-21 (F). (B) ImageJ measurement of a surface pit and figure (B) is of the red highlighted section of (A).

The dimension of pits, on the surface of the biomaterials, ranged between:

- 0.44 to 3.98 µm (Quadrathane B20)
- 0.44 to 5.88 µm (Bionate II)
- 0.48 to 3.99 µm (Quadrathane)
- 0.44 to 8.13 µm (Chronoflex C)
- 0.35 to 2.26 µm (Chronosil)

4.3.2 Hydrolysis

Figure 4-26 shows the discolouration between the (A) untreated biomaterials, (B) the biomaterials treated for 52 weeks with the ISO 10993-13 real-time degradation protocol [37 ± 1°C] and (C) the accelerated degradation protocol [70 ± 2°C]:

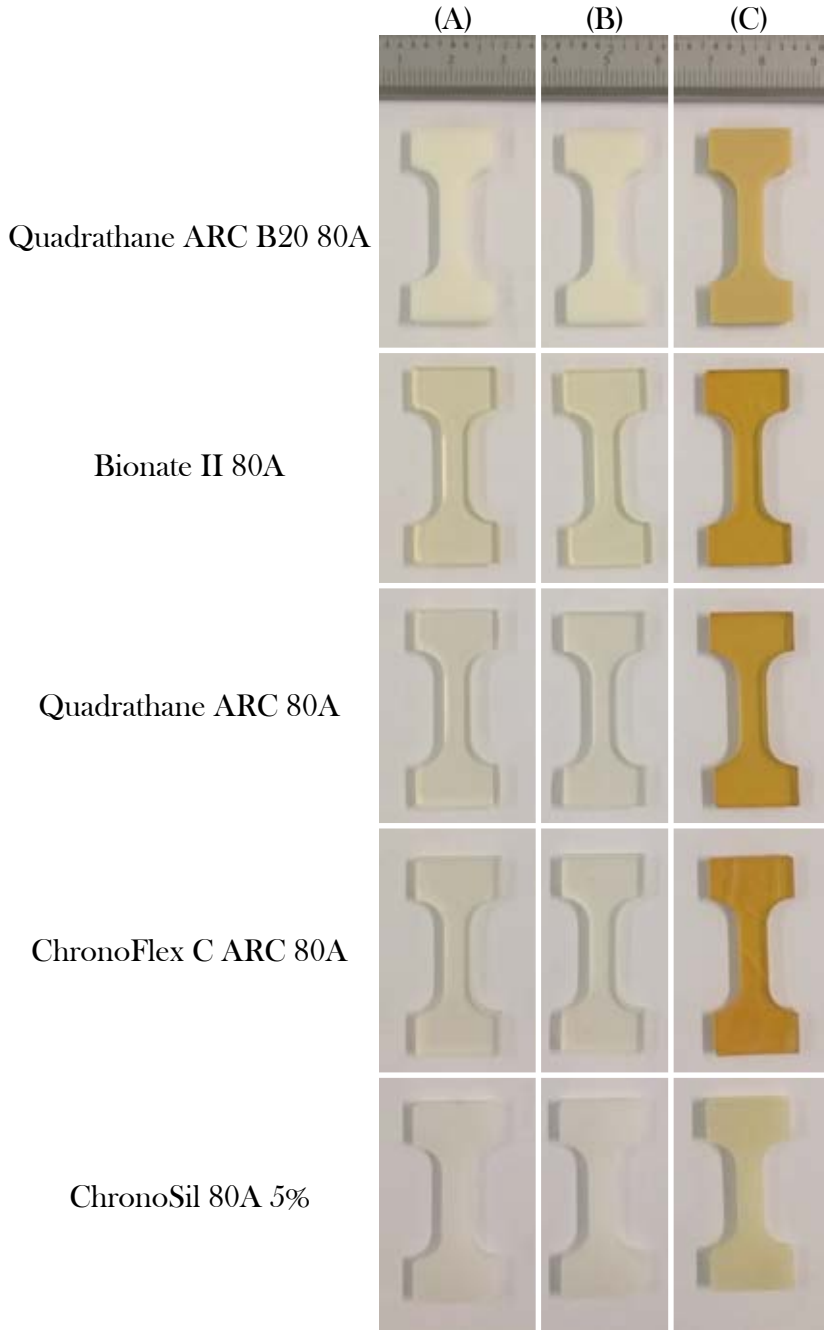

Figure 4-26: The five different biomaterials in three different groups; (A) Untreated (Control), (B) real-time degraded and (C) accelerated degraded groups.

4.3.2.1 HCI

The ATR-FTIR spectrum of the untreated and hydrolytic degraded biomaterials is illustrated in Figure 4-27. In comparison to the $H_2O_2/CoCl_2$ degraded specimens, no new absorbance peaks were observed at 930 cm^{-1} and 1174 cm^{-1} for the untreated, the real time degraded and the accelerated degraded specimens (Figure 4-27). Hyperspectral chemical images (HCIs) at 930 cm^{-1} showed a lack of regionally variation and this can be further seen with the lack of change of the range of 930 cm^{-1} absorbance intensity (arbitrary unit [AU]) range between the untreated, real time and accelerated hydrolytically degraded Quadrathane B20, Bionate II and Quadrathane specimens (Figure 4-28). For ChronoFlex C, the absorbance range changed from 1.45-1.65 AU (for the untreated) to 0.4-1.2 AU (for the accelerated hydrolytic degraded specimen (Figure 4-28).

As there were no new absorbance peaks identified at 1174 cm^{-1}, HCIs at 1174 cm^{-1} also showed a lack of regionally variation. Similar to the 930 cm^{-1} HCIs, lack of regional variation, and degradation specific variation, can be further seen with the lack of change of the range of 1174 cm^{-1} absorbance intensity range (arbitrary unit [AU]) between the untreated, real time and accelerated hydrolytically degraded Quadrathane B20, Quadrathane and ChronoFlex C specimens (Figure 4-29). For Bionate II 80A, the approximate untreated absorbance range (1.46-1.62 AU) changed to 1.5-2.2 AU for the real-time hydrolytic degraded specimen (Figure 4-29 (E)); however, no new absorbance peaks were identified at 1174 cm^{-1}.

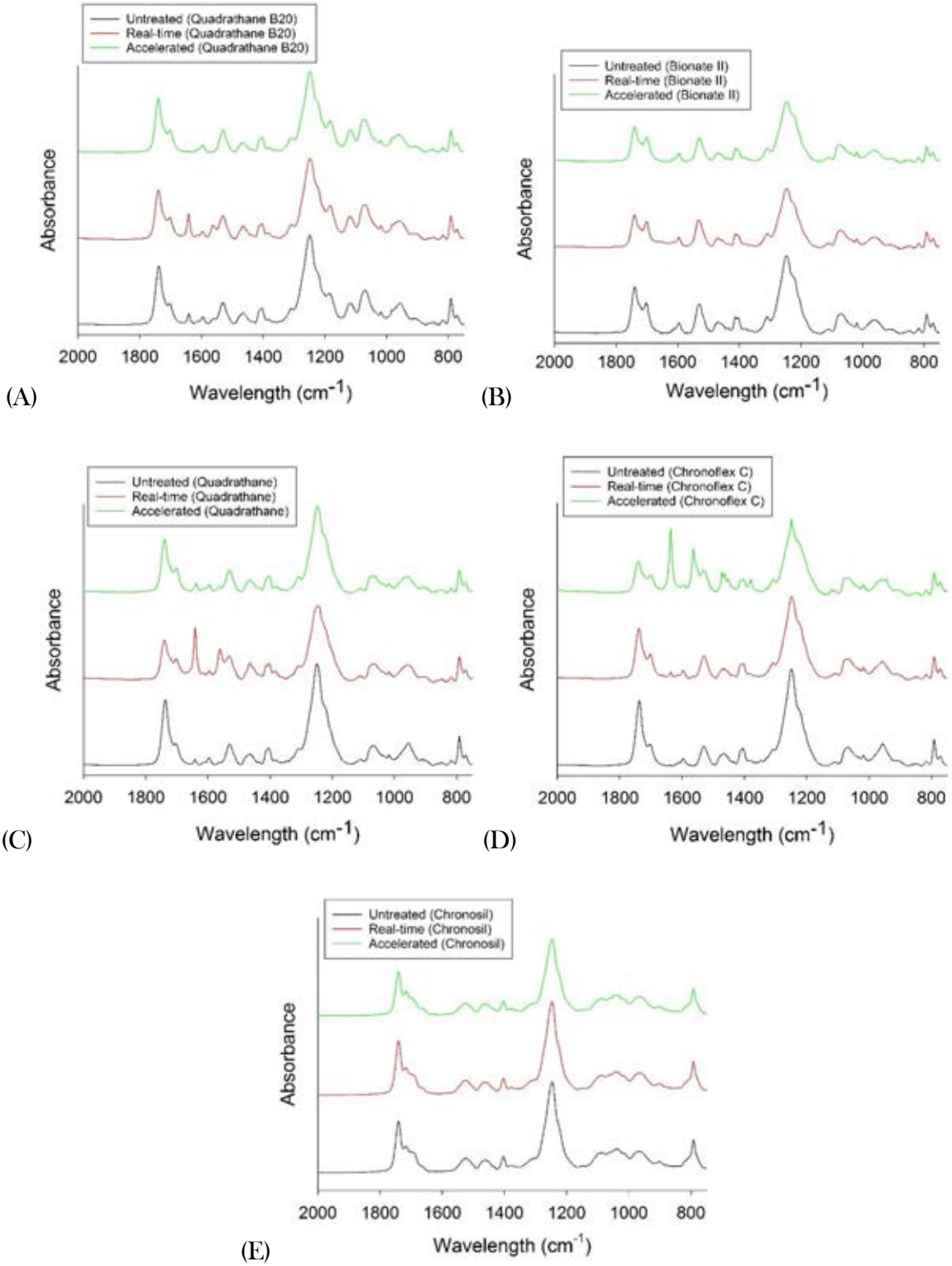

Figure 4-27: Stacked ATR-FTIR spectra of untreated and *in vitro* hydrolytic degraded five biomaterials; (A) Quadrathane ARC 80A B20, (B) Bionate II 80A, (C) Quadrathane ARC 80A, (D) ChronoFlex C 80A and (E) ChronoSil 80A 5%. Absorbance units are arbitrary units (AU).

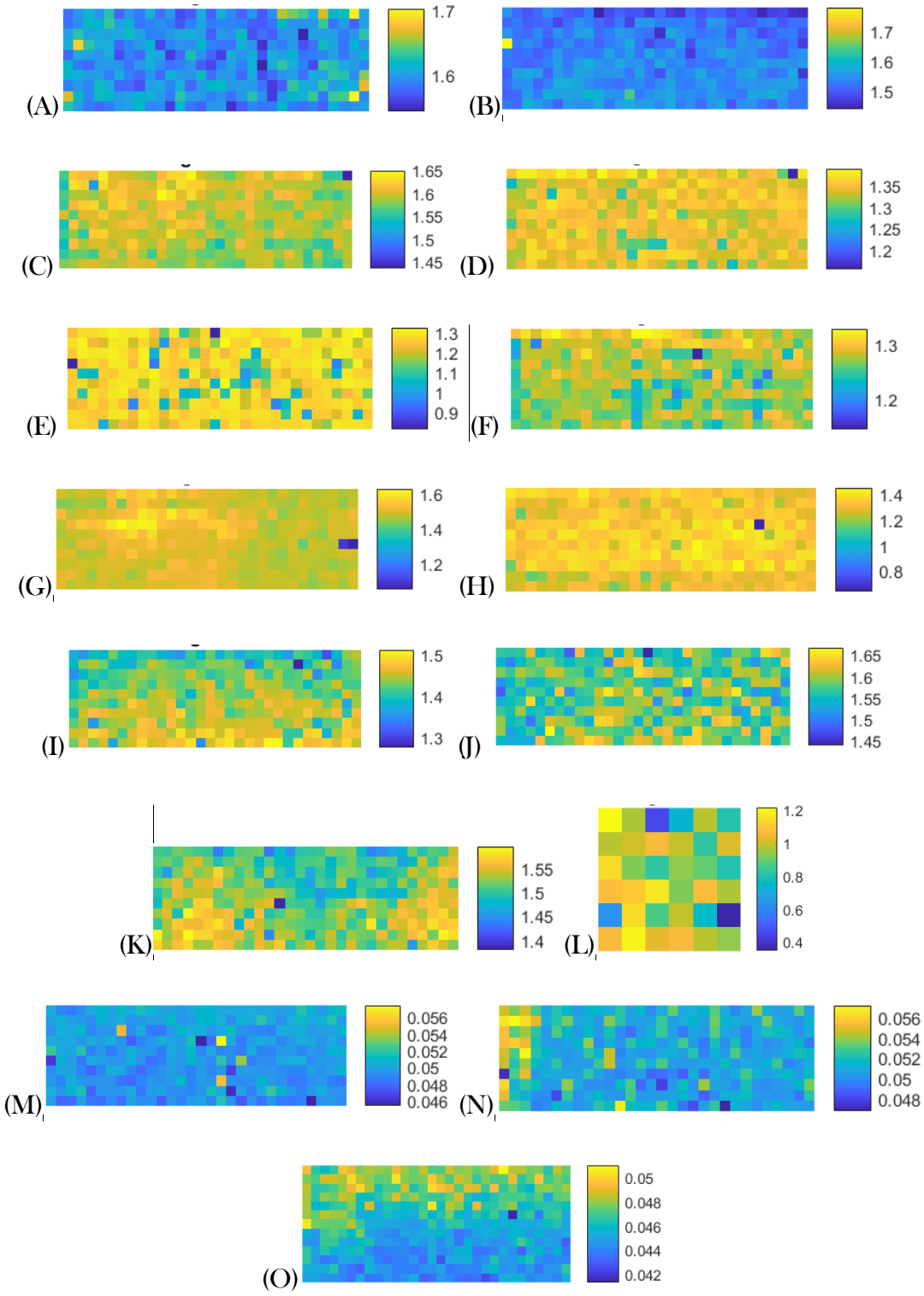

Figure 4-28: Spatial variation of the absorbance intensites at 930 cm^{-1} for the five biomaterials; (A, D, G, J, M) untreated, (B, E, H, K, N) *in vitro* real time and (C, F, I, L, O) accelerated hydrolytic degraded specimens; (A-C) Quadrathane ARC 80A B20, (D-F) Bionate II 80A, (G-I) Quadrathane ARC 80A, (J-L) ChronoFlex C 80A and (M-O) ChronoSil 80A 5%

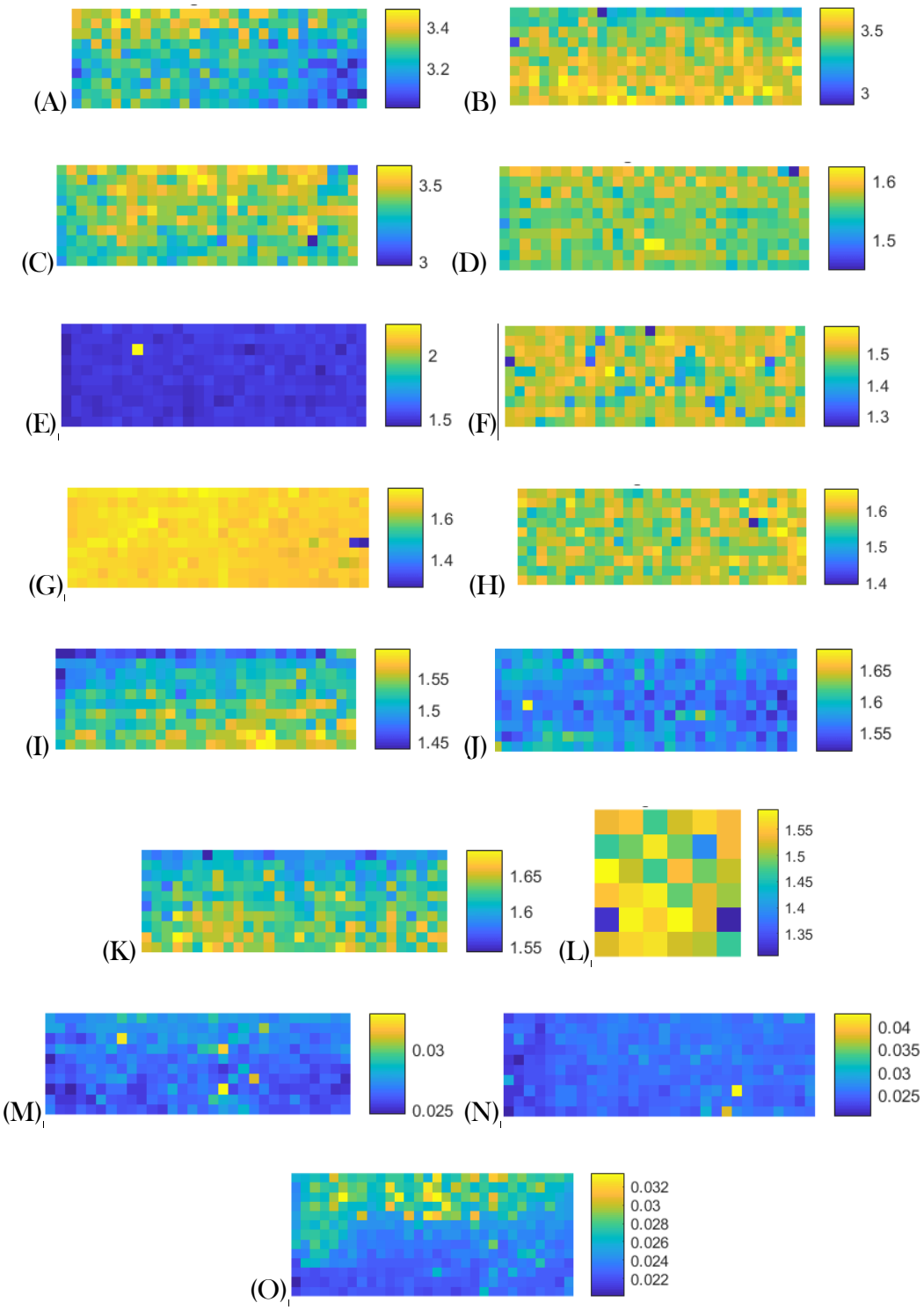

Figure 4-29: Spatial variation of the absorbance intensites at 1174 cm^{-1} for the five biomaterials; (A, D, G, J, M) untreated, (B, E, H, K, N) *in vitro* real time and (C, F, I, L, O) accelerated hydrolytic degraded specimens; (A-C) Quadrathane ARC 80A B20, (D-F) Bionate II 80A, (G-I) Quadrathane ARC 80A, (J-L) ChronoFlex C 80A and (M-O) ChronoSil 80A 5%

For Quadrathane 80A-B20 and Quadrathane 80A, HCIs at 1248 cm^{-1} showed a lack of regional variation and similar to 930 cm^{-1} and 1174 cm^{-1}, this can be seen with the lack of change of the range of absorbance intensity range between the untreated, real time and accelerated hydrolytically degraded specimens (Figure 4-30). Comparing the absorbance peak intensity range of the Bionate II untreated (Figure 4-30 (D)) and accelerated hydrolytic degraded (Figure 4-30 (F)) specimens, the approximate range differed between the untreated (5.8-8 AU) and accelerated (3.8-6.8 AU) specimens. Similarly to Bionate II, ChronoFlex C untreated (Figure 4-30 (D)) and accelerated hydrolytic degraded (Figure 4-30 (F)) specimens approximate absorbance range changed from 8.2-10.1 AU to 6.8-8.1 AU.

HCIs displayed isolated acquisitions of a new absorbance peak at 1650 cm^{-1} which was witnessed in 2 (out of 6) specimens for each of the groups; untreated, real time hydrolytic degraded and accelerated hydrolytic degraded groups. When compared to the untreated, the absorbance intensity peaks around 1635-1640 cm^{-1} of Quadrathane 80A-B20 and Quadrathane 80A specimens increased in intensity for the real time degraded specimens (Figure 4-27). This led to an increase in the 1650 cm^{-1} absorbance intensity range (Figure 4-31 (B) and (H)). ChronoFlex C absorbance range at 1650 cm^{-1} for the untreated (0.9-1.3 AU) and real time (1-1.5 AU) differed to the accelerated (1.8-3.6 AU).

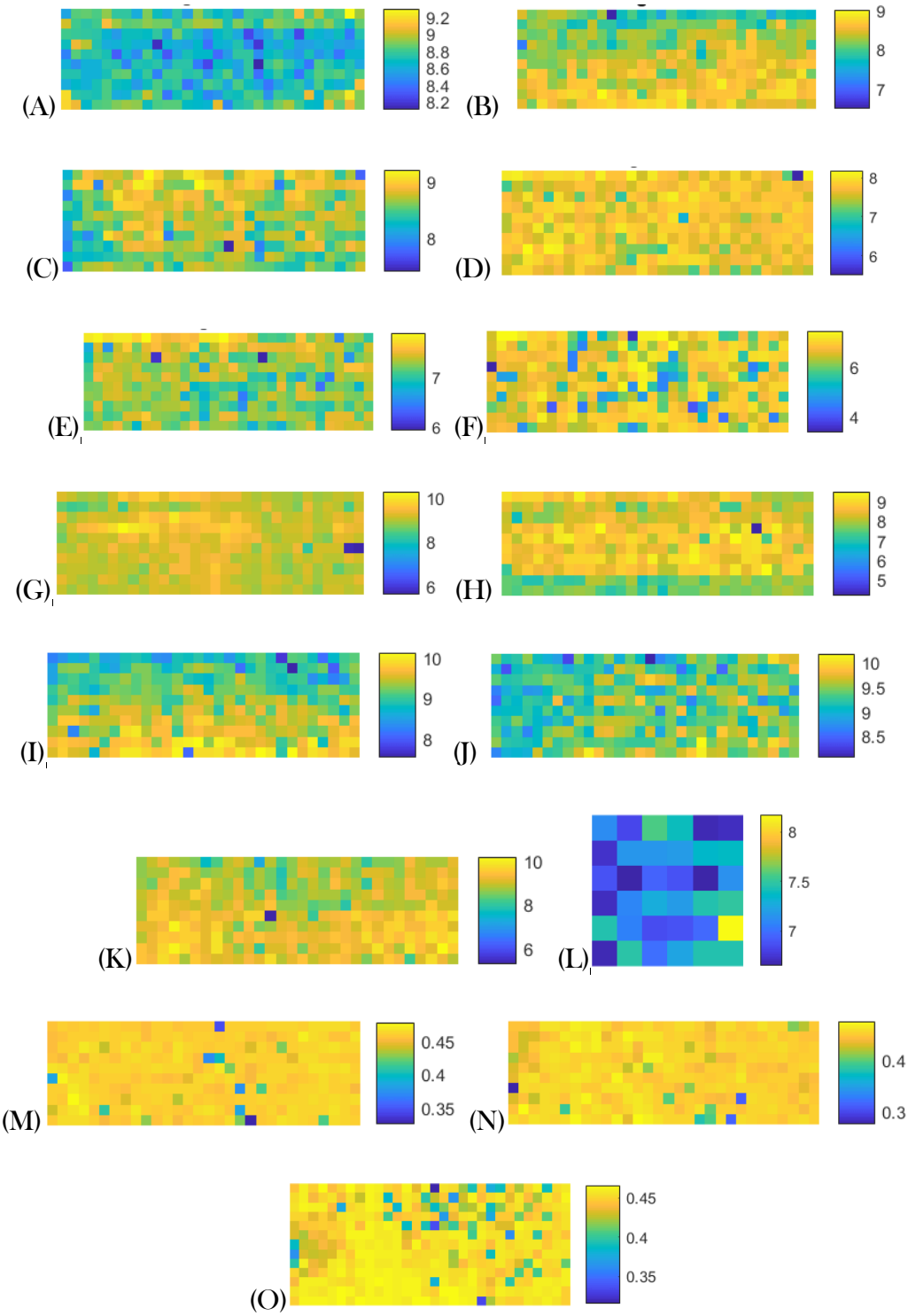

Figure 4-30: Spatial variation of the absorbance intensites at approximately 1248 cm^{-1} for the PCU biomaterials; (A, D, G, J, M) untreated, (B, E, H, K, N) *in vitro* real time hydrolytic degraded and (C, F, I, L, O) *in vitro* accelerated hydrolytic degraded specimens of the five biomaterials; (A-C) Quadrathane ARC 80A B20, (D-F) Bionate II 80A, (G-I) Quadrathane ARC 80A, (J-L) ChronoFlex C 80A and (M-O) ChronoSil 80A 5%

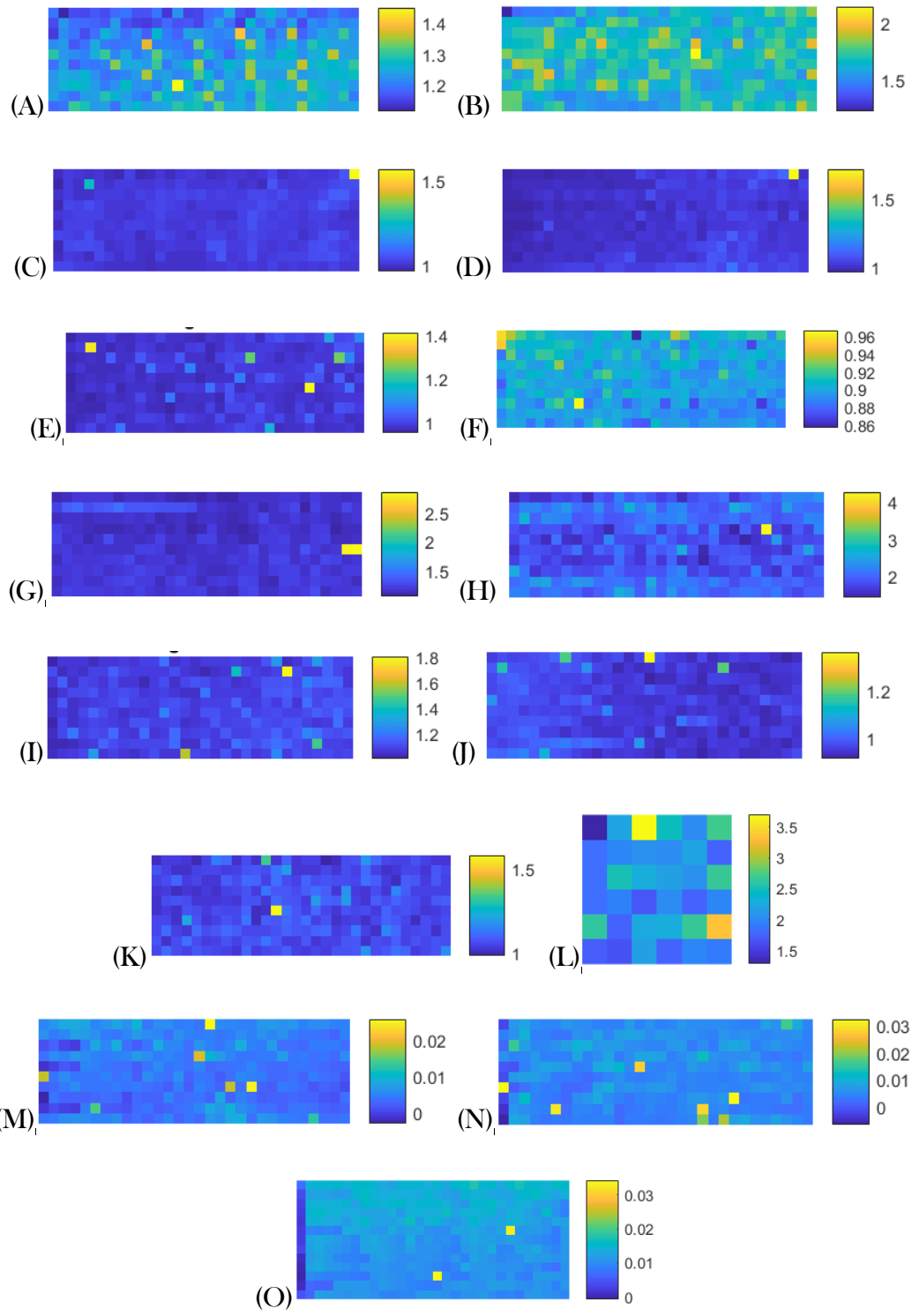

Figure 4-31: Spatial variation of 1650 cm^{-1} for the PCU biomaterials; (A, D, G, J, M) untreated, (B, E, H, K, N) *in vitro* real time hydrolytic degraded and (C, F, I, L, O) *in vitro* accelerated hydrolytic degraded specimens of the five biomaterials; (A-C) Quadrathane ARC 80A B20, (D-F) Bionate II 80A, (G-I) Quadrathane ARC 80A, (J-L) ChronoFlex C 80A and (M-O) ChronoSil 80A 5%

4.3.2.2 μDMA

Figure 4-32 and Figure 4-33 presents the storage stiffness and loss stiffness, respectively, of the five biomaterials, for normal and the *in vitro* hydrolytic degraded specimens.

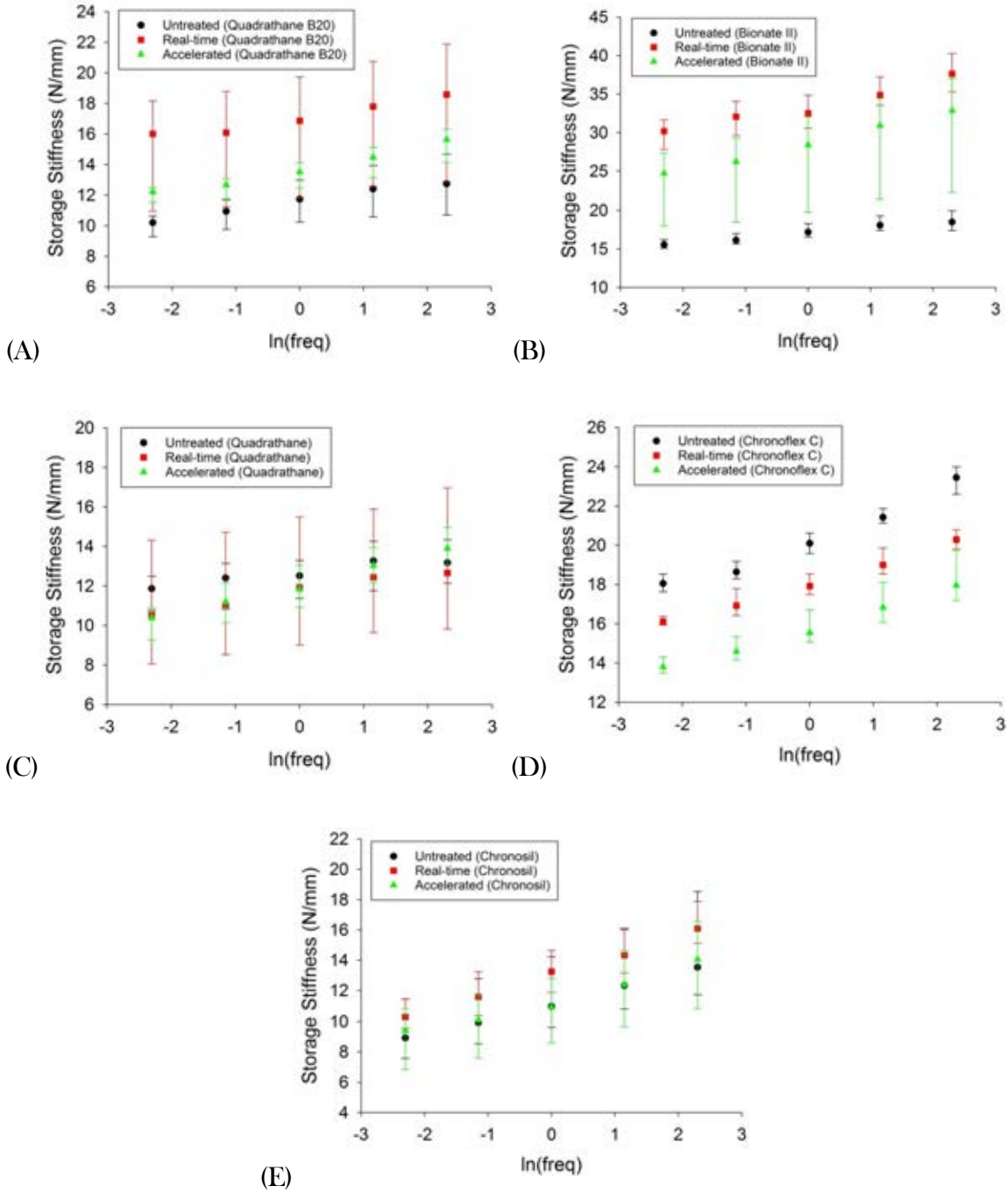

Figure 4-32: Micro-level storage stiffness of the untreated, *in vitro* real-time (Real-time) and accelerated (Accelerated) hydrolytic degradation methods of the five biomaterials; (A) Quadrathane ARC 80A B20, (B) Bionate II 80A, (C) Quadrathane ARC 80A, (D) ChronoFlex C 80A and (E) ChronoSil 80A 5% (median ± 95% confidence intervals)

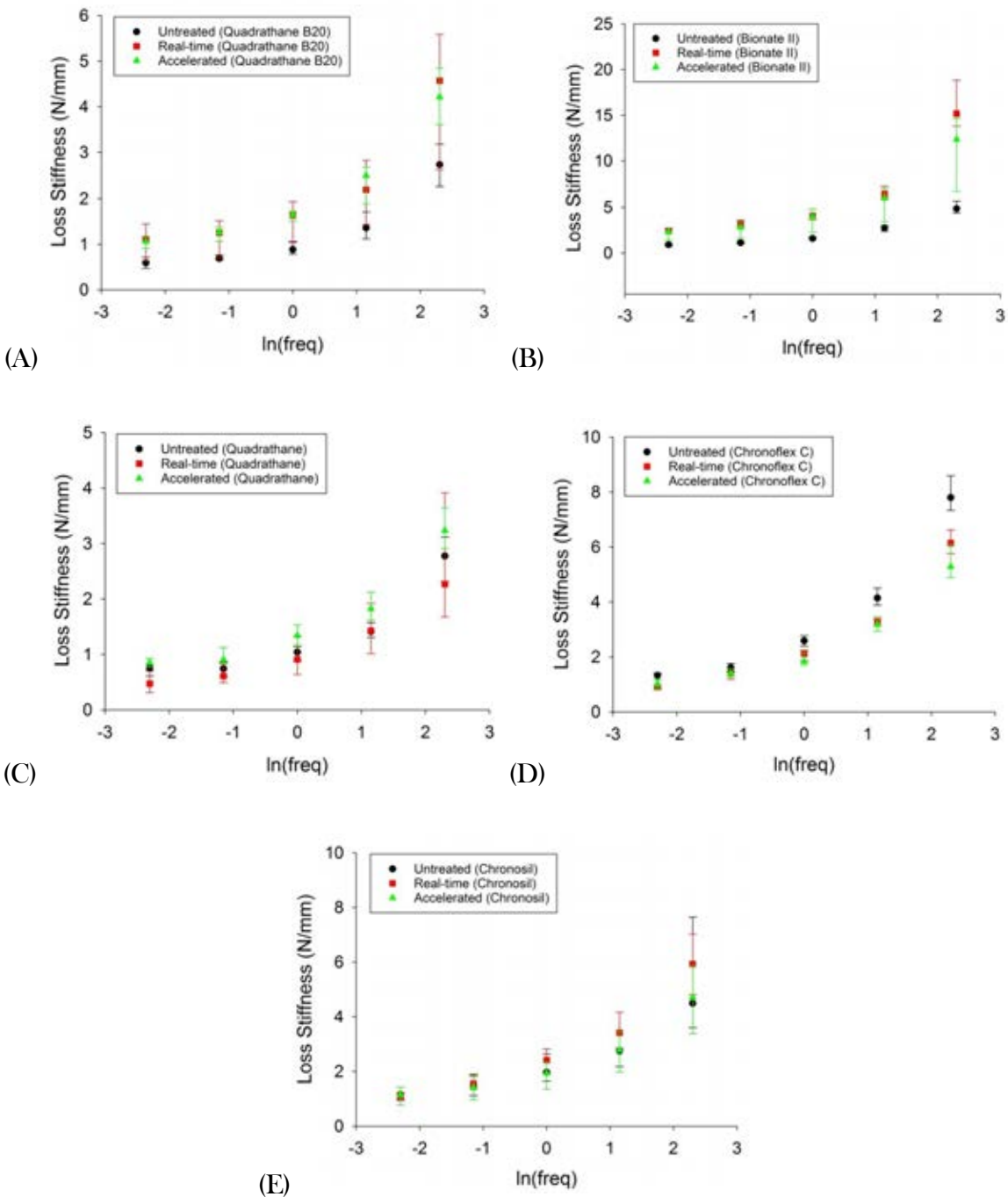

Figure 4-33: Comparison of the micro-level, surface loss stiffness of the untreated, *in vitro* ISO 10993-13 real-time (Real-time) and accelerated (Accelerated) hydrolytic degradation methods of the five biomaterials; (A) Quadrathane ARC 80A B20, (B) Bionate II 80A, (C) Quadrathane ARC 80A, (D) ChronoFlex C 80A and (E) ChronoSil 80A 5% (median ± 95% confidence intervals)

The median untreated and *in vitro* degraded storage stiffness (Figure 4-32) ranged, for the five biomaterials (Table 4-11).

Table 4-11: Median range of storage stiffness (N/mm) values per biomaterial

Biomaterial	Group	Range
Quadrathane B20	UNT	10.20 (0.1 Hz) to 12.74 (10 Hz)
	Real-time	16.01 (0.1 Hz) to 18.58 (10 Hz)
	Accelerated	12.22 (0.1 Hz) to 15.64 (10 Hz)
Bionate II	UNT	15.56 (0.1 Hz) to 18.49 (10 Hz)
	Real-time	30.17 (0.1 Hz) to 37.63 (10 Hz)
	Accelerated	24.71 (0.1 Hz) to 32.86 (10 Hz)
Quadrathane	UNT	11.86 (0.1 Hz) to 13.27 (3.16 Hz)
	Real-time	10.53 (0.1 Hz) to 12.66 (10 Hz)
	Accelerated	10.38 (0.1 Hz) to 13.91 (10 Hz)
Chronoflex C	UNT	18.05 (0.1 Hz) to 23.44 (10 Hz)
	Real-time	16.11 (0.1 Hz) to 20.29 (10 Hz)
	Accelerated	13.81 (0.1 Hz) to 17.96 (10 Hz)
Chronosil	UNT	8.93 (0.1 Hz) to 13.54 (10 Hz)
	Real-time	10.31 (0.1 Hz) to 16.09 (10 Hz)
	Accelerated	9.40 (0.1 Hz) to 14.05 (10 Hz)

While, the median untreated and *in vitro* degraded loss stiffness (Figure 4-33) ranged, for the five biomaterials (Table 4-12).

Table 4-12: Median range of loss stiffness (N/mm) values per biomaterial

Biomaterial	Group	Range
Quadrathane B20	UNT	0.59 (0.1 Hz) to 2.73 (10 Hz)
	Real-time	1.11 (0.1 Hz) to 4.57 (10 Hz)
	Accelerated	1.06 (0.1 Hz) to 4.21 (10 Hz)
Bionate II	UNT	0.91 (0.1 Hz) to 4.85 (10 Hz)
	Real-time	2.39 (0.1 Hz) to 15.18 (10 Hz)
	Accelerated	2.33 (0.1 Hz) to 12.35 (10 Hz)
Quadrathane	UNT	0.74 (0.316 Hz) to 2.78 (10 Hz)
	Real-time	0.47 (0.1 Hz) to 2.27 (10 Hz)
	Accelerated	0.85 (0.1 Hz) to 3.23 (10 Hz)
Chronoflex C	UNT	1.33 (0.1 Hz) to 7.80 (10 Hz)
	Real-time	0.91 (0.1 Hz) to 6.15 (10 Hz)
	Accelerated	1.02 (0.1 Hz) to 5.29 (10 Hz)
Chronosil	UNT	1.15 (0.1 Hz) to 4.49 (10 Hz)
	Real-time	1.10 (0.1 Hz) to 5.93 (10 Hz)
	Accelerated	1.16 (0.1 Hz) to 4.71 (10 Hz)

The micro-level storage stiffness frequency dependent trends increased logarithmically in relation to frequency ($p < 0.05$) for all biomaterials (untreated and hydrolytic degraded) except for one position on the surface of Bionate II degraded with PBS at 37°C (Real-time); see equation 4.1, where A is a coefficient and B is a constant, and 8.5 Appendix E - Table 8-1 to Table 8-5. The micro-level loss stiffness of Chronoflex C and Chronosil were logarithmically frequency dependent in relation to frequency ($p < 0.05$) (equation 4.2, where C is a coefficient and D is a constant, and 8.5 Appendix E - Table 8-1 to Table 8-5). For the three other biomaterials (Quadrathane B20, Bionate II and Quadrathane), the frequency dependent trends of the loss stiffness behaved logarithmically ($p < 0.05$) at specific positions on the surface of the biomaterials (8.5 Appendix E - Table 8-1 to Table 8-5).

The multiple comparison test results, that compared the untreated and *in vitro* hydrolytic degraded biomaterials, are shown in Table 4-13; the stated frequencies imply significant differences were detected ($p < 0.05$). Interestingly, the storage and loss stiffness of the Chronosil groups were not significantly different for all frequencies ($p > 0.05$); this result is similar to the Chronosil μDMA results for the oxidation study (see Table 4-6).

Table 4-13: Multiple comparison test results for the micro-level, surface viscoelastic properties of the untreated and hydrolytic degraded long-term implantable polymers. The frequencies stated indicates that the comparison were significantly different ($p < 0.05$) between the *in vitro* ISO 10993-13 real-time (Real-time) and accelerated (Accelerated) hydrolytic degradation methods of the specific biomaterial.

Biomaterial	Multiple Comparison Test	Storage Stiffness	Loss Stiffness
Quadrathane B20	UNT – Real time	0.1 to 10 Hz	1 and 10 Hz
	UNT – Accelerated	-	0.1 to 10 Hz
	Real time – Accelerated	-	-
Bionate II	UNT – Real time	0.1 to 10 Hz	0.1 to 10 Hz
	UNT – Accelerated	-	0.1 Hz
	Real time – Accelerated	-	-
Quadrathane	UNT – Real time	-	-
	UNT – Accelerated	-	0.316 and 3.16 Hz
	Real time – Accelerated	-	0.1 to 0.316 Hz
Chronoflex C	UNT – Real time	-	0.1 to 3.16 Hz
	UNT – Accelerated	0.1 to 10 Hz	1 to 10 Hz
	Real time – Accelerated	-	-
Chronosil	UNT – Real time	-	-
	UNT – Accelerated	-	-
	Real time – Accelerated	-	-

4.3.2.3 DMA

The macro storage stiffness and loss stiffness of the five biomaterials, for normal and the *in vitro* hydrolytic degraded specimens, are presented in Figure 4-34 and Figure 4-35.

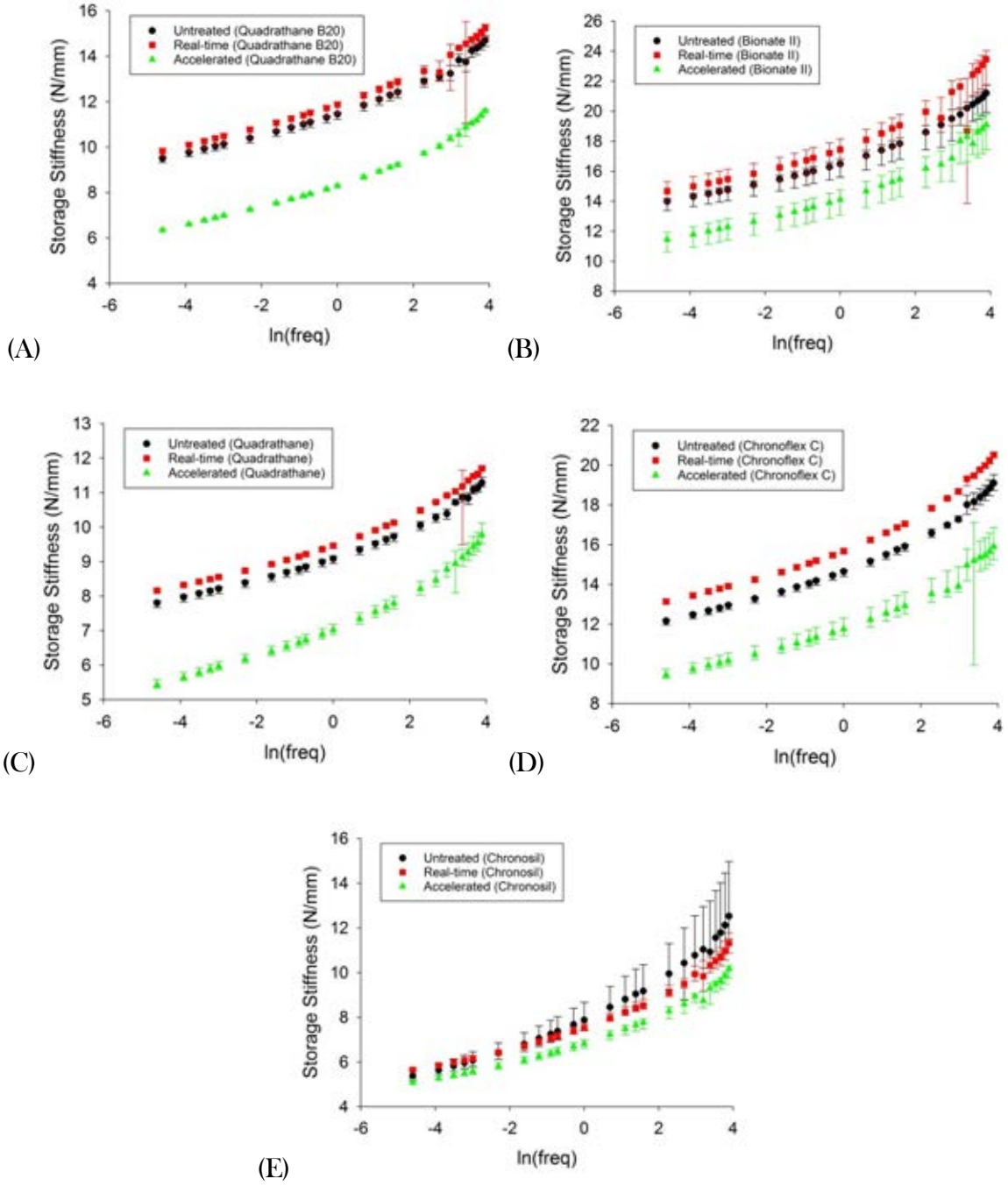

Figure 4-34: Macro storage stiffness of the untreated, *in vitro* real-time (Real-time) and accelerated (Accelerated) hydrolytic degradation methods of the five biomaterials; (A) Quadrathane ARC 80A B20, (B) Bionate II 80A, (C) Quadrathane ARC 80A, (D) ChronoFlex C 80A and (E) ChronoSil 80A 5% (median ± 95% confidence intervals)

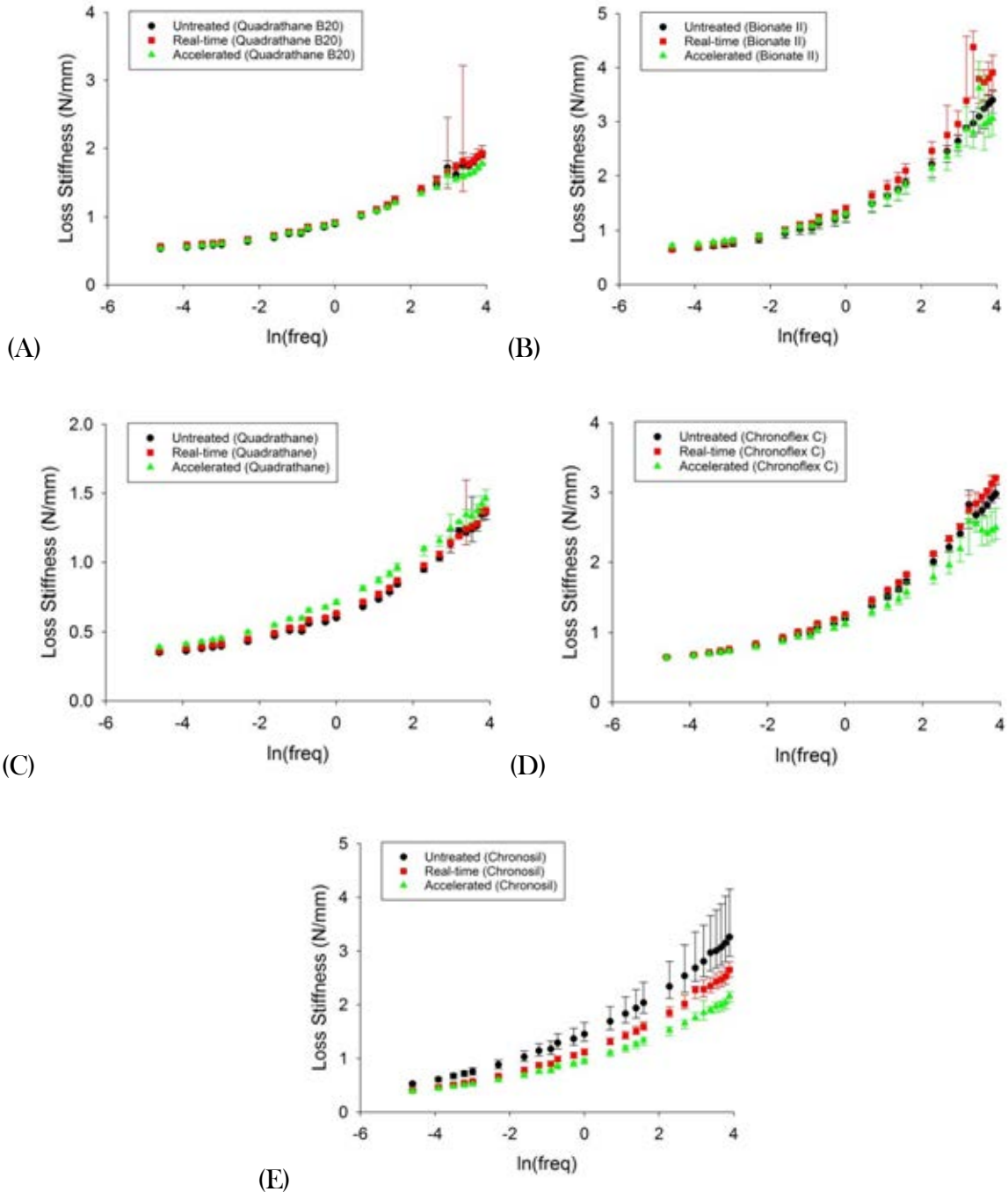

Figure 4-35: Comparison of the macro loss stiffness of the untreated, *in vitro* ISO 10993-13 real-time (Real-time) and accelerated (Accelerated) hydrolytic degradation methods of the five biomaterials; (A) Quadrathane ARC 80A B20, (B) Bionate II 80A, (C) Quadrathane ARC 80A, (D) ChronoFlex C 80A and (E) ChronoSil 80A 5% (median ± 95% confidence intervals)

The median untreated and *in vitro* degraded storage stiffness (Figure 4-34) ranged, for the five biomaterials (Table 4-14).

Table 4-14: Median range of storage stiffness (N/mm) values per biomaterial

Biomaterial	Group	Range
Quadrathane B20	UNT	9.51 (0.01 Hz) to 14.70 (49 Hz)
	Real-time	9.82 (0.01 Hz) to 15.24 (49 Hz)
	Accelerated	6.35 (0.01 Hz) to 11.60 (49 Hz)
Bionate II	UNT	13.99 (0.01 Hz) to 21.20 (49 Hz)
	Real-time	14.67 (0.01 Hz) to 23.45 (49 Hz)
	Accelerated	11.45 (0.01 Hz) to 19.08 (49 Hz)
Quadrathane	UNT	7.81 (0.01 Hz) to 11.29 (49 Hz)
	Real-time	8.16 (0.01 Hz) to 11.71 (49 Hz)
	Accelerated	5.43 (0.01 Hz) to 9.77 (49 Hz)
Chronoflex C	UNT	12.16 (0.01 Hz) to 19.10 (49 Hz)
	Real-time	13.14 (0.01 Hz) to 20.52 (49 Hz)
	Accelerated	9.44 (0.01 Hz) to 15.91 (49 Hz)
Chronosil	UNT	5.37 (0.01 Hz) to 12.53 (49 Hz)
	Real-time	5.65 (0.01 Hz) to 11.31 (49 Hz)
	Accelerated	5.08 (0.01 Hz) to 10.17 (49 Hz)

While, the median untreated and *in vitro* degraded loss stiffness (Figure 4-35) ranged, for the five biomaterials (Table 4-15).

Table 4-15: Median range of loss stiffness (N/mm) values per biomaterial

Biomaterial	Group	Range
Quadrathane B20	UNT	0.53 (0.01 Hz) to 1.90 (49 Hz)
	Real-time	0.57 (0.01 Hz) to 1.93 (49 Hz)
	Accelerated	0.53 (0.01 Hz) to 1.77 (49 Hz)
Bionate II	UNT	0.65 (0.01 Hz) to 3.40 (49 Hz)
	Real-time	0.65 (0.01 Hz) to 4.38 (29 Hz)
	Accelerated	0.72 (0.01 Hz) to 3.62 (34 Hz)
Quadrathane	UNT	0.35 (0.01 Hz) to 1.36 (49 Hz)
	Real-time	0.36 (0.01 Hz) to 1.38 (49 Hz)
	Accelerated	0.39 (0.01 Hz) to 1.46 (49 Hz)
Chronoflex C	UNT	0.65 (0.01 Hz) to 2.98 (49 Hz)
	Real-time	0.65 (0.01 Hz) to 3.21 (49 Hz)
	Accelerated	0.64 (0.01 Hz) to 2.49 (49 Hz)
Chronosil	UNT	0.53 (0.01 Hz) to 3.26 (49 Hz)
	Real-time	0.40 (0.01 Hz) to 2.65 (49 Hz)
	Accelerated	0.39 (0.01 Hz) to 2.16 (49 Hz)

Similarly to the macro viscoelastic properties' regression analyses in the oxidation study, all of the storage stiffness and loss stiffness trends increased logarithmically in relation to frequency ($p < 0.05$) for all biomaterials (equation 4.1, equation 4.2 and 8.6 Appendix F - Table 8-6 and Table 8-10).

Table 4-16 shows the multiple comparison test results that compared the macro viscoelastic response of the untreated and *in vitro* hydrolytic degraded biomaterials; stated frequencies in Table 4-16 imply significant differences were detected ($p < 0.05$) between the groups. The storage stiffness of the four aromatic PCU biomaterials (Quadrathane B20, Bionate II, Quadrathane and Chronoflex C) was not significantly different ($p > 0.05$) for all frequencies. However, comparing the real-time and accelerated groups viscoelastic properties for these four aromatic PCUs, the viscoelastic properties were significantly different ($p < 0.05$) at specific frequencies. Chronosil untreated and real-time degraded groups were not significantly different ($p > 0.05$) for all tested frequencies, while the untreated and accelerated groups were significantly different at specific frequencies ($p < 0.05$).

Table 4-16: Multiple comparison test results for the macro viscoelastic properties of the untreated and hydrolytic degraded long-term implantable polymers. The frequencies stated indicates that the comparison were significantly different ($p < 0.05$) between the *in vitro* ISO 10993-13 real-time (Real-time) and accelerated (Accelerated) hydrolytic degradation methods of the specific biomaterial.

Biomaterial	Multiple Comparison Test	Storage Stiffness	Loss Stiffness
Quadrathane B20	UNT – Real time	-	0.02 and 0.03 Hz
	UNT – Accelerated	-	-
	Real time – Accelerated	0.01 to 15, 24, 34 to 49 Hz	24 and 39 Hz
Bionate II	UNT – Real time	-	-
	UNT – Accelerated	-	-
	Real time – Accelerated	0.01 to 24, 35 to 49 Hz	15, 20, 44 and 49 Hz
Quadrathane	UNT – Real time	-	-
	UNT – Accelerated	-	0.01 to 15, 39 to 49 Hz
	Real time – Accelerated	0.01 to 24, 34 to 49 Hz	24 Hz
Chronoflex C	UNT – Real time	-	-
	UNT – Accelerated	-	-
	Real time – Accelerated	0.01 to 49 Hz	3 to 15, 29 to 49 Hz
Chronosil	UNT – Real time	-	-
	UNT – Accelerated	0.5 to 10, 20 to 49 Hz	0.01 to 49 Hz
	Real time – Accelerated	0.01 Hz	-

4.3.2.4 SEM

SEM images are presented of the surfaces of Quadrathane ARC 80A B20 (Figure 4-36), Bionate II 80A (Figure 4-37), Quadrathane ARC 80A (Figure 4-38), Chronoflex C 80A (Figure 4-39) and Chronosil 80A 5% (Figure 4-40). Similar to the SEM images in the oxidation study (section 4.3.1.4), images (A), (C) and (E) are recorded at x1.2k magnification while images (B), (D) and (F) are at x2.0k magnification. SEM images (A) and (B) are Untreated biomaterial, (C) and (D) are biomaterials treated with PBS at 37°C (Real-time) and (E) and (F) are biomaterials treated with PBS at 70°C (Accelerated).

There was no evidence of any other surface morphology changes, when comparing the untreated specimens to the *in vitro* hydrolytic degraded (Real-time and accelerated) specimens for the Quadrathane B20 biomaterial (Figure 4-36). There was no apparent visual surface morphological differences between Bionate II untreated and Real-time hydrolytic degraded specimens. However, compared to the untreated specimen, surface morphological changes of the Accelerated hydrolytic degraded specimen was witnessed (Figure 4-37). Small blistered areas on the surface of the Real-time and Accelerated degraded Quadrathane specimens was observed on the SEM images when compared to the untreated Quadrathane specimen (Figure 4-38). Chronoflex C Accelerated hydrolytic degraded specimen observed larger blistered area on the surface of the specimen when compared to the untreated and Real-time degraded specimens (Figure 4-39). Further, the Chronosil real-time hydrolytic degraded surface displayed a difference in the surface morphology when compared to the visually smooth surface morphology of the untreated specimen; the Accelerated degraded specimen displayed a vast area of blistering (Figure 4-40).

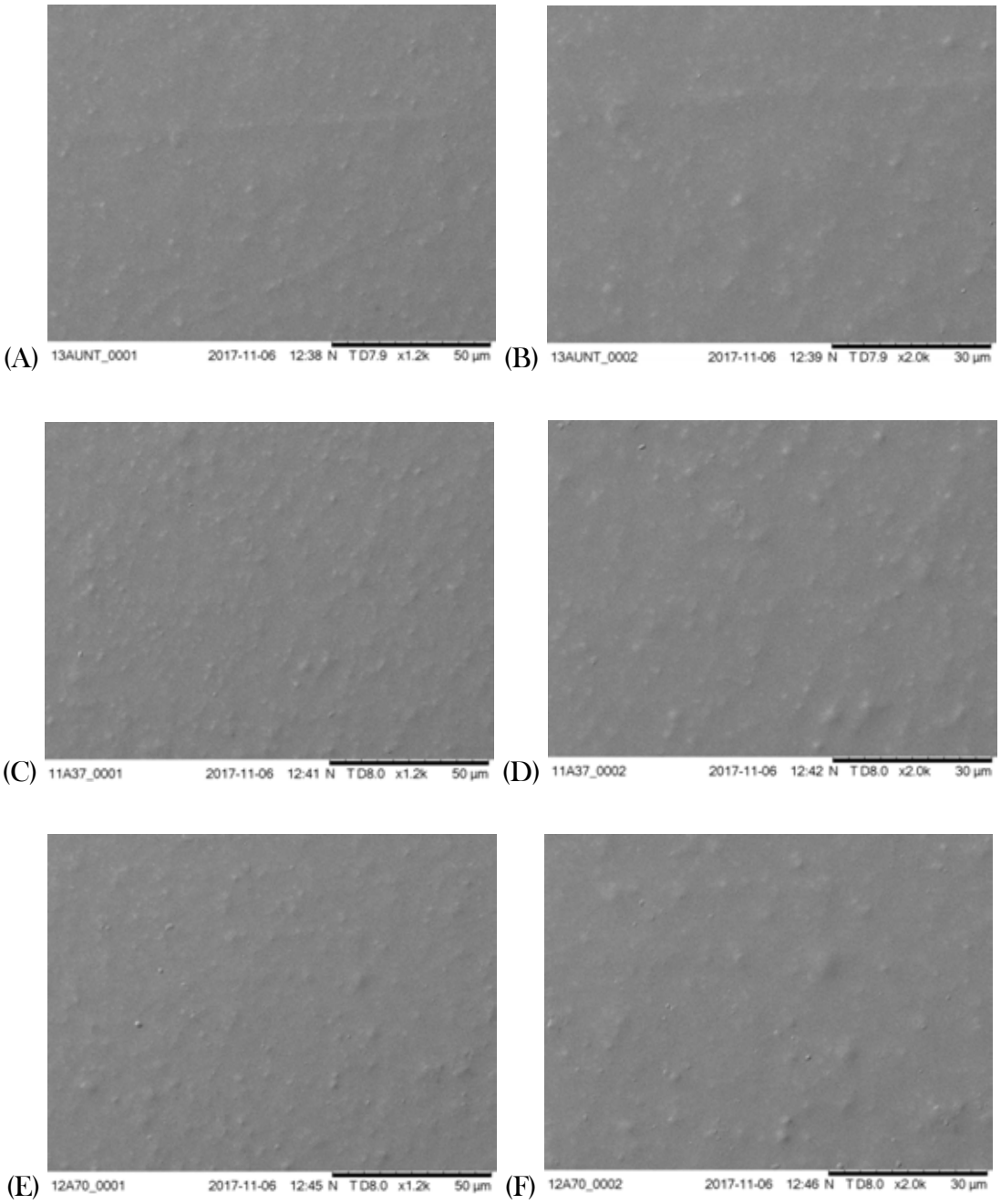

Figure 4-36: Scanning electron micrographs of Quadrathane with radiopacifiers (Quadrathane B20) at (A, C, E) x1.2k and (B, D, F) x2.0k. (A & B) Untreated, (C & D) treated with PBS at 37°C and (E & F) treated with PBS at 70°C.

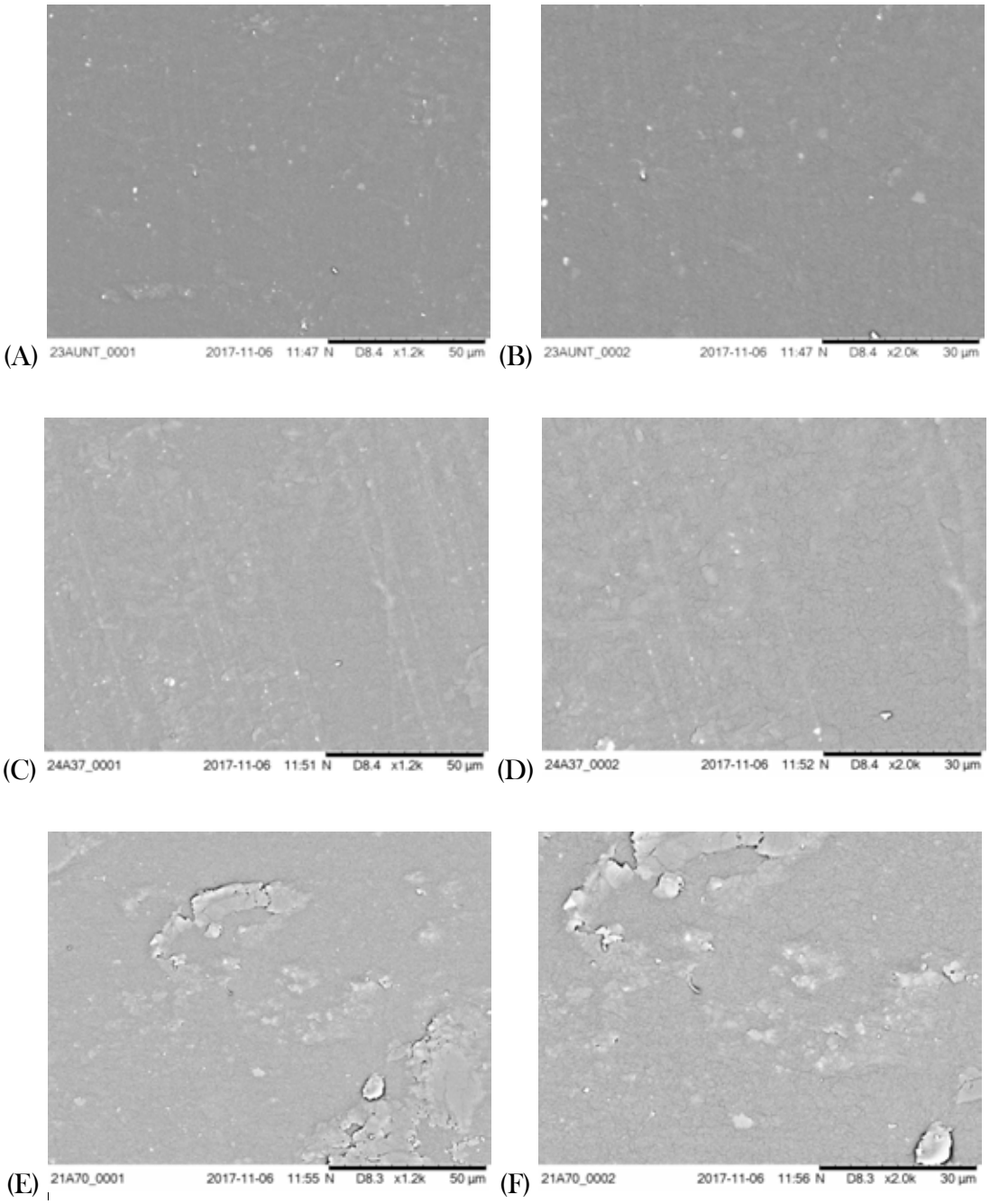

Figure 4-37: Scanning electron micrographs of Bionate II 80A at (A, C, E) x1.2k and (B, D, F) x2.0k. (A & B) Untreated, (C & D) treated with PBS at 37°C and (E & F) treated with PBS at 70°C.

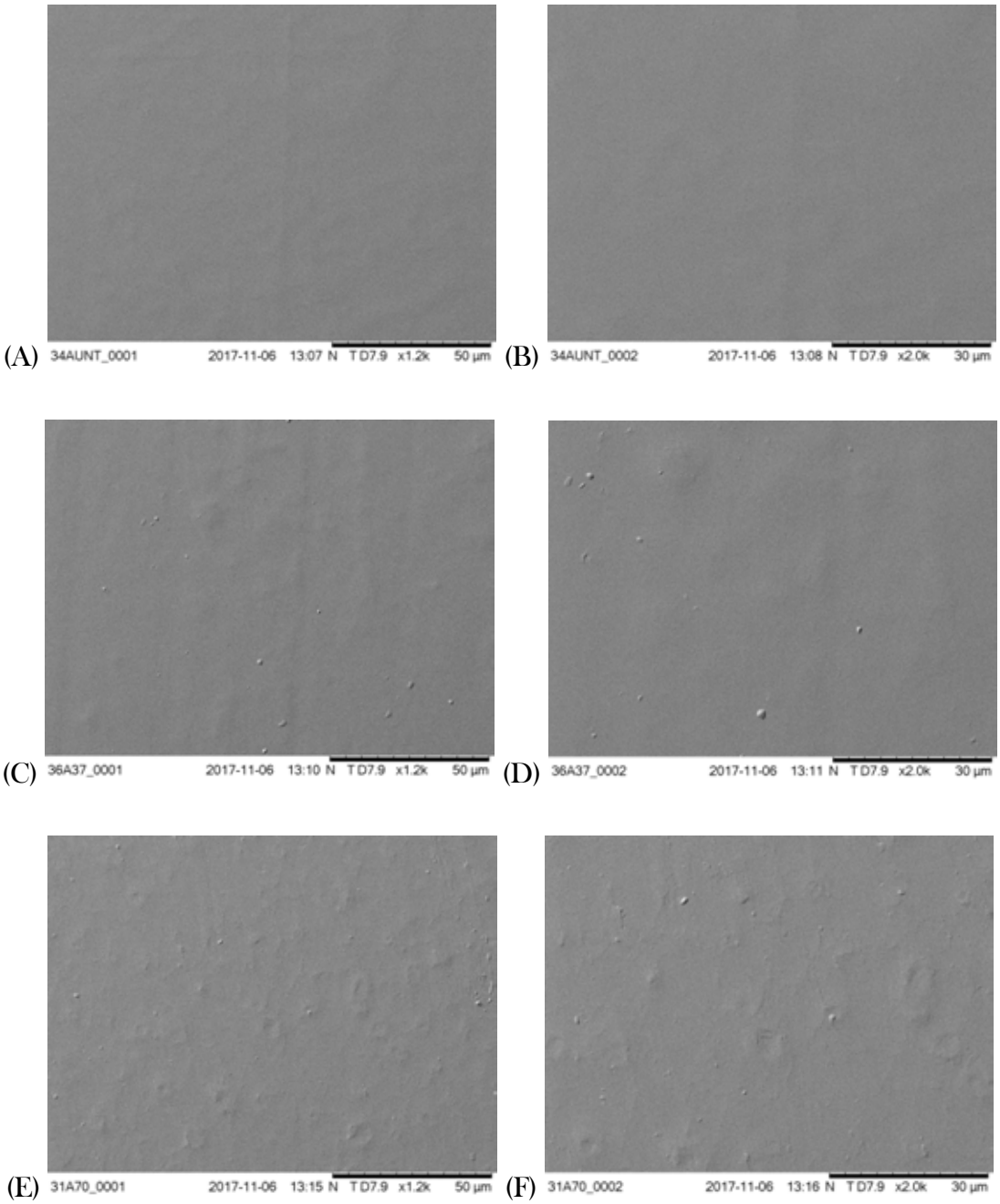

Figure 4-38: Scanning electron micrographs of Quadrathane ARC 80A at (A, C, E) x1.2k and (B, D, F) x2.0k. (A & B) Untreated, (C & D) treated with PBS at 37°C and (E & F) treated with PBS at 70°C.

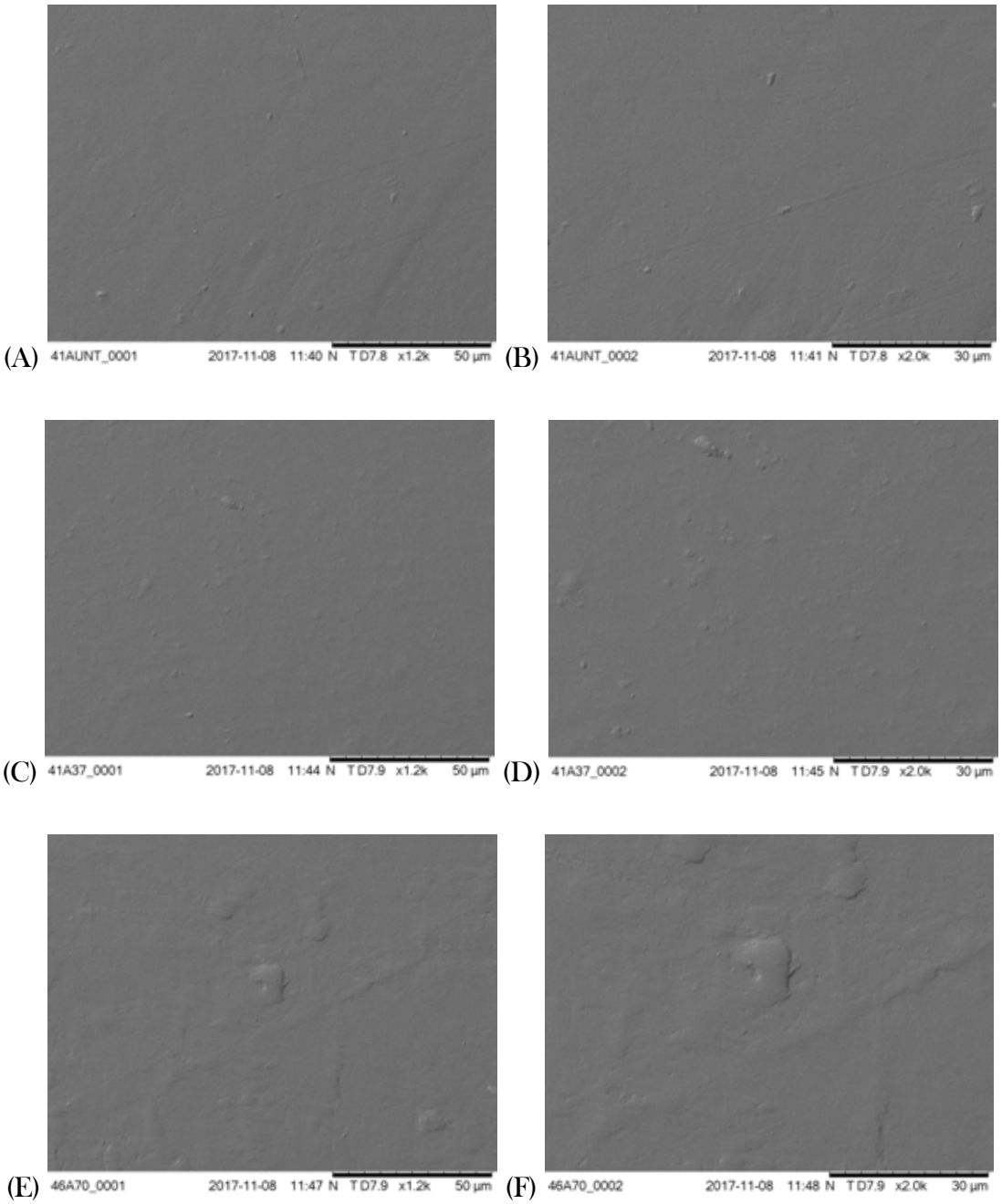

Figure 4-39: Scanning electron micrographs of Chronoflex C ARC 80A at (A, C, E) x1.2k and (B, D, F) x2.0k. (A & B) Untreated, (C & D) treated with PBS at 37°C and (E & F) treated with PBS at 70°C.

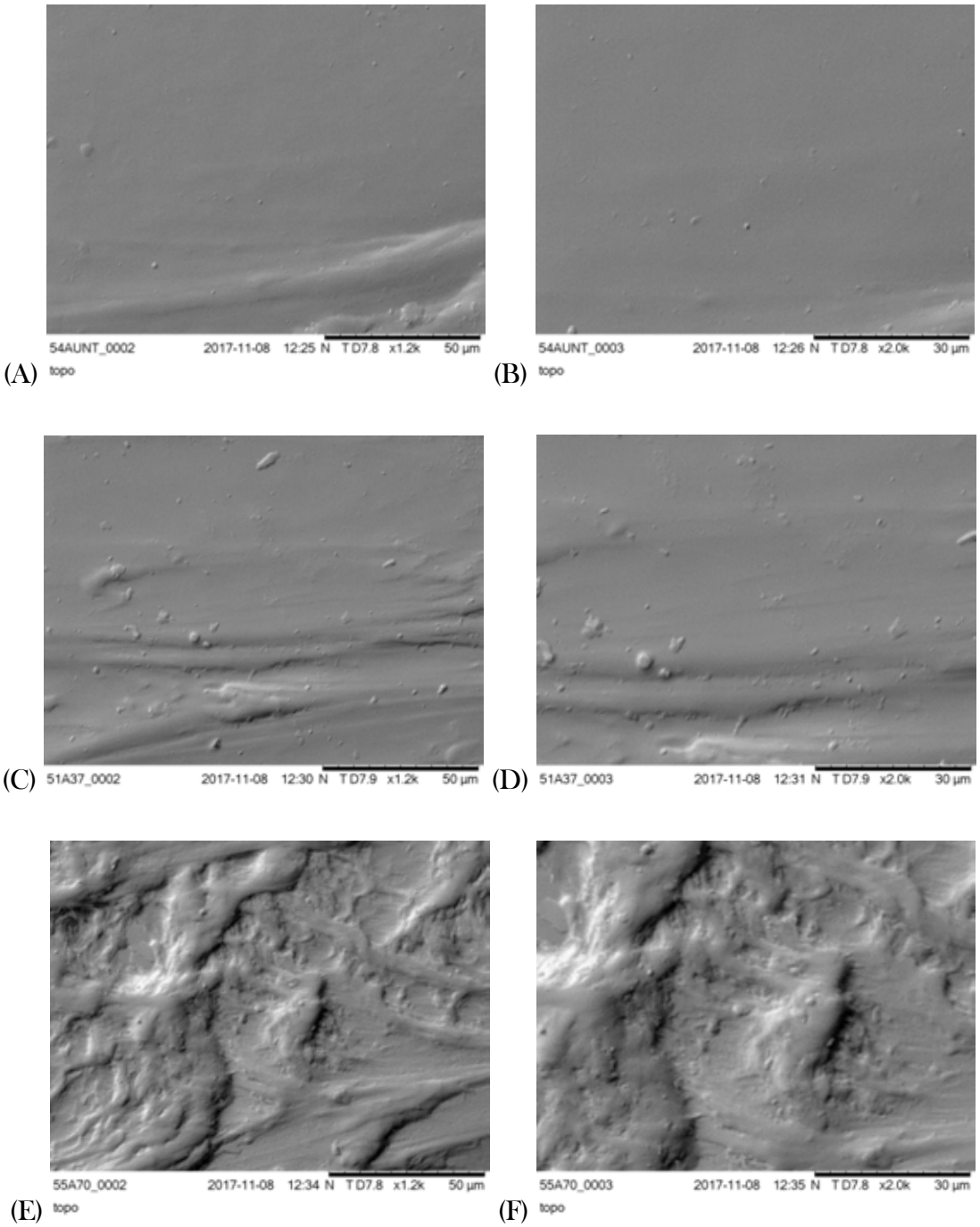

Figure 4-40: Scanning electron micrographs of Chronosil AL 80A 5% at (A, C, E) x1.2k and (B, D, F) x2.0k. (A & B) Untreated, (C & D) treated with PBS at 37°C and (E & F) treated with PBS at 70°C.

4.4 Discussion

Firstly, this chapter has quantified the frequency dependent viscoelastic behaviour of five long-term implantable biomaterials: Quadrathane ARC 80A-B20, Bionate II 80A, Quadrathane ARC 80A, ChronoFlex C 80A and ChronoSil 80A 5%. The five biomaterials were viscoelastic throughout the frequency range tested. The macro-viscoelastic responses, of the five untreated biomaterials, were logarithmic with respect to frequency ($p < 0.05$; see 8.6 Appendix F) for all biomaterial specimens tested. Between the five biomaterials, the multiple comparison test results show significant differences between specific untreated groups for the macro (Table 4-7) and the micro (Table 4-3) viscoelastic properties. There were no significant differences ($p > 0.05$), for the storage stiffness and the loss stiffness, between Quadrathane B20 – Quadrathane, Quadrathane B20 – Chronosil, and Bionate II – Chronoflex C, for all frequencies tested for the macro (Table 4-7) and the micro (Table 4-3) viscoelastic properties.

Secondly, this chapter investigated the effect of *in vitro* oxidative degradation and *in vitro* hydrolytic degradation on the viscoelastic response of these five biomaterials. Similarly to the five untreated biomaterials, the macro-viscoelastic properties of the degraded biomaterials, by oxidative and hydrolytic protocols, were logarithmic with respect to frequency ($p < 0.05$; see 8.6 Appendix F). The micro-viscoelastic properties of Chronosil were not significantly different when comparing the two oxidative degraded methods (3% H_2O_2 and $H_2O_2/CoCl_2$) to the untreated biomaterials. Comparing the untreated to the $H_2O_2/CoCl_2$ degradation methods, the storage stiffness and loss stiffness of Bionate II and Chronoflex C, for the micro and macro viscoelasticity, were not significantly different ($p > 0.05$) for any frequency tested. The *in vitro* $H_2O_2/CoCl_2$ degradation protocol has been used in numerous studies (Christenson et al., 2006b, 2004a; Hernandez et al., 2008) as it has been shown to have similar chemical structure and surface morphological changes when compared to *in vivo* degraded PCU biomaterials (Christenson et al., 2004a). The no significant differences of the untreated to the $H_2O_2/CoCl_2$ degradation Bionate II micro- and macro-viscoelastic properties at any frequency tested is an interesting finding. Therefore, future work is required to investigate the effect of *in vivo* degradation on the viscoelastic properties of these biomaterials and to investigate if the viscoelastic properties of the *in vivo* degraded biomaterials produces similar results to the *in vitro* $H_2O_2/CoCl_2$ degraded biomaterials.

The micro-viscoelastic properties of the untreated and the *in vitro* $H_2O_2/CoCl_2$ degradation method for Quadrathane B20 and Quadrathane biomaterials, the storage stiffness and loss

stiffness were not significantly different ($p > 0.05$) for all frequencies except for the viscous property (loss stiffness) at 1 Hz for Quadrathane B20. Comparing surface micro-level viscoelastic response of these specific biomaterials, these results suggest that the *in vitro* $H_2O_2/CoCl_2$ degradation method may not have an effect on the micro-level viscoelastic properties of Bionate II, Quadrathane, Chronoflex C and Chronosil; this finding is further discussed later in this discussion (section 4.4).

The micro-viscoelastic properties of the untreated and the *in vitro* 3% H_2O_2 degradation method for Quadrathane B20 were not significantly different ($p > 0.05$) at any frequencies tested. For Quadrathane, the loss stiffness at 0.1 Hz was the only viscoelastic property significantly different ($p < 0.05$) comparing the untreated and *in vitro* 3% H_2O_2 degraded groups. Unlike the comparison between the untreated to the $H_2O_2/CoCl_2$ degradation methods, the storage stiffness and loss stiffness of Bionate II and Chronoflex C, for the micro viscoelasticity between the untreated to the 3% H_2O_2 degradation, were significantly different ($p < 0.05$) at specific tested frequencies (Table 4-6). Bionate II 80A degraded with the *in vitro* 3% H_2O_2 degradation protocol has been shown to have a different chemical structure and surface morphological changes when compared to *in vivo* degraded PCU biomaterials (Dempsey et al., 2014). These reasons led to Dempsey et al. (2014) to recommend the $H_2O_2/CoCl_2$ degradation method when predicting segmented polyurethane (SPU) oxidative stability. However, a recent shape memory polyurethane study found that the 20% H_2O_2/0.1 *M* $CoCl_2$ method resulted in rapid oxidation and complete mass loss in less than 30 days (Weems et al., 2017). Thus, the use of the $H_2O_2/CoCl_2$ method may be too severe for certain scenarios.

The macro viscoelastic properties of the five biomaterials, quantified by DMA, of these specific biomaterials, were significantly different ($p < 0.05$) at specific frequencies when comparing the untreated and 3% H_2O_2 degradation method. When comparing the untreated specimens and the *in vitro* $H_2O_2/CoCl_2$ degraded specimens of Quadrathane B20 (0.3 Hz), Quadrathane (20 Hz) and Chronosil (0.01 to 0.5 Hz), the macro loss stiffness were significantly different ($p < 0.05$) at specific frequencies (stated in brackets and Table 4-10). Thus, the elastic property, which describes the ability of a structure to store energy, was not significantly different ($p > 0.05$) for any biomaterial, at any tested frequency, on the micro-scale or the macro-scale between the untreated and the *in vitro* $H_2O_2/CoCl_2$ degraded groups. It has been recommended to use the $H_2O_2/CoCl_2$ degradation method, when predicting segmented polyurethane (SPU) oxidative stability, due to the similarity between the chemical structure and surface morphological changes of the *in vitro* and *in vivo* degraded PCU biomaterials (Dempsey et al., 2014).

However, as the macro (by tensile DMA testing) and micro elastic property were not significantly different of all five biomaterials evaluated, it is concluded with caution that oxidation mechanisms, created by an *in vitro* mechanism that is comparative to the *in vivo* mechanism, may not affect the recoverable energy (also known as stored energy) of these five biomaterials. A caveat of this conclusion is that this does not apply to all forms of mechanical loading and potentially, all induced stress ranges.

Other studies have examined the effect of *in vitro* oxidative degradation in relation to tensile strain (Christenson et al., 2004b; Dempsey et al., 2014) and Dynamic Mechanical Thermal Analysis (DMTA) (Hernandez et al., 2008), but not viscoelastic properties calculated by μDMA or DMA techniques. Schubert et al. (1997) discovered a 10% decrease in stress at high strains of treated PEUU specimens when compared to the untreated PEUU specimens. This result was similar to those of Christenson et al. (2004a) who found a minor decrease in stress at high strains when comparing the tensile stress-strain behaviour of *in vitro* oxidised PEU and PCU to untreated PEU and PCU. Apart from this decrease in stress, the Young's modulus was unaffected (Christenson et al., 2004a). After 36 days of *in vitro* oxidation, Dempsey et al. (2014) stated that the ultimate tensile strength (UTS) of Bionate 80A, a PCU, was less when compared to the untreated specimens. However, the UTS of Bionate II 80A was greater for the specimens that were treated (Dempsey et al., 2014). The UTS of Bionate II 80A degraded with the 3% H_2O_2 degradation method was not significantly different from the untreated specimens (Dempsey et al., 2014). In contrast to Dempsey et al. (2014), for macro-viscoelasticity characterisation, Bionate II 80A storage and loss properties were not significant different, when comparing the untreated to the $H_2O_2/CoCl_2$ degradation specimen, at any frequency. Further, when comparing the untreated to the 3% H_2O_2 degradation specimens, the storage property of the degraded specimens was significantly greater ($p < 0.05$) at specific frequencies while the loss property was not significantly different. The differences between the Dempsey et al. (2014) study and this chapter may be due to the response of PCU biomaterials at low and high strains.

By using DMTA, Hernandez et al. (2008) discovered that the maximum loss factor (tan δ), of a PCU, reduced by approximately 0.05 while the storage modulus did not appreciably change after *in vitro* oxidation ($H_2O_2/CoCl_2$ solution). From this, the author suggested that there was no significant changes in the hard-soft segment organisation in the bulk (Hernandez et al., 2008). This present work discovered a similar result to Hernandez et al. (2008) with μDMA and DMA as the micro and macro storage property, of all five biomaterials, did not appreciably change after *in vitro* oxidation with the $H_2O_2/CoCl_2$ method (Table 4-17).

Similarly to the comparison between the untreated and oxidative degraded specimens, the micro-viscoelastic properties of Chronosil were not significantly different when comparing the two hydrolytic degraded methods (real-time and accelerated) and the untreated biomaterials (Table 4-17). Comparing the untreated to real-time degraded specimens, the micro viscoelasticity of Bionate II was significantly different ($p < 0.05$) for every frequency tested. The micro-level viscoelastic properties of Quadrathane B20 and Chronoflex C were significantly different ($p < 0.05$) at specific frequency tested between the untreated to real-time degraded specimens. The micro-viscoelastic properties of the untreated and the real-time degradation method for Quadrathane were not significantly different ($p > 0.05$) for all frequencies. Comparing the untreated to accelerated degraded specimens, the micro-level loss property was significantly different ($p < 0.05$), for specific frequencies, for Quadrathane B20, Bionate II and Quadrathane; the storage property was not significantly different ($p > 0.05$) for all frequencies. This was different for the micro-scale viscoelastic properties of Chronoflex C as the storage and loss stiffness was significantly different, between the untreated and accelerated degraded specimens, at specific frequencies.

Table 4-17: Summary table highlights the significant differences between the untreated and degraded groups [3% H_2O_2 (3%); $H_2O_2/CoCl_2$; Real-time (Real) and Accelerated (Accel)] of the micro (μDMA) and macro (DMA) viscoelastic response, of the five biomaterials. The significant differences between the untreated and degraded specimens were at specific tested frequencies (S.F), all tested frequencies (A.F) or not significantly different (-)

μDMA	Storage Stiffness				Loss Stiffness			
Biomaterial	3%	$H_2O_2/CoCl_2$	Real	Accel	3%	$H_2O_2/CoCl_2$	Real	Accel
Quad B20	-	-	A.F	-	-	S.F	S.F	A.F
Bionate II	S.F	-	A.F	-	S.F	-	A.F	S.F
Quadrathane	-	-	-	-	S.F	-	-	S.F
Chronoflex C	S.F	-	-	A.F	S.F	-	S.F	S.F
Chronosil	-	-	-	-	-	-	-	-
DMA	Storage Stiffness				Loss Stiffness			
Biomaterial	3%	$H_2O_2/CoCl_2$	Real	Accel	3%	$H_2O_2/CoCl_2$	Real	Accel
Quad B20	S.F	-	-	-	S.F	S.F	S.F	-
Bionate II	S.F	-	-	-	-	-	-	-
Quadrathane	S.F	-	-	-	S.F	S.F	-	S.F
Chronoflex C	S.F	-	-	-	-	-	-	-
Chronosil	S.F	-	-	S.F	-	S.F	-	A.F

Comparing the untreated specimens against the real-time and accelerated degradation methods, the macro-storage stiffness of Quadrathane B20, Bionate II, Quadrathane and Chronoflex C was not significantly different ($p > 0.05$) for all frequencies. Further, the loss stiffness of Bionate II, and Chronoflex C were not significantly different when comparing the untreated specimens against the real-time and accelerated degradation methods; these macro-viscoelastic results highlight the hydrolytic stability of Bionate II 80A and Chronoflex C 80A. The loss stiffness of the untreated and real-time hydrolytic degraded Quadrathane specimens were not significantly different ($p > 0.05$) for all tested frequencies while the loss stiffness of the untreated and accelerated degraded Quadrathane specimens were significantly different ($p < 0.05$) at specific frequencies. The opposite result was found for Quadrathane with the radiopacifier additive; the loss stiffness of the untreated and real-time hydrolytic degraded Quadrathane B20 specimens were significantly different ($p < 0.05$) for all tested frequencies while the loss stiffness of the untreated and accelerated degraded Quadrathane B20 specimens were not significantly different ($p > 0.05$) at specific frequencies. The viscoelastic properties of Chronosil untreated and real-time specimens were not significantly different for all tested frequencies; this shows that the real-time hydrolytic degradation protocol did not have an effect on the elastic property, of these five biomaterials, for the frequencies and method tested. The storage stiffness of the Chronosil untreated and accelerated degraded specimens were significantly different ($p < 0.05$) at specific frequencies while the loss stiffness was significantly different for all frequencies tested.

Similar to previous *in vitro* oxidation studies, studies have examined the effect of *in vitro* hydrolytic degradation in relation to tensile strain (Khan et al., 2005a; Serkis et al., 2015) of PCUs, but not viscoelastic properties calculated by μDMA or DMA techniques. Other studies have evaluated the effect of hydrolytic degradation of PEU (Chaffin et al., 2014, 2012; Mishra et al., 2015; Padsalgikar et al., 2015), PEU with silicone (Chaffin et al., 2014, 2013, 2012) and PDMS based polyurethane (Chaffin et al., 2014, 2013, 2012; Mishra et al., 2015; Padsalgikar et al., 2015); these materials were evaluated by quasi-static tensile tests (Chaffin et al., 2012; Mishra et al., 2015) and DMTA (Chaffin et al., 2012; Padsalgikar et al., 2015). The effect of hydrolytic degradation on the UTS (Khan et al., 2005a; Mishra et al., 2015), failure strain (Khan et al., 2005a) and secant modulus (Khan et al., 2005a) of PCU biomaterials were previously investigated. Corethane 80A, now known as Bionate 80A (Dumbleton et al., 2009), showed the smallest drop, approximately 20%, in the UTS with the dry control specimens showing no significant changes in mechanical properties (Khan et al., 2005a). The failure strain of the biomaterial increased within the first 3-4 months of incubation (Khan et al., 2005a). However,

after 3-4 months, the failure strain decreased with incubation time (Khan et al., 2005a). At 100% strain, the secant modulus of Corethane 80A exhibited the smallest overall change of approximately 8% decrease while Chronoflex 80A showed the greatest increase, at the same strain, of approximately 15% (Khan et al., 2005a). With regards to hydrolytic stability, this present work discovered that the macro-viscoelastic storage stiffness and loss stiffness of Bionate II and Chronoflex C were not significantly different ($p > 0.05$) for all frequencies tested; this is for the comparison of the untreated specimens to the real-time and accelerated degraded specimens. As Khan et al. (2005a) stated that Corethane 80A showed the best overall stability while Chronoflex 80A showed some evidence of very minor hydrolysis, the author agrees with the hydrolytic stability assessment of Khan et al. (2005a) due to the lack of significant differences of the macro-viscoelastic response. However, the present study revealed that the micro-viscoelastic properties of Bionate II and Chronoflex C were significantly different ($p < 0.05$) at specific frequencies tested. Thus, these results call into doubt the hydrolytic stability of these biomaterials and demonstrate the need to analyse material mechanical property changes on multiple scales.

Mishra et al. (2015) investigated the *in vitro* hydrolytic stability of Bionate 55D, Chronoflex 80A and Quadrathane 80A. The authors found that the UTS, of all biomaterials evaluated in the study, decreases with increasing time (degradation time) and temperature with the highest rate of decrease observed at 80 °C (Mishra et al., 2015). The relative decrease in UTS, at 80 °C for 52 weeks, was the highest for Chronoflex C, approximately 55-60%, while Quadrathane 80A was the lowest relative decrease of approximately 30%; other biomaterials, such as Bionate 55D, had a relative decrease of approximately 40% (Mishra et al., 2015). In the present work, only the macro-loss stiffness of the untreated Quadrathane specimens compared to the accelerated degraded specimens were significantly different at specific frequencies while, when comparing the untreated specimens to the accelerated degraded specimens, the macro-viscoelastic properties of Bionate II and Chronoflex C were not significantly different ($p > 0.05$) for all frequencies tested. The differences between Mishra et al. (2015) studies to this present work may be due to the differences in response of the degraded PCU biomaterials at low and high elongation strains.

In this present work, the macro-viscoelastic properties of all biomaterial specimens, both untreated and degraded, exhibited frequency-dependent dynamic viscoelastic properties ($p < 0.001$). Thus, it is suggested that when evaluating these biomaterials, the frequency dependent nature of these biomaterials is considered when designing experiments. A recent study

investigated the mechanisms of fatigue crack growth, of PCUs (Bionate 80A and Bionate 75D), with respect to time dependent effects and conditioning (Ford et al., 2018). Ford et al. (2018) discovered that specimens tested at 2, 5 and 10 Hz had a similar number of cycles to failure. However, the crack length at failure for 10 Hz was longer ($p < 0.002$) when compared to crack length of specimens tested at 2 and 5 Hz (Ford et al., 2018); this finding highlights the importance of evaluating the effect of frequency on these biomaterials. Interestingly, Ford et al. (2018) discovered that strain rate (10, 75 and 150 mm/min) did not have a statistically significant impact on the quasi-static tensile mechanical properties (Young's modulus, ultimate strength and ultimate strain) of Bionate 80 A. However, at a high strain rate (500 mm/min) used in the dry time study, the elastic moduli were approximately twice as high than the slower displacement rates (10, 75, and 150 mm/min) (Ford et al., 2018). This further highlights the need to consider the frequency dependent nature of these biomaterials when designing experiments.

With classical indenters, the force due to the water meniscus on the shaft of the indenter makes the analysis of indentation data more complicated (Chavan et al., 2012; Mattei et al., 2015). In order to perform AFM indentation in a liquid, the specimen needs to be mounted inside a specially designed fluid chamber which can limit the size of the specimen and increase the complexity of the equipment (Chavan et al., 2012). Further, the ferrule-top cantilever position is monitored by optical fibre interferometry rather than optical triangulation techniques used in AFM (Antonovaite et al., 2018). Thus, ferrule-top cantilevers offer advantages when testing specimens submerged in a liquid medium (Chavan et al., 2012; Mattei et al., 2015). Ferrule-top cantilever indenters have been used to develop high resolution images in air, vacuum, low temperatures and liquids (Chavan et al., 2012, 2011, 2010). Recently, ferrule-top indenters have been used to characterise the viscoelastic response of PDMS (Mattei et al., 2015) and hydrogels (Mattei et al., 2017, 2015) by the Nano-epsilon dot method, to measure the storage and loss properties of PDMS over a frequency range between 0.01-10 Hz (van Hoorn et al., 2016) and to gather viscoelastic maps, depth dependent and frequency dependent viscoelastic properties of mouse brain tissue (Antonovaite et al., 2018). Further, the ferrule-top technology has been designed and used to perform the integrated epidetection of Optical Coherence Tomography (OCT) depth-profiles and micron-scale indentation (Bartolini et al., 2017) and it has been inserted into an 18G needle to characterise the viscoelastic properties of soft tissues *in situ* (Beekmans et al., 2017). The μDMA work performed in this chapter, by a ferrule-top cantilever probe, adds to the recent work investigated with this technology and gives an understanding of

the effect of *in vitro* degradation on the micrometre-scale viscoelastic properties of PCU biomaterials.

This chapter quantified the chemical structure changes due to *in vitro* degradation by using hyperspectral chemical imaging. Aromatic PCU biomaterials (Quadrathane ARC 80A-B20, Bionate II 80A, Quadrathane 80A and ChronoFlex C 80A) demonstrated evidence of PCU oxidative degradation as new absorbance peaks were observed at 930 cm^{-1} and 1174 cm^{-1}; these new absorbance peaks have been associated with oxidative degradation (Cipriani et al., 2013; Faré et al., 1999). These new peaks were observed for all *in vitro* $H_2O_2/CoCl_2$ degraded Quadrathane ARC 80A-B20 (with radiopacifier), Bionate II 80A and Quadrathane ARC 80A specimens; however, 5 out of 6 *in vitro* $H_2O_2/CoCl_2$ degraded ChronoFlex C 80A specimens had new peaks at 930 cm^{-1} and 1174 cm^{-1}. The one ChronoFlex C 80A HCI that did not demonstrate the new peaks at 930 cm^{-1} and 1174 cm^{-1} was a 6 × 6 acquisition HCI. A larger acquisition of ChronoFlex C 80A (30 × 10 acquisition), shown in Figure 4-9 (L) and Figure 4-10 (L), highly the regional variation of the new peaks at 930 cm^{-1} and 1174 cm^{-1}, respectively. With this wide variation, the result of the randomly selected 6 × 6 acquisition area of the ChronoFlex C 80A *in vitro* $H_2O_2/CoCl_2$ degraded specimen, that did not have evidence of new peaks at 930 cm^{-1} and 1174 cm^{-1}, may be influenced by the small acquisition area (6 × 6). This further highlights the need of imaging a wide sample area to get a more in-depth understanding of the regional biomaterial degradation.

The regional variation of degradation on some *in vitro* $H_2O_2/CoCl_2$ degraded specimens was highly contrasting; see Figure 4-41 (A). New absorbance peaks at 930 cm^{-1} and 1174 cm^{-1} were witnessed to vary spatially across the biomaterial highlighting the heterogeneity of the biomaterial degradation. To highlight the contrasting heterogeneity nature of the degradation, one specific acquisition of the degraded ChronoFlex C specimen showed evidence of degradation with new absorbance peaks at 930 cm^{-1} and 1174 cm^{-1} present in the spectra while 50 μm away, there was no evidence of degradation with no absorbance peaks at 930 cm^{-1} and 1174 cm^{-1} present in the spectra. This contrasting spatial variation is shown in Figure 4-41; see Figure 4-41 (A) for the isolated, higher intensity (bright yellow) pixel in the HCI (pixel position 26(x) and 4(y); highlighted with a red box) and (B) for the chemical ATR-FTIR spectra of this specific pixel and a more common spectrum from the untreated specimen (pixel position; 24(x) and 4(y); highlighted with a black box). This further emphasises the need of imaging a wide sample area to understand spatial variation of biomaterial degradation.

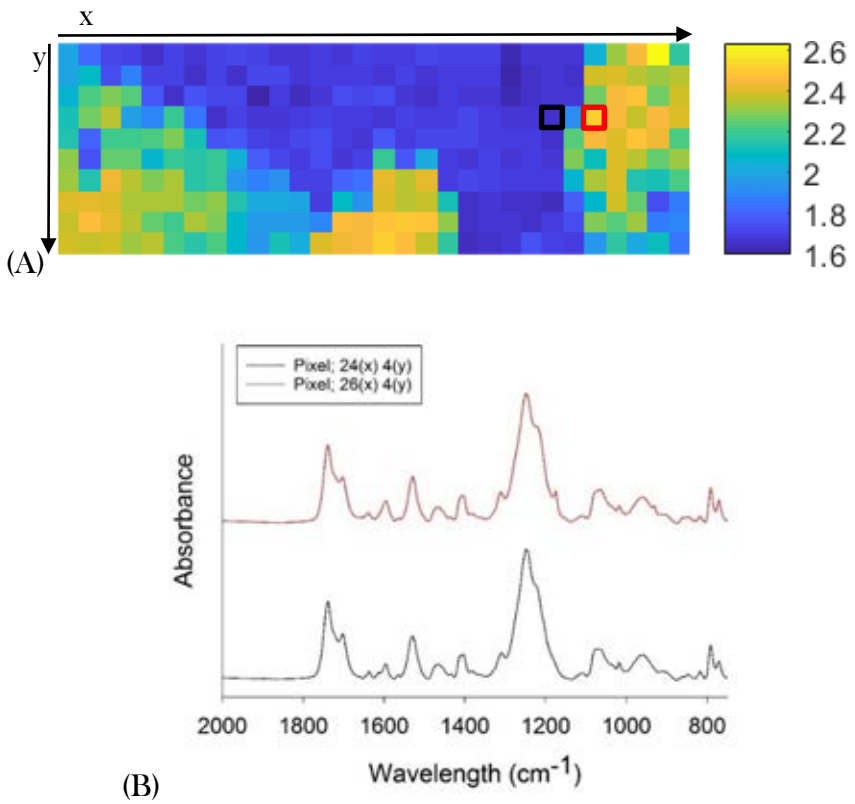

Figure 4-41: (A) $H_2O_2/CoCl_2$ degraded ChronoFlex HCI at 1174 cm^{-1}. On the HCI (A), at one specific point, a new 1174 cm^{-1} peak has been identified. (B) The chemical structure at this specific point (yellow pixel with a red box; pixel position 26(x) and 4(y)) is the different to another specific point (pixel with a black box around it; pixel position 24(x) and 4(y)) that did no show evidence of degradation (no absorbance peaks at 930 cm^{-1} and 1174 cm^{-1} present).

Christenson et al. (2004a) demonstrated that *in vitro* degradation of PEU and PCU, with the $H_2O_2/CoCl_2$, at 37 °C for 24 days, led to ATR-FTIR spectra changes. Such changes were similar to explanted PCU rods from rabbits after 15 months and PCU specimens from rats after 20 weeks (Christenson et al., 2004b) and after 1 year (Christenson et al., 2006a). From the ATR-FTIR spectrum and HCI, the new absorbance peak at 930 cm^{-1} provides evidence of O-H bending or bending of aliphatic CO_2H while the 1174 cm^{-1} provides evidence of chain scission and crosslinking of the soft segment (Christenson et al., 2004a; Hernandez et al., 2008; Tanzi et al., 2000; B. Ward et al., 2006; R. Ward et al., 2006); these new peaks are associated with oxidative degradation of PCU biomaterials (Christenson et al., 2004a; Cipriani et al., 2013; Faré et al., 1999). A new absorbance peak at 1650 cm^{-1} (the potential degradation product of the aromatic amine (Christenson et al., 2004b)) provides evidence of hard segment chain scission (Christenson et al., 2007, 2006a, 2004a). This hard segment degradation has been shown to be inhibited by using an antioxidant inhibitor (Christenson et al., 2006a).

In this present work, the spectrum changes of Bionate II 80A (new peaks observed at 1174 cm^{-1} and 1650 cm^{-1}) are similar to previous work that examined Bionate 80A (Christenson et al., 2006a, 2005, 2004a) and Bionate II 80A (Dempsey et al., 2014); Bionate 80A is the predecessor to Bionate II 80A. The *in vitro* $H_2O_2/CoCl_2$ degraded Bionate II 80A ATR-FTIR spectrum absorbance peaks at 1174 cm^{-1} and 1650 cm^{-1} are also similar to Dempsey et al. (2014). Dempsey et al. (2014) degraded DSM Biomedical (DSM Biomedical, Berkeley, CA, USA) commercially available biomaterial specimens; Bionate 80A [PCU], Bionate 75D [PCU], Bionate II 80A [PCU], Bionate II 75D [PCU], CarboSil 20 80A (a thermoplastic silicone polycarbonate urethane [TSPCU]) and CarboSil 20 55D [TSPCU]. These biomaterials were degraded by two degradation methods; the *in vitro* $H_2O_2/CoCl_2$ oxidation method for 36 days (instead of 24 days used in this thesis) and the *in vitro* 3 % H_2O_2 oxidation method for 1 year (Dempsey et al., 2014). Similar to this present work, Dempsey et al. (2014) discovered that Bionate II 80A degraded by the *in vitro* $H_2O_2/CoCl_2$ oxidation method for 36 days exhibited evidence of surface crosslinking with the new peak appearing at 1174 cm^{-1} and exhibited evidence of hard segment degradation with the new peak at 1650 cm^{-1}.

For Bionate II 80A degraded by the *in vitro* 3% H_2O_2 degradation method, Dempsey et al. (2014) discovered that no peaks at 1174 cm^{-1} or 1650 cm^{-1} were detected. In this present work, no new peak at 1174 cm^{-1} was detected for specimens degraded by the *in vitro* 3% H_2O_2 degradation method, however, new isolated peaks at 1650 cm^{-1} were detected in the HCI; this new peak at 1650 cm^{-1} on the surface of Bionate II 80A is a contradiction to Dempsey et al. (2014). Isolated acquisitions on 2 out of the 6 3% H_2O_2 oxidative degraded specimens, 2 out of 6 real-time hydrolytic degraded specimens, 2 out of 6 accelerated hydrolytic degraded specimens demonstrated a new peak at 1650 cm^{-1} on the surface of Bionate II 80A. Similar conclusions may have been drawn in line with Dempsey et al. (2014) had point spectroscopy methods been utilised instead of HCI as these isolated peaks may have gone unnoticed (Dorrepaal et al., 2018). In addition to the new peak at 1650 cm^{-1} on the surface of the *in vitro* degraded Bionate II 80A, isolated acquisitions with a new peak at 1650 cm^{-1} was discovered on the surface of the untreated (control) Bionate II 80A specimens. These isolated hard segment degraded regions were unexpected and may have been caused by inconsistencies in the biomaterial mixing, formulation, manufacturing and/or sterilisation of the PCU biomaterials (Dorrepaal et al., 2018).

In the present study, the lack of a new peak at 1174 cm^{-1} for specimens degraded by the *in vitro* 3% H_2O_2 degradation method leads to agreement with Dempsey et al. (2014) that the accelerated *in vitro* $H_2O_2/CoCl_2$ oxidation method should be the recommended choice for predicting oxidative stability of segmented polyurethanes. Dempsey et al. (2014) stated that the segmented polyurethanes tested were highly resistant to hydrolytic degradation as the *in vitro* 3% H_2O_2 degradation method is 97% water and that no peaks at 1174 cm^{-1} or 1650 cm^{-1} were detected in their study. With regards to hydrolytic stability, no new absorbance peaks were observed at 930 cm^{-1} and 1174 cm^{-1} for the untreated, the real time degraded and the accelerated degraded specimens. For Quadrathane 80A-B20 and Quadrathane 80A, HCIs at 1248 cm^{-1} (peak associated with O-C-O carbonate bonds) showed a lack of regionally variation and similar to 930 cm^{-1} and 1174 cm^{-1}, this can be seen with the lack of change of the range of absorbance intensity range (arbitrary unit [AU]) between the untreated, real time and accelerated hydrolytically degraded specimens (Figure 4-30). Comparing the absorbance peak intensity range of the Bionate II untreated (Figure 4-30 (D)) and accelerated hydrolytic degraded (Figure 4-30 (F)) specimens, the approximate range differed between the untreated (5.8-8 AU) and accelerated (3.8-6.8 AU) specimens. Similarly to Bionate II, ChronoFlex C untreated (Figure 4-30 (J)) and accelerated hydrolytic degraded (Figure 4-30 (L)) specimens approximate absorbance range changed from 8.2-10.1 AU to 6.8-8.1 AU. These findings between the biomaterials are different to Khan et al. (2005a) who stated that Corethane 80A, now known as Bionate 80A (Dumbleton et al., 2009), showed the best overall stability while Chronoflex 80A showed some evidence of very minor hydrolysis by the decrease in soft and hard segments.

Compared to the aromatic PCU biomaterials, Chronosil, an aliphatic PCU biomaterial synthesed with silicone, demonstrated no typical evidence of PCU degradation as no new absorbance peaks were observed at 930 cm^{-1} and 1174 cm^{-1} for specimens degraded by the four degradation methods. Further, there was no new peak at 1650 cm^{-1} and changes of the peak at approximately 1248 cm^{-1} were minimal. Minimal-to-no changes of other absorbance peaks were observed when comparing other peaks of the specimens degraded by the four degradation methods to the untreated Chronosil specimens. Similar to Quadrathane 80A-B20 and Quadrathane 80A, minimal published work on Chronosil is available in the literature with only two scientific publications existing (Francolini and Piozzi, 2016; Vogels et al., 2017); neither of these studies investigated the chemical structure of Chronosil.

Normalisation with the internal reference peak has been previously used in numerous studies (Christenson et al., 2006a, 2006b, 2005; Dempsey et al., 2014; Khan et al., 2005b). With this normalisation technique, peaks are normalised to the C=C bond stretching of an aromatic ring of the hard segment; this peak is approximately 1591-1600 cm^{-1} (Christenson et al., 2006a, 2006b, 2005, 2004a, 2004b; Dempsey et al., 2014; Khan et al., 2005b; Padsalgikar et al., 2015). This aromatic group and more specifically the 1591-1600 cm^{-1} peak, has been reported to remain unchanged with biodegradation (Wu et al., 1992). With this aromatic peak at approximately 1591-1600 cm^{-1}, it has been recently stated that the use of this peak in this normalisation technique is not suitable as a neighbouring peak overlaps the C=C stretch peak and the consistency of its intensity between spectra cannot be assumed (Dorrepaal et al., 2018). To add to the unsuitability of this aromatic peak at approximately 1591-1600 cm^{-1}, it can be seen in literature that this overlapping neighbouring peak is not present when specimens are degraded with the *in vitro* $H_2O_2/CoCl_2$ degraded method. Thus, the four aromatic PCU biomaterials (Quadrathane B20, Bionate II, Quadrathane and ChronoFlex C) the spectra were normalised to a stable aromatic C-H out of plane bending peak at 819 cm^{-1} in this present work (Cipriani et al., 2013; Dorrepaal et al., 2018). As Chronosil is an aliphatic PCU with silicone biomaterial, and not aromatic, no normalisation of the 819 cm^{-1} was performed for this biomaterial. To understand the changes of the wavelengths of Chronosil and the other four aromatic PCU biomaterials, a secondary normalisation method, the Savitzky Golay technique, was also performed.

Savitzky Golay is a method to pre-treat data (Savitzky and Golay, 1964). The method can be used to calculate the derivative at a particular wavelength by using a window of n data points and fitting a polynomial using the least squares method (Owen, 1995); in the present thesis a window size of 31 points (centre point ± 15 wave measurements) was used and the fit was a second order polynomial and a second order derivative. The *in vitro* $H_2O_2/CoCl_2$ degraded SG second derivative spectra of the aromatic PCU biomaterials (8.7 Appendix G - Figure 8-14 (A) to (D)) displayed an increase in gradient at 930 cm^{-1} and at 1174 cm^{-1}. The *in vitro* $H_2O_2/CoCl_2$ degraded SG second derivative spectra of Quadrathane with radiopacifier and Quadrathane displayed a decrease in gradient at 1635-1640 cm^{-1}; these findings correlate to the shrinking of the Quadrathane 80A-B20 and Quadrathane 80A $H_2O_2/CoCl_2$ degraded specimens peak around 1635-1640 cm^{-1} (Figure 4-8). By comparing the minimal changes in gradient of the *in vitro* degraded SG second derivative spectra (3% H_2O_2 [red] and

$H_2O_2/CoCl_2$ [green]) to the untreated (black), ChronoSil appeared to be the most stable to oxidation (8.7 Appendix G - Figure 8-14).

Savitzky Golay was also performed on the *in vitro* hydrolytic degraded biomaterials (8.7 Appendix G - Figure 8-15). The *in vitro* accelerated hydrolytic degraded ChronoFlex C SG second derivative spectra peaks (Green) decreased in gradient for a number of wavelength positions (when compared to the untreated (black) or real-time degraded (red) SG second derivative spectra peaks); this is particularly apparent at 1247 cm^{-1} which is indicative of the O-C-O carbonate bonds (8.7 Appendix G - Figure 8-15 (D)). The *in vitro* accelerated hydrolytic degraded Bionate II SG second derivative spectra (Green) peak gradient varied considerably (8.7 Appendix G - Figure 8-15 (B)); this variation of gradient was also witnessed for the *in vitro* accelerated hydrolytic degraded Chronosil SG second derivative spectra (Figure 8-15 (E)). Variation of peak gradient was witness for the real-time degraded SG second derivative spectra of Quadrathane with radiopacifier (Figure 8-15 (A)) and Quadrathane (Figure 8-15 (C)).

This chapter also investigated surface morphological changes due to *in vitro* degradation. SEM images of the five biomaterials degraded with the *in vitro* $H_2O_2/CoCl_2$ degradation method revealed various levels of pitting on the surface. The maximum dimension of the pits on the surface of the biomaterials varied; Quadrathane B20 0.44 to 3.98 μm, Bionate II 0.44 to 5.88 μm, Quadrathane 0.48 to 3.99 μm, Chronoflex C 0.44 to 8.13 μm and Chronosil 0.35 to 2.26 μm. Pitting on the surface of the PCU biomaterials has been previously documented for *in vitro* and *in vivo* oxidative degradation (Christenson et al., 2006a, 2004b; Dempsey et al., 2014). Christenson et al. (2004a) demonstrated that *in vitro* degradation of PEU and PCU, with the H_2O_2 / 0.1 *M* $CoCl_2$ solution at 37 °C for 24 days, led to surface pitting. PEU specimens had a large distribution of pit sizes ranging from 1 to 30 μm in diameter while PCU specimens pit sizes ranged from 1 to 10 μm (Christenson et al., 2004a); the pit size range of the present study is similar to Christenson et al. (2004a). Out of the five biomaterials investigated, Chronosil had the smallest pit sizes. This is not surprising as Chronosil is a PCU based silicone (PCU-S) elastomer. From an oxidation biostability perspective, PCU-S biomaterials have been ranked as the most superior when compared to PCU, PEU and PEU based silicone biomaterials; PEU < PEU-S ≤ PCU < PCU-S (Christenson et al., 2007, 2005).

One pit was identified, by examining SEM images, on the surface of the 3% H_2O_2 degraded Quadrathane specimen while SEM images of Quadrathane B20, Bionate II and Chronoflex C biomaterials degraded with the *in vitro* 3% H_2O_2 degradation method revealed no evidence of

surface pitting when compared to the untreated specimens. This result was not a surprise as Dempsey et al. (2014) previously discovered that no significant evidence of erosion was found on the surface of PCU biomaterials after 12 months degradation with the *in vitro* 3% H_2O_2 method. The lack of surface morphological differences with the 3% H_2O_2 method does not correlate with the surface pitting observed after 12 months *in vivo* exposure (Dempsey et al., 2014). Dempsey et al. (2014) stated that as the 3% H_2O_2 method is immersed in 97% water medium, these PCU biomaterials are highly resistant to hydrolytic degradation. Comparing the untreated specimens to the *in vitro* real-time hydrolytic degraded specimens, there was no apparent visual surface morphological differences for Quadrathane B20 and Bionate II. Small localised blistered areas on the surface of the Real-time and Accelerated degraded Quadrathane specimens was observed when compared to the untreated Quadrathane specimens. While, a larger blistered area on the surface of the Chronoflex C accelerated hydrolytic degraded specimen was observed when compared to the untreated and real-time degraded specimens. Surface morphological changes of the accelerated hydrolytic degraded Bionate II specimens were witnessed when compared to the untreated specimen. With only small localised blistered areas on Quadrathane for the real-time degraded specimens, the author agrees with Dempsey et al. (2014) that the little-to-no surface morphological changes of the real-time degraded specimens, and the little-to-no surface pitting witnessed in the highly aqueous 3% H_2O_2 method, suggests that these PCU biomaterials are highly resistant to surface morphological changes due to hydrolytic degradation. This finding further affirms the statement of Dempsey et al. (2014) on the hydrolytic stability of PCU. As discussed earlier in this discussion, the hydrolytic stability statement of PCU biomaterials is further supported by the findings that the macro-viscoelastic properties of Bionate II and Chronoflex C were not significantly different for all frequencies tested while, the loss property of Quadrathane B20 and Quadrathane were only significantly different at specific frequencies. However, as previously discussed above, the micro-level viscoelastic properties, calculated by μDMA, were significantly different, at specific frequencies, between the surfaces of the untreated and real-time hydrolytic degraded specimens for Quadrathane B20, Bionate II and Chronoflex C; these findings question the hydrolytic stability of these biomaterials.

Chronosil is different to the other four PCU biomaterials in two different ways: (1) ChronoSil is an aliphatic biomaterial (not aromatic like the other biomaterials) and (2) ChronoSil has a 5% silicone additive. The difference between aliphatic and aromatic lies in the organisation of the hydrocarbons; aromatic compounds have hydrocarbons in one or more ring shape while

functional groups are aliphatic if there is no aromatic ring directly attached (Speight, 2017). The organisation of the functional group affects the chemical and physical properties of molecules (Speight, 2017). Secondly, the use of silicone as an additive to PCU has been shown to improve the biostability of the biomaterial; PEU < PEU-S ≤ PCU < PCU-S (Christenson et al., 2007, 2005). Interestingly, when comparing the untreated specimens to the specimens degraded by the *in vitro* oxidative and *in vitro* hydrolytic methods, the micro-viscoelastic properties of Chronosil were not significantly different for all frequencies ($p > 0.05$); this result highlights the *in vitro* oxidation and hydrolytic stability of Chronosil. Factors such as specimen surface roughness and surface contaminations have been stated as potential influences on the calculated specimen moduli (Chavan et al., 2012). All five biomaterials degraded with the $H_2O_2/CoCl_2$ oxidation method displayed pitting on the surface of the biomaterials. The pit size range differed depending on the biomaterial and Chronosil had the smallest range of pit sizes; this result, alongside the minimal changes in gradient of the *in vitro* oxidative degraded SG second derivative spectra of Chronosil, highlights the oxidative stability of Chronosil over the other PCU biomaterials evaluated. However, in the comparison of the untreated specimens to the $H_2O_2/CoCl_2$ specimens, the micro-scale viscoelastic properties were found to be not significantly different ($p > 0.05$) for all frequencies except for the viscous property (loss stiffness) at 1 Hz for Quadrathane B20. This highlights that the increase in surface roughness, due to pitting of the surface from oxidation, may not have a major influence on the micro-viscoelasticity of these biomaterials (apart from Quadrathane B20).

Earlier in this discussion, a comparison of the micro viscoelastic properties between the untreated to the $H_2O_2/CoCl_2$ degraded biomaterials, for the five separate biomaterials, was discussed. From the analysis of the multiple comparison test (Table 4-6), the storage stiffness and loss stiffness were not significantly different ($p > 0.05$) for all frequencies except for the viscous property (loss stiffness) at 1 Hz for Quadrathane B20. It was suggested that the *in vitro* $H_2O_2/CoCl_2$ degradation method may not have an effect on the micro-level viscoelastic properties of four of the biomaterials evaluated (Bionate II, Quadrathane, Chronoflex C and Chronosil) Further, the viscous property of Quadrathane B20 at 1 Hz was the only significant difference ($p < 0.05$) recorded and the *in vitro* $H_2O_2/CoCl_2$ degradation method did not have an effect on the micro-level elastic response of Quadrathane B20 at any tested frequency. These suggestions should be interpreted with caution.

Firstly, it is currently unknown what effect implantation and *in vivo* degradation has on the micro-level viscoelastic response of the surface of these biomaterials; future work of quantifying

changes of the viscoelastic properties due to *in vivo* degradation, by μDMA, is required. Therefore, the conclusions in comparing the surface of these biomaterials to the widely used *in vitro* $H_2O_2/CoCl_2$ degradation method may or may not represent what happens to the biomaterials in the *in vivo* environment. *In vitro* biostability studies are useful to provide directional guidance for *in vivo* studies (Wilkoff et al., 2015). Once components/devices are implanted, the body attempts to breakdown biomaterials by numerous degradative reactions which includes oxidative, hydrolytic and enzymatic. No *in vitro* method can fully replicate and predict the *in vivo* performance of a biomaterial (Padsalgikar et al., 2015) and fully replicates the biochemical and biomechanical stresses experienced in the body (Wilkoff et al., 2015). Therefore, the *in vitro* $H_2O_2/CoCl_2$ degradation method may not replicate changes that occur with the micro-viscoelasticity due to *in vivo* degradation even though the method has been shown to replicate chemical structure and surface morphological changes; this may be a potential limitation of the *in vitro* $H_2O_2/CoCl_2$ degradation method.

It has been stated that this chemical degradation and surface morphological changes are only on the surface of the polymers (Christenson et al., 2006a; Trommsdorff et al., 2004a, 2004b; Trommsdorff and Koettig, 2005) and 100 μm below the surface, the chemical composition remained unchanged when compared to the control (Trommsdorff and Koettig, 2005). Cipriani et al. (2013) stated that most of the observed surface changes, due to *in vivo* degradation, occurred less than 10 μm. Therefore, an indentation of 5 μm with amplitude of 100 nm was used to characterise the viscoelastic response. Complex viscoelastic responses are produced when micro and nano-indentations are produced upon the surfaces of polymers (Briscoe et al., 1998). The viscoelastic response of these materials provide mechanical properties which are often a function of the geometry of the contact, the penetration depth (strain), the loading (or strain) rate and the ambient temperature (Briscoe et al., 1998). Therefore, the viscoelastic properties quantified by μDMA may be dependent on one or more of these factors.

As stated in the statistical analysis section in the material and methods of this chapter (section 4.2.6), it must be noted that findings and conclusions made from the micro-level viscoelastic properties, calculated with the μDMA method, is limited by statistical pseudo-replication, i.e. multiple observations on the same unit. Thus, findings and conclusions are specific to the surface of the specific biomaterials evaluated so, it may not give a fair representation of a wider comparison of all biomaterials. However, the author is unaware of a study that has quantified the micro-level frequency dependent viscoelastic properties of untreated and *in vitro* degradation PCU biomaterials; this work gives an insight into the viscoelastic response. Further,

van Hoorn et al. (2016) demonstrated that this ferrule-top indentation method can provide spatially-resolved map of large variations in the mechanical properties. These variations can be orders of magnitude across the surface of a soft specimen thanks to high sensitivity over larger cantilever deflections (> μm) (van Hoorn et al., 2016). Future work is required to: (1) quantify the micro-level viscoelastic properties, by μDMA, with independent measurements, (2) map local viscoelastic properties across the surface of specific specimens (in X and Y directions) to variations in regional viscoelastic response and (3) correlate the regional viscoelastic response map to the HCI of the biomaterials and investigate if localised chemical structure changes has an effect on the localised viscoelastic response.

Previous work have evaluated the hydrolytic stability of biomaterials have been evaluated by accelerated degradation methods (Chaffin et al., 2014, 2013, 2012; Khan et al., 2005a; Mahomed et al., 2010; Mishra et al., 2015). These accelerated hydrolytic degradation methods used evaluated temperatures above 37 °C. To correlate mechanical differences of a biomaterial degraded at an elevated temperature to mechanical differences at 37 °C, the principle of the time-temperature superposition (TTS) can be applied. An assumption of TTS is that the material's behaviours responds equally in the temperature range being tested i.e., the material's response is independent of temperature (Padsalgikar et al., 2015). This is stated in a Note in ISO 10993-13 where, *"consideration of the thermal properties of the additives in the polymeric material is recommended"* (ISO, 2010). To investigate a material's temperature independence, a DMTA temperature sweep can be utilised and the log-log plotting of the storage and loss moduli can identify the temperature independence; if this plot is linear, TTS assumption has been fulfilled (Padsalgikar et al., 2015). Padsalgikar et al. (2015) showed that studies which used accelerated hydrolytic degradation methods to degrade inhomogeneous (multiphase) systems may potentially not have met TTS; this previous study showed this non-linearity of Elast-Eon (AorTech, Weybridge, Surrey, UK). Future work is required to investigate the temperature independence of the biomaterials used in this thesis and used in previous studies. Thus, findings of accelerated hydrolytic degradation biomaterials used in this thesis and in previous studies should be interpreted with caution as these findings, by accelerated hydrolysis, may not correlate to the actual findings in an *in vitro* real-time degradation study with a longer time period or to the actual findings an *in vivo* degradation study. The lack of correlation between the *in vitro* accelerated hydrolytic degraded specimens and *in vivo* degraded specimens was shown by Padsalgikar et al. (2015). The authors found that the *in vitro* accelerated hydrolytic degraded specimens' molecular weight and tensile properties were not correlated to the *in vivo*

degraded specimens (Padsalgikar et al., 2015). This finding further highlights the need for caution when interpreting the results and findings of the accelerated hydrolytic degradation biomaterials. No *in vitro* degradation method fully replicates the biochemical and biomechanical stresses experienced in the body (Wilkoff et al., 2015). Thus, it is important to examine explanted implants, by a retrieval analysis, to assess the implant's performances and investigate whether the implant, and its material components, has been affected from the biological environment (Kurtz et al., 2009).

DMA is commonly known as a forced, non-resonance technique (Placet and Foltête, 2010). As the materials are tested with a frequency scan, occasionally, conditions can be found where the material-instrument system begins to resonate at certain frequencies (Menard, 2008). These resonant frequencies obscure the desired information about the material at the specific, resonant frequencies (Menard, 2008). To overcome these resonant frequencies, changes of the specimen shape, which in turn changes the mass of the specimen, or change of the applied sinusoidal loading are required (Menard, 2008). Influential factors that have an effect on the experiments include the type of load, frequency evaluated, clamps used, temperature program and specimen geometry (Ehrenstein et al., 2004). By using a BOSE Electroforce 3200 apparatus, Placet and Foltête (2010) reported a resonance effect due to the dynamic behaviour of the whole setup. The authors noted that this resonant frequency slightly moved depending on the specimen type and geometry (Placet and Foltête, 2010). Further, this resonance disturbed the measurements of the viscoelastic properties of the specimen at this specific frequency (Placet and Foltête, 2010). Even though DMA is considered a non-resonance technique, on a frequency sweep, some resonance phenomena is inevitable to appear whatever the apparatus and specimen geometry used (Placet and Foltête, 2010). In this present work, these resonance phenomena occurred at specific tested frequencies ($f \geq 20$ Hz). The appearance of this resonance was specific to a biomaterial and/or a group (untreated or degraded) and may have only appeared for one (or more) specimens in the sample; the appearance of this resonance can be seen by the large 95% confidence interval error bars in Figure 4-18, Figure 4-19, Figure 4-34 and Figure 4-35.

4.5 Chapter Summary

- The five biomaterials (Quadrathane ARC 80A-B20, Bionate II 80A, Quadrathane ARC 80A, ChronoFlex C 80A and ChronoSil 80A 5%) were viscoelastic throughout the frequency range tested; this highlights the need to evaluate biomaterials utilising frequency dependent mechanical testing techniques.
- Chronosil was the most biostable biomaterial as no new absorbance peaks were observed at 930 cm^{-1} and 1174 cm^{-1} for all specimens degraded by the four degradation methods. The micro-viscoelastic properties of Chronosil were not significantly different when comparing the four degraded methods to the untreated biomaterials.
- Aromatic PCU biomaterials degraded by the *in vitro* $H_2O_2/CoCl_2$ method demonstrated evidence of PCU oxidative degradation as new absorbance peaks were observed at 930 cm^{-1} and 1174 cm^{-1}. Regional variation of degradation on some *in vitro* $H_2O_2/CoCl_2$ degraded specimens was highly contrasting; this emphasises the need of imaging a wide sample area to understand spatial variation of biomaterial degradation. No new peaks at 930 cm^{-1} and 1174 cm^{-1} were detected for specimens degraded by the 3% H_2O_2 degradation method, the real time hydrolytic degradation method and the accelerated hydrolytic degradation method.
- Comparing the untreated to the $H_2O_2/CoCl_2$ degradation methods, the storage stiffness and loss stiffness of Bionate II and Chronoflex C, for the micro and macro viscoelasticity, were not significantly different ($p > 0.05$) for any frequency tested. The macro-viscoelastic properties of the five biomaterials were significantly different ($p < 0.05$) at specific frequencies when comparing the untreated and 3% H_2O_2 degradation method.
- Comparing the untreated specimens against the hydrolytic degradation methods, the macro-storage stiffness of Quadrathane B20, Bionate II, Quadrathane and Chronoflex C was not significantly different ($p > 0.05$) for all frequencies.
- SEM images of the five biomaterials degraded with the *in vitro* $H_2O_2/CoCl_2$ degradation method revealed various levels of pitting on the surface; Chronosil had the smallest pit sizes. One pit was identified on the surface of the 3% H_2O_2 degraded Quadrathane specimen while SEM images of Quadrathane B20, Bionate II and Chronoflex C revealed no evidence of surface pitting.

The next chapter investigates the biostability of the PCU and silicone components of the BDyn posterior dynamic stabilisation device.

Chapter 5

Biostability of the BDyn Posterior Dynamic Stabilisation device

5 Biostability of the BDyn Posterior Dynamic Stabilisation device

This chapter is based on two peer-reviewed articles published in the Journal of Mechanical Behaviour of Biomedical Materials (Lawless et al., 2016) and the Journal of Biomedical Materials Research Part B: Applied Biomaterials (Lawless et al., 2018).

5.1 Introduction

Low back pain has been associated with factors such as age, whole body vibration, lifting, twisting, psychosocial factors, and low educational status (Hoogendoorn et al., 2000; Hoy et al., 2010). Alongside heavy and frequent lifting, long term vibration exposure was stated as a high risk factor of low back pain (Magnusson et al., 1996). Numerous studies have evaluated the effect of vibration and quantified the viscoelastic properties of the spinal structures *in vitro* (Gadd and Shepherd, 2011; Holmes and Hukins, 1996; Kasra et al., 1992; Zhou et al., 2014) and *in vivo* (Panjabi et al., 1986; Wilder et al., 1982).

In the seated position, the human lumbar spine has been reported to be resonant between 4–5 Hz (Panjabi et al., 1986; Wilder et al., 1982). Thus, it is important to assess the frequency dependant behaviour of these viscoelastic spinal implants, its components, and assess how these implants behave at spinal resonant frequencies. Some studies have investigated the dynamic stiffness of spinal implants (Benzel et al., 2011; Dahl et al., 2011; LeHuec et al., 2003), while Gloria et al. (2011) quantified the dynamic viscoelastic properties of a disc prosthesis. However, a detailed assessment of the BDyn posterior dynamic stabilisation device is absent.

Once implanted, the body attempts to breakdown biomaterials by numerous degradative reactions which includes oxidative, hydrolytic and enzymatic. It is important that the materials of an implant can withstand the environment in the human body and not become degraded to a point where the implant cannot perform its intended function (Gurappa, 2002). *In vitro* biostability studies are useful to provide directional guidance for *in vivo* studies (Wilkoff et al., 2015). To understand how the degradation affects the mechanical behaviour of a material, many studies focus on the *in vitro* degradation of films (Christenson et al., 2005, 2004a; Dempsey et al., 2014; Hernandez et al., 2008; Schubert et al., 1997) or standard tensile specimen shapes (Dempsey et al., 2014) and not how degradation affects the components of orthopaedic implants and the implant itself.

In vitro degradation methods are useful as a biomaterial screening method or to analyse the degradation behaviour of a material and/or component in body contact; however, they do not fully reproduce degradation that happens *in vivo* (ISO, 2010; Wilkoff et al., 2015). No *in vitro* degradation method fully replicates the biochemical and biomechanical stresses experienced in the body (Wilkoff et al., 2015). Thus, it is important to examine explanted implants, by a retrieval analysis, to assess the implant's performances and investigate whether the implant, and its material components, have been affected by the biological environment (Kurtz et al., 2009).

The aim of this chapter is to provide a detailed investigation of the effect of biodegradation on the BDyn posterior dynamic stabilisation device and compare the viscoelastic response of the untreated (control), *in vitro* degraded and *in vivo* degraded elastomeric components of the BDyn device. Between the untreated (control), *in vitro* degraded and *in vivo* degraded elastomeric components, this study will:

- Quantify and compare the frequency dependent viscoelasticity of the untreated BDyn devices and its components; this comparison is to assess if a particular elastomeric component had an influence, or had a dominant effect, on the viscoelastic properties of the device.
- Quantify and compare the frequency dependent viscoelasticity of the control, *in vitro* and *in vivo* degraded BDyn device components; these are also compared to the assembled BDyn device with degraded components.
- Compare the chemical structure changes of the control, *in vitro* and *in vivo* degraded BDyn device components.
- Compare the macro morphological and surface morphological changes of the control, *in vitro* and *in vivo* degraded BDyn device components.

5.2 Materials and Methods

5.2.1 BDyn devices and components

Six BDyn 1 level, six BDyn 2 level PDS devices, six silicone and six polycarbonate urethane (PCU) components (Figure 5-1) were obtained from S14 Implants (Pessac, France). All devices and elastomeric components were sterilised using ethylene oxide (EtO) (Steriservices, Bernay, France) (see section 3.2).

Figure 5-1: From left to right; BDyn 1 level (BDyn 1), BDyn 2 level (BDyn 2), polycarbonate urethane (PCU) component and silicone component. BDyn can be used to bridge one segment level (vertebra-disc-vertebra) or multiple segment levels; see section 2.4.2 for more information on the BDyn implant.

After publication of the study which compared the viscoelastic properties of the BDyn devices and its components (Lawless et al., 2016), the PCU rings and silicone cushions were degraded using a 20% hydrogen peroxide (H_2O_2) and 0.1 M cobalt (II) chloride hexahydrate ($CoCl_2.6H_2O$) oxidative solution method (see section 3.3).

Six BDyn 1 level explanted devices from three patients, which contained six silicone and six PCU components were sent to S14 Implants (Pessac, France) after complications with the devices (see Table 5-1). The titanium alloy housing was carefully cut along the laser weld to expose the PCU and silicone components and the components were sterilised. Patient details were unobtainable, however, estimated implantation time (based on distribution of implants to retrieval surgery date) were approximated (see Table 5-1).

Table 5-1: Clinical information for the six explants from three individual patients.

Patient ID	BDyn ID		Approx. Implant Time (months)	Reason for Revision
PAT1	Explant 1	Explant 2	17	"Failure of Device"
PAT2	Explant 3	Explant 4	21	Screw Breakage
PAT3	Explant 5	Explant 6	6	Unknown

5.2.2 Spectroscopy – ATR-FTIR and HCM

5.2.2.1 ATR-FTIR

Attenuated total reflectance Fourier transform infra-red (ATR-FTIR) point spectroscopy was performed on the untreated and *in vitro* degraded BDyn components (PCU ring and silicone cushion). Twenty spectra, with a spectral resolution of 2 cm^{-1} between 600 and 4000 cm^{-1}, were acquired and mean averaged to obtain each spectrum (Simmons et al., 2004). The PCU spectra were cut between 750 and 2000 cm^{-1} and normalised to the internal reference 819 cm^{-1} peak, the stable aromatic C–H out of plane bending peak (Dorrepaal et al., 2018). Linear baseline correction was performed subsequent to the internal reference normalisation and followed by a baseline shift of one arbitrary unit (Dorrepaal et al., 2018).

5.2.2.2 HCM

Attenuated total reflectance Fourier transform infra-red hyperspectral chemical mapping (HCM) was performed on the untreated and the explanted BDyn components (PCU ring and silicone cushion). The light aperture size of 150 μm (in the x and y dimension) was selected which implies that the single point detector was 37.5 μm. For the HCM of the explant specimens, a grid of data points was selected and the distance between each pixel was 100 μm; this creates a spatially resolved, non-contiguous map. This HCM method has been shown to be advantageous in the assessment of larger specimen regions and time-sensitive studies (Dorrepaal et al., 2018). For each map, a minimum of 100-pixel spectra were recorded; the maximum was 300-pixel spectra for Explant 5 HCMs.

Twenty spectra with a spectral resolution of 2 cm^{-1} between 675 and 4000 cm^{-1} were acquired and mean averaged to obtain each spectrum (Simmons et al., 2004). Similar to the ATR-FTIR spectra (see section 5.2.2.1), the PCU spectra were cut between 750 and 2000 cm^{-1}, normalised to the internal reference 819 cm^{-1} peak and linear baseline correction was performed subsequent to the internal reference normalisation and followed by a baseline shift of one arbitrary unit (Dorrepaal et al., 2018).

A secondary normalisation method, the Savitzky Golay (SG) technique (Savitzky and Golay, 1964), was also performed to understand the changes of the wavelengths of the PCU and silicone explanted components. The SG window size was 31 wave measurements (a buffer size of 15 on either side of the centre point), the fit was a second order polynomial and a second order derivative.

Spectral assignments and wavenumbers (cm^{-1}) for the PCU ring and Silicone cushion are listed in Table 5-2 and Table 5-3, respectively.

Table 5-2: Spectral assignment and wavenumber for the BDyn PCU component (Christenson et al., 2004a, 2004b; Cipriani et al., 2013; Dorrepaal et al., 2018; Hernandez et al., 2008; Shen et al., 2011; Smith, 1998; B. Ward et al., 2006; R. Ward et al., 2006)

Spectral assignment	Wavenumber (cm^{-1})
C=O stretching vibration of free carbonate	1740-1737
C=O stretching vibration of hydrogen-bonded carbonate	1720
C=O stretching vibration of hydrogen-bonded urethane	1705-1701
NH_2 free aromatic amine	1650
Aromatic C=C stretching vibration	1598-1596
CH_2 bending vibration	1466
O-C-O stretching vibration of carbonate	1254-1246
N–H bending and C–N stretching vibration of urethane	1223-1220
C-C crosslinking (branched ether)	1174
C-O	1110
C-O-C of urethane	1079
C-H bending in plane aromatic ring	1018
O-H bending or bending of aliphatic CO_2H	930-931
C-H bending out of plane aromatic ring	816-819

Table 5-3: Spectral assignment and wavenumber for the BDyn silicone component (Ghanbari-Siahkali et al., 2005; Mahomed et al., 2015; Simmons et al., 2006, 2004)

Spectral assignment	Wavenumber (cm^{-1})
O=H stretch	3318
C-H stretch in CH_3 bend	2958
C=O stretch	1704
N-H bend and C-N stretch	1529
Si-CH_3 stretch	1257
Si-O-Si stretch	1065
Si-O-Si stretch	1016
(Si-CH_3)$_2$ stretch	792

5.2.3 Dynamic Mechanical Analysis (DMA)

To facilitate the comparison of viscoelastic properties, the testing protocol for viscoelastic properties of control, *in vitro* and *in vivo* degraded BDyn devices, and its components, were kept consistent. The experimental factors such as applied sinusoidal load, investigated frequencies, machine fixtures used, etc. discussed henceforth were kept consistent for control, *in vitro* and *in vivo* degraded BDyn devices, and its components unless stated otherwise.

The storage and loss stiffness were calculated for 21 different frequencies between 0.01 Hz to 30 Hz; see section 2.2.3.2 for more information on how the storage and loss stiffness was calculated. This frequency range is greater than the ASTM F2346 stated physiological frequency range of 0.1 Hz to 8 Hz (ASTM, 2011); the maximum tested frequency (30 Hz) is the same as the maximum recommended frequency for cyclical loading of components used in spinal surgical fixation (ASTM, 2014; Kurtz and Edidin, 2006).

All devices and components were tested in air at 37°C ± 1°C and the temperature was monitored throughout the test (see section 3.7, Figure 3-7 and 8.4 Appendix D). Custom-designed grips were used to clamp the titanium alloy rods and/or titanium alloy elastomer housing of the BDyn device and the devices were secured by twelve horizontal screws (Figure 5-2).

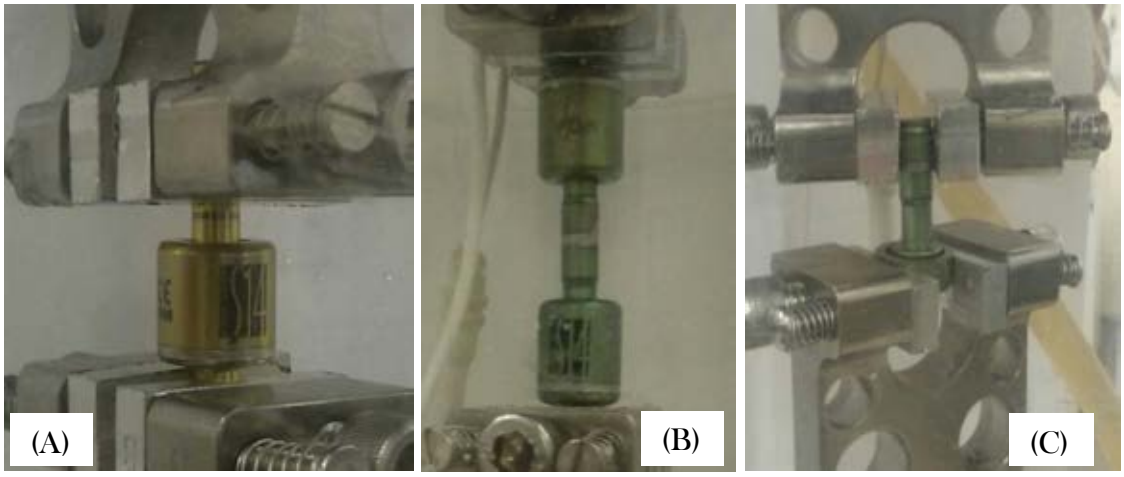

Figure 5-2: Testing of (A) BDyn 1 level, (B) BDyn 2 level and (C) one of the elastomeric components

For testing of the BDyn 1 level and BDyn 2 level devices, the titanium alloy mobile and fixed rods were gripped (Figure 5-2 (A) and (B)). The BDyn device is designed to work in both

tension and compression, therefore, a sinusoidally varying load of between +20 N (tension) and -20 N (compression) was applied to the devices.

The silicone and PCU components were tested inside the titanium alloy housing, with the mobile titanium rod and the titanium housing gripped for testing (Figure 5-2 (C)). The silicone and PCU components are only loaded in compression, therefore, a sinusoidally varying load of between -1 N and -20 N (compression) was applied to the elastomeric components. Testing the elastomeric components to this load range and inside the titanium alloy housing gave a direct comparison between the BDyn devices and the silicone and PCU components.

The *in vitro* degraded individual components were tested first, then the degraded PCU and silicone components were randomly paired, assembled in the BDyn titanium housing and tested (Table 5-4). Similarly to the *in vitro* testing, the *in vivo* degraded individual components were tested then the PCU and silicone components were paired, assembled and tested in the BDyn titanium housing. The pairing of the explanted PCU and silicone components were the same as the explanted BDyn devices. Testing the device assembled with degraded components gave a direct comparison between the untreated (control) BDyn devices to the BDyn device with degraded components.

Table 5-4: Number of specimens used in the control (untreated) (Lawless et al., 2016), *in vitro* degraded (Lawless et al., 2018) and *in vivo* degraded studies. The PCU ring and silicone cushion, used in the control study, were *in vitro* degraded (†). The *in vitro* degraded PCU rings (†) and silicone cushions (†) were randomly assembled in the BDyn device (‡) and tested; the explanted, *in vivo* degraded PCU rings (ᶿ) and silicone cushions (ᶿ) were assembled in the BDyn device (ᵠ) and tested.

Study	BDyn 1 level	BDyn 2 level	PCU ring	Silicone cushion
Control	Six	Six	Six	Six
in vitro	Six‡	-	Six†	Six†
in vivo	Sixᵠ	-	Sixᶿ	Sixᶿ

The order of device and component testing was randomised by using the Excel Random Function (Redmond, Washington, USA). A custom MATLAB (MathWorks, Natick, MA, USA) script was created (and validated against the calculated viscoelastic properties from the DMA software) to further analyse the mechanical response of the BDyn components and devices (8.8 Appendix H).

5.2.4 Scanning Electron Microscopy (SEM)

Untreated and *in vitro* specimens were sputter coated with ~30 nm layer of gold by using an Agar B7340 sputter coater (Agar Scientific, Stansted, Essex, UK). *In vivo* specimens were sputter coated with ~25 nm layer of gold by using an Emscope SC500 sputter coater (Emscope Laboratories, Kent, UK). ImageJ 1.48v (National Institutes of Health, Bethesda, MD, USA) was used to measure surface pits. The scale bar on a specific SEM image was used to calibrate the image. As the pits were irregular in shape, the major diameters of numerous pits were recorded and a range of pit sizes (μm) was reported.

5.2.5 Statistical analysis

The 95% confidence intervals were calculated (n = 6) for the storage and loss stiffness of the untreated (control) and *in vitro* degraded specimens. Due to the variability of the explanted components, no 95% confidence intervals were calculated and the explanted components (PCU rings and silicone cushions) and BDyn device, with the explanted components, were plotted individually. To evaluate the differences among the untreated BDyn devices and untreated components (i.e. to assess if a particular elastomeric component had a dominant effect on the viscoelastic properties of the device), Kruskal-Wallis one-way analysis of variance (ANOVA) on ranks was performed. If the Kruskal-Wallis ANOVA showed significant differences ($p < 0.05$), the multiple comparison Tukey test was used to evaluate significant differences ($p < 0.05$). Wilcoxon signed rank tests were performed to compare the differences of the elastomeric components before and after *in vitro* degradation. Whereas a Wilcoxon rank sum test compared the normal BDyn viscoelastic properties to the BDyn device assembled with the degraded components. Due to the variability of the explanted components, no sample comparison tests were performed. Instead, whether the individual explanted component's viscoelastic properties lie within the 95% confidence interval error bounds of the control and *in vitro* oxidation specimens was recorded. Regression analyses were performed to evaluate the frequency dependent nature of the storage (k') and loss (k'') property and the significance of the fit (equation 5.1 and 5.2):

$$k' = A\ln(f) + B \quad \text{for } 0.01 \le f \le 30 \qquad \text{Equation 5.1}$$

$$k'' = C\ln(f) + D \quad \text{for } 0.01 \le f \le 30 \qquad \text{Equation 5.2}$$

where f is frequency (independent variable), A and C are coefficients and B and D are the constants of the logarithmic regression. All results with $p < 0.05$ were considered significant.

5.3 Results

5.3.1 Comparison of viscoelasticity of BDyn devices and its components

The frequency dependent trends of the storage and loss stiffness of the BDyn 1 level device, BDyn 2 level device, the silicone component and the PCU component are shown in Figure 5-3. The BDyn devices and its components were viscoelastic throughout the frequency range tested. Also, the storage stiffness was larger than the loss stiffness for all frequencies tested.

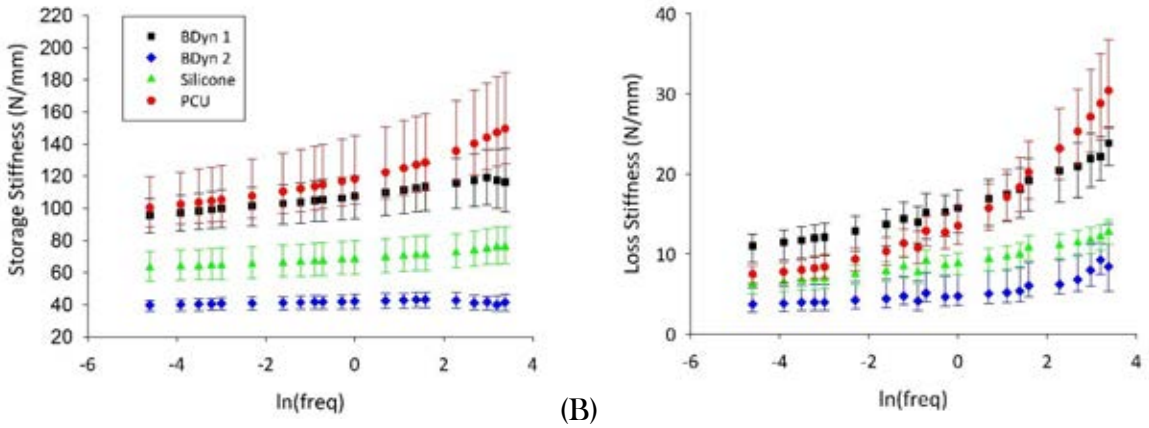

(A) (B)

Figure 5-3: (A) Storage stiffness (k') and (B) loss stiffness (k") against ln(frequency) for the 1 level BDyn device (BDyn 1), 2 level BDyn device (BDyn 2), silicone component (Silicone) and polycarbonate urethane (PCU) component (median ± 95% confidence intervals). Graph legend is consistent for both plots and can be seen in the k' plot.

The storage stiffness and loss stiffness of the BDyn 1 level device, BDyn 2 level device, silicone component and PCU component were defined by logarithmic fits (Equation 5.1 and 5.2). The mean storage stiffness and loss stiffness logarithmic trends of the devices and components were all found to be significant ($p < 0.05$). The coefficients (A and C) and constants (B and D) which define the storage and loss stiffness logarithmic trends for individual specimens are provided in Table 5-5.

Table 5-5: Storage stiffness (equation 5.1) and loss stiffness (equation 5.2) regression analyses of the BDyn devices and its components. Cofficients for the individual specimens' storage and loss trends are provided.

	k'				k''			
Specimen ID	A	B	R^2	P Value	C	D	R^2	P Value
BDyn 1 - 1	2.86	104.7	0.98	0.0001	1.51	16.69	0.96	0.0001
BDyn 1 - 2	3.03	112.0	0.99	0.0001	1.57	16.60	0.95	0.0001
BDyn 1 - 3	4.11	125.1	0.97	0.0001	1.59	18.16	0.97	0.0001
BDyn 1 - 4	2.56	96.94	0.98	0.0001	1.37	15.65	0.94	0.0001
BDyn 1 - 5	3.85	119.9	0.97	0.0001	1.82	18.69	0.96	0.0001
BDyn 1 - 6	1.68	90.40	0.93	0.0001	1.28	11.68	0.85	0.0001
BDyn 1 - Mean	**3.02**	**108.2**	**0.98**	**0.0001**	**1.52**	**16.25**	**0.95**	**0.0001**
PCU - 1	8.70	158.0	0.96	0.0001	3.76	20.66	0.90	0.0001
PCU - 2	7.70	146.6	0.96	0.0001	3.38	18.86	0.89	0.0001
PCU - 3	5.30	110.9	0.96	0.0001	2.43	13.83	0.88	0.0001
PCU - 4	6.44	129.3	0.95	0.0001	2.93	16.86	0.90	0.0001
PCU - 5	5.53	115.1	0.93	0.0001	2.73	15.89	0.90	0.0001
PCU - 6	4.81	106.6	0.95	0.0001	2.40	13.66	0.90	0.0001
PCU - Mean	**6.41**	**127.8**	**0.95**	**0.0001**	**2.94**	**16.63**	**0.89**	**0.0001**
Silicone - 1	2.02	84.11	0.97	0.0001	0.84	10.76	0.95	0.0001
Silicone - 2	1.76	78.13	0.97	0.0001	0.83	10.51	0.95	0.0001
Silicone - 3	1.37	62.44	0.96	0.0001	0.72	7.90	0.95	0.0001
Silicone - 4	1.53	64.36	0.96	0.0001	0.75	8.87	0.96	0.0001
Silicone - 5	1.28	58.89	0.96	0.0001	0.70	7.56	0.95	0.0001
Silicone - 6	1.72	73.81	0.96	0.0001	0.81	9.65	0.96	0.0001
Silicone - Mean	**1.61**	**70.29**	**0.97**	**0.0001**	**0.78**	**9.21**	**0.95**	**0.0001**
BDyn 2 - 1	0.12	36.40	0.11	0.1405	0.43	4.88	0.82	0.0001
BDyn 2 - 2	0.34	39.79	0.60	0.0001	0.48	4.95	0.83	0.0001
BDyn 2 - 3	0.10	43.32	0.02	0.4991	0.65	6.00	0.71	0.0001
BDyn 2 - 4	0.40	44.92	0.34	0.0055	0.86	9.73	0.77	0.0001
BDyn 2 - 5	0.16	37.61	0.19	0.0454	0.53	4.69	0.70	0.0001
BDyn 2 - 6	0.49	46.11	0.73	0.0001	0.55	6.84	0.90	0.0001
BDyn 2 - Mean	**0.27**	**41.36**	**0.45**	**0.0010**	**0.58**	**6.18**	**0.82**	**0.0001**

The storage stiffness of the individual BDyn 1 level device, silicone component and PCU component specimens also all followed a logarithmic trend which was found to be significant ($p < 0.05$; Table 5-5). Two out of the six BDyn 2 level devices did not follow a significant logarithmic trend. The range of the BDyn 2 level device mean storage stiffness was between 39.41 N/mm to 42.82 N/mm for the 0.01 Hz – 29 Hz frequency range (Figure 5-3); this differed to the BDyn 1 level device storage stiffness range (95.56 N/mm to 119.29 N/mm). Due

to this 8% change in the BDyn 2 level storage stiffness range, the mean and standard deviation was analysed individually for all six BDyn 2 level devices (see Table 5-6).

The loss stiffness of the BDyn 1 level device ranged from 10.72 N/mm to 23.42 N/mm while the BDyn 2 level device ranged from 4.26 N/mm to 9.57 N/mm. Unlike the storage stiffness of individual specimens, the loss stiffness of all the individual devices and components followed a significant logarithmic trend ($p < 0.05$, see Table 5-5).

Table 5-6: Mean and standard deviation of the storage stiffness (N/mm) for the BDyn 2 level device.

Specimen ID	Mean	Standard Deviation
BDyn 2 - 1	36.36	0.89
BDyn 2 - 2	39.69	1.10
BDyn 2 - 3	43.30	1.57
BDyn 2 - 4	45.97	1.72
BDyn 2 - 5	37.57	0.91
BDyn 2 - 6	45.97	1.44

The Kruskal-Wallis ANOVA on ranks detected significant differences ($p \leq 0.001$) for the storage and loss stiffness, for all tested frequencies. The multiple comparison test results are shown in Table 5-7. The frequencies stated in this table indicate that the difference between the components and devices were significantly different ($p < 0.05$).

Table 5-7: Multiple comparison test results for the 1 level BDyn device (BDyn 1), 2 level BDyn device (BDyn 2), silicone component (Sil) and polycarbonate urethane (PCU) component. The frequencies stated indicates that the comparison were significantly different ($p < 0.05$).

Multiple Comparison Test	Storage Stiffness	Loss Stiffness
BDyn 2 – BDyn 1	0.01 Hz to 29 Hz	0.01 Hz to 29 Hz
PCU – BDyn 1	-	-
Sil – BDyn 1	-	0.01 Hz to 0.2 Hz, 0.4 Hz, 0.75 Hz, 1 Hz
PCU – BDyn 2	0.01 Hz to 29 Hz	0.1 Hz to 29 Hz
Sil – BDyn 2	-	-
Sil – PCU	1 Hz to 29 Hz	10 Hz to 29 Hz

5.3.2 Macro-morphological (control, *in vitro* and *in vivo* degraded specimens)

In vitro degradation of the BDyn elastomeric components led to a change in transparency of the PCU ring (Figure 5-4 (A) and (B)) and the silicone cushion (Figure 5-4 (C) and (D)).

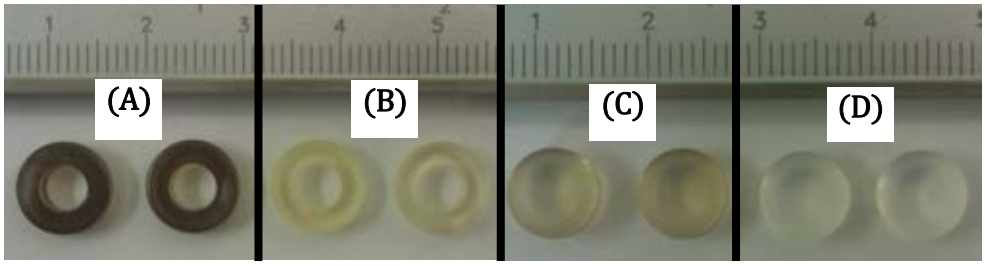

Figure 5-4: PCU components (A) before and (B) after *in vitro* degradation. Silicone components (C) before and (D) after *in vitro* degradation.

When compared to the explanted *in vivo* degraded elastomeric components, none of the explanted components became more transparent; increased transparency was seen with the *in vitro* oxidative degraded components (see Figure 5-5 and Figure 5-6).

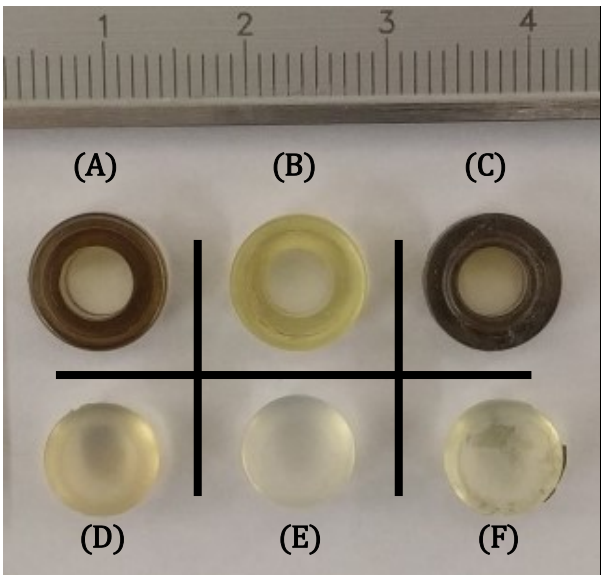

Figure 5-5: PCU rings (A-C) and Silicone cushions (D-F). Normal (A & D), *in vitro* degraded components (B & E) and explanted, *in vivo* degraded components (C & E). Component (C) and (E) are Explant 4 from patient 2.

All six PCU rings and all six silicone cushions, from the explanted BDyn devices, displayed some form of morphological changes (Figure 5-6). The silicone cushion of Explant 1 (see Figure 5-6(A)) and Explant 2 (see Figure 5-6 (B)) displayed plastic deformation with the silicone cushion of Explant 2 being more severe than Explant 1. The PCU ring of Explant 3 (see Figure 5-6(C)) and Explant 4 (see Figure 5-6 (D)) displayed plastic deformation associated with extensive flexion of the BDyn implants. The silicone cushion explanted component of Explant 5 (see Figure 5-6 (E)) has an imprint of the mobile rod and is more severe than the silicone cushion of Explant 6 (see Figure 5-6 (F)). Both PCU rings from Explant 5 (Figure 5-6 (E)) and Explant 6 (Figure 5-6 (F)) have extensive plastic deformation with the PCU ring from Explant 6 being compressed at an angle due to contact with the titanium housing.

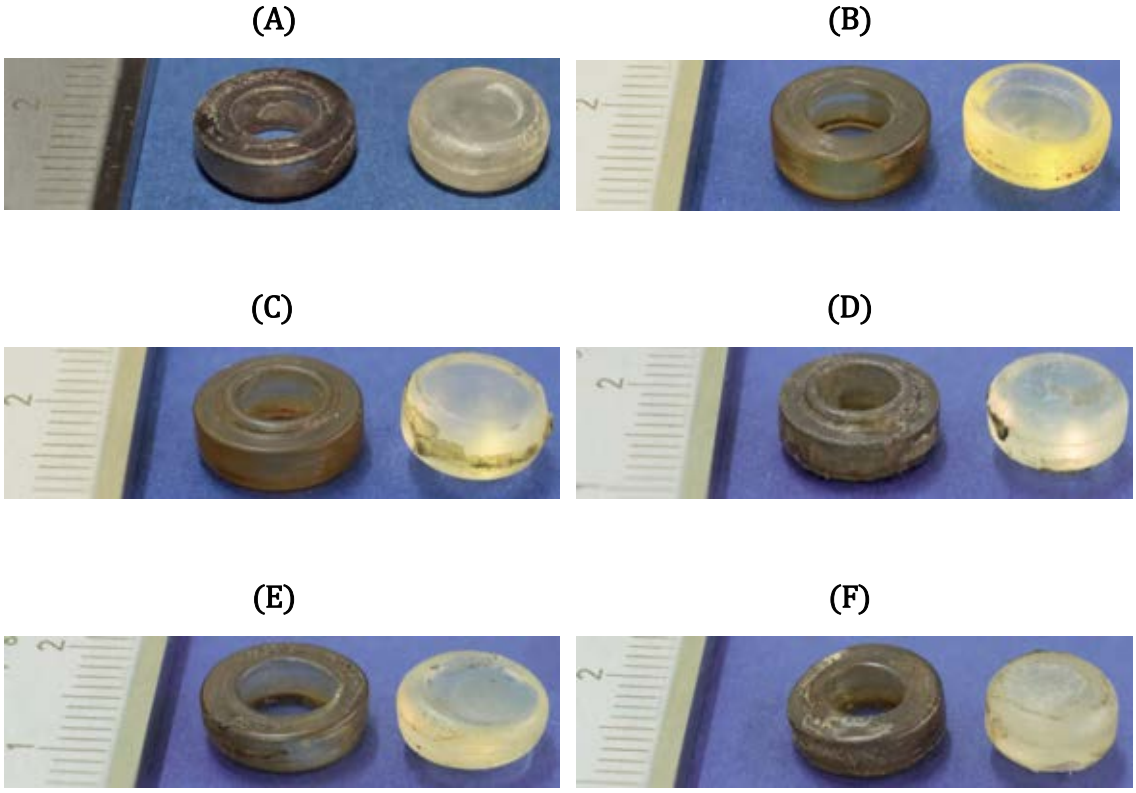

Figure 5-6: Explanted PCU rings and silicone cushion components from PAT1 (A) Explant 1, (B) Explant 2; PAT2 (C) Explant 3, (D) Explant 4; PAT3 (E) Explant 5 and (F) Explant 6. The approximate implantation time was 17 months for PAT1, 21 months for PAT2 and 6 months for PAT3.

5.3.3 Viscoelasticity (control, *in vitro* and *in vivo* degraded specimens)

Figure 5-7 presents the storage stiffness and loss stiffness of the BDyn implant, the PCU component and the silicone component, for normal and the *in vitro* degraded components.

The mean *in vitro* degraded PCU and silicone components storage stiffness ranged between 87.5 N/mm to 135.3 N/mm and 51.6 N/mm to 60.7 N/mm, respectively. The BDyn implant storage stiffness ranged between 84.46 N/mm to 99.36 N/mm. The storage stiffness logarithmically increased in relation to frequency ($p < 0.05$) (equation 5.1, where A is a coefficient and B is a constant, and Table 5-8). For the PCU component, silicone component and BDyn implant assembled with the degraded components, the storage stiffness was larger than the loss stiffness for all frequencies tested.

The *in vitro* degraded PCU and silicone components loss stiffness ranged between 6.03 N/mm to 24.45 N/mm and 4.59 N/mm to 10.83 N/mm, respectively. The BDyn implant loss stiffness ranged between 8.13 N/mm to 21.99 N/mm. Similarly to the storage stiffness, the loss stiffness logarithmically increased in relation to frequency ($p < 0.05$) (equation 5.2, where C is a coefficient and D is a constant, and Table 5-8).

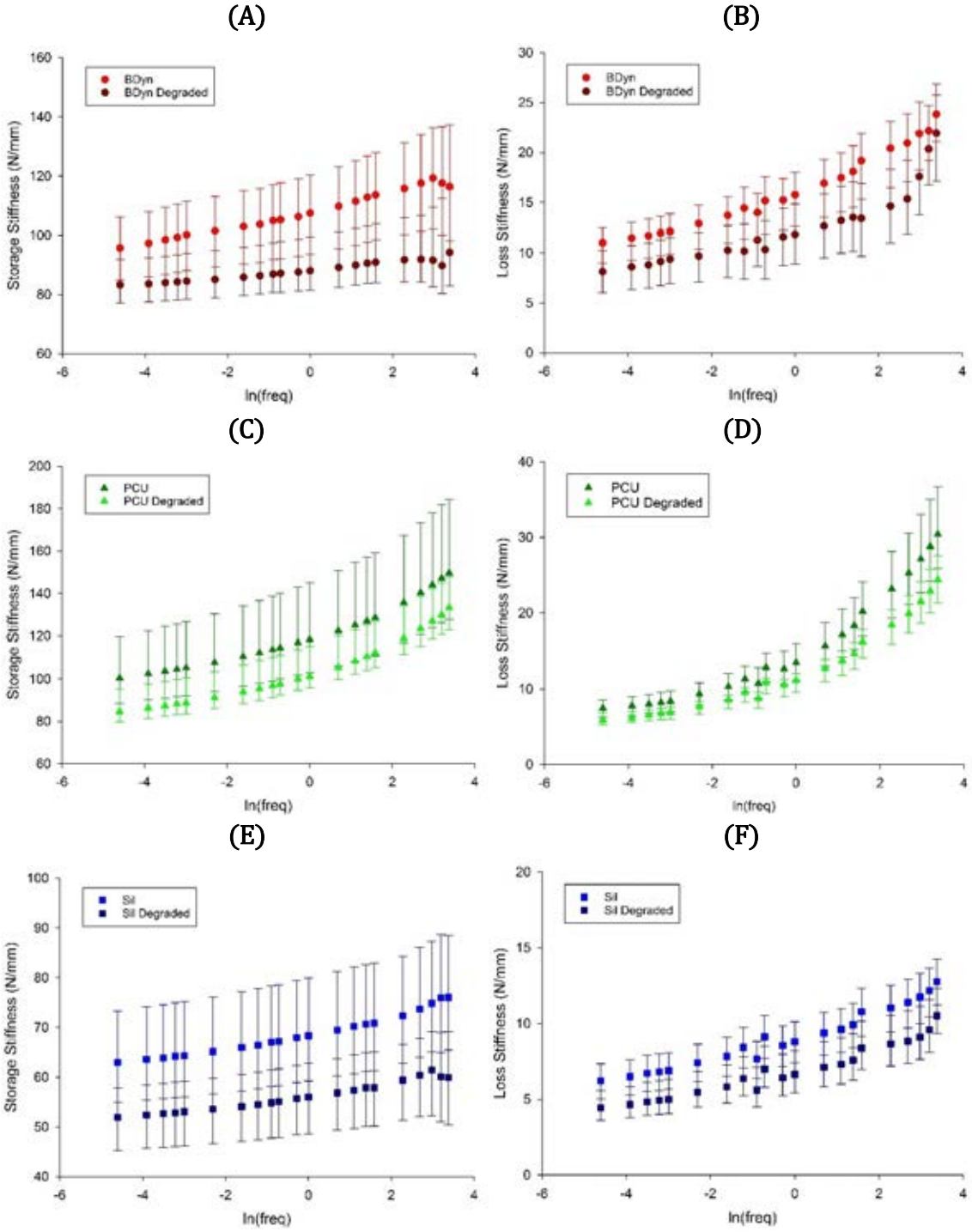

Figure 5-7: Storage stiffness (k') against ln(f) for normal and degraded (A) BDyn device (BDyn), (C) PCU component (PCU), and (E) silicone component (Sil). Loss stiffness (k'') against ln(f) for normal and degraded (B) BDyn device (BDyn), (D) PCU component (PCU), and (F) silicone component (Sil). All plots are median ± 95% confidence intervals.

Table 5-8: Storage stiffness (equation 5.1) and loss stiffness (equation 5.2) regression analyses of the BDyn devices and its components. Cofficients (*A, B, C* and *D*) for the individual specimens' storage and loss stiffness (N/mm) trends are provided.

	k'				k''			
Specimen ID	*A*	*B*	R^2	P Value	*C*	*D*	R^2	P Value
BDyn 1 – 1	2.70	105.1	0.93	<0.001	1.71	16.44	0.90	<0.001
BDyn 1 – 2	1.30	86.97	0.81	<0.001	1.21	11.13	0.80	<0.001
BDyn 1 – 3	1.18	89.60	0.96	<0.001	1.43	14.64	0.81	<0.001
BDyn 1 – 4	0.78	85.13	0.64	<0.001	1.21	11.03	0.82	<0.001
BDyn 1 – 5	3.10	99.41	0.87	<0.001	1.77	15.20	0.80	<0.001
BDyn 1 – 6	1.25	80.33	0.97	<0.001	1.11	8.88	0.77	<0.001
BDyn 1 - Mean	**1.72**	**91.10**	**0.97**	**<0.001**	**1.41**	**12.89**	**0.82**	**<0.001**
PCU – 1	6.31	102.7	0.94	<0.001	2.73	14.25	0.90	<0.001
PCU – 2	6.75	123.0	0.96	<0.001	2.45	14.59	0.89	<0.001
PCU – 3	6.32	118.8	0.96	<0.001	2.25	13.71	0.89	<0.001
PCU – 4	5.19	101.2	0.96	<0.001	1.93	11.31	0.88	<0.001
PCU – 5	5.82	107.5	0.95	<0.001	2.07	12.94	0.89	<0.001
PCU – 6	5.13	101.5	0.96	<0.001	1.87	11.43	0.89	<0.001
PCU – Mean	**5.92**	**109.1**	**0.95**	**<0.001**	**2.22**	**13.02**	**0.89**	**<0.001**
Silicone – 1	1.07	52.47	0.96	<0.001	0.64	6.22	0.93	<0.001
Silicone – 2	1.50	63.66	0.97	<0.001	0.86	9.54	0.96	<0.001
Silicone – 3	0.66	45.32	0.90	<0.001	0.61	5.96	0.90	<0.001
Silicone – 4	1.40	62.22	0.97	<0.001	0.72	7.63	0.95	<0.001
Silicone – 5	1.09	53.44	0.96	<0.001	0.66	6.49	0.93	<0.001
Silicone – 6	1.23	59.42	0.96	<0.001	0.71	7.78	0.95	<0.001
Silicone - Mean	**1.16**	**56.09**	**0.97**	**<0.001**	**0.70**	**7.27**	**0.94**	**<0.001**

Table 5-9 provides the frequencies at which the PCU and silicone components were significantly different before and after *in vitro* degradation. The storage and loss stiffness of the silicone component, before and after *in vitro* degradation, were significantly different for the frequency range tested while the PCU component loss stiffness was only significantly different for certain frequencies namely 0.5 Hz, 4 Hz to 29 Hz. Also, the storage stiffness of the BDyn device, assembled with *in vitro* degraded components, was significantly different from 0.2 Hz to 20 Hz while, the loss stiffness was significantly different from 0.01 Hz to 0.3 Hz and 0.5 Hz to 15 Hz.

Table 5-9: Wilcoxon Signed Rank test results for the PCU and Silcone components and Wilcoxon Rank Sum test for the BDyn Device. The frequencies stated indicates a significantly different ($p < 0.05$) between the untreated and degraded specimens.

Component	Storage Stiffness	Loss Stiffness
PCU	-	0.5 Hz, 4 Hz to 29 Hz
Silicone	0.01 Hz to 29 Hz	0.01 Hz to 29 Hz
BDyn Device	0.2 Hz to 20 Hz	0.01 Hz to 0.3 Hz, 0.5 Hz to 15 Hz

Figure 5-8 presents the storage stiffness of the BDyn device assembled with the explanted components, the explanted PCU components and the explanted silicone components. The loss stiffness of the BDyn device assembled with the explanted components, the explanted PCU components and the explanted silicone components are also presented in Figure 5-8. The normal and *in vitro* degraded viscoelastic properties of the BDyn implant, PCU component and silicone component, presented in Figure 5-7, are illustrated in Figure 5-8 to show differences between the viscoelasticity of the normal, the *in vitro* degraded and *in vivo* degraded scenarios.

A wide variability of the explanted PCU and silicone components storage and loss stiffness exist. However, the frequency dependent behaviour of the PCU ring storage stiffness seemed to be in "pairs" and these "pairs" match the set of explants from a specific patient (see Figure 5-8 (C) and (D) and Table 5-1). The storage and loss stiffness of the explanted PCU and silicone components were logarithmically frequency-dependent ($p < 0.001$; see Table 5-10). The storage stiffness of three BDyn devices were logarithmically frequency dependent, namely Explant 1, Explant 2 and Explant 6. The loss stiffness of the BDyn devices, assembled with the explanted components, were logarithmically frequency-dependent ($p < 0.001$; see Table 5-10).

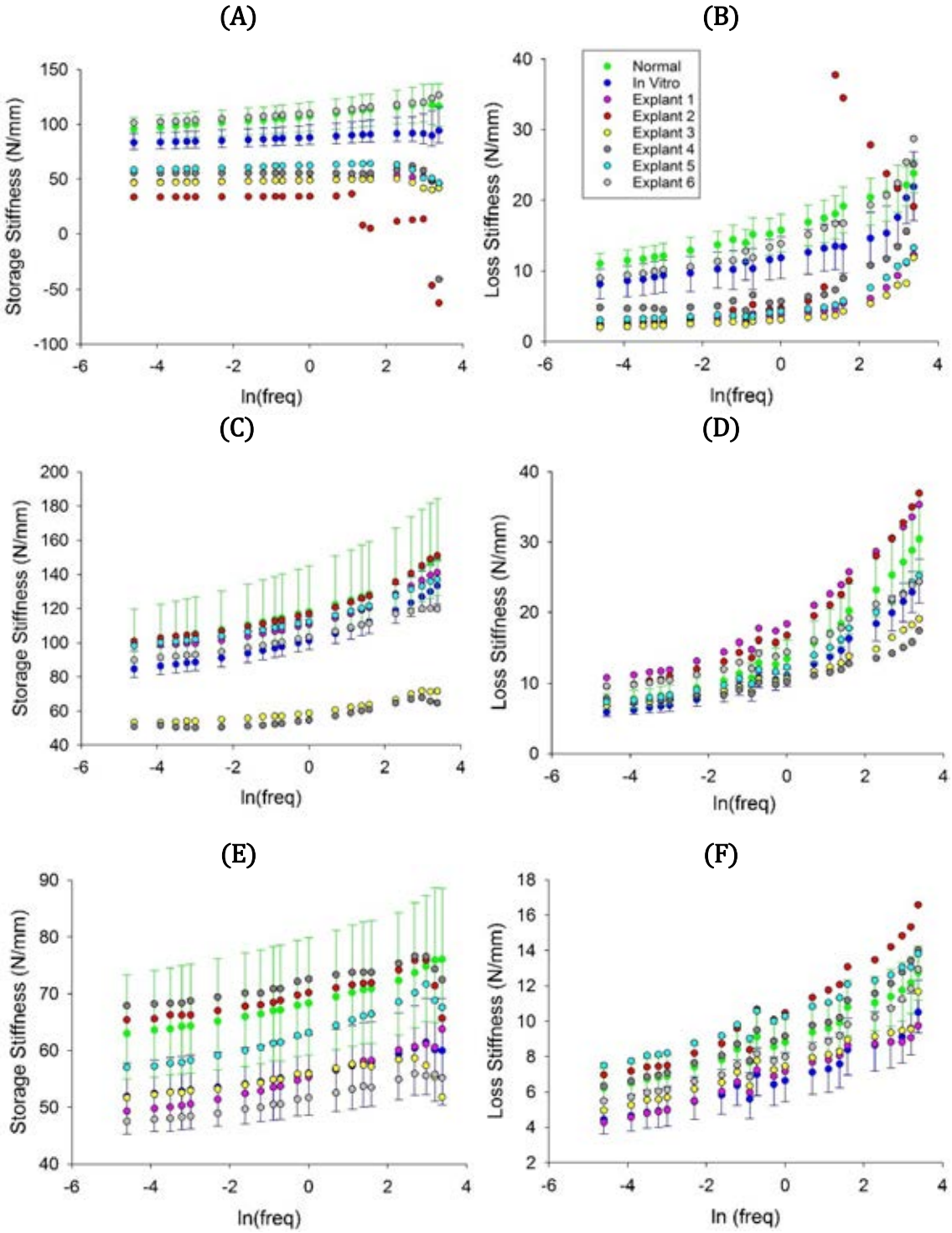

Figure 5-8: Storage stiffness (A, C, E) and loss stiffness (B, D, F) against ln(freq) for normal, *in vitro* and *in vivo* degraded (A & B) BDyn devices, (C & D) PCU ring components and (E & F) Silicone cushion components. Normal and *in vitro* data are median ± 95% confidence intervals. Graph legend (B) is consistent for all plots (A – F).

Table 5-10: Storage stiffness *(k')* and loss stiffness *(k'')* regression analyses of the explanted BDyn components (Explant PCU and Explant Silicone). These components were reassembled into the Ti Alloy housing of the BDyn device (Explant BDyn 1). *A* and *C* represent the coefficients of the logarithmic regression of *k'* and *k''*, respectively. *B* and *D* are the constants of *k'* and *k''*, respectively.

	k' = Aln(f) + B				k'' = Cln(f) + D			
Specimen ID	*A*	*B*	R^2	*p* Value	*C*	*D*	R^2	*p* Value
Explant BDyn 1 – 1	0.45	49.26	0.331	0.006	0.95	5.15	0.690	<0.001
Explant BDyn 1 – 2	-7.19	17.94	0.450	<0.001	3.32	12.20	0.528	<0.001
Explant BDyn 1 – 3	-0.32	47.22	0.083	0.207	0.83	4.29	0.652	<0.001
Explant BDyn 1 – 4	-2.71	50.43	0.104	0.155	1.52	8.40	0.570	<0.001
Explant BDyn 1 – 5	-0.58	59.52	0.095	0.173	1.01	5.76	0.696	<0.001
Explant BDyn 1 – 6	2.87	111.95	0.943	<0.001	2.04	15.57	0.847	<0.001
BDyn 1 – Control	**3.02**	**108.17**	**0.98**	**<0.001**	**1.52**	**16.25**	**0.95**	**<0.001**
BDyn 1 – *in vitro*	**1.72**	**91.10**	**0.97**	**<0.001**	**1.41**	**12.89**	**0.82**	**<0.001**
Explant PCU – 1	5.43	115.35	0.901	<0.001	3.11	20.99	0.928	<0.001
Explant PCU – 2	6.08	121.81	0.914	<0.001	3.33	20.17	0.898	<0.001
Explant PCU – 3	2.47	61.08	0.906	<0.001	1.47	11.86	0.915	<0.001
Explant PCU – 4	2.32	57.22	0.858	<0.001	1.14	11.10	0.892	<0.001
Explant PCU – 5	4.87	115.85	0.946	<0.001	2.23	14.51	0.905	<0.001
Explant PCU – 6	4.12	105.38	0.971	<0.001	1.91	16.00	0.935	<0.001
PCU – Control	**6.41**	**127.77**	**0.95**	**<0.001**	**2.94**	**16.63**	**0.89**	**<0.001**
PCU – *in vitro*	**5.92**	**109.1**	**0.95**	**<0.001**	**2.22**	**13.02**	**0.89**	**<0.001**
Explant Silicone – 1	1.72	55.76	0.971	<0.001	0.67	7.152	0.978	<0.001
Explant Silicone – 2	1.10	69.78	0.597	<0.001	1.15	11.06	0.943	<0.001
Explant Silicone – 3	0.64	55.22	0.506	<0.001	0.67	7.72	0.924	<0.001
Explant Silicone – 4	1.04	72.08	0.875	<0.001	0.90	9.71	0.935	<0.001
Explant Silicone – 5	1.78	63.62	0.946	<0.001	0.76	10.57	0.968	<0.001
Explant Silicone – 6	1.14	51.90	0.978	<0.001	0.83	8.54	0.930	<0.001
Silicone – Control	**1.61**	**70.29**	**0.97**	**<0.001**	**0.78**	**9.21**	**0.95**	**<0.001**
Silicone – *in vitro*	**1.16**	**56.09**	**0.97**	**<0.001**	**0.70**	**7.27**	**0.94**	**<0.001**

BDyn 1 level specimen 2 ('Explant BDyn 1 – 2' in Table 5-10), which was one of the three BDyn devices whose storage stiffness was logarithmically frequency dependent ($p < 0.05$; Table 5-10), had a negative coefficient *(A)* of -7.19. Between 3 Hz to 4 Hz, the storage stiffness of the BDyn Explant 2 decreased from 36.54 N/mm to 7.84 N/mm. At 29 Hz, the storage stiffness of the BDyn Explant 2 was -62.35 N/mm. The loss stiffness of Explant BDyn 1 – 2 had a sharp increase from 3 Hz to 4 Hz with the loss stiffness increasing from 7.70 N/mm to 35.75 N/mm. Highlighting this sharp increase in the loss stiffness is important as it is believed that this BDyn

device, with explanted components, is resonant around this frequency; between 3 and 5 Hz. Further discussion of this finding can be found in section 5.4.

Explant BDyn device 6 was the only device to have its storage stiffness within the 95% confidence interval error bars for every frequency tested (Figure 5-8 (A) and Table 5-10). Further, the storage and loss stiffness, of the explanted PCU rings, explanted silicone cushions and the BDyn device with explanted components, were within the normal and *in vitro* 95% confidence intervals at specific frequencies (Table 5-11).

Table 5-11: Stated frequencies indicate that the viscoelastic properties lies between the untreated (normal) or the in vitro degraded (in vitro) 95% confidence interval bounds.

normal	*Ex 1*	*Ex 2*	*Ex 3*	*Ex 4*	*Ex 5*	*Ex 6*
k'						
BDyn	-	-	-	-	-	0.01-29
PCU	0.01-29	0.01-29	-	-	0.01-29	0.01-10
Sil	-	0.01-29	-	0.01-29	0.01-29	-
k"						
BDyn	-	15-20	-	29	-	0.01-20
PCU	15-29	10-24	0.01-0.2, 0.4	0.01-0.1	0.01-24	0.2-15
Sil	-	0.01-0.4	0.02, 0.05-0.3, 0.5-3, 29	0.01-29	5-29	0.01-29
in vitro	*Ex 1*	*Ex 2*	*Ex 3*	*Ex 4*	*Ex 5*	*Ex 6*
k'						
BDyn	-	-	-	-	-	-
PCU	0.04-29	-	-	-	0.2-29	0.01-20
Sil	0.01-29	29	0.01-29	-	0.01-0.5, 24-29	0.01-29
k"						
BDyn	-	20, 29	-	29	-	0.01-5
PCU	-	-	0.1-4	0.2-2	4-29	15-29
Sil	0.01-29	-	0.01-29	-	-	0.01-15

5.3.4 Chemical structure (control, *in vitro* and *in vivo* degraded specimens)

The ATR-FTIR spectrum of the PCU and silicone components is illustrated in Figure 5-9 and Figure 5-10, respectively.

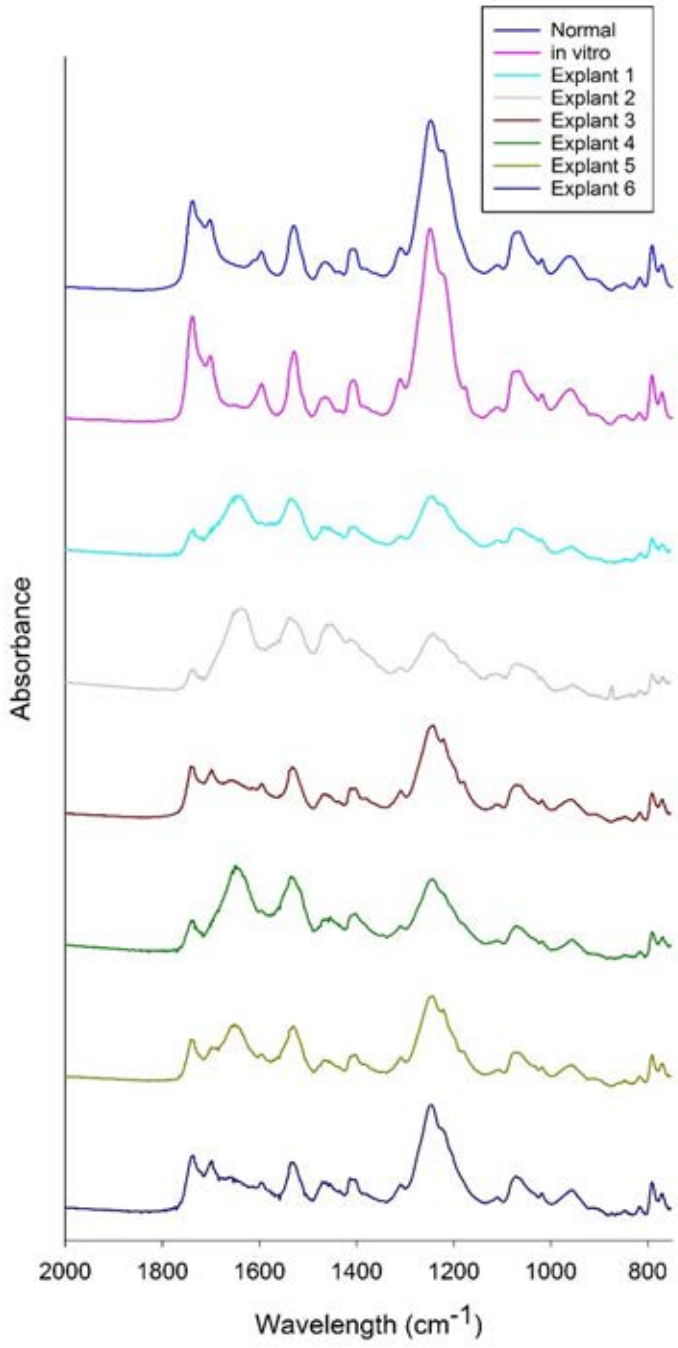

Figure 5-9: Stacked ATR-FTIR spectra of PCU control (Normal), *in vitro* oxidative degraded and six explanted components. Absorbance units are arbitrary units (AU).

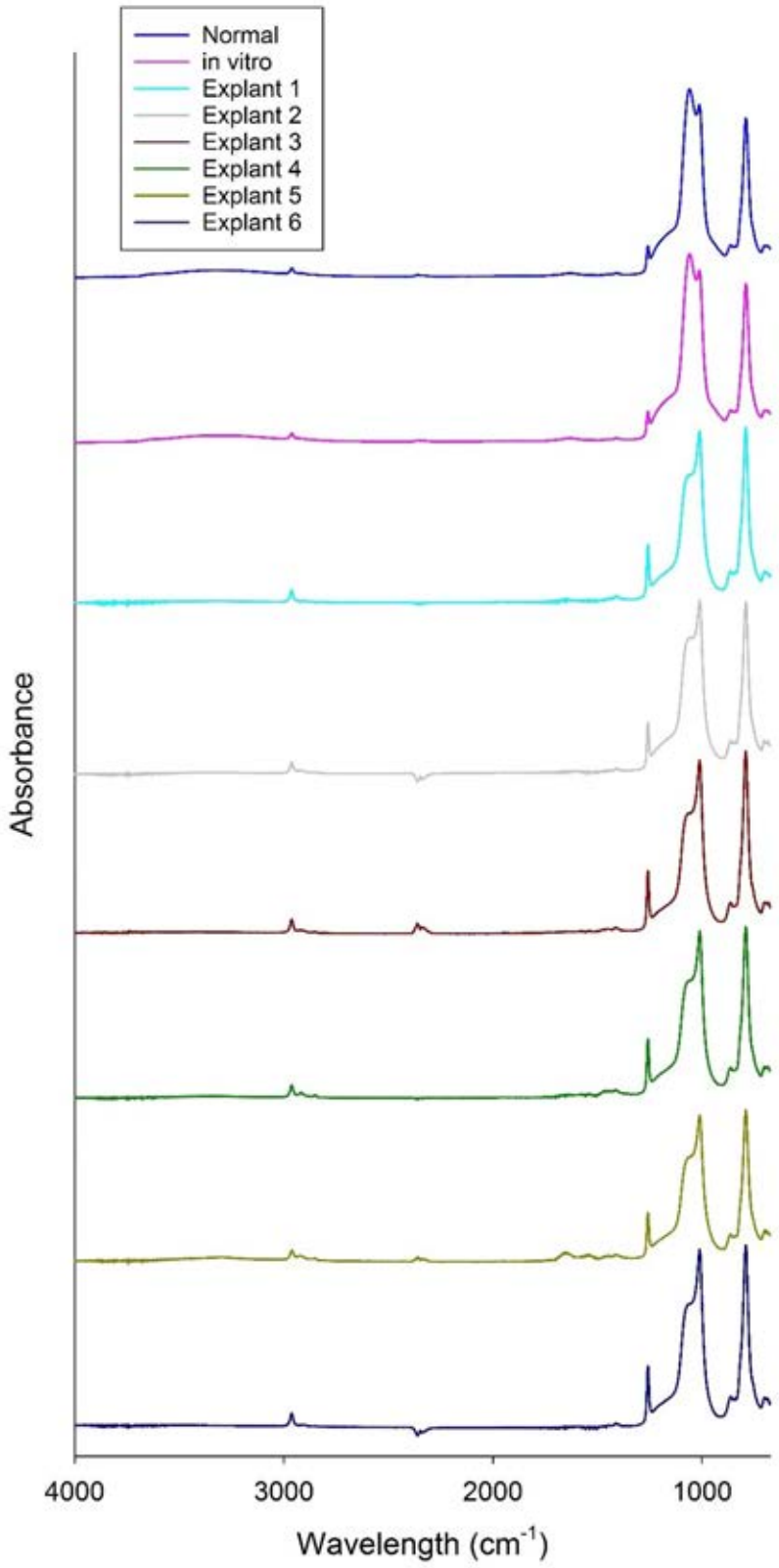

Figure 5-10: Stacked ATR-FTIR spectra of silicone control (Normal), *in vitro* oxidative degraded and six explanted components. Absorbance units are arbitrary units (AU).

Evidence of crosslinking of the PCU has been established as a new absorbance peak was observed at 1174 cm^{-1} [range: 1183 cm^{-1} to 1160 cm^{-1}] for the *in vitro* and *in vivo* degraded explants except for one explanted PCU component (Explant 6), as seen in Figure 5-9. The PCU *in vitro* and *in vivo* degraded PCU specimens also showed hard segment degradation with the presence of a new aromatic amine group at 1650 cm^{-1} [range: 1662 cm^{-1} to 1630 cm^{-1}] this hard segment degradation was more prominent for the *in vivo* degraded, explanted PCU components (Figure 5-11 (A)).

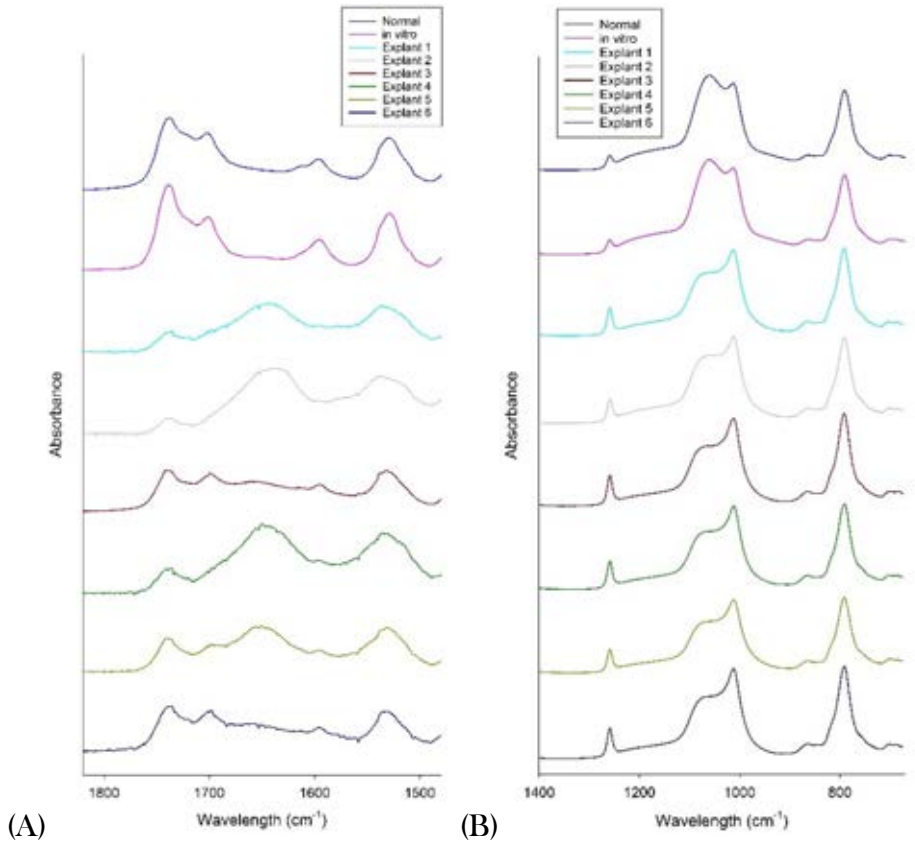

Figure 5-11: Stacked ATR-FTIR cut spectra of (A) PCU control (Normal), *in vitro* oxidative degradation and the six explanted components; cut wavelength range of 1350 cm^{-1} to 1950 cm^{-1} and (B) silicone control (Normal), *in vitro* oxidative degradation and the six explanted components; cut wavelength range of 675 cm^{-1} to 1400 cm^{-1}.

There was no evidence of changes to the chemical structure of the *in vitro* degraded silicone specimens (Figure 5-10). However, when compared to the untreated and *in vitro* degraded specimens, changes to the chemical structure of the explanted components with the reduction in the peak at 1065 cm^{-1}; this bond is associated with the Si-O-Si stretch of the silicone (Figure 5-11 (B)). Further, the explanted silicone components displayed a slight increase in peak height at 1257 cm^{-1} which is associated with the Si-CH_3 stretch of the silicone components.

Hyperspectral chemical maps demonstrated a new peak at 1650 cm^{-1} was observed regionally at one or multiple locations, on all explanted silicone components (see Figure 5-12).

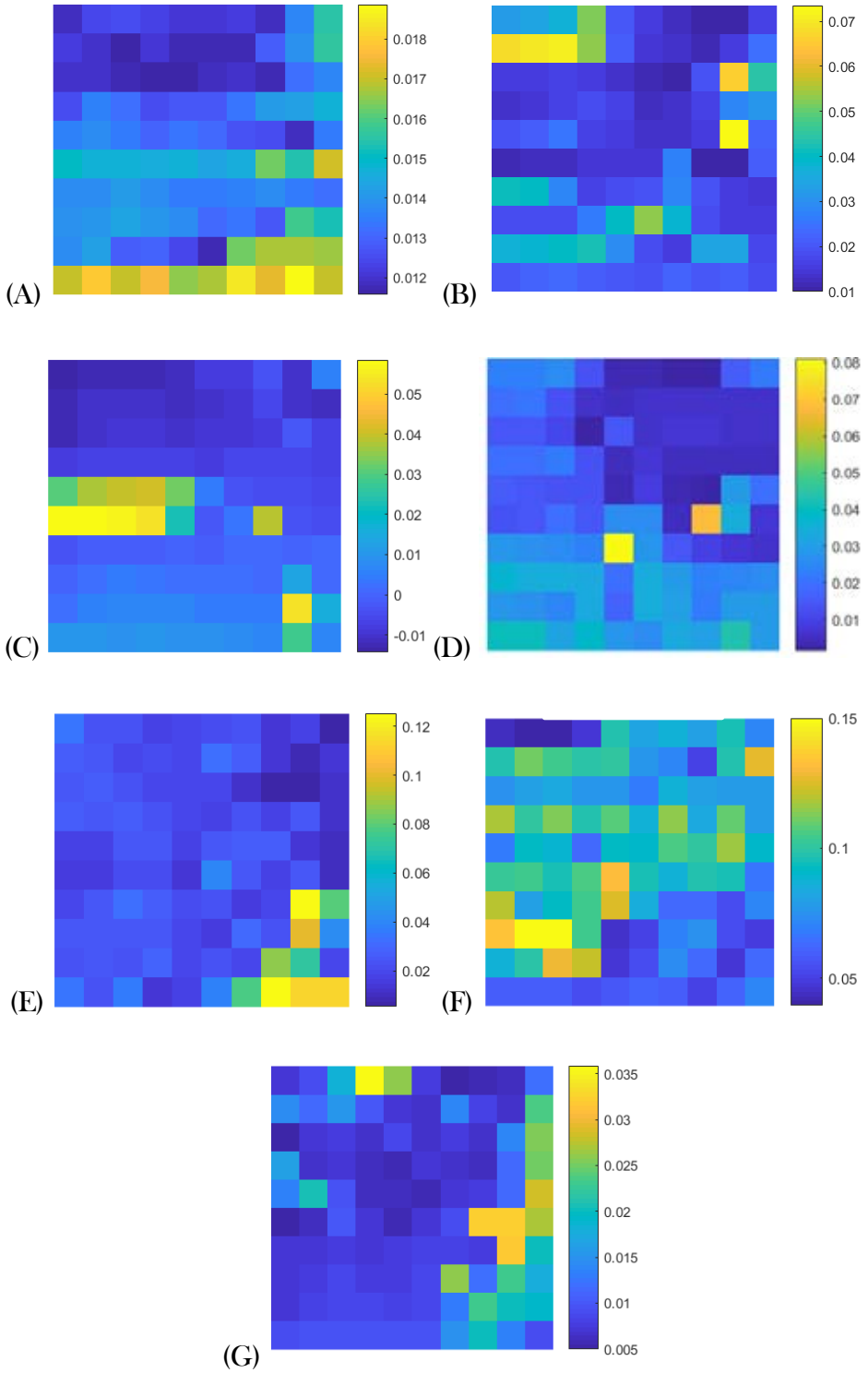

Figure 5-12: Spatial variation of the new peak witnessed at approximately 1650 cm^{-1} for the silcione components; (A) untreated, (B) Explant 1, (C) Explant 2, (D) Explant 3, (E) Explant 4, (F) Explant 5 and (G) Explant 6. The height of the 1650 cm^{-1} peak varied across the surface of the component; for the range of the peak height across the specimens; see

the scale bar at each HCM. The variation (approximate range) of the (A) untreated specimen is low (0.012-0.019 AU) compared to the explanted components with regionally high peak heights (range of (E) is approximately 0.01-0.12 AU). These are HCMs (not a continuous images) and the distance between acquisitions is 100 µm.

HCM demonstrated that the chemical structure changes at 1065 cm^{-1} (associated with the Si-O-Si stretch; see Figure 5-13) and 1257 cm^{-1} (associated with the Si-CH_3 stretch; see Figure 5-14) varied regionally across the explanted silicone components.

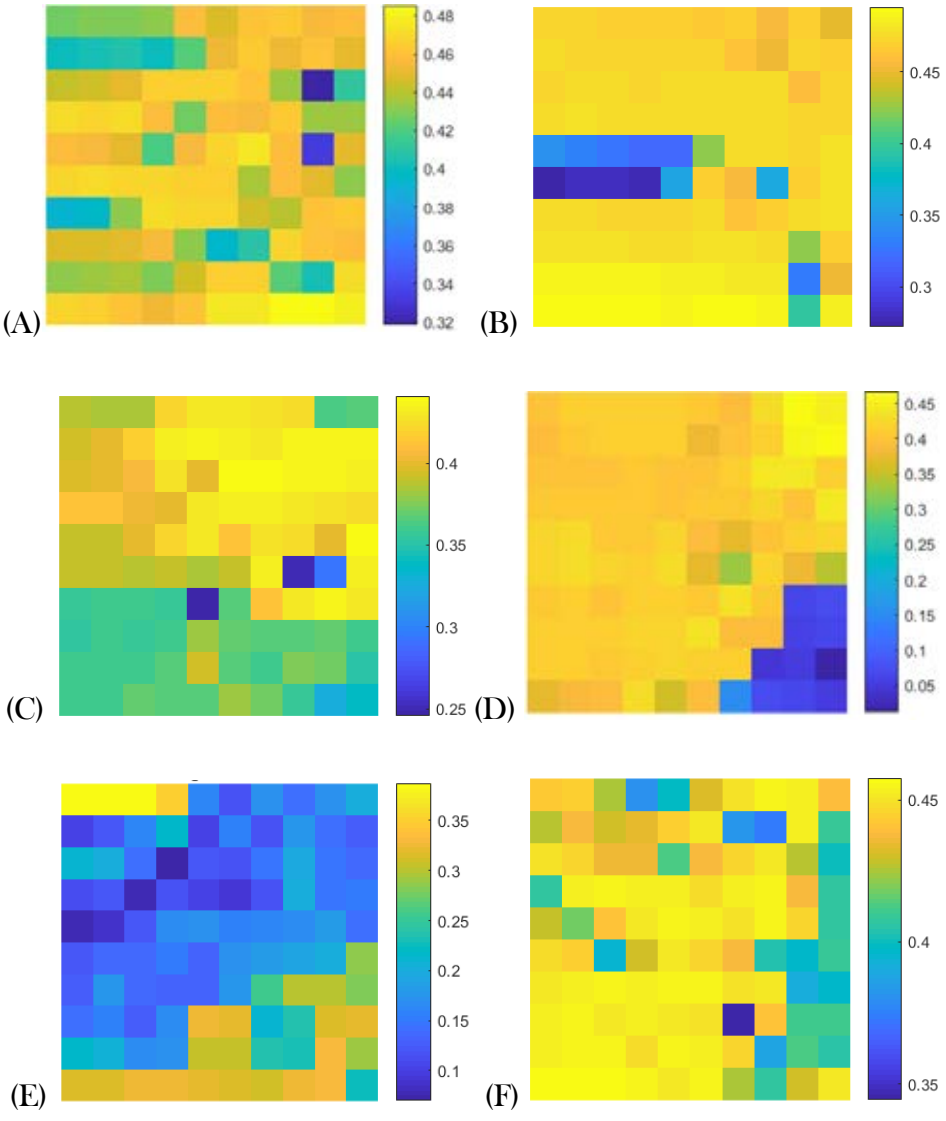

Figure 5-13: Spatial variation of 1065 cm^{-1} for the silcione components; (A) Explant 1, (B) Explant 2, (C) Explant 3, (D) Explant 4, (E) Explant 5 and (F) Explant 6. These are HCMs (not a continuous images) and the distance between acquisitions is 100 µm.

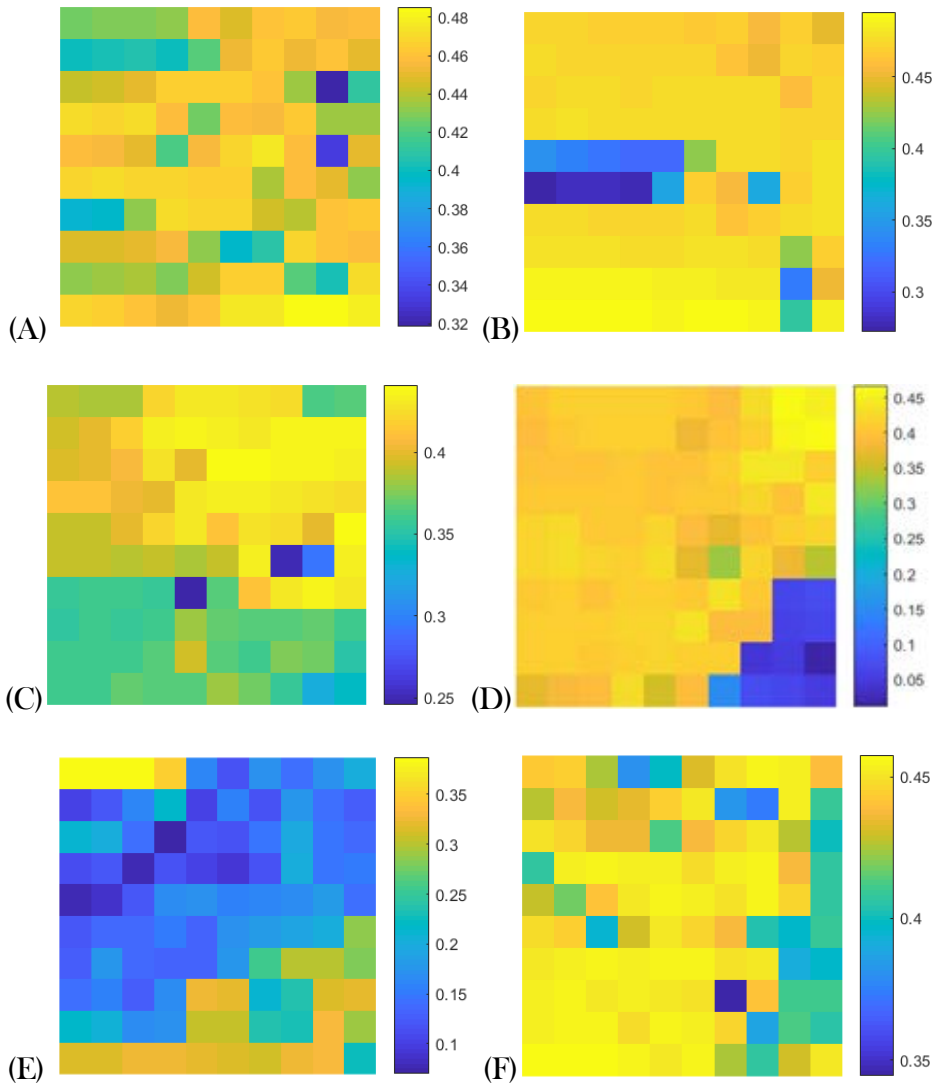

Figure 5-14: Spatial variation of 1257 cm^{-1} for the silicone components; (A) Explant 1, (B) Explant 2, (C) Explant 3, (D) Explant 4, (E) Explant 5 and (F) Explant 6. These are HCMs (not a continuous images) and the distance between acquisitions is 100 µm.

From the HCM of the *in vivo* degraded, explanted PCU rings, a decrease and a spatial variation in absorbance peak intensity at 1248 cm^{-1} [range: 1235 cm^{-1} to 1260 cm^{-1}] was observed (Figure 5-15). Further, a new absorbance peak at 1174 cm^{-1}, which provides evidence of chain scission and crosslinking of the soft segment, was detected and varied across all explanted PCU components except for Explant 6 (Figure 5-16); for Explant 6, no new peak was detected for any of the individually acquired spectra.

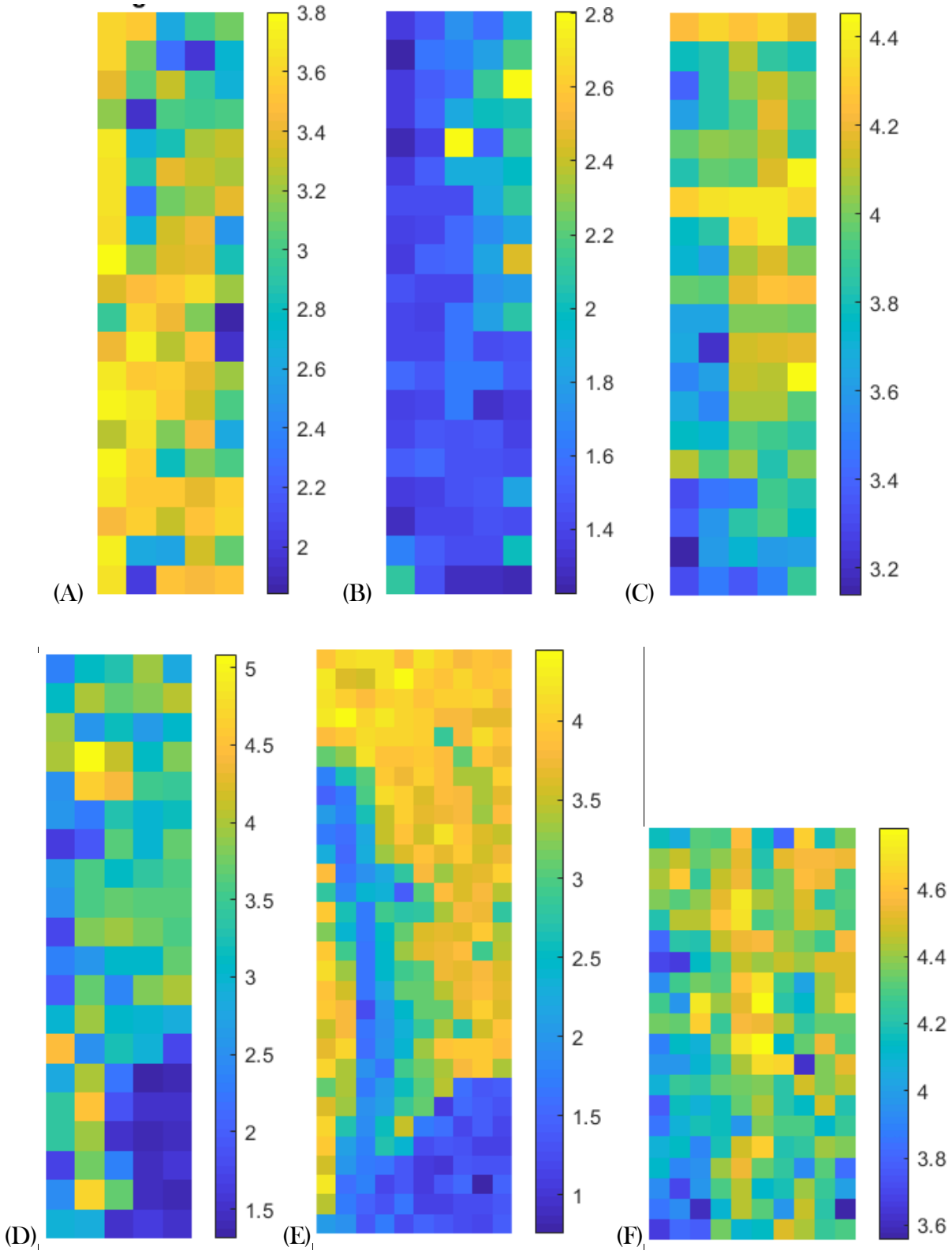

Figure 5-15: Spatial variation of 1248 cm^{-1} for the PCU components; (A) Explant 1, (B) Explant 2, (C) Explant 3, (D) Explant 4, (E) Explant 5 and (F) Explant 6. These are HCMs (not a continuous images) and the distance between acquisitions is 100 µm.

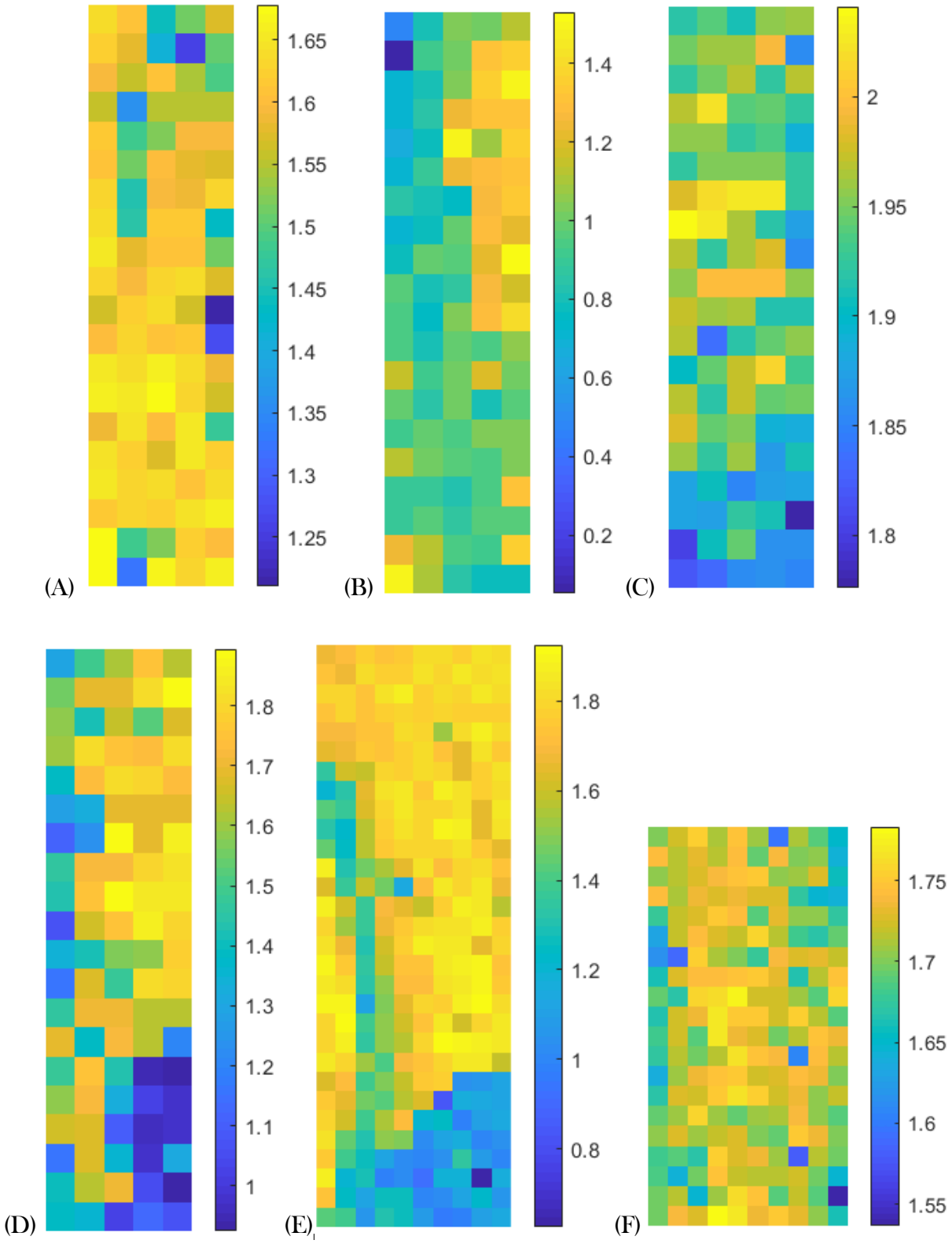

Figure 5-16: Spatial variation of 1174 cm^{-1} for the PCU components; (A) Explant 1, (B) Explant 2, (C) Explant 3, (D) Explant 4, (E) Explant 5 and (F) Explant 6. These are HCMs (not a continuous images) and the distance between acquisitions is 100 µm.

A new absorbance peak at 1650 cm^{-1}, which provides evidence of hard segment chain scission, was witnessed in all six explanted component HCMs (Figure 5-17).

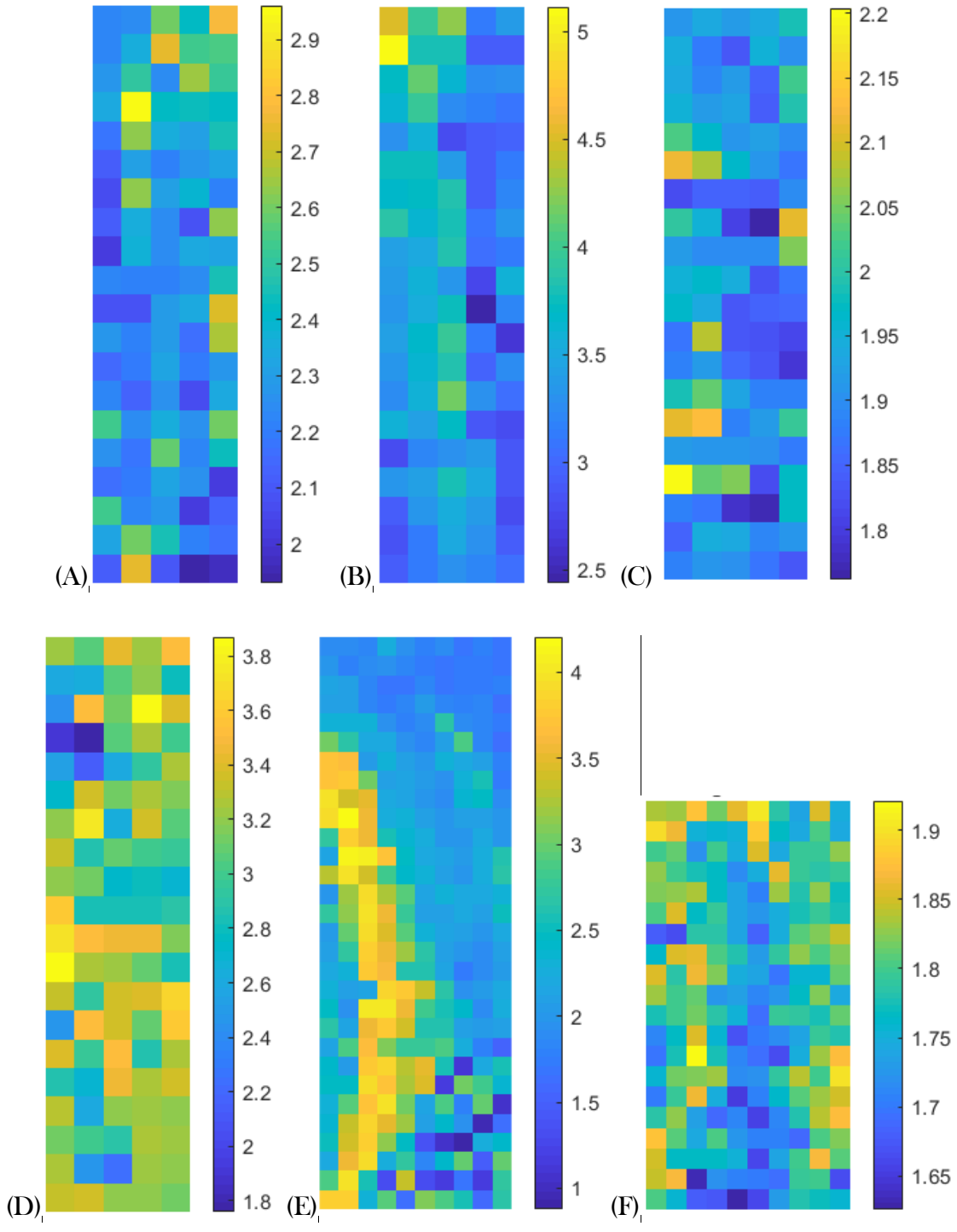

Figure 5-17: Spatial variation of 1650 cm^{-1} for the PCU components; (A) Explant 1, (B) Explant 2, (C) Explant 3, (D) Explant 4, (E) Explant 5 and (F) Explant 6. These are HCMs (not a continuous images) and the distance between acquisitions is 100 µm.

A new absorbance peak at 1650 cm^{-1} was witnessed in one specific acquisition of the untreated PCU component HCM; see Figure 5-18 (A) for the isolated, higher intensity (bright yellow) pixel in the HCM (pixel position 2(x) and 2(y); highlighted with a red box) and (B) for the chemical ATR-FTIR spectra of this specific pixel and a more common spectrum from the untreated specimen (pixel position; 7(x) and 10(y); highlighted with a black box).

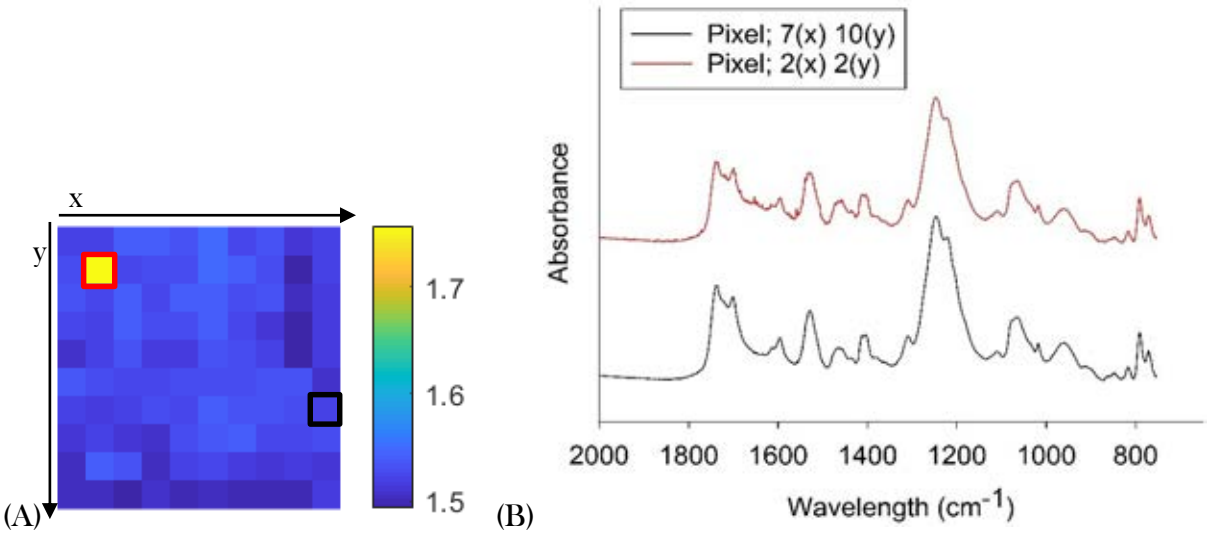

Figure 5-18: (A) Untreated (control) PCU specimen HCM at 1650 cm^{-1}. On the HCM (A), at one specific point, a new 1650 cm^{-1} peak has been identified. This specific point (yellow pixel with a red box around it; pixel position 2(x) and 2(y)). (B) is the chemical structure spectra of the one specific point (pixel position 2(x) and 2(y)) and another, more common, spectra (pixel with a black box around it; pixel position 7(x) and 10(y)) witnessed on the surface of the untreated PCU specimen. The PCU specimen is a HCM (not a continuous images) and the distance between acquisitions is 100 µm.

5.3.5 Surface morphological (control, *in vitro* and *in vivo* degraded specimens)

Representative SEM images of the surface morphology of the PCU and silicone components are shown in Figure 5-19 and Figure 5-20, respectively. The PCU specimens degraded for 24 days, with the 20% H_2O_2/0.1 *M* $CoCl_2$ method, demonstrated surface pitting. The major diameter of these surface pits ranged from 0.65 μm to 4.58 μm. For the *in vitro* degraded silicone specimens, there was no evidence of surface pitting, or any other surface morphology changes, with when compared to the untreated silicone specimens (Figure 5-20).

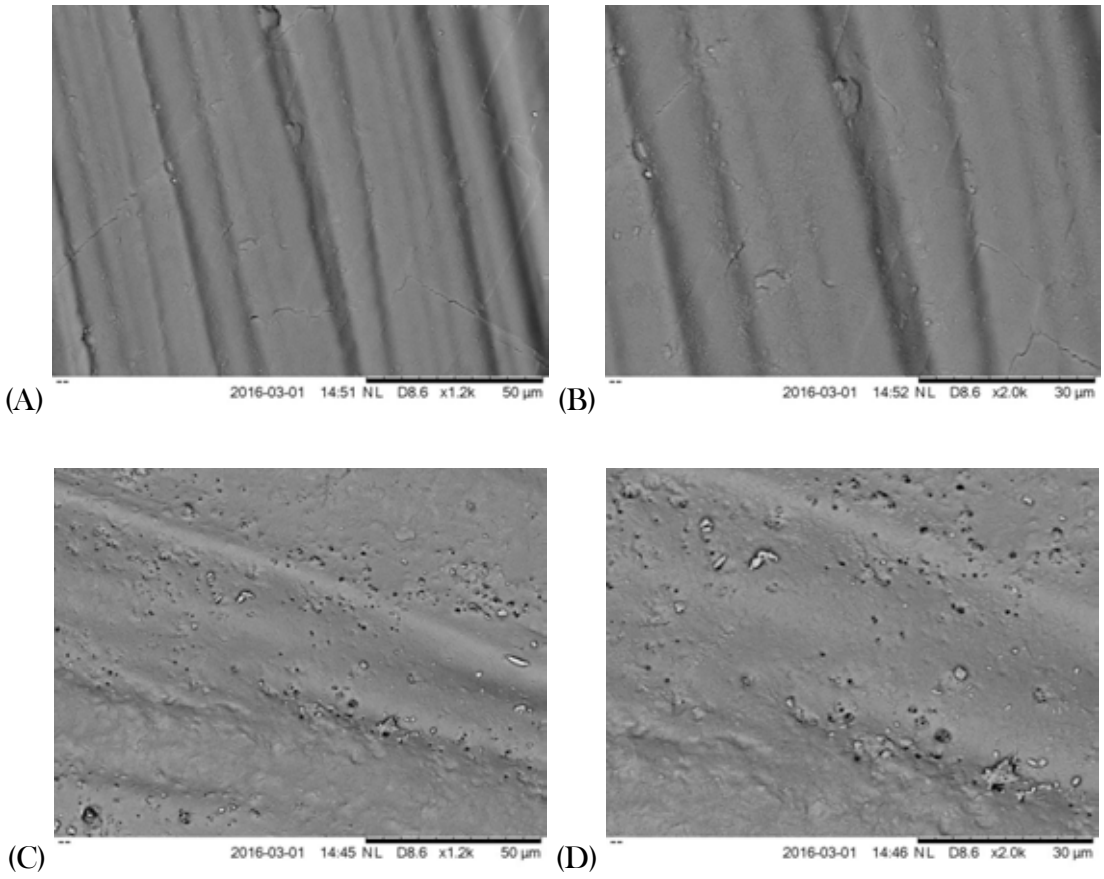

Figure 5-19: Scanning electron micrographs of Bionate II 80A PCU rings at (A & C) x1.2k and (B & D) x2.0k. (A & B) Untreated and (C & D) treated with 20% H_2O_2/0.1*M* $CoCl_2$ at 37°C.

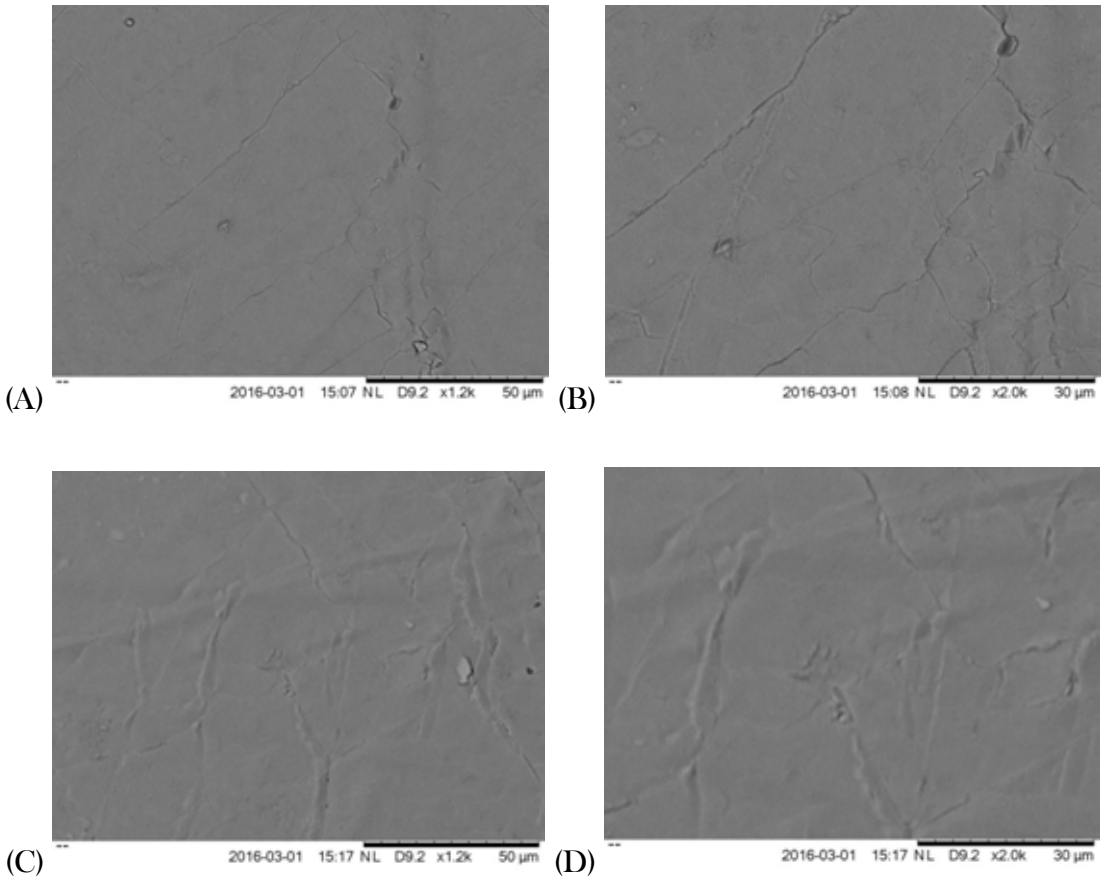

Figure 5-20: Scanning electron micrographs of MED 4770 silicone cushion at (A & C) x1.2k and (B & D) x2.0k. (A & B) Untreated and (C & D) treated with 20% H_2O_2/0.1M $CoCl_2$ at 37°C.

Figure 5-21 and Figure 5-22 show the surface morphology of the explanted PCU rings and silicone cushions, respectively. All explanted PCU rings and silicone components demonstrated micro-level surface morphological changes. The PCU rings explanted from Patient 1 (Explant BDyn 1 and Explant BDyn 2) both had partial tears close to the inner radius of the annulus (Figure 5-21 (B)). Environmental stress cracks (ESC) were witnessed on the surface of all six PCU rings, with the PCU ring from Explant 5 having the least, and pockets of surface pits were witnessed on specific areas of all six PCU rings; pits measured ranged between 0.26 µm to 8.34 µm. The surface morphological changes on the PCU varied per specimen which is demonstrated with Figure 5-21 (H) and Figure 5-21 (I); both images are from the same specimen (PCU 5) but the pitting and ESC is in a localised area and not across the whole surface.

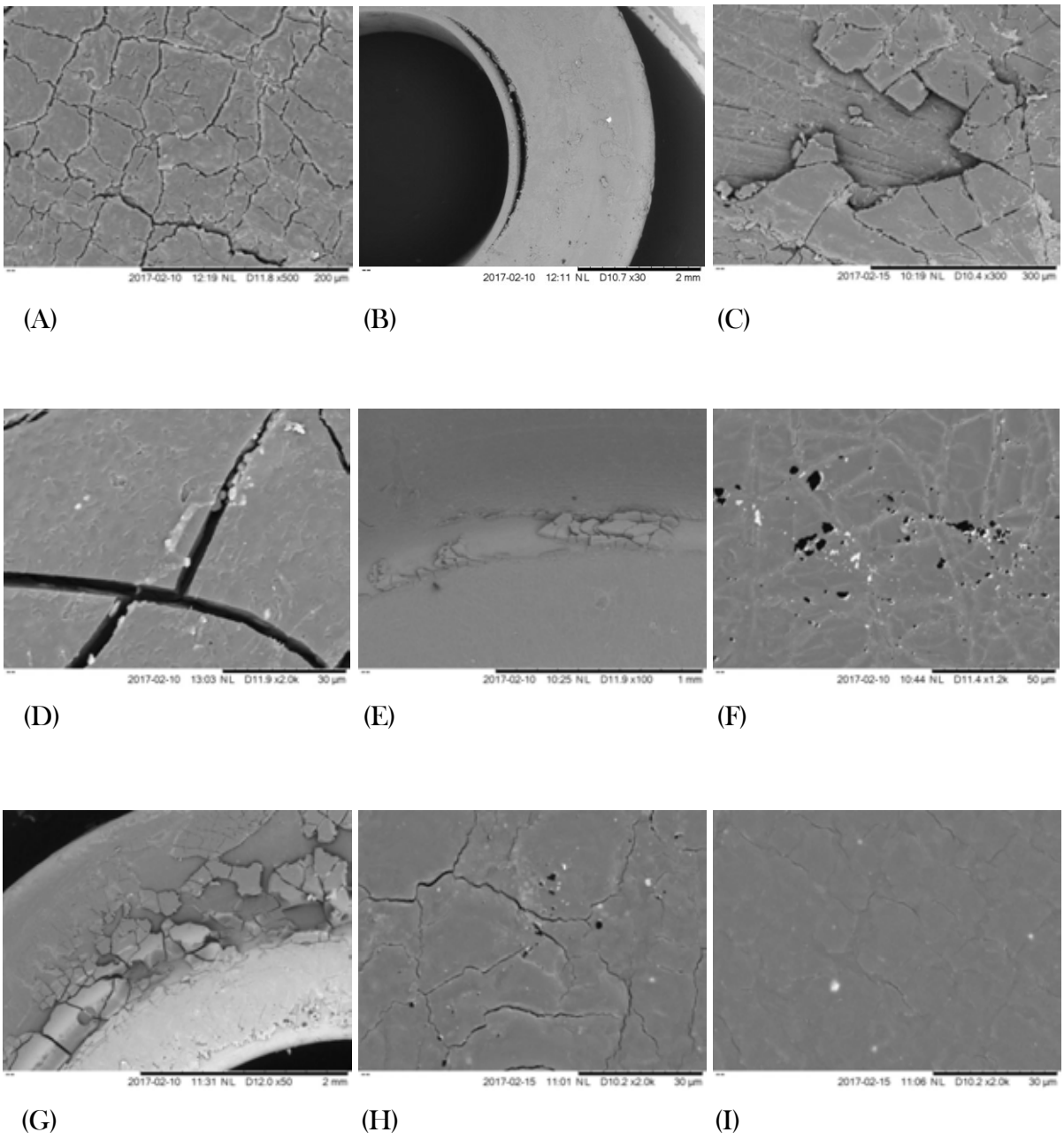

Figure 5-21: (A) Environment Stress Cracking (ESC) of PCU 1; (B) Circumferential partial tear near the inner radius of the PCU annulus [PCU 1]; (C) De-laminated (gouged) area of PCU 2; (D) Environment Stress Cracking (ESC) of PCU 2 (E) Abrasion (gouging) track [PCU 3]; (F) Pitting on exposed area of PCU 3; (G) Delamination (flaking) and plastic deformation [PCU 4]; (H) Isolated pitting and ESC [PCU 5]; (I) minimal-to-little surface deformation [PCU 5].

Similarly to the PCU rings, the silicone cushions illustrated a wide variety of surface morphological changes from abrasive wear track (Figure 5-22 (A)), gouged areas (Figure 5-22 (B)) to minimal surface morphological changes (Figure 5-22 (E)). Various levels of ESC were witnessed on the surface of all six specimens while adhesive surface morphological changes, similar to (D) and (I), was witnessed in 2 out of 6 explants.

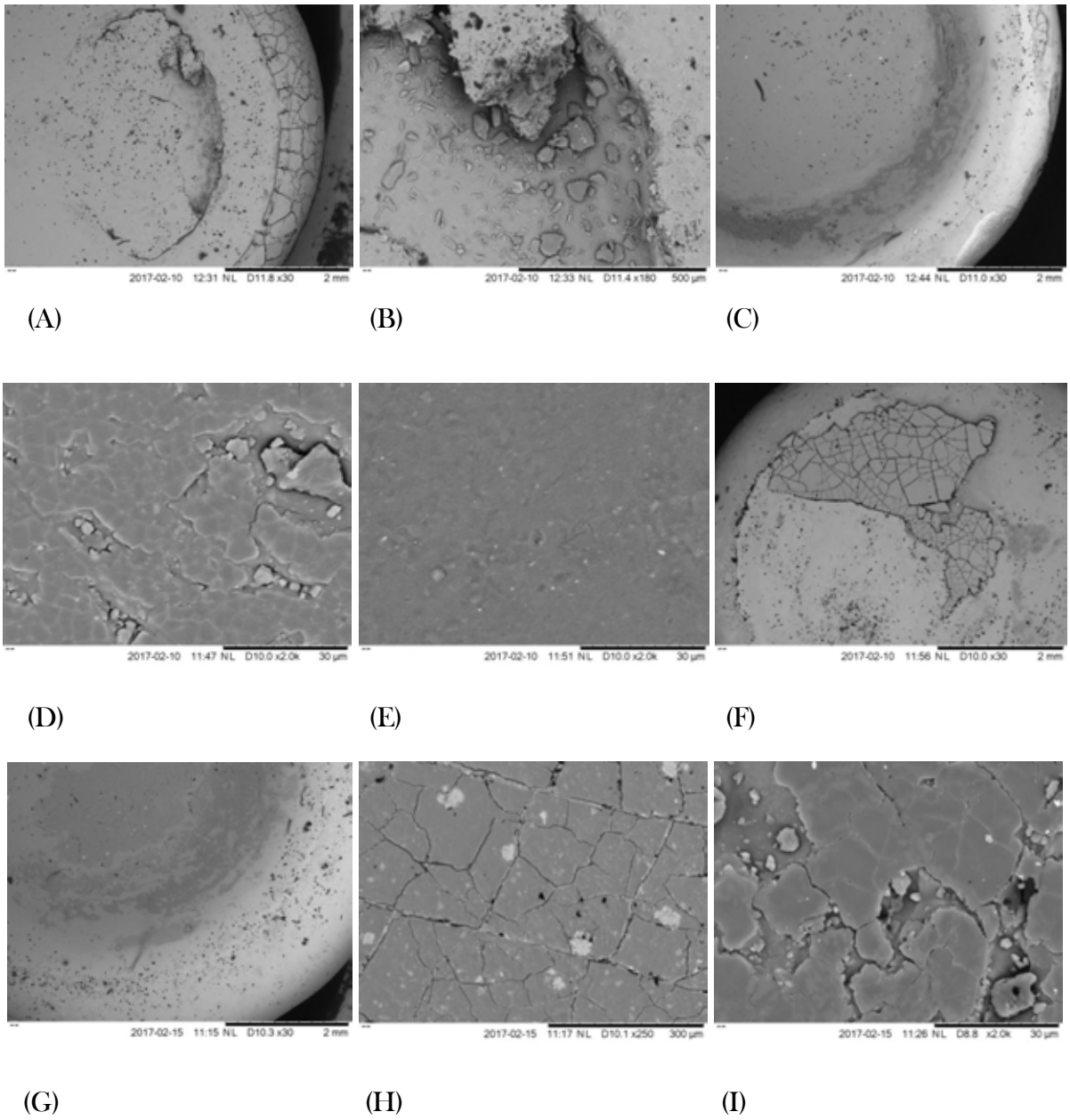

(A) (B) (C)

(D) (E) (F)

(G) (H) (I)

Figure 5-22: (A) Abrasive edge shearing and gouged area of Sil 1; (B) Gouged area of Sil 1; (C) Creep depression of Sil 2; (D) Adhesive surface damage [Sil 3]; (E) little-to-no surface morphological changes [Sil 3]; (F) ESC [Sil 4]; (G) Creep depression [Sil 5] (H) ESC on the base of Sil 5; (I) Adhesive surface damage [Sil 6]

5.4 Discussion

Firstly, this chapter has quantified the frequency dependent viscoelastic properties of a posterior dynamic stabilisation (PDS) spinal implant. The BDyn devices and its components were viscoelastic throughout the frequency range tested. As shown in Figure 5-3, the BDyn 1 level device storage stiffness (95.56 N/mm to 119.29 N/mm) and the loss stiffness (10.72 N/mm to 23.42 N/mm). Within the physiological frequency range tested, the elastic property of the BDyn device is influenced by the PCU ring and the silicone cushion for every frequency. However, the viscous response of the BDyn device is influenced by the PCU ring for every frequency and only at a specific frequency by the silicone cushion; the silicone cushion was significantly different at 0.01 to 0.2, 0.4, 0.75 and 1 Hz ($p < 0.05$).

Secondly, this chapter has quantified the frequency-dependent viscoelastic properties of a posterior dynamic stabilisation device with *in vitro* oxidative degraded components. Similarly to the untreated components and BDyn device, the degraded components and BDyn device, assembled with degraded components, were viscoelastic throughout the frequency range tested. The degraded BDyn 1 level device storage stiffness (84.46 N/mm to 99.36 N/mm) and loss stiffness (8.13 N/mm to 21.99 N/mm) were less than the storage stiffness (95.56 N/mm to 119.29 N/mm) and loss stiffness (10.72 N/mm to 23.42 N/mm) for the normal BDyn 1 level device. However, the reductions in viscoelastic properties of the PCU ring (Bionate II 80A) and silicone cushion components, due to the *in vitro* degradation process, are significantly different for specific frequencies ($p < 0.05$; Table 5-9). The same PCU biomaterial (Bionate II 80A) was evaluated by the same *in vitro* degradation process ($H_2O_2/CoCl_2$) for ASTM D1708 specimens in Chapter 4 (Table 4-17). The micro (μDMA with an indenter) and macro (tension) viscoelastic properties of Bionate II 80A were not significantly different for any frequency when comparing the untreated to the $H_2O_2/CoCl_2$ degradation method. This demonstrates the importance of understanding the viscoelastic properties of specimens and implantable components in relation to frequency.

As *in vitro* testing can only give a certain amount of insight into the degradation of an orthopaedic device or its components, there was a need to assess the viscoelastic, chemical composition and surface morphological changes, of the BDyn device, from implantation in the body environment. Thirdly, a retrieval analysis of six BDyn posterior dynamic stabilisation devices (from three patients) was presented in this chapter. The range of the approximate implantation was 6-21 months (an average time of 14.67 ± 7.77 months). A wide variability of

the explanted PCU and silicone components storage and loss stiffness existed. At specific frequencies, the storage and loss stiffness, of the explanted PCU rings, explanted silicone cushions and the BDyn device with explanted components, were within the normal and *in vitro* 95% confidence intervals (Table 5-11). This finding further demonstrated the importance of analysing the changes of viscoelasticity of specimens over a frequency sweep.

The viscoelastic properties of intervertebral disc replacement devices have been quantified with frequency sweeps (Dahl et al., 2011; Gloria et al., 2011; van den Broek et al., 2012a). As shown in Figure 5-3, the BDyn 1 level device storage stiffness (95.56 N/mm to 119.29 N/mm) and the loss stiffness (10.72 N/mm to 23.42 N/mm) were less than the storage stiffness (541.7 N/mm to 957 N/mm) and loss stiffness (approximately 62 N/mm to 200 N/mm) of a multi-structural intervertebral disc (IVD) replacement device (Gloria et al., 2011). Depending on the degenerated state of the IVD, the transfer of load through the posterior elements can range from 8% to 40% (Pollintine et al., 2004). With less than 10% of the net compressive load transferred through the posterior elements of a healthy IVD (Kurtz and Edidin, 2006; Pollintine et al., 2004), the differences between the BDyn PDS implant and IVD replacement storage stiffness and loss stiffness ranges were expected. Furthermore, Gloria et al. (2011) applied 40 N ± 10 N sinusoidal load through a frequency range of 0.01 Hz to 30 Hz.

The BDyn 1 level dynamic stiffness ranged from 96.16 N/mm (0.01 Hz) to 120.02 N/mm (29 Hz) while the BDyn 2 level device ranged from 39.66 N/mm (0.01 Hz) to 42.44 N/mm (29 Hz). These values are comparable to the dynamic stiffness of a polyurethane nucleus device (216.24 N/mm–285.47 N/mm; 0.25 Hz–20 Hz), but an order of magnitude less stiff than polyethylene and titanium-alloy cervical disc replacements (Dahl et al., 2011). The dynamic stiffness for the AxioMed Freedom Lumbar device, tested between 1200 N to 2000 N at 3 Hz by Benzel et al. (2011), varied between 1.55 – 3.48 kN/mm. Rischke et al. (2011) stated that a previous study of the AxioMed Freedom device showed that the response of the polymer core did not change between 1 Hz and 3 Hz, but at 4 Hz, or higher, the core temperature increased and the polymer response decreased. Van der Broek et al. (2012a) demonstrated that the Biomimetic Artificial Intervertebral Disc axial dynamic stiffness, for 0.01 Hz to 10 Hz range, was between 3.0 kN/mm to 4.7 kN/mm; this range was within the standard deviation range of the natural intervertebral disc tested by Smeathers and Joanes (1988). Alongside the variation in material properties, the differences between the dynamic stiffness of the intervertebral disc replacement studies (Benzel et al., 2011; Dahl et al., 2011; van den Broek et al., 2012a) and the present study are also a result of testing differences.

Another issue with comparison of dynamic stiffness stated from different studies is that various authors calculate the dynamic stiffness by using different techniques. Dahl et al. (2011) determined the dynamic stiffness by calculating the best-fit slope of the force-displacement curve while, Benzel et al. (2011) calculated the force/displacement for the first 1,000 cycles, at 3 Hz. This present study calculated the viscoelastic properties by following ISO 6721 (ISO, 2011). As the dynamic stiffness can be affected by load (Kasra et al., 1992), any comparison between different methods and studies must be made with caution. To characterise the dynamic viscoelastic properties (storage and loss stiffness) of a structure, one must acquire the dynamic stiffness (k^*) and the phase angle (δ) between the force and displacement sinusoidal cycle. If δ is not reported with k^*, then the dynamic viscoelastic behaviour of a structure cannot be ascertained. Some studies (Dahl et al., 2011; LeHuec et al., 2003) have examined the damping effect of disc replacement spinal implants. Both Dahl et al. (2011) and LeHuec et al. (2003) calculated the transmissibility damping ratio (ζ), but not the loss factor (η), to determine the viscous dissipation of disc replacement implants. As the BDyn devices possess multiple degrees of freedom and are non-linear in behaviour, an approximate comparison to ζ was not performed as the damping ratio is defined on the grounds of the linear single degree of freedom viscous model (Carfagni et al., 1998). Even though an approximate η can be determined from ζ, to fully characterise the viscoelastic properties of a structure or a material, both the storage and loss stiffness (or modulus for a material) should be quantified.

The retrieval analysis section of this chapter analysed six explanted BDyn posterior dynamic stabilisation devices from three patients. Failure of an implant may involve a variety of factors which includes patient, surgeon and implant related (Kurtz et al., 2009). Natural variability in the human environment, biomechanical loading differences, physicians' implantation and explantation may cause damage to an explanted device (Wilkoff et al., 2015). Thus, it is difficult to definitively state what has affected the explanted BDyn devices. However, hereafter, the author makes hypotheses on the failure of the devices.

As the average implantation time is 14.67 months, it is believed that the reasons for the explanation were not due to infectious reasons. This average implantation time is close to the implantation mean average (19.91 months) for non-infection complications with the Dynesys device (Lutz et al., 2012); the mean average implantation time for infection complications was 43.25 months (Lutz et al., 2012). However, one patient had an infectious complication, requiring material removal, 2 months post-operation while another patient had a wound infection after 1 month (Lutz et al., 2012).

For Patient 1 (Explant 1 and Explant 2), the surgical construction used was asymmetrical with three pedicle screws on one side (Explant 1) of the spinous process and four pedicle screws on the other side (Explant 2). The authors do not know what the purpose of this construct was but from this construct, it seems that there may have been an applied bending moment or an asymmetrical distribution of load through the bilateral system. This may have led to high level of load being applied to the silicone cushion of Explant 2 and this creep may have plastically deformed the silicone cushion (see Figure 5-6 (B) and Figure 5-23). To investigate this hypothesis further, an investigation of this asymmetrical pedicle screw construct, using ISO 12189 or ASTM F1717, is required.

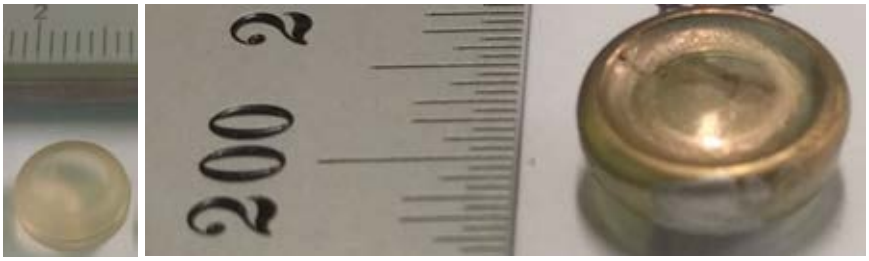

Figure 5-23: (Left) Silcone cushion untreated and (Right) Explant 2 silicone cushion from Patient 1. The Explant 2 silicone cushion image (Right) was taken after SEM hence, the gold coating on the silicone cushion.

The plastic deformation of Explant 3 and 4 PCU ring suggests that the device was under tension within the patient and the deformation, of the PCU rings, were potentially caused by creep. The abnormal application of the load due to the tension of the system may have further led to the screw breakage complication; this is further evident as the caudal-most screw fractured. On the top side of Explant 3 (see Figure 5-6 (C) and Figure 5-24 (A)) and Explant 4 (see Figure 5-6 (D)), the inner section, close to the inner radius of the PCU annuli, have extruded through the gap at the top of the titanium housing. Further evidence of this tension of the mobile rod is apparent on the underside of the PCU ring as an imprint is visible (Figure 5-24).

(A)  (B) 

Figure 5-24: (A) Explant 3 top side and (B) Explant 3 underside. Evidence of the creep tension of the BDyn device (compression of the PCU ring) by the extrusion of the PCU ring with (A) the imprint of the titanium housing on the topside of the PCU ring and (B) the imprint of the mobile rod on the underside of the PCU ring.

Unlike Explants 3 and 4, where the deformation seems consistent with each other, the plastic deformation of Explant 5 and Explant 6 (from Patient 3) components varied. The inner annulus PCU ring of Explant 5 has warped to an elliptical shape which was potentially due to an angulation of the titanium alloy mobile rod (Figure 5-6 (E)). Further evidence of this is witnessed in the plastic deformation of the silicone cushion of Explant 5. This angulation of the bilateral system may also be the reason why the PCU ring of Explant 6 has been compressed on one side of the PCU annulus (see Figure 5-6 (E) and Figure 5-6 (F)). Unfortunately, no information of the cause of the removal, of the BDyn devices from Patient 3, is available.

All six PCU rings and six silicone cushions displayed some form of macroscopic (Figure 5-6) or microscopic (Figure 5-19 and Figure 5-20) surface morphological changes. Plastic deformation (Cipriani et al., 2013; Ianuzzi et al., 2010; Neukamp et al., 2015) and microscopic surface damage (Neukamp et al., 2015; Trommsdorff et al., 2004b) of explanted devices are not uncommon. Explanted Dynesys PCU spacers have demonstrated imprints from the articulating pedicle screw and polyethylene-terephthalate (PET) cord (Cipriani et al., 2013; Ianuzzi et al., 2010; Neukamp et al., 2015; Shen et al., 2011). Interestingly, the two PCU rings from Patient 1 had deep circumferential partial cracks near the inner radius of the PCU annulus; these were discovered with scanning electron microscopy. A previous study of explanted Dynesys PCU spacers revealed that two of the PCU spacers had cracks, one of which extended from the centre of the PCU spacer to the outer surface (Ianuzzi et al., 2010). Further, a recent study discovered that higher loading frequencies of PCU biomaterials in tension resulted in the formation of multiple crack tips, variable crack growth rate and out of plane crack growth (Ford et al., 2018). This further demonstrates the importance of understanding these viscoelastic biomaterials in relation to frequency.

It has been previously noted that explanted Dynesys PCU spacers had mild scratches (Cipriani et al., 2013; Neukamp et al., 2015; Shen et al., 2011), potentially from the removal procedures (Cipriani et al., 2013; Shen et al., 2011), and also, abrasive wear zones likely from impingement with surrounding bony structures (Cipriani et al., 2013; Ianuzzi et al., 2010; Neukamp et al., 2015). In this present work, none of the deformation of the PCU rings or silicone cushions is attributed to bony structure interaction as the PCU ring and silicone cushion are encased in a titanium alloy housing (Figure 2-15). However, the deformation of the PCU rings and silicone cushions has been attributed to interactions with the BDyn titanium housing and/or the mobile rod. Neukamp et al. (2015) discovered that the Dynesys PCU spacers with abrasive wear zones had tissue with either isolated or extensive inflammation and wear debris. It would be beneficial for future BDyn retrieval studies to examine periprosthetic tissue samples for wear debris and inflammation; this would give an understanding of the benefits of the BDyn titanium housing as a protection barrier between the tissue and the elastomeric components.

The mean storage stiffness trends of the normal and *in vitro* degraded BDyn components and the BDyn devices, assembled with normal or *in vitro* degraded components, all followed a logarithmic increasing trend with frequency ($p < 0.05$; Table 5-8). Further, the storage stiffness of the explanted BDyn device components (PCU ring and silicone cushion were logarithmically frequency-dependent ($p < 0.001$; Table 5-10). This is deemed a positive result for the BDyn device and its components as the elastic (storage) property of various spinal structures has been widely documented to increase as the frequency increases (Gadd and Shepherd, 2011; Holmes and Hukins, 1996; Izambert et al., 2003; Zhou et al., 2014). Discrete Fourier Transforms of load-relaxation curves demonstrated that the storage modulus of the human lumbar spine increased with frequency (Holmes and Hukins, 1996). Between 0.01 Hz to 10 Hz, Smeathers and Joanes (1988) reported that the stiffness of the intervertebral disc increased as the loading rate increased; Izambert et al. (2003) also reported that the axial dynamic stiffness, of the intervertebral disc, increased between 10 Hz – 30 Hz. By performing DMA on intact and denucleated intervertebral discs, Gadd and Shepherd (2011) reported an increasing logarithmic trend for the storage stiffness for intact and denucleated IVD, while Zhou et al. (2014) stated a significantly increasing storage moduli of intact, denucleated and hydrogel injected porcine intervertebral discs.

The low range of standard deviation (Table 5-6), the minimal logarithmic slope coefficients (coefficient *A*; Table 5-5) and the varied R^2 values (Table 5-5) raise questions regarding the BDyn 2 level device storage stiffness logarithmic trends. This minimal increase in storage

stiffness with frequency was unexpected as the elastomer components of the device exhibit a logarithmically increasing trend. It is speculated that the minimal storage stiffness increase of the BDyn 2 level device is due to the testing configuration. With the BDyn 2 level device, a mobile rod is located between four elastomeric components. The BDyn 1 level and 2 level DMA testing configuration stated here is not similar to the *in vivo* scenario. By securing the BDyn device to the vertebra, an applied load to the device may not displace the two polymer systems equally; hence, the difference in displacement will affect the dynamic stiffness *(k*)* and in turn, the storage *(k')* and loss *(k")* stiffness. However, viscoelastic data described in this thesis could be used to validate a BDyn finite element model and by incorporating a BDyn FE model with the Lumbar Model Generator (Lavecchia et al., 2018), the effect of BDyn on the lumbar spine could be assessed.

The loss stiffness trends of the normal, *in vitro* and *in vivo* degraded BDyn components and BDyn devices, assembled with the respected components, all followed a logarithmically increasing trend as the frequency increased ($p < 0.05$; Table 5-5, Table 5-8 and Table 5-10). These results are different to the studies of Holmes and Hukins (1996) and Gadd and Shepherd (2011). Holmes and Hukins (1996) reported that the loss modulus decreased as the frequency increased. However, similar to the storage stiffness trends, the *in vitro* degradation did not affect the frequency-dependant behaviour when compared to the untreated components or BDyn 1 level device. However, the logarithmic equation coefficients *(A* and *C)* and constants *(B* and *D)* of the *in vitro* degraded specimens were lower than the normal specimens. In relation to the explanted (*in vivo* degraded) components, the *in vivo* degradation did not affect the significance of the logarithmic frequency-dependant behaviour when compared to the untreated components. However, the logarithmic trends coefficients *(A* or *C)* and constants *(B* or *D)*, of the components and BDyn 1 level device, assembled with the *in vivo* degraded components, varied for the storage and loss stiffness. Interestingly, some of the storage and loss stiffness coefficients *(A* and *C)* and constants *(B* and *D)* are similar in specific pairings and these pairs are patient specific, e.g. the coefficient *(A)* of Patient 2, the PCU Explant 3 is 2.47 N/mm while PCU Explant 4 is 2.32 N/mm (see Table 5-10 for coefficients and constants value and Figure 5-8 for plots). These pairings highlight that the changes in the viscoelastic response of the elastomeric components may be due to the specific environmental conditions that the bilateral system is exposed to.

No resonant frequencies were identified for the normal (untreated) and *in vitro* degraded BDyn 1 level devices and components. Holmes and Hukins (1996) have shown that the lumbar specimens did not exhibit shock absorbing properties in pure compression. If shock absorbing properties existed, there would be a sharp peak detected in the loss modulus in the frequency range (Holmes and Hukins, 1996). This result is similar to Gadd and Shepherd (2011) and Zhou et al. (2014) as they also did not find a peak in the loss modulus for a nucleated or de-nucleated ovine and porcine IVD, respectively. Other studies, which examined *in vitro* human intervertebral disc specimens without the posterior elements, have recorded resonant frequencies between 8 Hz – 10.4 Hz (Izambert et al., 2003), 22.2 Hz – 40.9 Hz (Marini et al., 2015) and 23.5 Hz – 33 Hz (Kasra et al., 1992). The response differences between these studies could be due to the different applied preloads and the amplitude of the oscillation (Marini et al., 2015) and the method of testing.

Unlike the normal (untreated) and *in vitro* degraded BDyn 1 level devices, a sharp peak in the loss property *(k")* was detected for the BDyn device Explant BDyn 1 level – 2 (see Explant 2 plot in Figure 5-8 (B), Figure 5-25 (B) and Figure 5-25 (C)). The BDyn device was assembled with Explant 2 PCU ring and silicone cushion (Figure 5-6 (B)). In the frequency sweep test of BDyn Explant 2, the sharp increase of the loss stiffness occurred at 4 Hz (see Figure 5-25 (C)). Alongside the sharp increase in the loss stiffness, the storage stiffness *(k')* decreased sharply and tan delta sharply increased after the increase in k" (Figure 5-25 (C); this is similar to the ideal DMA curves (see Figure 5-25 (A)).

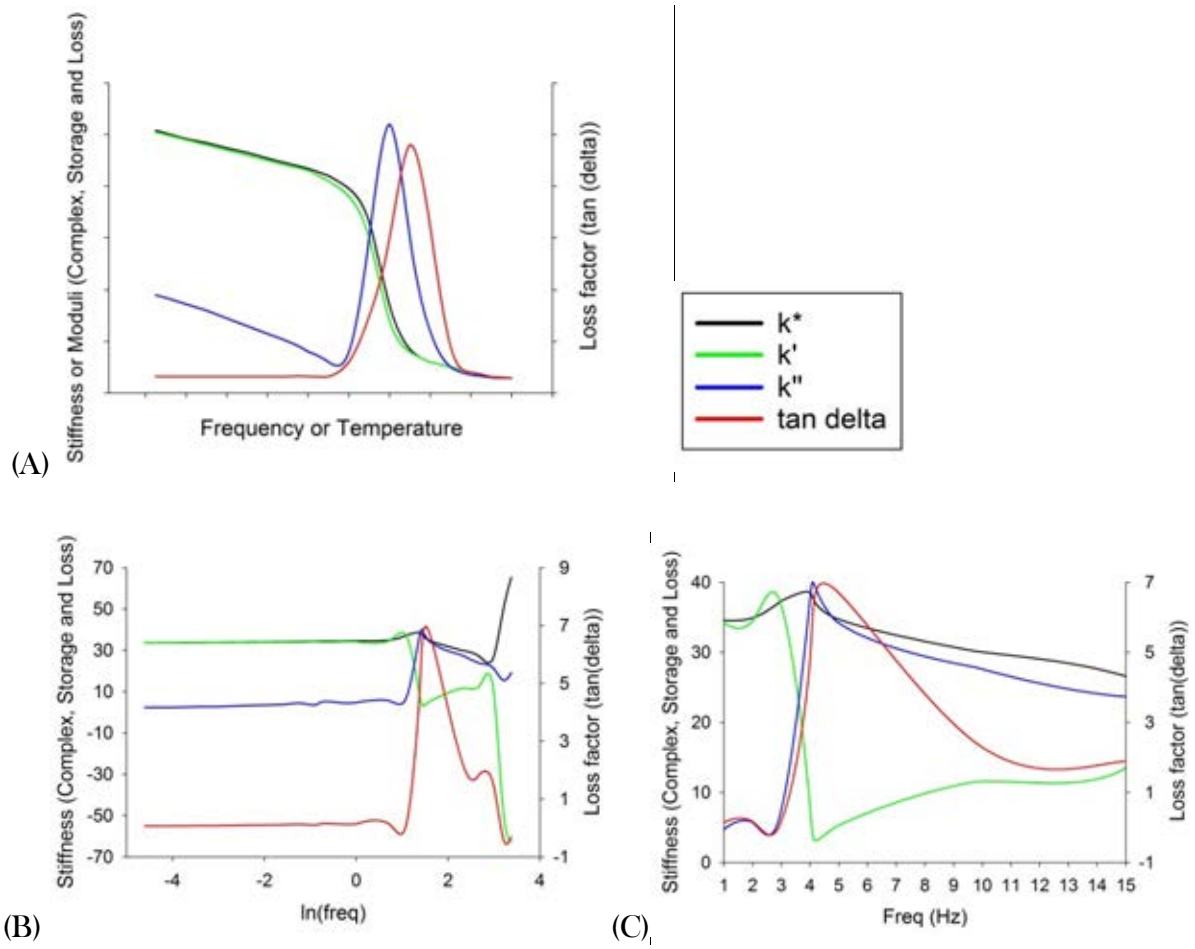

Figure 5-25: (A) Typical, ideal DMA curves for an amorphous polymer [adapted from the book Thermal Analysis of Plastics by Ehrenstein et al. (2004)], (B) BDyn Explant 2 DMA curves [complex *(k*)*, storage *(k')*, loss *(k")* stiffness and tan delta] versus ln(freq) for the full frequency range, (C) BDyn Explant 2 DMA curves [complex *(k*)*, storage *(k')*, loss *(k")* stiffness and tan delta] versus frequency (1 to 15 Hz). The curves for (C) are zoomed in to the frequency range 1 to 15 Hz to show the resonant frequency at 4 Hz.

As previously discussed in section 4.4, to overcome these resonant frequencies, changes of the specimen shape or change of the applied sinusoidal loading method are required (Menard, 2008). Unlike the discussion of resonance in section 4.4, it is believed that the resonant frequency, which occurred at 4 Hz, is due to the severely plastically deformed silicone cushion (see Figure 5-6 (B) and Figure 5-23 (Right)) and interaction of the BDyn implant between its PCU ring and plastically deformed silicone cushion. Further, no other BDyn device assembled with explanted components experienced a resonant frequency at 4 Hz, therefore, the plastic deformation of the silicone cushion, i.e. specimen shape change, and the interaction with this plastically deformed component is believed to be the cause.

The identified resonant frequency of 4 Hz, indicated by the sharp increase in the viscous property (Holmes and Hukins, 1996) is not a beneficial finding. Any resonance of the device at any frequency is a limitation of the device as the resonance may damage the device and in a worst-case scenario, the device may fail. To highlight the severity of this resonant issue, Panjabi et al. (1986) recorded the average *in vivo* lumbar vertebrae resonant frequency at 4.4 Hz for the axial direction with the person in the seated position. This resonant frequency, for the seated position, is similar to the frequencies at which Wilder et al. (1982) recorded the greatest transmissibility in the male and female lumbar spine of 4.9 Hz and 4.75 Hz, respectively. Wilder et al. (1982) also recorded two further resonant frequencies at 9.5 Hz and 12.7 Hz for both genders.

From the ATR-FTIR spectra of the *in vitro* oxidative degraded PCU rings, new absorbance peak at 1174 cm^{-1} and 1650 cm^{-1} were observed. These new absorbance peaks provided evidence of chain scission and crosslinking of the soft segment (Christenson et al., 2004a; Hernandez et al., 2008; Tanzi et al., 2000) and evidence of hard segment chain scission (Christenson et al., 2007, 2006a, 2004a), respectively. These spectrum changes are similar to previous work (Christenson et al., 2006a, 2004a); however, the new peaks observed at 1174 cm^{-1} and 1650 cm^{-1} are not as prominent as previous studies (Christenson et al., 2005, 2004a). The *in vitro* degraded PCU ATR-FTIR spectrum absorbance peaks at 1174 cm^{-1} and 1650 cm^{-1}, are similar to another study (Dempsey et al., 2014) that degraded PCU specimens with an accelerated oxidation method for 36 days. The PCU spectra in previous work were normalised to the internal reference peak which is the C=C bond stretch of the aromatic ring of the hard segment (range: 1591 cm^{-1} to 1600 cm^{-1} peak) (Christenson et al., 2006a, 2004a, 2004b; Padsalgikar et al., 2015), which has been stated to remain unchanged in degradation (Wu et al., 1992). However, such an approach is not suitable as a neighbouring peak overlaps the C=C bond stretch and consistency of its intensity cannot be assumed (Dorrepaal et al., 2018). Thus, the stable aromatic C–H out of plane bending peak was used as the internal reference peak (Dorrepaal et al., 2018).

Silicone has demonstrated excellent biostability with no identifiable *in vivo* degradation (Wilkoff et al., 2015) and due to this excellent biostability, silicone has been used to modify PEU and PCU to increase the biostability with the intention to inhibit degradation. The oxidation method, used in this study, has been previously used to analyse how degradation affects PCU/PEU (Christenson et al., 2005, 2004a; Dempsey et al., 2014; Hernandez et al., 2008; Schubert et al., 1997) and PCU/PEU modified with silicone (Christenson et al., 2005). In comparison to unmodified PEU and PCU, the percent loss of silicone-modified PEU and PCU soft-segment was less than the unmodified PEU and PCU; this may be an indication of slower rates of crosslinking due to the addition on silicone (Christenson et al., 2005). The $H_2O_2/CoCl_2$ *in vitro* method has been shown to reproduce chemical and physical degradation similar to *in vivo* oxidative degradation of PEU and PCU (Christenson et al., 2006a), but not for silicone. It was expected that there would be no significant change in the viscoelastic properties of the silicone cushion, by using this $H_2O_2/CoCl_2$ degradation method. However, the storage and loss stiffness of the treated silicone component was significantly different, for every frequency tested, when compared to viscoelastic properties before degradation (Table 5-9). That said, there were no changes evident in the ATR-FTIR spectra of the *in vitro* degraded silicone component (Figure 5-10) and unlike the PCU ring, no pitting or surface morphology changes were observed for the silicone cushions (Figure 5-20).

For *in vitro* degradation, the components were completely exposed to the $H_2O_2/CoCl_2$ solution without taking into account the effect of the titanium alloy housing, as titanium and hydrogen peroxide are incompatible. As the BDyn elastomeric components are surrounded by a titanium alloy housing, previously, it was hypothesised that the titanium housing will have an effect on the degradation of the polymer components (Lawless et al., 2018). By using hyperspectral chemical mapping, this present chapter shows degradation occurred, in some form, for all six PCU rings; these results demonstrate that the titanium housing does not have a role in stopping degradation of the PCU rings. Five out of six explanted PCU rings HCMs had new absorbance peaks at 1174 cm^{-1} and all six explanted PCU rings had new absorbance peaks at 1650 cm^{-1}; these findings were further confirmed by the SG second derivative spectra of the explanted PCU components (8.9 Appendix I - Figure 8-16) displayed an increase in prominence at 1650 cm^{-1} for all explants and at 1174 cm^{-1} for PCU Explants 1 to 5 (Figure 8-16 (A) to (E)).

It must be stated that new absorbance peaks at 1650 cm^{-1} were discovered by hyperspectral chemical mapping on a specific acquisition of the untreated PCU ring. This demonstrates that the hard segment degradation was localised for this particular ring and oxidation and implantation play no part in this degradation. This observation of a localised, hard segment degraded region on the untreated PCU component was not unexpected as hard segment degradation of separate, untreated PCU components has been recently discovered in a recent publication in which I am co-first author (Dorrepaal et al., 2018). This hard segment degradation may have been caused by one or more factors including, potential inconsistencies in the biomaterial mixing/formulation/manufacture process and/or in the sterilisation of the PCU components; at this time the hard segment changes cannot be attributed to a single factor (Dorrepaal et al., 2018). However, this finding highlights the importance of the objective nature of hyperspectral mapping as this localised hard segment degradation, of the untreated PCU ring, may have been unnoticed or could be over-represented (Dorrepaal et al., 2018).

Explanted orthopaedic implants, which contain PCU components, have demonstrated new absorbance peaks at 1650 cm^{-1} and/or 1174 cm^{-1} to demonstrate biological oxidative degradation (Cipriani et al., 2013; Ianuzzi et al., 2010; Neukamp et al., 2015). However, another explant study did not find new absorbance peaks linked to biological oxidative degradation (Shen et al., 2011). Ianuzzi et al. (2010) discovered that 10 PCU spacers, from six patients, had evidence of PCU biodegradation and experienced this degradation on the surface where the spacer would make contact with tissue. Examination of retrieved Dynesys PCU spacers revealed that chemical changes were negligible 100 μm below the surface (Cipriani et al., 2013; Shen et al., 2011; Trommsdorff et al., 2004a) and that significant chemical changes are confined to the surface (Cipriani et al., 2013). It was suggested that with only 10 μm of the surface alteration would suggest no influence on the bulk mechanical properties of the entire device (Cipriani et al., 2013). The *in vitro* degradation, of the BDyn PCU and silicone components, section of this chapter demonstrated that the viscoelastic properties of the BDyn spinal PDS device, and its individual components, were significantly different, at certain frequencies, due to *in vitro* oxidation (see Table 5-9). Further, explanted components, and the explanted components assembled in the BDyn titanium alloy housing, section of this chapter demonstrated that the viscoelastic properties of the BDyn spinal PDS device, and its individual components, outside the 95% confidence interval error bars, at certain frequencies, due to *in vivo* degradation (see Table 5-11). These findings demonstrate the importance of performing mechanical tests and quantifying viscoelastic properties of the frequency dependent viscoelastic

medical devices and not to suggest that due to a small layer of the surface being affected by oxidation, that it will not affect the mechanical properties of the device.

Even though Wilkoff et al. (2015) stated that explanted silicone components had demonstrated excellent biostability with no identifiable *in vivo* degradation, in the authors' study, 3 out of 22 specimens after 2–3 years implantation and 1 out of 24 specimens after 4–5 years implantation demonstrated new peaks near 1650 cm^{-1} (Wilkoff et al., 2015). As stated earlier in this discussion, *in vitro* oxidative degraded silicone BDyn component demonstrated good biostability with no change to the ATR-FTIR spectra and no surface morphology changes. However, HCMs demonstrated that a new peak at 1650 cm^{-1} was observed regionally at one or multiple locations, on all explanted silicone components (Figure 5-12). Further, chemical structure changes at 1065 cm^{-1} (associated with the Si-O-Si stretch) and 1257 cm^{-1} (associated with the $Si\text{-}CH_3$ stretch) were witnessed and these changes varied regionally across the explanted silicone components (Figure 5-13 and Figure 5-14). The findings of a new peak at 1650 cm^{-1}, chemical structure changes at 1065 cm^{-1} and at 1257 cm^{-1} were further confirmed with Savitzky Golay as a new sharp increase at 1650 cm^{-1}, a decrease in gradient at 1065 cm^{-1} and an increase in gradient at 1257 cm^{-1}, respectively (8.9 Appendix I - Figure 8-17). Similar to the observation of a localised, hard segment degraded region on the untreated PCU component, the regionalised nature of new peak at 1650 cm^{-1} on the silicone components may have gone unnoticed or could be over-represented if HCMs were not utilised (Dorrepaal et al., 2018).

SEM images of the *in vitro* and *in vivo* degraded PCU components revealed pitting on the surface of the PCU components which has been previously documented for *in vitro* and *in vivo* oxidation of PCU (Christenson et al., 2004b; Dempsey et al., 2014). The pit shapes and sizes varied between the *in vitro* degraded and explanted, *in vivo* degraded PCU rings with the measured pit diameters of the *in vitro* degraded PCU ring ranging between 0.65 μm and 4.58 μm while the *in vivo* degraded PCU pit diameters ranged between 0.26 μm – 8.34 μm. These ranges, for the *in vitro* and *in vivo* degraded PCU rings pit diameters, are similar to the *in vitro* degraded Bionate II 80A (0.44 μm – 5.88 μm) and, from a previous study, *in vitro* degraded Bionate 80A (1 μm – 10 μm) (Christenson et al., 2004a).

SEM images (Figure 5-21 (A), (C), (D) and (G)) displayed environmental stress cracking (ESC) of the explanted PCU surfaces; ESC was witnessed on the surface of some silicone components (Figure 5-22 (F) and (H)). It has been stated that ESC, of explanted Dynesys PCU spacers, is one of the most evident factors in the detection of oxidative degradation as these degraded areas were abraded and cracked potentially from mechanical loading (Cipriani et al., 2013); however, oxidative degradation was apparent in homogenous zones i.e. no abrasion or surface cracked zones (Cipriani et al., 2013). It has been shown that ion implantation increases the scratch resistance and increases the hardness of a surface layer of polymers (Calcagno et al., 1992; Kondyurin and Bilek, 2014). The silicone cushion viscoelastic properties were shown to be significantly affected, for each tested frequency, by the level of ion treatment ($p < 0.05$) while the PCU ring viscoelastic properties remain unchanged due to the level of ion treatment, for every frequency tested ($p > 0.05$); see 8.10 Appendix J – section 8.10.3.1. Due to ion treatment, the polymer surface layer becomes carbonised and the hardness of the surface layer is higher than the hardness of the underlying polymer (Kondyurin and Bilek, 2014). This increase of hardness of the surface layer may make the surface layer more brittle. Thus, ESC and delamination may be more likely to occur. Further research is required to investigate the advantages (increase scratch resistance, altering the coefficient of friction, etc.) over the disadvantages (surface layer becoming more brittle) of polymers to be used in orthopaedic devices. Also, further research is required to investigate the influence of ESC on the viscoelastic response of these biomaterials. The *in vitro* replication of ESC could be performed by utilising two methods decribed by Zhao et al. (1995, 1993). The Zhao-type, or modified Zhao-type, uses human plasma or glass wool soaked with a H_2O_2 and $CoCl_2$ to replicate ESC. These ESC replication methods are widely used in literature (Gallagher et al., 2017; Khan et al., 2005a; Martin et al., 2001; Taylor et al., 2005). However, the precise mechanism of action remains unknown (Gallagher et al., 2017).

Due to the complex, multi-material structure of the BDyn device and the desired test configuration, difficulties in the Proportional-Integral-Derivative-Offset (PIDO) tuning of the BOSE 3200 testing machine load control transpired. For consistent, comparable data of the devices and its individual components, a maximum load of ± 20 N was applied. Load has been shown to affect the mechanical properties of an elastomeric total disc replacement (Mahomed et al., 2012) while an increase of preload has been shown to significantly increase the dynamic stiffness of the intervertebral disc (Kasra et al., 1992). As the dynamic stiffness can be affected by load (Kasra et al., 1992), any comparison between different methods and studies must be made with caution. For consistency reasons, the methods between testing the untreated, *in vitro*

degraded and *in vivo* degraded explanted components all remained unchanged; this was important to understand how the degradation processes affects the frequency dependent viscoelastic properties.

Regardless, no *in vitro* degradation method fully replicates the biochemical and biomechanical stresses experienced in the body (Wilkoff et al., 2015) thus, the *in vivo* degraded scenario was also investigated. However, the DMA test configuration is not similar to the *in vivo* scenario where the mobile and fixed rods are secured to the pedicles (Figure 2-15). By securing the mobile rod to the vertebra, an applied load to the device may not displace the two, bilateral polymer systems equally; hence, the difference in displacement will affect the dynamic stiffness *(k*)* and in turn, the storage *(k')* and loss *(k")* stiffness. The BDyn device is designed to allow partial movement along the anatomical planes. This chapter quantified the viscoelastic properties of the normal, *in vitro* and *in vivo* degraded BDyn components, and BDyn 1 level device with the assembled components in the device, uniaxially. Rotation of the moveable rod, around an anatomical plane, may affect the response of the out-of-phase displacement to an applied force and hence, affect the viscoelastic properties. However, these limitations do not alter the conclusions of this chapter because the sinusoidally applied loads ensured a direct comparison between the normal and degraded components/devices.

5.5 Chapter Summary

- The viscoelastic properties of the posterior stabilisation BDyn device and its components are frequency dependent. As the frequency increased, the storage stiffness and the loss stiffness increased for the untreated components and BDyn devices; this highlights the need to evaluate biomaterials and devices utilising frequency dependent mechanical testing techniques.
- *In vitro* oxidation degradation affected the viscoelasticity of the specific components and the BDyn device, assembled with the degraded components, at specific frequencies; this highlights the importance of analysing changes of viscoelastic properties, of degraded biomaterials, in terms of frequency and medical devices into which they are incorporated, using a frequency sweep.
- *In vitro* oxidation degradation displayed changes to the chemical structure and exhibited surface morphology changes of the PCU components. There were no changes evident in the ATR-FTIR spectra and no surface morphology changes of the *in vitro* degraded silicone component.
- All six explanted PCU rings displayed changes to the chemical structure associated to hard segment degradation while 5 (out of 6) explanted PCU rings evidence of soft segment degradation on hyperspectral chemical maps (HCMs). HCMs of the silicone components demonstrated that a new peak at 1650 cm^{-1} was observed regionally at one or multiple locations, on all explanted silicone components.
- All six explanted PCU rings and explanted six silicone cushions displayed some form of macroscopic or microscopic surface morphological changes.
- No resonant frequencies were reported for the untreated and *in vitro* degraded components and devices. Resonance was detected in the frequency sweep test of BDyn Explant 2 with the sharp increase of the loss stiffness occurred at 4 Hz; this is not a beneficial finding for the device and further adds to the importance of evaluating orthopaedic devices with frequency dependent mechanical testing techniques.

The next chapter provides an overall discussion, future research necessary to further develop our understanding of the biostability of elastomeric orthopaedic devices and biomaterials and general conclusions of this thesis.

Chapter 6

Overall discussion, future work and conclusions

6 Overall discussion, future work and conclusions

This thesis investigated the *in vitro* and *in vivo* biostability of the BDyn posterior dynamic stabilisation (PDS) orthopaedic (spinal) device elastomeric biomaterials and the *in vitro* biostability of five long-term implantable polycarbonate urethane biomaterials. To reduce exposure to potentially harmful frequencies of the spine, understanding the resonance or natural frequencies, of the spine, is important (Panjabi et al., 1986). In addition, assessing the behaviour of such spinal implant devices, especially at spinal resonant frequencies, is important. Any resonance of a spinal device, at any frequency, is a limitation of the device as the resonance may damage the device and in a worst-case scenario, the device may fail. This thesis adds to the minimal work that has been previously undertaken in understanding the frequency dependent response of implantable devices and the frequency dependent behaviour of the biomaterials used in such implants.

The viscoelasticity (calculated by DMA) of the untreated, *in vitro* and *in vivo* degraded BDyn components and the BDyn device assembled with degraded components were compared. The viscoelastic properties of the BDyn device and its components are frequency dependent. As the frequency increased, the storage stiffness and the loss stiffness increased for the untreated components and BDyn devices; this highlights the need to evaluate biomaterials and devices utilising frequency dependent mechanical testing techniques. *In vitro* oxidation degradation affected the viscoelasticity of the specific components and the BDyn device, assembled with the degraded components, at specific frequencies; this highlights the importance of analysing changes of viscoelastic properties, of degraded biomaterials, in terms of frequency and medical devices into which they are incorporated, using a frequency sweep.

The BDyn components chemical structure (HCI and ATR-FTIR), macro-morphological plastic deformation and surface morphology (SEM) were compared. *In vitro* oxidation degradation displayed changes to the chemical structure and exhibited surface morphology changes of the PCU components while the *in vitro* degraded silicone components displayed no changes in the ATR-FTIR spectra and surface morphology. All six explanted, *in vivo* degraded PCU rings and silicone cushions displayed some forms of macroscopic or microscopic surface morphological changes. All six explanted PCU rings displayed changes to the chemical structure associated to hard segment degradation while 5 (out of 6) explanted PCU rings had evidence of soft segment degradation on hyperspectral chemical maps (HCMs). HCMs of the silicone components demonstrated that a new peak at 1650 cm^{-1} was observed regionally at one or multiple

locations, on all explanted silicone components. Further, chemical structure changes associated with the Si-O-Si stretch (1065 cm^{-1}) and the Si-CH_3 stretch (1257 cm^{-1}) were witnessed.

Unlike the untreated and *in vitro* degraded components and devices, resonance was detected in the frequency sweep test of the BDyn Explant 2 with the sharp increase of the loss stiffness which occurred at 4 Hz; this resonant frequency is similar to the frequencies recorded by Panjabi et al. (1986) and Wilder et al. (1982). Further, this resonant frequency is not a beneficial finding for the device and further adds to the importance of evaluating orthopaedic devices with frequency dependent mechanical testing techniques.

The *in vitro* biostability of five commercially available, long-term implantable polycarbonate urethane (PCU) biomaterials with regards to viscoelasticity (μDMA and DMA), chemical structure (HCI) and surface morphology (SEM) were investigated. This was performed by degrading the biomaterials by four separate *in vitro* degradation protocols. The five biomaterials (Quadrathane ARC 80A-B20, Bionate II 80A, Quadrathane ARC 80A, ChronoFlex C 80A and ChronoSil 80A 5%) were viscoelastic throughout the frequency range tested. Further, the macro-viscoelastic properties of the five untreated and degraded biomaterials were logarithmic with respect to frequency for all biomaterial specimens tested. Similar to the BDyn device and its components, this highlights the need to evaluate biomaterials utilising frequency dependent mechanical testing techniques and the frequency dependent nature of these materials must be considered by researchers.

The *in vitro* $H_2O_2/CoCl_2$ degradation method, used to degrade PCU, has been shown to produce similar chemical structure and surface morphological changes to PCU biomaterials degraded *in vivo*. Interestingly, the micro- and macro-viscoelastic properties of Bionate II and Chronoflex C $H_2O_2/CoCl_2$ degraded specimens were not significantly different ($p > 0.05$) for any frequency tested when compared to the untreated; this highlights the oxidative stability, with regards to their viscoelastic properties, of these biomaterials. Further, the macro-viscoelastic properties of Bionate II and Chronoflex C real-time and accelerated hydrolytic degraded specimens were not significantly different ($p > 0.05$) for any frequency tested when compared to the untreated; this highlights the hydrolytic stability, with regards to their macro-viscoelastic properties, of these biomaterials. However, the micro-viscoelastic properties of Bionate II and Chronoflex C were significantly different ($p < 0.05$) at specific frequencies tested; thus, this calls into doubt the hydrolytic stability of these biomaterials and highlights the importance of the need to assess material mechanical response property changes on different scales.

The surface micro-level viscoelastic response of the Quadrathane $H_2O_2/CoCl_2$ degraded specimens were not significantly different when compared to the untreated. The micro-scale and the macro-scale elastic property (storage stiffness) was not significantly different ($p > 0.05$) for any biomaterial, at any tested frequency, between the untreated and the *in vitro* $H_2O_2/CoCl_2$ degraded groups. Therefore, it is concluded with caution that oxidation mechanisms, created by an *in vitro* mechanism that is comparative to the *in vivo* mechanism, may not affect the recoverable energy of these five biomaterials; a caveat of this conclusion is that this does not apply to all forms of mechanical loading and potentially, all induced stress ranges. To add to this conclusion, the macro-elastic property of the real-time and accelerated hydrolytic degraded Quadrathane B20, Bionate II, Quadrathane and Chronoflex C specimens was not significantly different ($p > 0.05$), to the untreated specimens, for all tested frequencies; this finding demonstrates the hydrolytic stability of these biomaterials. However, with regards to viscoelastic properties, the oxidative and hydrolytic stability of these biomaterials is called into doubt as the macro-viscoelastic properties, of the five biomaterials, were significantly different ($p < 0.05$) at specific frequencies when comparing the untreated and 3% H_2O_2 degradation method; the hydrolytic stability is called into doubt as the 3% H_2O_2 method is 97% water.

For all Chronosil specimens degraded by the four degradation methods, the micro-viscoelastic properties Chronosil was not significantly different for all tested frequencies and no new absorbance peaks were observed at 930 cm^{-1} and 1174 cm^{-1} on all HCIs; this highlights the biostability of this polycarbonate urethane based silicone biomaterial. Further, SEM images of the five biomaterials degraded with the *in vitro* $H_2O_2/CoCl_2$ degradation method revealed various levels of pitting on the surface and Chronosil had the smallest range of pit sizes. This finding, alongside the minimal changes in gradient of the *in vitro* oxidative degraded SG second derivative spectra of Chronosil, further highlights the biostability of Chronosil over the other PCU biomaterials evaluated. HCIs of the aromatic PCU biomaterials degraded by the *in vitro* $H_2O_2/CoCl_2$ method demonstrated evidence of PCU oxidative degradation as new absorbance peaks were observed at 930 cm^{-1} and 1174 cm^{-1}. Regional variation of degradation on some *in vitro* $H_2O_2/CoCl_2$ degraded specimens was highly contrasting; this emphasises the need of imaging a wide sample area to understand spatial variation of biomaterial degradation. No new peaks at 930 cm^{-1} and 1174 cm^{-1} were detected for specimens degraded by the 3% H_2O_2 degradation method, the real time or the accelerated hydrolytic degradation methods.

As these motion preserving implants are novel and clinical precedence is slowly emerging with retrieval analysis studies, it is challenging for engineers to develop *in vitro* tests to accurately predict *in vivo* performance (Kurtz et al., 2009). At the cell membrane-biomaterial surface interface, the macrophages and FBGCs release degradative agents such as reactive oxygen intermediates (oxygen free radicals), enzymes and acid (Anderson et al., 2008; Christenson et al., 2007; Heiple et al., 1990; Sheikh et al., 2015; Wright and Silverstein, 1983). From the explanted BDyn components, micro-scale (ESC and surface pitting) and macro-scale morphological changes were witnessed. To further develop our understanding of the biostability of implantable devices and biomaterials, I believe future *in vitro* studies should be in performed with multiple *in vitro* tests, on implantable devices, to more accurately predict *in vivo* performance and these *in vitro* tests should include:

- Cholesterol Esterase (CE) or another enzyme (to replicate enzymatic degradation)
- Human plasma or glass wool (to replicate ESC)
- $H_2O_2/CoCl_2$ (to replicate pitting)
- Mechanical fatigue testing (to replicate plastic deformation)

The order of these experiments would have to be decided following preliminary testing. By encapsulating different characteristics caused by implantation (*in vivo* degradation), this could help biomedical engineers to more accurately predict *in vivo* performances by *in vitro* methods.

It would be beneficial, of future BDyn retrieval studies, to examine periprosthetic tissue samples for wear debris and inflammation; this would give an understanding of the benefits of the BDyn titanium housing as a protection barrier between the tissue and the elastomeric components. As the explant that had a resonant frequency had an asymmetrical pedicle screw construct, it would be beneficial to investigate the load transfer through an asymmetrical pedicle screw construct by using, as a general and not strict guidance, the ISO 12189 or ASTM F1717 standard. Further, future work should involve fatigue test of BDyn under ISO 12189 and the investigation of the effect of this fatigue loading to the viscoelastic properties of the device and components.

Future work should focus on assessing the effect of component manufacturing factors (sterilisation, ion treatment, etc.) on the viscoelastic properties of these biomaterials. To give a better understanding of the effect of regionalised degradation on mechanical response, it is purposed that future work combines HCI and micro-DMA to correlate if a change in the mechanical response, of the biomaterials, can be detected by a change in the chemical structure. If a correlation exists and can be quantified, this would be further advantage of the use of HCI. Further, it is proposed that new, developing technology, such as optical coherence elastography (OCE) (Bartolini et al., 2017), is utilised in future studies to investigate potential spatial variations and depth penetration of degraded biomaterials.

The overall conclusions from this thesis are:

- The five biomaterials (Quadrathane ARC 80A-B20, Bionate II 80A, Quadrathane ARC 80A, ChronoFlex C 80A and ChronoSil 80A 5%), the posterior stabilisation BDyn device and the BDyn components were viscoelastic throughout the frequency ranges tested;
- Except for Chronosil, the micro- and macro-viscoelastic properties of all biomaterials were affected by one (or more) *in vitro* degradation method(s); only the macro-viscoelastic properties of Chronosil was affected by *in vitro* degradation methods;
- Aromatic PCU biomaterials degraded by the *in vitro* $H_2O_2/CoCl_2$ method demonstrated evidence of PCU oxidative degradation; this degradation regionally varied across the surface some specimens;
- Chronosil was the most biostable biomaterial degraded by the four degradation methods. The micro-viscoelastic properties of Chronosil were not significantly different when comparing the four degraded methods to the untreated biomaterials;
- *In vitro* oxidation degradation affected the viscoelasticity of the specific components and the BDyn device, assembled with the degraded components, at specific frequencies. No resonant frequencies were reported for the untreated and *in vitro* degraded components and devices. Resonance was detected in the frequency sweep test of a BDyn device, assembled with explanted components, at 4 Hz;
- SEM images of the six explanted PCU rings and explanted six silicone cushions displayed microscopic surface morphological changes. SEM images of the five biomaterials degraded with the *in vitro* $H_2O_2/CoCl_2$ degradation method, the *in vitro* and *in vivo* degraded BDyn PCU components revealed pitting on the surface. The range of the measured pit diameters of the *in vitro* degraded five biomaterials, *in vitro* and *in vivo* degraded PCU rings varied; Chronosil had the smallest pit sizes.

Chapter 7

References

7 References

Abdul-Kader, A.M., El-Badry, B.A., Zaki, M.F., Hegazy, T.M., Hashem, H.M., 2010. Ion beam modification of surface properties of CR-39. Philos. Mag. 90, 2543–2555. https://doi.org/10.1080/14786431003630728

Adams, M.A., 2004. Biomechanics of back pain. Acupunct. Med. 22, 178–188. https://doi.org/10.1136/aim.22.4.178

Adams, M.A., Bogduk, N., Burton, K., Dolan, P., 2002. The Biomechanics of Back Pain, 1st Editio. ed. Churchill Livingstone, Edinburgh.

Akutsu, T., Dreyer, B., Kolff, W.J., 1959. Polyurethane artificial heart valves in animals. J. Appl. Physiol. 14, 1045–1048.

An, H.S., Anderson, P.A., Haughton, V.M., Iatridis, J.C., Kang, J.D., Lotz, J.C., Natarajan, R.N., Oegema, T.R., Roughley, P., Setton, L.A., Urban, J.P., Videman, T., Andersson, G.B.J., Weinstein, J.N., 2004. Introduction. Disc degeneration: Summary. Spine (Phila. Pa. 1976). 29, 2677–2678. https://doi.org/10.1097/01.brs.0000147573.88916.c6

Anderson, J.M., Rodriguez, A., Chang, D.T., 2008. Foreign body reactions to biomaterials. Semin. Immunol. 20, 86–100. https://doi.org/10.1016/j.smim.2007.11.004

Andriani, Y., Morrow, I.C., Taran, E., Edwards, G.A., Schiller, T.L., Osman, A.F., Martin, D.J., 2013. In vitro biostability of poly(dimethyl siloxane/hexamethylene oxide)-based polyurethane/layered silicate nanocomposites. Acta Biomater. 9, 8308–17. https://doi.org/10.1016/j.actbio.2013.05.021

Antonovaite, N., Beekmans, S. V., Hol, E.M., Wadman, W.J., Iannuzzi, D., 2018. Structure-stiffness relation of live mouse brain tissue determined by depth-controlled indentation mapping. arXiv Prepr. arXiv1802.02245 1–18.

Arjun, G.N., Ramesh, P., 2012. Structural characterization, mechanical properties, and in vitro cytocompatibility evaluation of fibrous polycarbonate urethane membranes for biomedical applications. J. Biomed. Mater. Res. Part A 100, 3042–3050. https://doi.org/10.1002/jbm.a.34255

Arora, N., Ali, A., Jana, N.K., Basak, P., 2013. Biodegradation of Poly(etherurethanes), in: AIP Conference Proceedings. pp. 1225–1227. https://doi.org/10.1063/1.4810682

ASTM, 2014. ASTM F2193: Standard Specifications and Test Methods for Metallic Angled Orthopedic Fracture Fixation Devices. https://doi.org/10.1520/F0384-12

ASTM, 2013. ASTM D1708: Standard Test Method for Tensile Properties of Plastics by Use of Microtensile Specimens. ASTM. https://doi.org/10.1520/D1708-13.

ASTM, 2011. ASTM F2346-05: Standard Test Methods for Static and Dynamic Characterization of Spinal Artificial Discs. https://doi.org/10.1520/F2346-05R11

Barnes, H.A., Hutton, J.F., Walters, K., 1989. An introduction to rheology, Vol. 3. ed. Elservier, Amsterdam, The Netherlands.

Barnes, S.C., Lawless, B.M., Shepherd, D.E.T., Espino, D.M., Bicknell, G.R., Bryan, R.T., 2016. Viscoelastic properties of human bladder tumours. J. Mech. Behav. Biomed. Mater. 61, 250–257. https://doi.org/10.1016/j.jmbbm.2016.03.012

Barnes, S.C., Shepherd, D.E.T., Espino, D.M., Bryan, R.T., 2015. Frequency dependent viscoelastic properties of porcine bladder. J. Mech. Behav. Biomed. Mater. 42, 168–176.

https://doi.org/10.1016/j.jmbbm.2014.11.017

Bartolini, L., Feroldi, F., Weda, J.J.A., Slaman, M., de Boer, J.F., Iannuzzi, D., 2017. Multimodal probe for optical coherence tomography epidetection and micron-scale indentation. J. Innov. Opt. Health Sci. 10, 1742007. https://doi.org/10.1142/S179354581742007X

Battié, M.C., Videman, T., Parent, E., 2004. Lumbar disc degeneration: Epidemiology and genetic influences. Spine (Phila. Pa. 1976). 29, 2679–2690. https://doi.org/10.1097/01.brs.0000146457.83240.eb

Beekmans, S. V., 2018. Minimally invasive micro-indentation. VU Amsterdam.

Beekmans, S. V., Emanuel, K.S., Smit, T.H., Iannuzzi, D., 2017. Minimally Invasive Micro-Indentation: Mapping tissue mechanics at the tip of an 18G needle. Sci. Rep. 7, 1–8. https://doi.org/10.1038/s41598-017-10526-4

Beekmans, S. V., Iannuzzi, D., 2015. A metrological approach for the calibration of force transducers with interferometric readout. Surf. Topogr. Metrol. Prop. 3, 25004. https://doi.org/10.1088/2051-672X/3/2/025004

Benzel, E.C., Lieberman, I.H., Ross, E.R., Linovitz, R.J., Kuras, J., Zimmers, K.B., 2011. Mechanical characterisation of a viscoelastic disc for lumbar total disc replacement. J. Med. Device. 5, 11005, 1–7. https://doi.org/10.1115/1.4003536

Blatz, P.J., Ko, W.L., 1962. Application of Finite Elastic Theory to the Deformation of Rubbery Materials. Trans. Soc. Rheol. 6, 223–252. https://doi.org/10.1122/1.548937

Bothmann, M., Kast, E., Boldt, G.J., Oberle, J., 2008. Dynesys fixation for lumbar spine degeneration. Neurosurg. Rev. 31, 189–96. https://doi.org/10.1007/s10143-007-0101-9

Briscoe, B.J., Fiori, L., Pelillo, E., 1998. Nano-indentation of polymeric surfaces. J. Phys. D. Appl. Phys. 31, 2395–2405. https://doi.org/10.1088/0022-3727/31/19/006

Burton, H.E., Freij, J.M., Espino, D.M., 2017. Dynamic viscoelasticity and surface properties of porcine left anterior descending coronary arteries. Cardiovasc. Eng. Technol. 8, 41–56. https://doi.org/10.1007/s13239-016-0288-4

Calcagno, L., Compagnini, G., Foti, G., 1992. Structural modification of polymer films by ion irradiation. Nucl. Instruments Methods Phys. Res. Sect. B Beam Interact. with Mater. Atoms 65, 413–422.

Carbone, G., Persson, B.N.J., 2005. Crack motion in viscoelastic solid: The role of the flash temperature. Eur. Phys. J. 17, 261–281.

Carfagni, M., Lenzi, E., Pierini, M., 1998. The loss factor as a measure of mechanical damping, in: 1998 IMAC XVI - 16th International Modal Analysis Conference. pp. 580–584.

Chaffin, K.A., Buckalew, A.J., Schley, J.L., Chen, X., Jolly, M., Alkatout, J.A., Miller, J.P., Untereker, D.F., Hillmyer, M.A., Bates, F.S., 2012. Influence of water on the structure and properties of PDMS-containing multiblock polyurethanes. Macromolecules 45, 9110–9120. https://doi.org/10.1021/ma301965y

Chaffin, K.A., Chen, X., McNamara, L., Bates, F.S., Hillmyer, M.A., 2014. Polyether Urethane Hydrolytic Stability after Exposure to Deoxygenated Water. Macromolecules 47, 5220–5226. https://doi.org/10.1021/ma500904d

Chaffin, K.A., Wilson, C.L., Himes, A.K., Dawson, J.W., Haddad, T.D., Buckalew, A.J.,

Miller, J.P., Untereker, D.F., Simha, N.K., 2013. Abrasion and fatigue resistance of PDMS containing multiblock polyurethanes after accelerated water exposure at elevated temperature. Biomaterials 34, 8030–8041. https://doi.org/10.1016/j.biomaterials.2013.06.049

Chamoli, U., Diwan, A.D., Tsafnat , N., 2014. Pedicle screw-based posterior dynamic stabilizers for degenerative spine: *In vitro* biomechanical testing and clinical outcomes. J. Biomed. Mater. Res. Part A 102, 3324–3340. https://doi.org/10.1002/jbm.a.34986

Chan, K.L.A., Kazarian, S.G., 2006. High-throughput study of poly(ethylene glycol)/ibuprofen formulations under controlled environment using FTIR imaging. J. Comb. Chem. 8, 26–31. https://doi.org/10.1021/cc050041x

Chandy, T., Van Hee, J., Nettekoven, W., Johnson, J., 2009. Long-term in vitro stability assessment of polycarbonate urethane micro catheters: resistance to oxidation and stress cracking. J. Biomed. Mater. Res. Part B Appl. Biomater. 89, 314–324. https://doi.org/10.1002/jbm.b.31218

Chavan, D., Andres, D., Iannuzzi, D., 2011. Note: Ferrule-top atomic force microscope. II. Imaging in tapping mode and at low temperature. Rev. Sci. Instrum. 82, 2010–2012. https://doi.org/10.1063/1.3579496

Chavan, D., Gruca, G., De Man, S., Slaman, M., Rector, J.H., Heeck, K., Iannuzzi, D., 2010. Ferrule-top atomic force microscope. Rev. Sci. Instrum. 81. https://doi.org/10.1063/1.3516044

Chavan, D., Van De Watering, T.C., Gruca, G., Rector, J.H., Heeck, K., Slaman, M., Iannuzzi, D., 2012. Ferrule-top nanoindenter: An optomechanical fiber sensor for nanoindentation. Rev. Sci. Instrum. 83. https://doi.org/10.1063/1.4766959

Christenson, E.M., Anderson, J.M., Hiltner, A., 2007. Biodegradation mechanisms of polyurethane elastomers. Corros. Eng. Sci. Technol. 42, 312–323. https://doi.org/10.1179/174327807X238909

Christenson, E.M., Anderson, J.M., Hiltner, A., 2006a. Antioxidant inhibition of poly(carbonate urethane) in vivo biodegradation. J. Biomed. Mater. Res. Part A 76, 480–90. https://doi.org/10.1002/jbm.a.30506

Christenson, E.M., Anderson, J.M., Hiltner, A., 2004a. Oxidative mechanisms of poly(carbonate urethane) and poly(ether urethane) biodegradation: In vivo and in vitro correlations. J. Biomed. Mater. Res. Part A 70, 245–255.

Christenson, E.M., Dadsetan, M., Anderson, J.M., Hiltner, A., 2005. Biostability and macrophage-mediated foreign body reaction of silicone-modified polyurethanes. J. Biomed. Mater. Res. Part A 74, 141–155. https://doi.org/10.1002/jbm.a.30317

Christenson, E.M., Dadsetan, M., Wiggins, M., Anderson, J.M., Hiltner, A., 2004b. Poly(carbonate urethane) and poly(ether urethane) biodegradation: In vivo studies. J. Biomed. Mater. Res. Part A 69A, 407–416. https://doi.org/10.1002/jbm.a.30002

Christenson, E.M., Patel, S., Anderson, J.M., Hiltner, A., 2006b. Enzymatic degradation of poly(ether urethane) and poly(carbonate urethane) by cholesterol esterase. Biomaterials 27, 3920–3926. https://doi.org/10.1016/j.biomaterials.2006.03.012

Cipriani, E., Bracco, P., Kurtz, S.M., Costa, L., Zanetti, M., 2013. In-vivo degradation of poly(carbonate-urethane) based spine implants. Polym. Degrad. Stab. 98, 1225–1235. https://doi.org/10.1016/j.polymdegradstab.2013.03.005

Coe, J.D., Kitchel, S.H., Meisel, H.J., Wingo, C.H., Lee, S.E., 2012. NFlex Dynamic Stabilization System: Two-Year Clinical Outcomes of Multi-Center Study. Korean Neurol. Soc. 51, 343–349. https://doi.org/10.3340/jkns.2012.51.6.343

Constable, M., Burton, H.E., Lawless, B.M., Gramigna, V., Buchan, K.G., Espino, D.M., 2018. Effect of glutaraldehyde based cross-linking on the viscoelasticity of mitral valve basal chordae tendineae. Biomed. Eng. Online 17: 93. https://doi.org/10.1186/s12938-018-0524-2

Cooke, M.E., Lawless, B.M., Jones, S.W., Grover, L.M., 2018a. Matrix degradation in osteoarthritis primes the superficial region of cartilage for mechanical damage. Acta Biomater. 78, 320–328. https://doi.org/10.1016/j.actbio.2018.07.037

Cooke, M.E., Lawless, B.M., Jones, S.W., Grover, L.M., 2018b. Loss of proteoglycan content primes articular cartilage for mechanically induced damage. Osteoarthr. Cartil. 26, S371. https://doi.org/10.1016/j.joca.2018.02.731

Cunningham, B.W., Dawson, J.M., Hu, N., Kim, S.W., McAfee, P.C., Griffith, S.L., 2010. Preclinical evaluation of the Dynesys posterior spinal stabilization system: a nonhuman primate model. Spine J. 10, 775–783. https://doi.org/10.1016/j.spinee.2010.04.005

Dahl, M.C., Jacobsen, S., Metcalf, N., Sasso, R., Ching, R.P., 2011. A comparison of the shock-absorbing properties of cervical disc prosthesis bearing materials. SAS J. 5, 48–54. https://doi.org/10.1016/j.esas.2011.01.002

Dang, T.T., Nikkhah, M., Memic, A., Khademhosseini, A., 2014. Natural and Synthetic Biomedical Polymers, Natural and Synthetic Biomedical Polymers. Elsevier. https://doi.org/10.1016/B978-0-12-396983-5.00020-X

de Lima, A.M.G., Rade, D.A., Lacerda, H.B., Araújo, C.A., 2015. An investigation of the self-heating phenomenon in viscoelastic materials subjected to cyclic loadings accounting for prestress. Mech. Syst. Signal Process. 58, 115–127. https://doi.org/10.1016/j.ymssp.2014.12.006

Dempsey, D.K., Carranza, C., Chawla, C.P., Gray, P., Eoh, J.H., Cereceres, S., Cosgriff-hernandez, E.M., 2014. Comparative analysis of in vitro oxidative degradation of poly (carbonate urethanes) for biostability screening. J. Biomed. Mater. Res. Part A 102, 3649–3665. https://doi.org/10.1002/jbm.a.35037

Dorrepaal, R.M., Lawless, B.M., Burton, H.E., Espino, D.M., Shepherd, D.E.T., Gowen, A.A., 2018. Hyperspectral chemical imaging reveals spatially varied degradation of polycarbonate urethane (PCU) biomaterials. Acta Biomater. 73, 81–89. https://doi.org/10.1016/j.actbio.2018.03.045

Dumbleton, J., Manley, M., Wang, A., Jones, E., Sutton, K., 2009. New Developments in Alternative Hip Bearing Surfaces, First Edit. ed, Surgical Treatment of Hip Arthritis: Reconstruction, Replacement, and Revision. Elsevier Inc. https://doi.org/10.1016/B978-1-4160-5898-4.00064-1

Ehrenstein, G.W., Riedel, G., Trawiel, P., 2004. Dynamic Mechanical Analysis (DMA), in: Thermal Analysis of Plastics. Carl Hanser Verlag GmbH & Co. KG, pp. 236–299. https://doi.org/10.3139/9783446434141

Erdodi, G., Kang, J., Kennedy, J.P., 2010. Polyisobutylene-based polyurethanes. VI. Unprecedented combination of mechanical properties and oxidative/hydrolytic stability by H-bond acceptor chain extenders. J. Polym. Sci. Part A Polym. Chem. 48, 2361–2371. https://doi.org/10.1002/pola.24003

Espino, D.M., Shepherd, D.E.T., Hukins, D.W.L., 2014. Viscoelastic properties of bovine knee joint articular cartilage: dependency on thickness and loading frequency. BMC Musculoskelet. Disord. 15;205. https://doi.org/10.1186/1471-2474-15-205

Faré, S., Petrini, P., Motta, A., Cigada, A., Tanzi, M.C., 1999. Synergistic effects of oxidative environments and mechanical stress on in vitro stability of polyetherurethanes and polycarbonateurethanes. J. Biomed. Mater. Res. 45, 62–74. https://doi.org/10.1002/(SICI)1097-4636(199904)45:1<62::AID-JBM9>3.0.CO;2-F

Ferry, J.D., 1980. Viscoelastic Properties of Polymers, Third Edit. ed. John Wiley & Sons, New York, USA.

Ford, A.C., Gramling, H., Li, S.C., Sov, J. V., Srinivasan, A., Pruitt, L.A., 2018. Micromechanisms of fatigue crack growth in polycarbonate polyurethane: Time dependent and hydration effects. J. Mech. Behav. Biomed. Mater. 79, 324–331. https://doi.org/10.1016/j.jmbbm.2018.01.008

Formica, M., Cavagnaro, L., Basso, M., Zanirato, A., Felli, L., Formica, C., 2015. Is it possible to preserve lumbar lordosis after hybrid stabilization? Preliminary results of a novel rigid–dynamic stabilization system in degenerative lumbar pathologies. Eur. Spine J. 24, 849–854. https://doi.org/10.1007/s00586-015-4264-8

Franco, J.M., Partal, P., 2010. The Newtonian fluid, in: Rheology - Vol. 1. Encyclopedia of Life Support Systems (EOLSS), Paris, France, pp. 205–246.

Francolini, I., Piozzi, A., 2016. Antimicrobial Polyurethanes for Intravascular Medical Devices, Advances in Polyurethane Biomaterials. Elsevier Ltd. https://doi.org/10.1016/B978-0-08-100614-6.00012-3

Frautschi, J.R., Chinn, J.A., Phillips, R.E., Zhao, Q.H., Anderson, J.M., Joshi, R., Levy, R.J., 1993. Degradation of polyurethanes in vitro and in vivo: comparison of different models. Colloids Surf. B. Biointerfaces 1, 305–313.

Fulcher, G.R., Hukins, D.W.L., Shepherd, D.E.T., 2009. Viscoelastic properties of bovine articular cartilage attached to subchondral bone at high frequencies. BMC Musculoskelet. Disord. 10;61. https://doi.org/10.1016/j.jmbbm.2011.04.018

Gadd, M.J., Shepherd, D.E.T., 2011. Viscoelastic properties of the intervertebral disc and the effect of nucleus pulposus removal. Proc. Inst. Mech. Eng. Part H J. Eng. Med. 255, 335–341. https://doi.org/10.1177/2041303310393410

Gallagher, G., Padsalgikar, A., Tkatchouk, E., Jenney, C., Iacob, C., Runt, J., 2017. Environmental stress cracking performance of polyether and PDMS-based polyurethanes in an in vitro oxidation model. J. Biomed. Mater. Res. - Part B Appl. Biomater. 105, 1544–1558. https://doi.org/10.1002/jbm.b.33691

Gere, J.M., Timoshenko, S.P., 1997. Mechanics of Materials, Fourth. ed. Nelson Engineering, Boston, MA.

Ghanbari-Siahkali, A., Mitra, S., Kingshott, P., Almdal, K., Bloch, C., Rehmeier, H.K., 2005. Investigation of the hydrothermal stability of cross-linked liquid silicone rubber (LSR). Polym. Degrad. Stab. 90, 471–480. https://doi.org/10.1016/j.polymdegradstab.2005.04.016

Ghanbari, H., Viatge, H., Kidane, A.G., Burriesci, G., Tavakoli, M., Seifalian, A.M., 2009. Polymeric heart valves: new materials, emerging hopes. Trends Biotechnol. 27, 359–67. https://doi.org/10.1016/j.tibtech.2009.03.002

Gille, O., Challier, V., Parent, H., Cavagna, R., Poignard, A., Faline, A., Fuentes, S., Ricart, O., Ferrero, E., Ould Slimane, M., 2014. Degenerative lumbar spondylolisthesis. Cohort of 670 patients, and proposal of a new classification. Orthop. Traumatol. Surg. Res. 100, 311–315. https://doi.org/10.1016/j.otsr.2014.07.006

Gloria, A., De Santis, R., Ambrosio, L., Causa, F., Tanner, K.E., 2011. A Multi-component Fiber-reinforced PHEMA-based Hydrogel/HAPEXTM Device for Customized Intervertebral Disc Prosthesis. J. Biomater. Appl. 25, 795–810. https://doi.org/10.1177/0885328209360933

Gonzalez Alvarez, A., Dearn, K.D., Lawless, B.M., Lavecchia, C.E., Vommaro, F., Martikos, K., Greggi, T., Shepherd, D.E.T., 2018. Design and mechanical evaluation of a novel dynamic growing rod to improve the surgical treatment of Early Onset Scoliosis. J. Mater. Des. 155, 334–345. https://doi.org/10.1016/j.matdes.2018.06.008

Gowen, A.A., Dorrepaal, R.M., 2016. Multivariate chemical image fusion of vibrational spectroscopic imaging modalities. Molecules 21. https://doi.org/10.3390/molecules21070870

Gray, H., 1918. Anatomy of the Human Body. Lea & Febiger, Philadelphia and New York, USA.

Griesser, H.J., 1991. Degradation of polyurethanes in biomedical applications—A review. Polym. Degrad. Stab. 33, 329–354. https://doi.org/10.1016/0141-3910(91)90080-B

Guerin, P., Gille, O., Persohn, S., Campana, S., Vital, J.M., Skalli, W., 2011. Effect of new dynamic stabilization system on the segmental motion and intradiscal pressure: An in vitro biomechanical study, in: ORS 2011 Annual Meeting.

Gurappa, I., 2002. Characterization of different materials for corrosion resistance under simulated body fluid conditions. Mater. Charact. 49, 73–79. https://doi.org/10.1016/S1044-5803(02)00320-0

Haddad, Y.M., 1995. Viscoelasticity of Engineering Materials, First Edit. ed. Chapman and Hall, London, UK.

Han, C.D., Kim, K.K., 1993. On the use of time-temperature superposition in multicomponent/multiphase polymer systems. Polymer (Guildf). 34, 2533–2539.

Hartford, J., 2013. New Extrusion Techniques Advance Catheter Design [WWW Document]. Med. Device Diagnostic Ind. URL http://www.mddionline.com/article/new-extrusion-techniques-advance-catheter-design (accessed 5.30.17).

Heiple, J.M., Wright, S.D., Allen, N.S., Silverstein, S.C., 1990. Macrophages form circular zone of close apposition to IgG-coated surfaces. Cell Motil. Cytoskelet. 15.

Henson, P.M., 1971a. The immunologic release of constituents from neutrophil leukocytes. I. The role of antibody and complement on nonphagocytosable surfaces or phagocytosable particles. J. Immunol. 107, 1535–1546.

Henson, P.M., 1971b. The immunologic release of constituents from neutrophil leukocytes. II. Mechanisms of release during phagocytosis, and adherence to nonphagocytosable surfaces. J. Immunol. 107, 1547–1557.

Herbert, E.G., Oliver, W.C., Pharr, G.M., 2008. Nanoindentation and the dynamic characterization of viscoelastic solids. J. Phys. D. Appl. Phys. 41, 74021. https://doi.org/10.1088/0022-3727/41/7/074021

Hernandez, R., Weksler, J., Padsalgikar, A., Runt, J., 2008. In vitro oxidation of high polydimethylsiloxane content biomedical polyurethanes: correlation with the microstructure. J. Biomed. Mater. Res. Part A 87, 546–56. https://doi.org/10.1002/jbm.a.31823

Holmes, A.D., Hukins, D.W.L., 1996. Analysis of load-relaxation in compressed segments of lumbar spine. J. Med. Eng. Phys. 18, 99–104. https://doi.org/10.1016/1350-4533(95)00047-X

Hoogendoorn, W.E., van Poppel, M.N., Bongers, P.M., Koes, B.W., Bouter, L.M., 2000. Systematic review of psychosocial factors at work and private life as risk factors for back pain. Spine (Phila. Pa. 1976). 25, 2114–2125. https://doi.org/10.1097/00007632-200008150-00017

Hoy, D., Brooks, P., Blyth, F., Buchbinder, R., 2010. The Epidemiology of low back pain. Best Pract. Res. Clin. Rheumatol. 24, 769–781. https://doi.org/10.1016/j.berh.2010.10.002

Hukins, D.W.L., Mahomed, a, Kukureka, S.N., 2008. Accelerated aging for testing polymeric biomaterials and medical devices. Med. Eng. Phys. 30, 1270–4. https://doi.org/10.1016/j.medengphy.2008.06.001

Ianuzzi, A., Kurtz, S.M., Kane, W., Shah, P., Siskey, R., Ooij, A. Van, Bindal, R., Ross, R., Lanman, T., Buttner-Janz, K., Isaza, J., 2010. In Vivo Deformation, Surface Damage, and Biostability of Retrieved Dynesys Systems. Spine (Phila Pa 1976) 35, 1310–1316.

ISO, 2017. BS ISO 13781:2017 Implants for surgery — Homopolymers , copolymers and blends on poly(lactide) — In vitro degradation testing.

ISO, 2014. BS ISO 2393: Rubber test mixes — Preparation, mixing and vulcanization — Equipment and procedures.

ISO, 2011. BS EN ISO 6721: Plastics — Determination of dynamic mechanical properties.

ISO, 2010. BS EN ISO 10993-13: Identification and quantification of degradation products from polymeric medical device.

ISO, 2009. ISO 10993-18:2009 Biological evaluation of medical devices. Chemical characterisation of materials.

Izambert, O., Mitton, D., Thourot, M., Lavaste, F., 2003. Dynamic stiffness and damping of human intervertebral disc using axial oscillatory displacement under a free mass system. Eur. Spine J. 12, 562–566. https://doi.org/10.1007/s00586-003-0569-0

Jaganathan, S.K., Supriyanto, E., Murugesan, S., Balaji, A., Asokan, M.K., 2014. Biomaterials in cardiovascular research: applications and clinical implications. Biomed Res. Int. 2014, 1–11. https://doi.org/10.1155/2014/459465

Jewrajka, S.K., Kang, J., Erdodi, G., Kennedy, J.P., Yilgor, E., Yilgor, I., 2009. Polyisobutylene-Based Polyurethanes. II. Polyureas Containing Mixed PIB/PTMO Soft Segments. J. Polym. Sci. Part A Polym. Chem. 47, 2787–2797. https://doi.org/10.1002/pola

Kang, J., Erdodi, G., Brendel, C.M., Ely, D., Kennedy, J.P., 2010. Polyisobutylene-based polyurethanes. V. Oxidative-hydrolytic stability and biocompatibility. J. Polym. Sci. Part A Polym. Chem. 48, 2194–2203. https://doi.org/10.1002/pola.23989

Kanyanta, V., Ivankovic, A., 2010. Mechanical characterisation of polyurethane elastomer for biomedical applications. J. Mech. Behav. Biomed. Mater. 3, 51–62. https://doi.org/10.1016/j.jmbbm.2009.03.005

Kao, W.J., Zhao, Q.H., Hiltner, A., Anderson, J.M., 1994. Theoretical analysis of in vivo macrophage adhesion and foreign body gaint cell formation on polydimethylsiloxane, low density polyethylene, and polyetherurethanes. J. Biomed. Mater. Res. Part A 28, 73–79.

Kasra, M., Shirazi-Adl, A., Drouin, G., 1992. Dynamics of Human Lumbar Intervertebral Joints: Experimental and Finite-Element Investigations. Spine (Phila Pa 1976) 17, 93–102.

Khan, I., Smith, N., Jones, E., Finch, D.S., Cameron, R.E., 2005a. Analysis and evaluation of a biomedical polycarbonate urethane tested in an in vitro study and an ovine arthroplasty model. Part I: materials selection and evaluation. Biomaterials 26, 621–31. https://doi.org/10.1016/j.biomaterials.2004.02.065

Khan, I., Smith, N., Jones, E., Finch, D.S., Cameron, R.E., 2005b. Analysis and evaluation of a biomedical polycarbonate urethane tested in an in vitro study and an ovine arthroplasty model. Part II: in vivo investigation. Biomaterials 26, 633–43. https://doi.org/10.1016/j.biomaterials.2004.02.064

Khoueir, P., Kim, K.A., Wang, M.Y., 2007. Classification of posterior dynamic stabilization devices. Neurosurg. Focus 22, E3, 1–8. https://doi.org/10.3171/foc.2007.22.1.3

Kondyurin, A., Bilek, M., 2015. Chapter 7: Hardness, in: Ion Beam Treatment of Polymers. pp. 161–173. https://doi.org/10.1016/B978-0-08-099445-1.00007-9

Kondyurin, A., Bilek, M., 2014. Ion beam treatment of polymers: application aspects from medicine to space, Second. ed. Elservier.

Kuimova, M.K., Chan, K.L., Kazarian, S.G., 2009. Chemical imaging of live cancer cells in the natural aqueous environment. Appl Spectrosc 63, 164–171. https://doi.org/10.1366/000370209787391969

Kurtz, S.M., Edidin, A.A., 2006. Spine Technology Handbook, 1st ed. Elservier Academic Press, USA.

Kurtz, S.M., Steinbeck, M., Ianuzzi, A., Ooij, A. Van, Punt, I.M., Isaza, J., Ross, E.R.S., 2009. Retrieval analysis of motion preserving spinal devices and periprosthetic tissues. SAS J. 3, 161–177. https://doi.org/10.1016/j.esas.2009.11.003

Labow, R., Meek, E., Santerre, J., 1999. The biodegradation of poly(urethanes) by the esterolytic activity of serine proteases and oxidative enzyme systems. J. Biomater. Sci. Polym. Ed. 10, 669–713.

Lavecchia, C.E., Espino, D.M., Moerman, K.M., Tse, K.M., Robinson, D., Lee, P.V.S., Shepherd, D.E.T., 2018. Lumbar model generator: a tool for the automated generation of a parametric scalable model of the lumbar spine. J. R. Soc. Interface 15, 1–13. https://doi.org/10.1098/rsif.2017.0829

Lawless, B.M., Barnes, S.C., Espino, D.M., Shepherd, D.E.T., 2016. Viscoelastic properties of a spinal posterior dynamic stabilisation device. J. Mech. Behav. Biomed. Mater. 59, 519–526. https://doi.org/10.1016/j.jmbbm.2016.03.011

Lawless, B.M., Espino, D.M., Shepherd, D.E.T., 2018. In vitro oxidative degradation of a spinal posterior dynamic stabilisation device. J. Biomed. Mater. Res. Part B Appl. Biomater. 106, 1237–1244. https://doi.org/10.1002/jbm.b.33913

Lawless, B.M., Sadeghi, H., Temple, D.K., Dhaliwal, H., Espino, D.M., Hukins, D.W.L., 2017. Viscoelasticity of articular cartilage: Analysing the effect of induced stress and the restraint of bone in a dynamic environment. J. Mech. Behav. Biomed. Mater. 75, 293–

301. https://doi.org/10.1016/j.jmbbm.2017.07.040

Leahy, J.C., Hukins, D.W.L., 2001. Viscoelastic properties of the nucleus pulposus of the intervertebral disk in compression. J. Mater. Sci. Mater. Med. 12, 689–692. https://doi.org/10.1023/A:1011212425029

Lee, S.-E., Park, S.-B., Jahng, T.-A., Chung, C.-K., Kim, H.-J., 2008. Clinical experience of the dynamic stabilization system for the degenerative spine disease. J. Korean Neurosurg. Soc. 43, 221–226. https://doi.org/10.3340/jkns.2008.43.5.221

LeHuec, J.C., Kiaer, T., Freisem, T., Mathews, T., Liu, M., Eisermann, L., 2003. Shock absorption in lumbar disc prosthesis: a preliminary mechanical study. J. Spinal Disord. Tech. 16, 346–351.

Li, Y., Xu, M., 2007. Hysteresis loop and energy dissipation of viscoelastic solid models. Mech. Time-Dependent Mater. 11, 1–4.

Liu, J., Qi, H., 2010. Dissipated energy function, hysteresis and precondition of a viscoelastic solid model. Nonlinear Anal. Real World Appl. 11, 907–912. https://doi.org/10.1016/j.nonrwa.2009.01.033

Lumoa, K., Riihimaki, H., Raininko, R., Luukkonen, R., Lamminen, A., Viikari-Juntura, E., 1998. Lumbar disc degeneration in relation to occupation. Scand. J. Work. Environ. Health 358–366.

Lutz, J.A., Otten, P., Maestretti, G., 2012. Late infections after dynamic stabilization of the lumbar spine with Dynesys. Eur. Spine J. 21, 2573–9. https://doi.org/10.1007/s00586-012-2366-0

Magnusson, M.L., Pope, M.H., Wilder, D.G., Areskoug, B., 1996. Are occupational drivers at an increased risk for developing musculoskeletal disorders? Spine (Phila. Pa. 1976). 21, 710–717. https://doi.org/10.1097/00007632-199603150-00010

Mahomed, A., Chidi, N.M., Hukins, D.W.L., Kukureka, S.N., Shepherd, D.E.T., 2008. Frequency dependence of viscoelastic properties of medical grade silicones. J. Biomed. Mater. Res. B. Appl. Biomater. 89, 210–216. https://doi.org/10.1002/jbm.b.31208

Mahomed, A., Hukins, D.W.L., Kukureka, S.N., 2015. Effect of accelerated aging on the viscoelastic properties of a medical grade silicone. Biomed. Mater. Eng. 25, 415–23. https://doi.org/10.3233/BME-151538

Mahomed, A., Hukins, D.W.L., Kukureka, S.N., 2009a. Viscoelastic Properties of Silastic Medical Grade Silicones: Implications for Finger-Joint Replacement. J. Polym. Mater.

Mahomed, A., Hukins, D.W.L., Kukureka, S.N., 2009b. Viscoelastic Properties of Medical Grade Silicones in tension. J. Polym. Mater. 26, 199–206.

Mahomed, A., Hukins, D.W.L., Kukureka, S.N., Shepherd, D.E.T., 2010. Effect of accelerated aging on the viscoelastic properties of Elast-Eon: A polyurethane with soft poly(dimethylsiloxane) and poly(hexamethylene oxide) segments. Mater. Sci. Eng. C 30, 1298–1303. https://doi.org/10.1016/j.msec.2010.07.014

Mahomed, A., Moghadas, P.M., Shepherd, D.E.T., Hukins, D.W.L., Roome, A., Johnson, S., 2012. Effect of Axial Load on the Flexural Properties of an Elastomeric Total Disc Replacement. Spine J. 37, 908–912. https://doi.org/10.1097/BRS.0b013e31824da3ba

Majumdar, T., Cooke, M.E., Lawless, B.M., Bellier, F., Hughes, E.A.B., Grover, L.M., Jones, S.W., Cox, S.C., 2018. Formulation and viscoelasticity of mineralised hydrogels for use in

bone-cartilage interfacial reconstruction. J. Mech. Behav. Biomed. Mater. 80, 33–41. https://doi.org/10.1016/j.jmbbm.2018.01.016

Marini, G., Huber, G., Püschel, K., Ferguson, S.J., 2015. Nonlinear dynamics of the human lumbar intervertebral disc. J. Biomech. 48, 479–488. https://doi.org/10.1016/j.jbiomech.2014.12.006

Marketsandmarkets.com, 2016. Biomaterials Market by Type of Material (Metallic, Ceramic, Polymers, Natural Biomaterials) & Application (Cardiovascular, Orthopedic, Dental, Plastic Surgery, Wound Healing, Neurology, Tissue Engineering, Ophthalmology) - Global Forecast to 2021 [WWW Document]. Marketsandmarkets.com. URL http://www.marketsandmarkets.com/Market-Reports/biomaterials-393.html

Martin, D.J., Poole Warren, L.A., Gunatillake, P.A., McCarthy, S.J., Meijs, G.F., Schindhelm, K., 2001. New methods for the assessment of in vitro and in vivo stress cracking in biomedical polyurethanes. Biomaterials 22, 973–978. https://doi.org/10.1016/S0142-9612(00)00262-3

Martini, F., Nath, J., Bartholomew, E., 2012. Fundamentals of anatomy and physiology, 9th Ed. ed. Pearson.

Mattei, G., Cacopardo, L., Ahluwalia, A., 2017. Micro-mechanical viscoelastic properties of crosslinked hydrogels using the nano-epsilon dot method. Materials (Basel). 10. https://doi.org/10.3390/ma10080889

Mattei, G., Gruca, G., Rijnveld, N., Ahluwalia, A., 2015. The nano-epsilon dot method for strain rate viscoelastic characterisation of soft biomaterials by spherical nano-indentation. J. Mech. Behav. Biomed. Mater. 50, 150–159. https://doi.org/10.1016/j.jmbbm.2015.06.015

McBane, J.E., Santerre, J.P., Labow, R.S., 2007. The interaction between hydrolytic and oxidative pathways in macrophage-mediated polyurethane degradation. J. Biomed. Mater. Res. Part A 82, 984–994. https://doi.org/10.1002/jbm.a

Meijs, G.F., McCarthy, S.J., Rizzardo, E., Chen, Y.-C., Chatelier, R.C., Brandwood, A., Schindhelm, K., 1993. Degradation of medical-grade polyurethane elastomers: The effect of hydrogen peroxide in vitro. J. Biomed. Mater. Res. 27, 345–356.

Menard, K.P., 2008. Dynamic Mechanical Analysis: A Practical Introduction, 2nd ed. CRC press, Taylor & Francis Group, Boca Raton, Florida.

Mishra, A., Seethamraju, K., Delaney, J., Willoughby, P., Faust, R., 2015. Long-term *in vitro* hydrolytic stability of thermoplastic polyurethanes. J. Biomed. Mater. Res. Part A 103, 3798–3806. https://doi.org/10.1002/jbm.a.35523

Mukherjee, S., Gowen, A., 2015. A review of recent trends in polymer characterization using non-destructive vibrational spectroscopic modalities and chemical imaging. Anal. Chim. Acta 895, 12–34. https://doi.org/10.1016/j.aca.2015.09.006

Murata, H., Taguchi, N., Hamada, T., McCabe, J.F., 2000. Dynamic viscoelastic properties and the age changes of long-term soft denture liners. Biomaterials 21, 1421–1427. https://doi.org/10.1016/S0142-9612(00)00010-7

Neukamp, M., Roeder, C., Veruva, S.Y., MacDonald, D.W., Kurtz, S.M., Steinbeck, M.J., 2015. In vivo compatibility of Dynesys spinal implants: a case series of five retrieved periprosthetic tissue samples and corresponding implants. Eur. Spine J. 24, 1074–84. https://doi.org/10.1007/s00586-014-3705-0

NHS England, 2013. Complex Spinal Surgery (all ages), NHS England. https://doi.org/10.1080/14999013.2014.906516

Owen, A.J., 1995. Uses of Derivative Spectroscopy. Agil. Technol. 8.

Padsalgikar, A., Cosgriff-Hernandez, E., Gallagher, G., Touchet, T., Iacob, C., Mellin, L., Norlin-weissenrieder, A., Runt, J., 2015. Limitations of predicting in vivo biostability of multiphase polyurethane elastomers using temperature-accelerated degradation testing. J. Biomed. Mater. Res. Part B Appl. Biomater. 103, 159–168. https://doi.org/10.1002/jbm.b.33161

Palepu, V., Kodigudla, M., Goel, V.K., 2012. Biomechanics of Disc Degeneration. Adv. Orthop. 2012, 1–17. https://doi.org/10.1155/2012/726210

Panjabi, M.M., Andersson, G.B., Jorneus, L., Hult, E., Mattsson, L., 1986. In vivo measurements of spinal column vibrations. J. Bone Jt. Surg. 68, 695–702.

Placet, V., Foltête, E., 2010. Is Dynamic Mechanical Analysis (DMA) a non-resonance technique? EPJ Web Conf. 6, 1–8. https://doi.org/10.1051/epjconf/20100641004

Pollintine, P., Dolan, P., Tobias, J.H., Adams, M. a., 2004. Intervertebral Disc Degeneration Can Lead to "Stress-Shielding" of the Anterior Vertebral Body. Spine (Phila. Pa. 1976). 29, 774–782. https://doi.org/10.1097/01.BRS.0000119401.23006.D2

Pretsch, T., Jakob, I., Müller, W., 2009. Hydrolytic degradation and functional stability of a segmented shape memory poly(ester urethane). Polym. Degrad. Stab. 94, 61–73. https://doi.org/10.1016/j.polymdegradstab.2008.10.012

Rajaee, S.S., Bae, H.W., Kanim, L.E. a., Delamarter, R.B., 2012. Spinal Fusion in the United States. Spine (Phila. Pa. 1976). 37, 67–76. https://doi.org/10.1097/BRS.0b013e31820cccfb

Ramakrishna, S., Mayer, J., Wintermantel, E., Leong, K.W., 2001. Biomedical applications of polymer-composite materials: a review. Compos. Sci. Technol. 61, 1189–1224. https://doi.org/10.1016/S0266-3538(00)00241-4

Ratner, B.D., Gladhill, K.W., Horbett, T. a, 1988. Analysis of in vitro enzymatic and oxidative degradation of polyurethanes. J. Biomed. Mater. Res. 22, 509–27. https://doi.org/10.1002/jbm.820220607

Rischke, B., Ross, R.S., Jollenbeck, B.A., Zimmers, K.B., Defibaugh, N.D., 2011. Preclinical and clinical experience with a viscoelastic total disc replacement. SAS J. 5, 97–107. https://doi.org/10.1016/j.esas.2011.08.001

S14 Implants, 2017. B Dyn - Dynamic Stabilization [WWW Document]. S14 Implant. Website. URL http://www.s14-implants.com/en/b-dyn/ (accessed 2.18.17).

Sarkar, D., Lopina, S.T., 2007. Oxidative and enzymatic degradations of L-tyrosine based polyurethanes. Polym. Degrad. Stab. 92, 1994–2004. https://doi.org/10.1016/j.polymdegradstab.2007.08.003

Savitzky, A., Golay, M.J.E., 1964. Smoothing and Differentiation of Data by Simplified Least Squares Procedures. Anal. Chem. 36, 1627–1639. https://doi.org/10.1021/ac60214a047

Schmoelz, W., Erhart, S., Unger, S., Disch, A.C., 2012. Biomechanical evaluation of a posterior non-fusion instrumentation of the lumbar spine. Eur. Spine J. 21, 939–945. https://doi.org/10.1007/s00586-011-2121-y

Schmoelz, W., Huber, J.F., Nydegger, T., Claes, L., Wilke, H.J., 2003. Dynamic Stabilization

of the Lumbar Spine and Its Effects on Adjacent Segments An In Vitro Experiment. J. Spinal Disord. Tech. 16, 418–423.

Schubert, M.A., Wiggins, M.J., Anderson, J.M., Hiltner, A., 1997. Role of oxygen in biodegradation of poly(etherurethane urea) elastomers. J. Biomed. Mater. Res. 34, 519–30.

Schubert, M.A., Wiggins, M.J., Schaefeq, M.P., Hiltner, A., Anderson, J.M., 1995. Oxidative biodegradation mechanisms of biaxially strained poly (etherurethane urea) elastomers. J. Biomed. Mater. Res. 29, 337–347.

Schwarzenbach, O., Rohrbach, N., Berlemann, U., 2010. Segment-by-segment stabilization for degenerative disc disease: A hybrid technique. Eur. Spine J. 19, 1010–1020. https://doi.org/10.1007/s00586-010-1282-4

Sengupta, D., Bucklen, B., Ingalhalikar, A., Muzumdar, A., Khalil, S., 2013. Does Semi-Rigid Instrumentation Using Both Flexion and Extension Dampening Spacers Truly Provide an Intermediate Level of Stabilization? Adv. Orthop. 2013, 1–9.

Sengupta, D.K., 2004. Dynamic stabilization devices in the treatment of low back pain. Orthop. Clin. North Am. 35, 43–56. https://doi.org/10.1016/S0030-5898(03)00087-7

Serhan, H., Mhatre, D., Defossez, H., Bono, C.M., 2011. Motion-preserving technologies for degenerative lumbar spine: The past, present and future horizons. SAS J. 5, 75–89. https://doi.org/10.1016/j.esas.2011.05.001

Serkis, M., Špírková, M., Poręba, R., Hodan, J., Kredatusová, J., Kubies, D., 2015. Hydrolytic stability of polycarbonate-based polyurethane elastomers tested in physiologically simulated conditions. Polym. Degrad. Stab. 119, 23–34. https://doi.org/10.1016/j.polymdegradstab.2015.04.030

Sheikh, Z., Brooks, P.J., Barzilay, O., Fine, N., Glogauer, M., 2015. Macrophages, foreign body giant cells and their response to implantable biomaterials. Materials (Basel). 8, 5671–5701. https://doi.org/10.3390/ma8095269

Shen, M., Zhang, K., Koettig, P., Welch, W.C., Dawson, J.M., 2011. In vivo biostability of polymeric spine implants: retrieval analyses from a United States investigational device exemption study. Eur. Spine J. 20, 1837–49. https://doi.org/10.1007/s00586-011-1812-8

Shi, W., Li, X.Y., Dong, H., 2001. Improved wear resistance of ultra-high molecular weight polyethylene by plasma immersion ion implantation. Wear 250, 544–552. https://doi.org/10.1016/S0043-1648(01)00636-6

Simmons, A., Hyvarinen, J., Odell, R.A., Martin, D.J., Gunatillake, P.A., Noble, K.R., Poole-Warren, L.A., 2004. Long-term in vivo biostability of poly(dimethylsiloxane)/poly(hexamethylene oxide) mixed macrodiol-based polyurethane elastomers. Biomaterials 25, 4887–4900. https://doi.org/10.1016/j.biomaterials.2004.01.004

Simmons, A., Hyvarinen, J., Poole-Warren, L., 2006. The effect of sterilisation on a poly(dimethylsiloxane)/poly(hexamethylene oxide) mixed macrodiol-based polyurethane elastomer. Biomaterials 27, 4484–97. https://doi.org/10.1016/j.biomaterials.2006.04.017

Simmons, A., Padsalgikar, A.D., Ferris, L.M., Poole-Warren, L.A., 2008. Biostability and biological performance of a PDMS-based polyurethane for controlled drug release. Biomaterials 29, 2987–95. https://doi.org/10.1016/j.biomaterials.2008.04.007

Smeathers, J.E., Joanes, D.N., 1988. Dynamic compressive properties of human lumbar intervertebral joints: a comparison between fresh and thawed specimens. J. Biomech. 21, 425–433. https://doi.org/10.1016/0021-9290(88)90148-0

Smith, B.C., 1998. Infrared spectral interpretation: a systematic approach, First Edit. ed. CRC Press.

Speight, J.G., 2017. Organic Chemistry, Environmental Organic Chemistry for Engineers. https://doi.org/10.1016/B978-0-12-804492-6.00002-2

St John, K.R., 2014. The use of polyurethane materials in the surgery of the spine: a review. Spine J. 14, 3038–47. https://doi.org/10.1016/j.spinee.2014.08.012

Steidel, R.F., 1989. An Introduction to Mechanical Vibrations, Third Edit. ed. John Wiley & Sons, New York, USA.

Stokes, K., 1988. Polyether polyurethanes: biostable or not? J. Biomater. Appl. 3, 228–259.

Stokes, K., Anderson, J.M., McVenes, R., 1995. Polyurethane Elastomer Biostability. J. Biomater. Appl. 9, 321–354.

Stokes, K., Coury, A., Urbanski, P., 1987. Autooxidative Degradation of Implanted Polyether Polyurethane Devices. J. Biomater. Appl. 1, 411–448.

Sze, J.Y., Tay, B.K., 2006. Carbon ion implantation of ultra-high molecular weight polyethylene using filtered cathodic vacuum arc with substrate pulse biasing. Surf. Coatings Technol. 200, 4104–4110. https://doi.org/10.1016/j.surfcoat.2005.04.001

Takahara, A., Coury, A.J., Hergenrother, R.W., Cooper, S.L., 1991. Effect of soft segment chemistry on the biostability of segmented polyurethanes. I. In vitro oxidation. J. Biomed. Mater. Res. 25, 341–356.

Tanzi, M.C., Farè, S., Petrini, P., 2000. In vitro stability of polyether and polycarbonate urethanes. J. Biomater. Appl. 14, 325–348.

Tanzi, M.C., Mantovani, D., Petrini, P., Guidoin, R., Laroche, G., 1997. Chemical stability of polyether urethanes versus polycarbonate urethanes. J. Biomed. Mater. Res. 36, 550–559.

Taylor, J.E., Laity, P.R., Freeburn, S., Wong, S.S., Norris, K., Khunkamchoo, P., Cable, M., Andrews, G., Johnson, A.F., Cameron, R.E., 2005. Effect of processing route and acetone pre-treatment on the biostability of pellethane materials used in medical device applications. Biomaterials 26, 6467–6476. https://doi.org/10.1016/j.biomaterials.2005.04.009

Temple, D.K., Cederlund, A.A., Lawless, B.M., Aspden, R.M., Espino, D.M., 2016. Viscoelastic properties of human and bovine articular cartilage: a comparison of frequency-dependent trends. BMC Musculoskelet. Disord. 17;419. https://doi.org/10.1186/s12891-016-1279-1

Thoma, R.J., Phillips, R.E., 1987. Note: Studies of poly(ether) urethane pacemaker lead insulation oxidation. J. Biomed. Mater. Res. 21, 525–530.

Trommsdorff, U., Koettig, P., 2005. Analysis of retrievals of a dynamic stabilization system for the spine, in: Eurospine 2005. Barcelona, Spain, p. Poster.

Trommsdorff, U., Zurbrugg, D., Abt, N., 2004a. Analysis of retrieved components of a dynamic stabilization system for the spine, in: 68th Annuak Meeting of the German Society for Surgery. Berlin, Germany.

Trommsdorff, U., Zurbrugg, D., Stoll, T.M., 2004b. In-vivo degradation of polycarbonate-urethane with and without contact to an abscess, in: 7th World Biomaterials Congress. Sydney, Australia.

van den Broek, P.R., Huyghe, J.M., Ito, K., 2012a. Biomechanical Behavior of a Biomimetic Artificial Intervertebral Disc. Spine (Phila. Pa. 1976). 37, E367–E373. https://doi.org/10.1097/BRS.0b013e3182326305

van den Broek, P.R., Huyghe, J.M., Wilson, W., Ito, K., 2012b. Design of next generation total disk replacements. J. Biomech. 45, 134–40. https://doi.org/10.1016/j.jbiomech.2011.09.017

van Hoorn, H., Kurniawan, N.A., Koenderink, G.H., Iannuzzi, D., 2016. Local dynamic mechanical analysis for heterogeneous soft matter using ferrule-top indentation. Soft Matter 12, 3066–3073. https://doi.org/10.1039/C6SM00300A

Vogels, R.R.M., Lambertz, A., Schuster, P., Jockenhoevel, S., Bouvy, N.D., Disselhorst-Klug, C., Neumann, U.P., Klinge, U., Klink, C.D., 2017. Biocompatibility and biomechanical analysis of elastic TPU threads as new suture material. J. Biomed. Mater. Res. - Part B Appl. Biomater. 105, 99–106. https://doi.org/10.1002/jbm.b.33531

Wands, I., Shepherd, D.E.T., Hukins, D.W.L., 2008. Viscoelastic properties of composites of calcium alginate and hydroxyapatite. J. Mater. Sci. Mater. Med. 19, 2417–21. https://doi.org/10.1007/s10856-007-3364-3

Ward, B., Anderson, J., Ebert, M., McVenes, R., Stokes, K., 2006. In vivo biostability of polysiloxane polyether polyurethanes: Resistance to metal ion oxidation. J. Biomed. Mater. Res. Part A 77, 380–389. https://doi.org/10.1002/jbm.a.30553

Ward, R., Anderson, J., McVenes, R., Stokes, K., 2006. In vivo biostability of polysiloxane polyether polyurethanes: Resistance to biologic oxidation and stress cracking. J. Biomed. Mater. Res. Part A An Off. J. Soc. Biomater. Japanese Soc. Biomater. Aust. Soc. Biomater. Korean Soc. Biomater. 77, 580–589. https://doi.org/10.1002/jbm.a

Ward, R., Jones, R., 2011. Polyurethanes and Silicone Polyurethane Copolymers, Vol. I. ed, Comprehensive Biomaterials. Elsevier Ltd. https://doi.org/10.1016/B978-0-08-055294-1.00272-5

Weems, A.C., Wacker, K.T., Carrow, J.K., Boyle, A.J., Maitland, D.J., 2017. Shape memory polyurethanes with oxidation-induced degradation: In vivo and in vitro correlations for endovascular material applications. Acta Biomater. 59, 33–44. https://doi.org/10.1016/j.actbio.2017.06.030

Weiss, A.J., Elixhauser, A., Andrews, R.M., 2014. Characteristics of Operating Room Procedures in U.S. Hospitals, 2011: Statistical Brief #170, Healthcare Cost and Utilization Project (HCUP): Agency for Health Care Policy and Research (US).

Welch, W.C., Cheng, B.C., Awad, T.E., Davis, R., Maxwell, J.H., Delamarter, R., Wingate, J.K., Sherman, J., Macenski, M.M., 2007. Clinical outcomes of the Dynesys dynamic neutralization system: 1-year preliminary results. Neurosurg. Focus 22, E8. https://doi.org/10.3171/foc.2007.22.1.8

Wiggins, M.J., Macewan, M., Anderson, J.M., Hiltner, A., 2004. Effect of soft-segment chemistry on polyurethane biostability during in vitro fatigue loading. J. Biomed. Mater. Res. 68, 668–683.

Wiggins, M.J., Wilkoff, B., Anderson, J.M., Hiltner, A., 2001. Biodegradation of polyether

polyurethane inner insulation in bipolar pacemaker leads. J. Biomed. Mater. Res. 58, 302–7.

Wilder, D.G., Woodworth, B.B., Frymoyer, J.W., Pope, M.H., 1982. Vibration and the human spine. Spine (Phila. Pa. 1976). 7, 243–254.

Wilke, H.J., Heuer, F., Schmidt, H., 2009. Prospective design delineation and subsequent in vitro evaluation of a new posterior dynamic stabilization system. Spine (Phila. Pa. 1976). 34, 255–61. https://doi.org/10.1097/BRS.0b013e3181920e9c

Wilkoff, B.L., Rickard, J., Tkatchouk, E., Padsalgikar, A.D., Gallagher, G., Runt, J., 2015. The biostability of cardiac lead insulation materials as assessed from long-term human implants. J. Biomed. Mater. Res. Part B Appl. Biomater. 104, 411–421. https://doi.org/10.1002/jbm.b.33405

Wright, S.D., Silverstein, S.C., 1983. Phagocytosing macrophages exclude proteins from the zones of contact with opsonized targets. Nature 209.

Wu, Y., Sellitti, C., Anderson, J.M., Hiltner, A., Lodoen, G.A., Payet, C.R., 1992. An FTIR-ATR Investigation of In Vivo Poly(ether urethane) Degradation. J. Appl. Polym. Sci. 46, 201–211.

Zhao, Q., Topham, N., Anderson, J.M., Hiltner, A., Lodoen, G., Payet, C.R., 1991. Foreign-body giant cells and polyurethane biostability: in vivo correlation of cell adhesion and surface cracking. J. Biomed. Mater. Res. 25, 177–83. https://doi.org/10.1002/jbm.820250205

Zhao, Q.H., Casas-Bejar, J., Urbanski, P., Stokes, K., 1995. Glass Wool-H2O2/CoCl2 test system for in vitro evaluation of biodegradative stress cracking in polyurethane elastomers. J. Biomed. Mater. Res. 29, 467–475.

Zhao, Q.H., McNally, A.K., Rubin, K.R., Renier, M., Wu, Y., Rose-Caprara, V., Anderson, J.M., Hiltner, A., Urbanski, P., Stokes, K., 1993. Human plasma α2-macroglobulin promotes in vitro oxidative stress cracking of pellethane 2363-80A: In vivo and in vitro correlations. J. Biomed. Mater. Res. Part A 27, 379–388.

Zhou, Z., Gao, M., Wei, F., Liang, J., Deng, W., Dai, X., Zhou, G., Zou, X., 2014. Shock absorbing function study on denucleated intervertebral disc with or without hydrogel injection through static and dynamic biomechanical tests in vitro. Biomed Res. Int. Vol: 2014, 461724, 7 Pages. https://doi.org/10.1155/2014/461724

Chapter 8

Appendices

8 Appendices

8.1 Appendix A – dimensions of the ASTM D1708 specimens

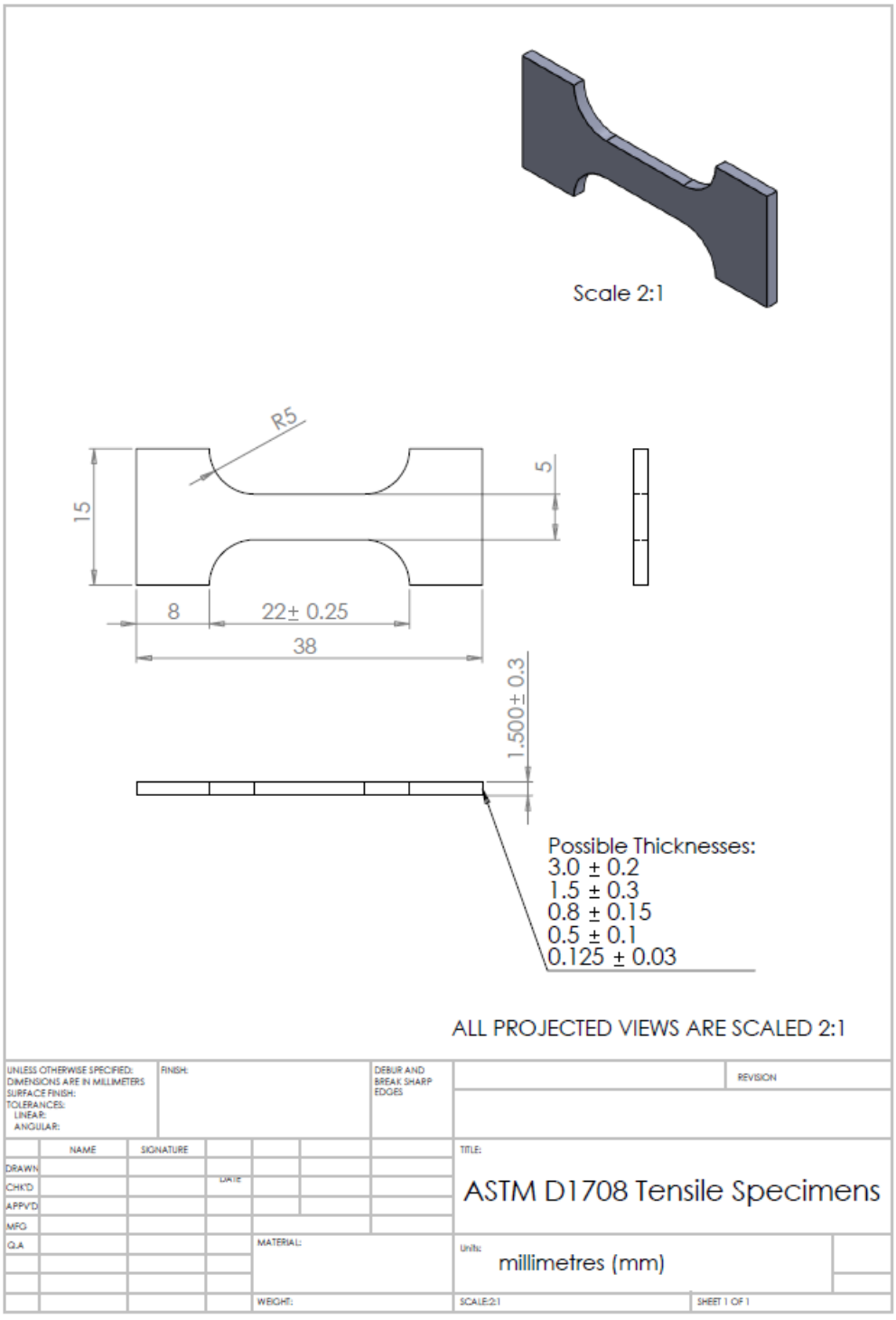

Figure 8-1: Dimensions of the ASTM D1708 specimens

8.2 Appendix B – dimensions of the BDyn device and components

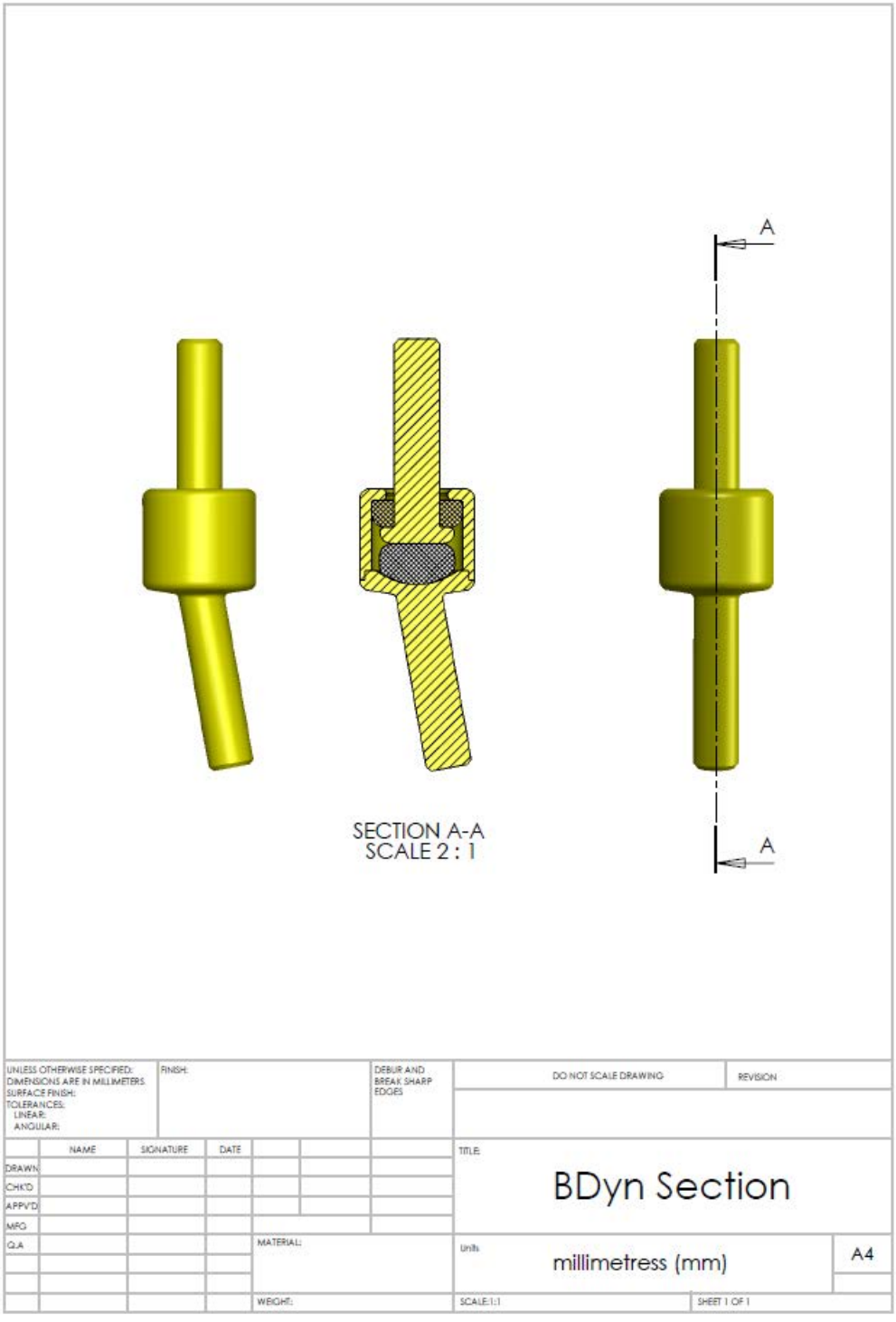

Figure 8-2: Section view of the BDyn device

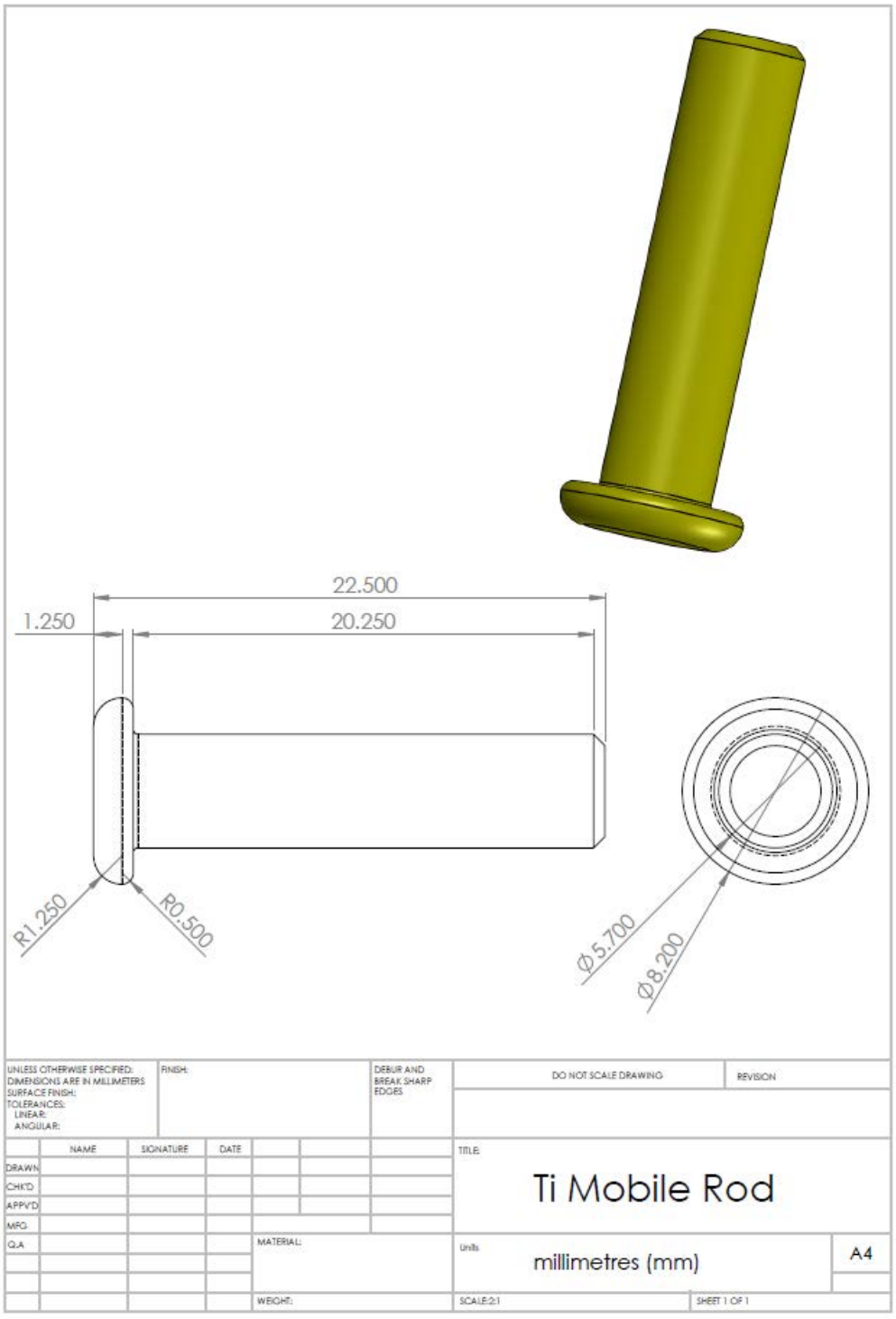

Figure 8-3: Dimensions of the titanium alloy mobile rod of the BDyn device

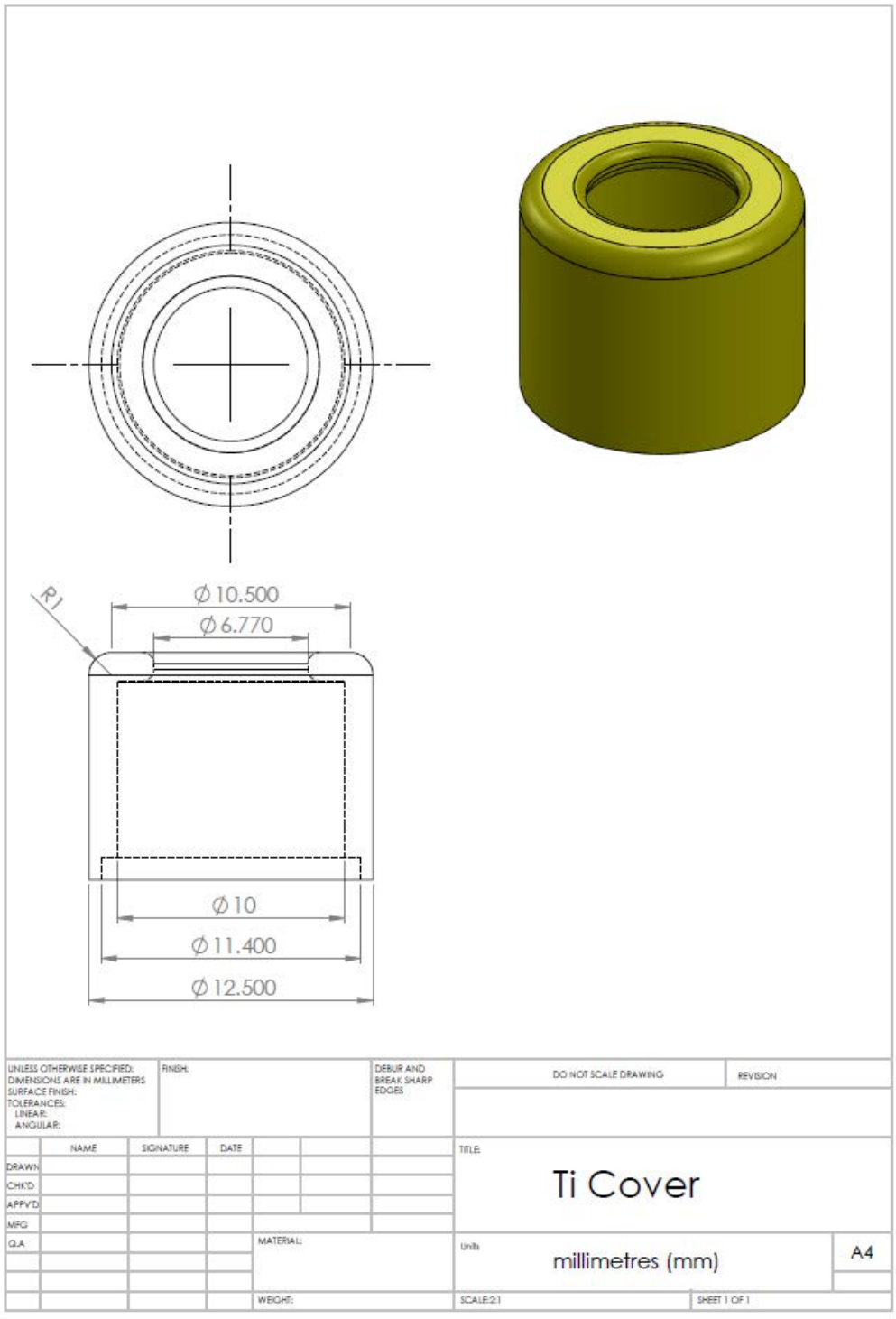

Figure 8-4: Dimensions of the titanium alloy housing of the BDyn device

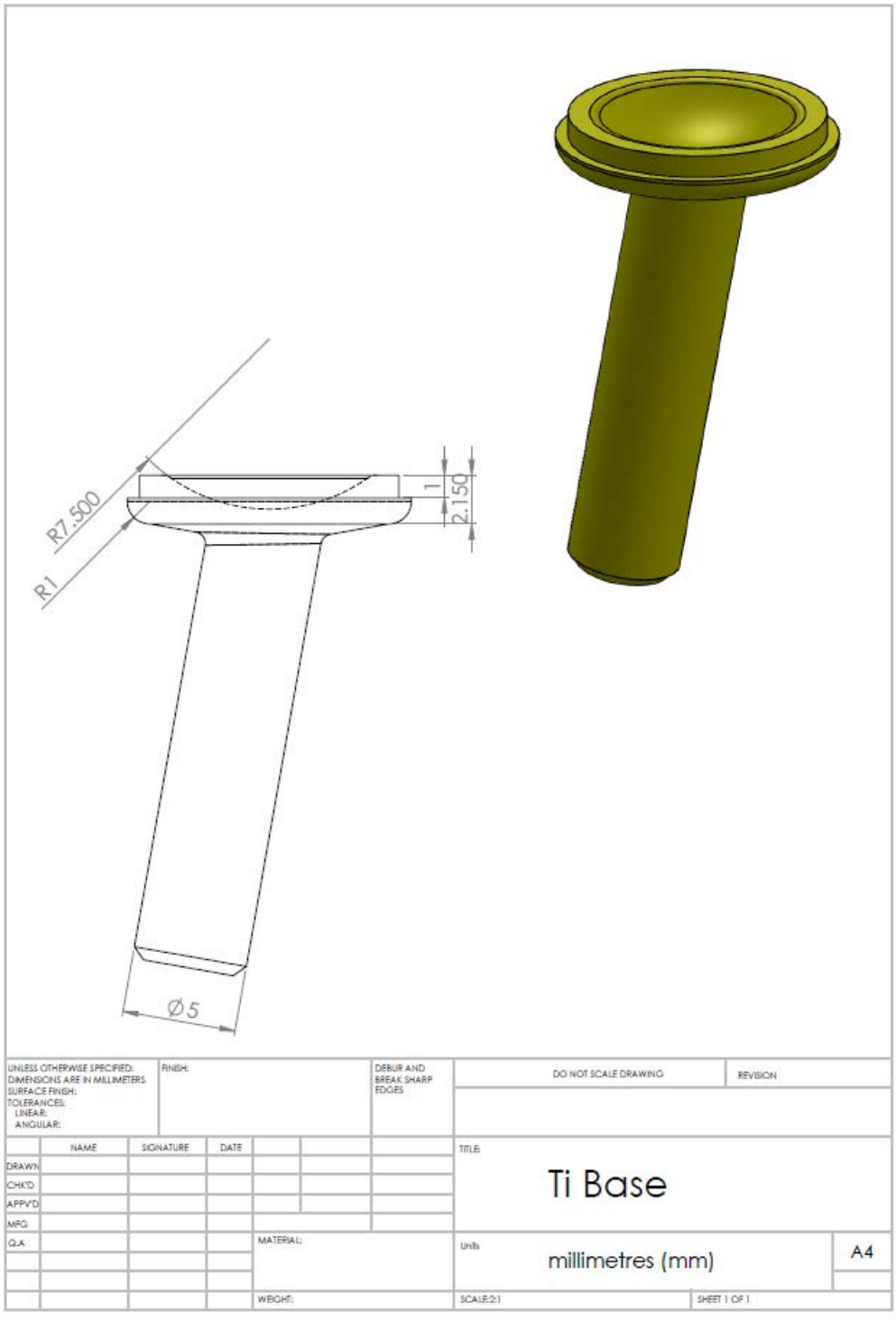

Figure 8-5: Dimensions of the titanium alloy fixed rod of the BDyn device

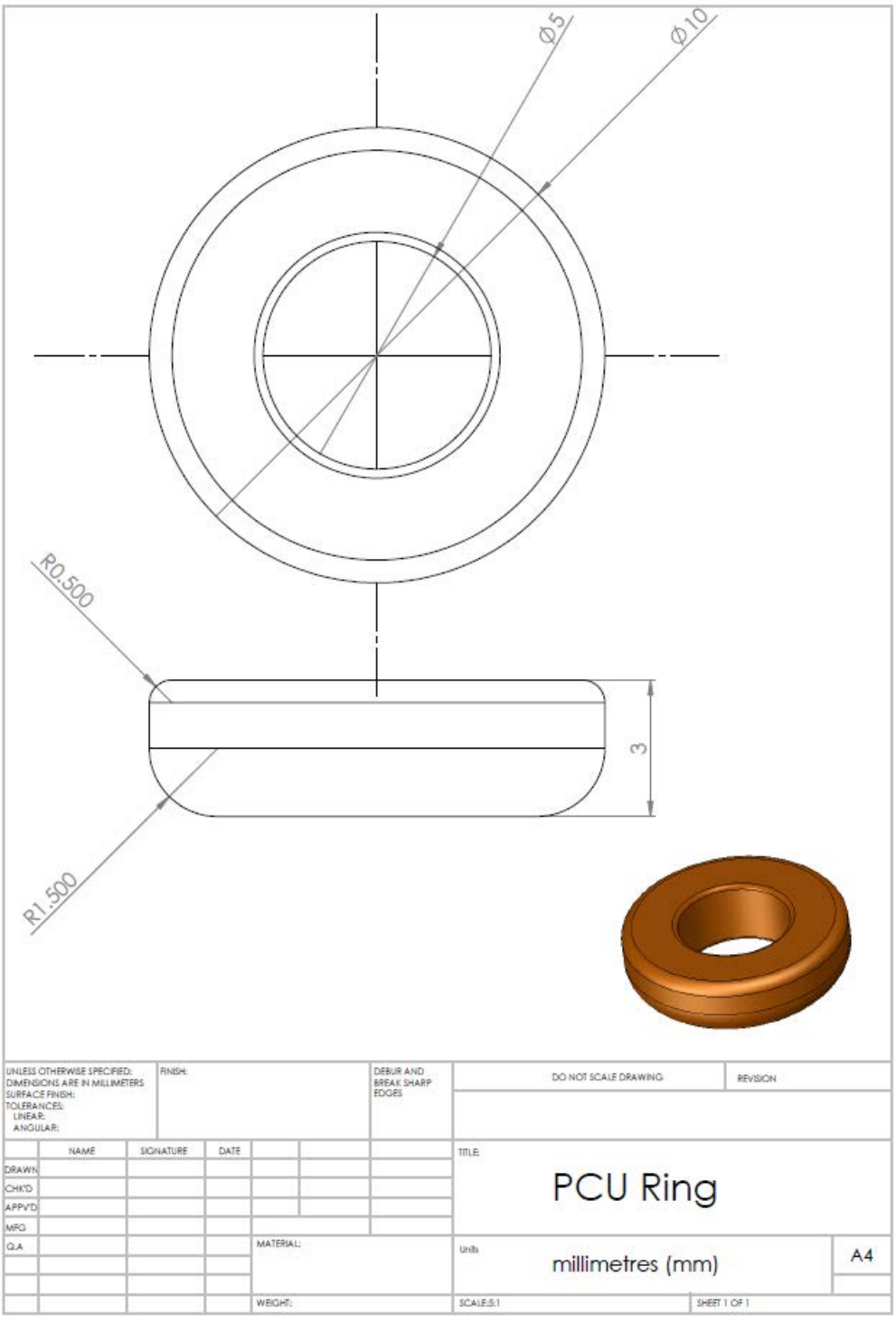

Figure 8-6: Dimensions of the PCU ring of the BDyn device

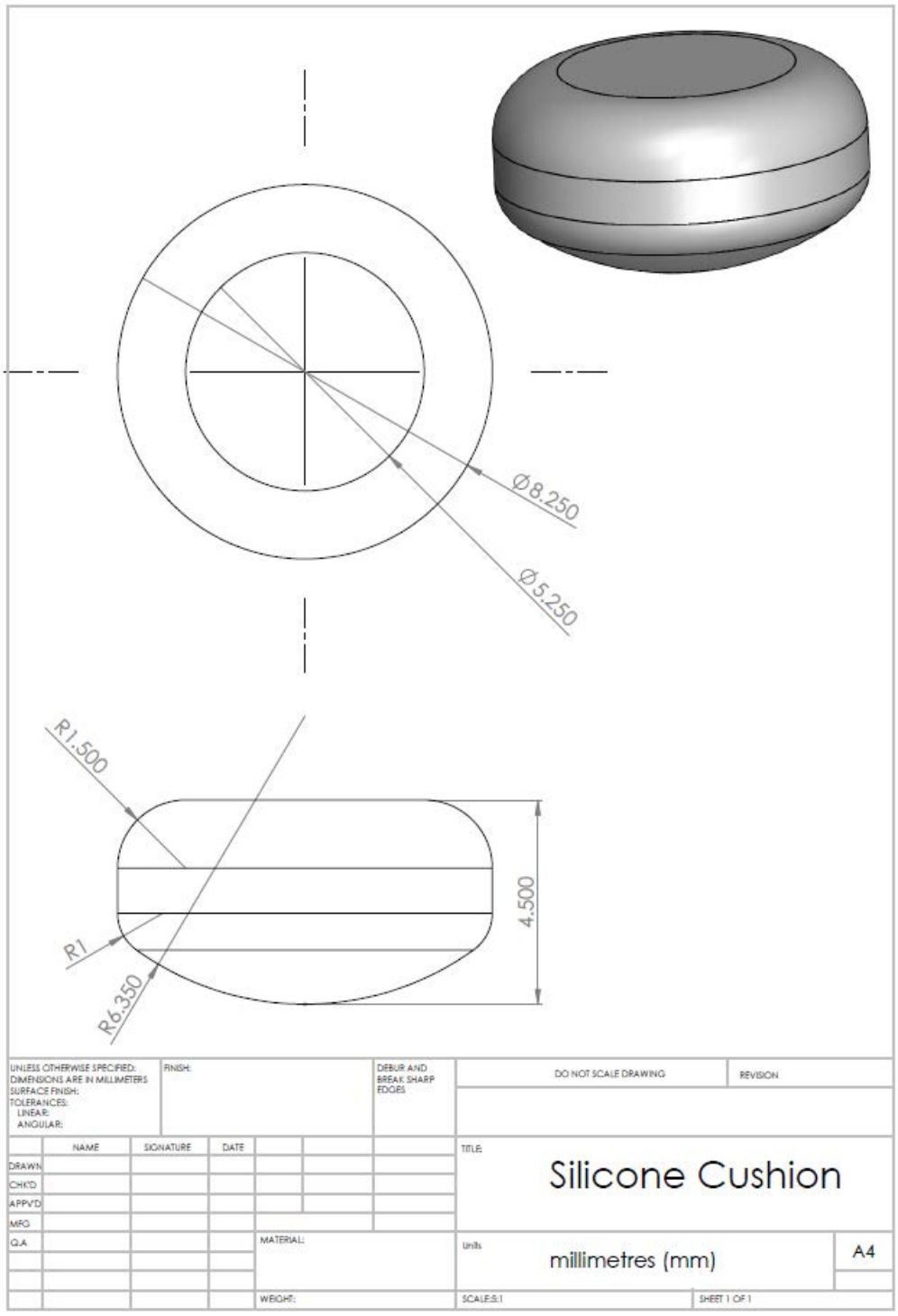

Figure 8-7: Dimensions of the silicone cushion of the BDyn device

8.3 Appendix C – dimensions of the µDMA probe

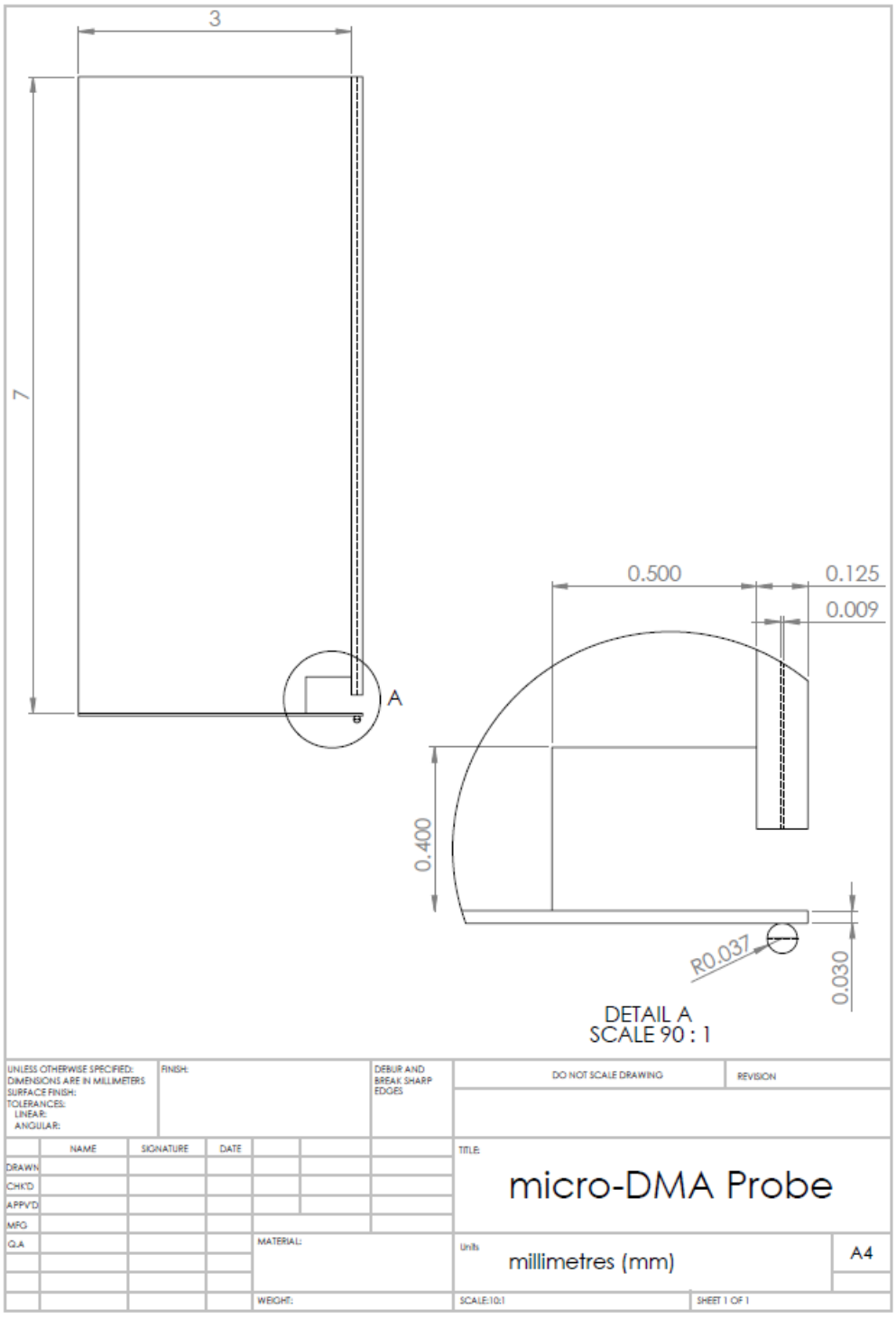

Figure 8-8: Dimensions of the micro-DMA probe

8.4 Appendix D – dimensions of the DMA water bath chamber

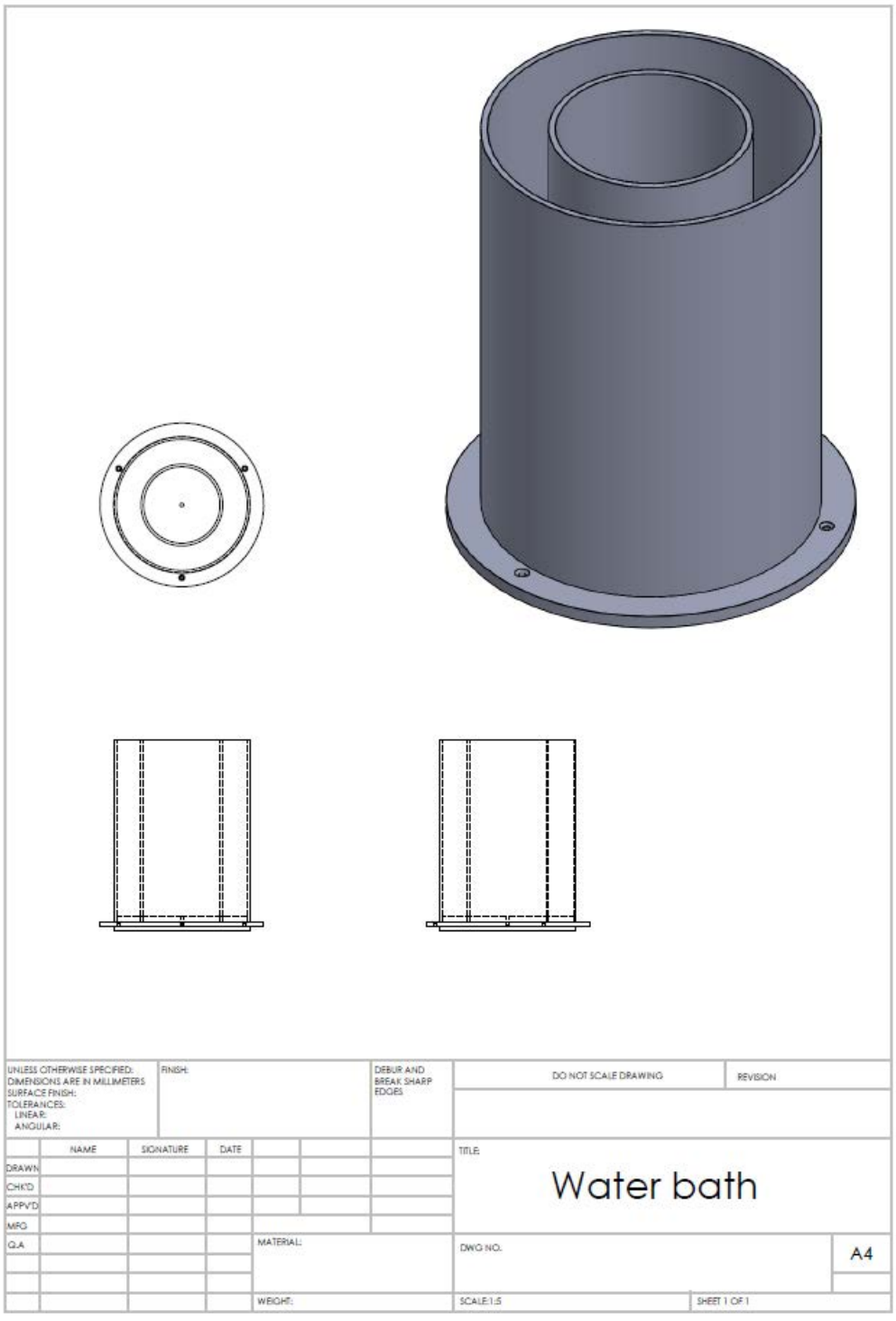

Figure 8-9: Water bath used in DMA testing

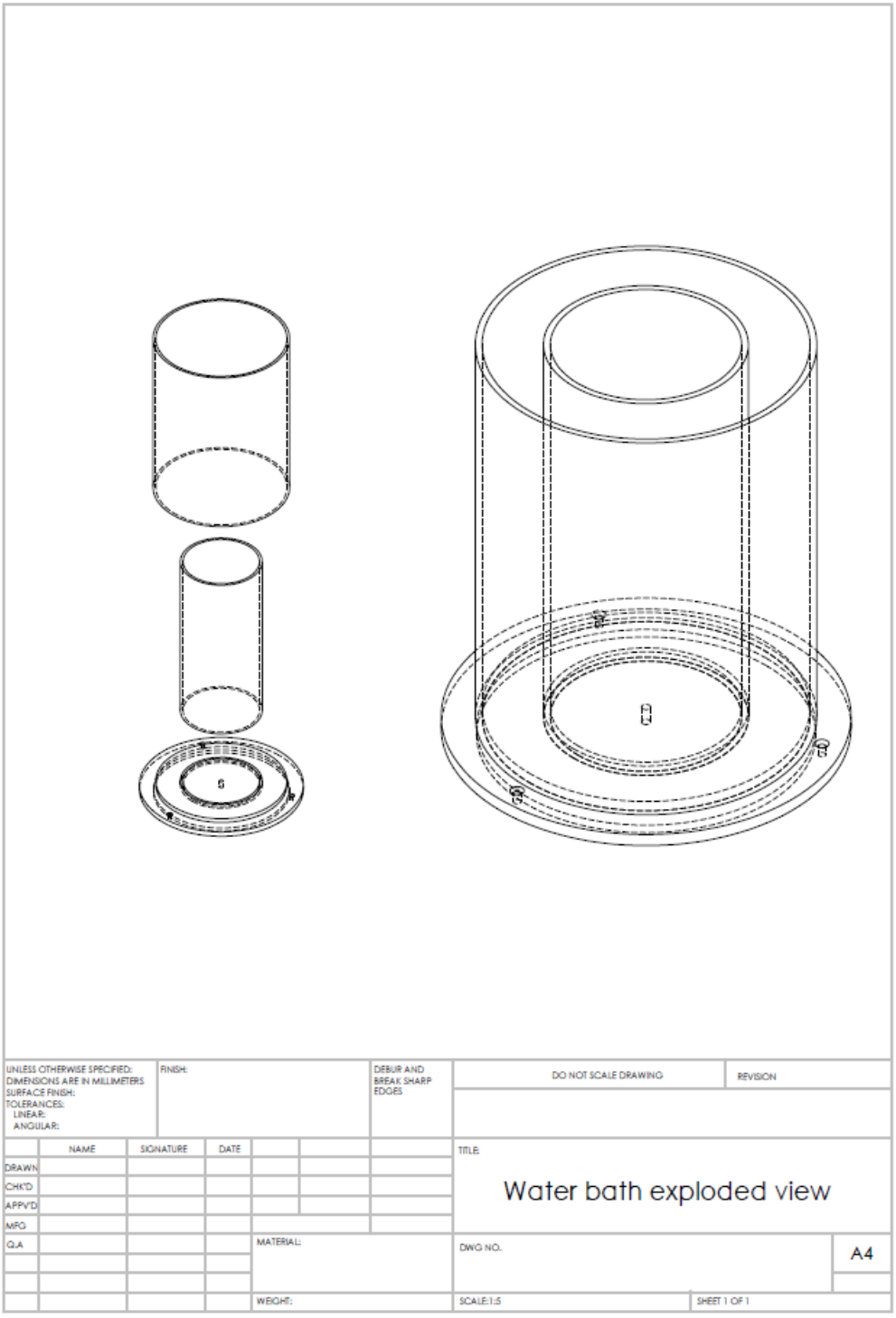

Figure 8-10: Exploded view of the water bath

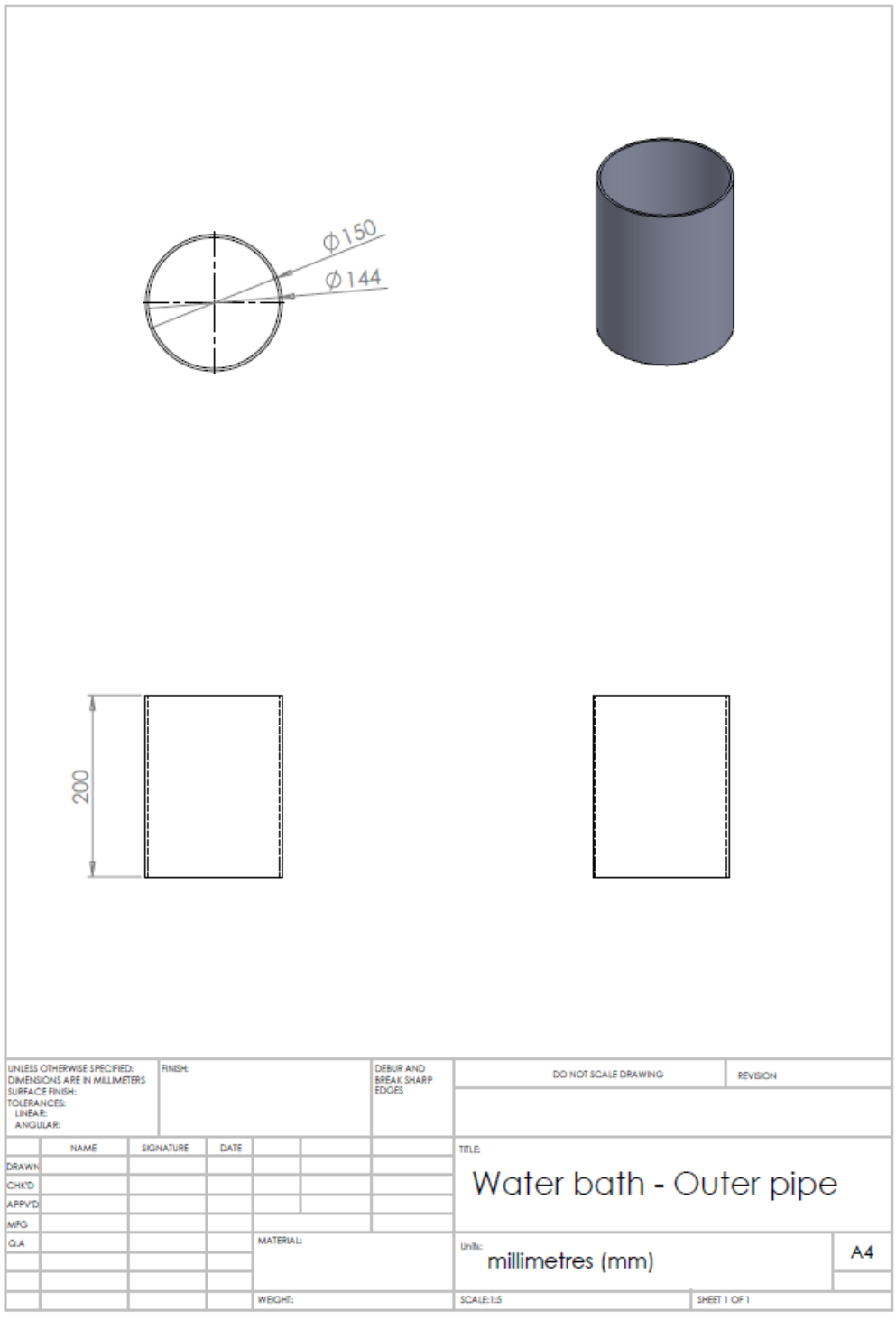

Figure 8-11: Dimensions of the outer pipe of the water bath

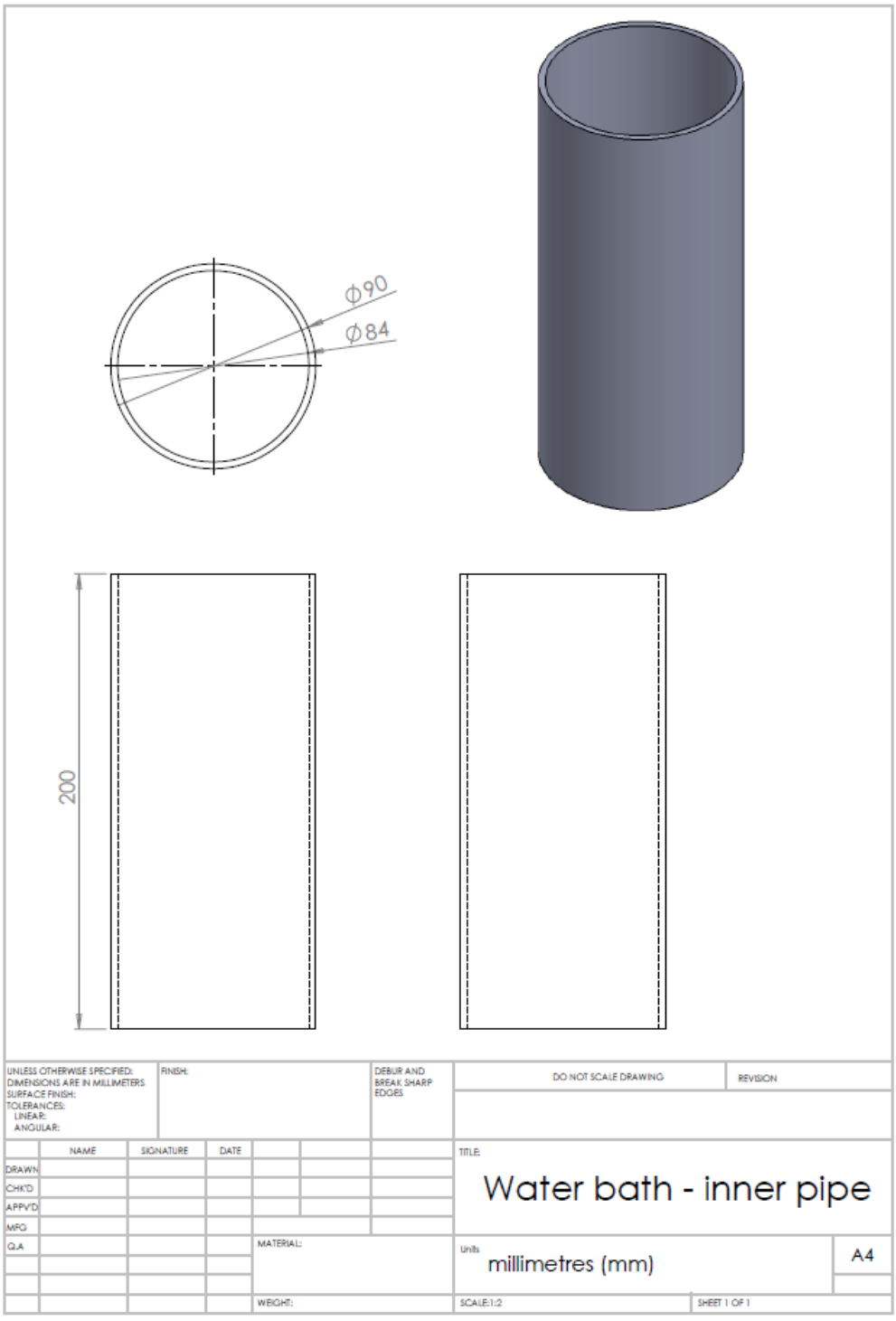

Figure 8-12: Dimensions of the inner pipe of the water bath

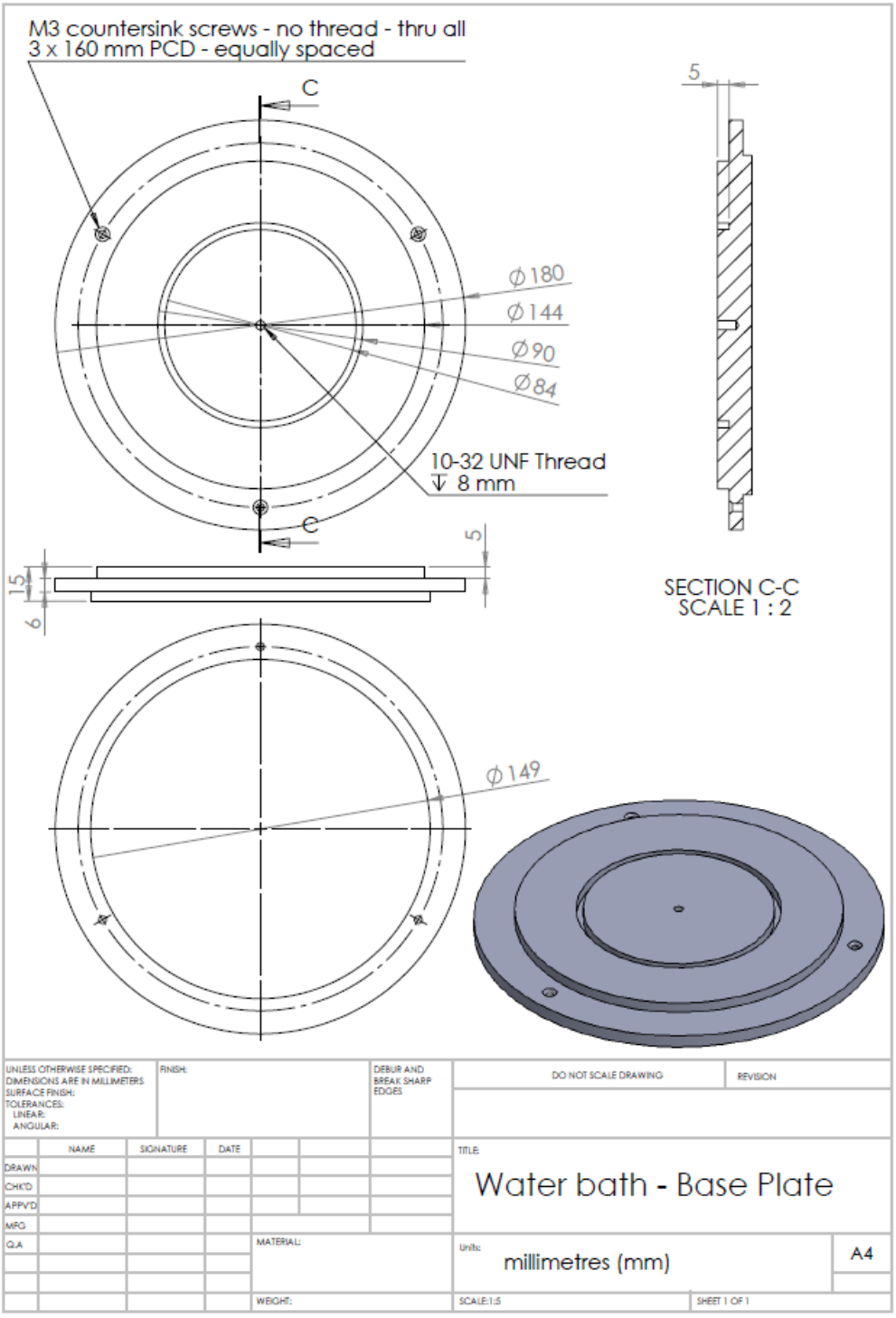

Figure 8-13: Dimensions of the base plate of the water bath

8.5 Appendix E – Regression (μDMA)

Table 8-1: Storage stiffness (equation 4.1) and loss stiffness (equation 4.2) regression analyses of Quadrathane ARC 80A B20.

	k'				k''			
Specimen ID	A	B	R^2	P Value	C	D	R^2	P Value
UNT – M1	0.692	12.02	0.972	0.002	0.527	1.485	0.776	0.048
UNT – M2	1.111	12.98	0.989	0.001	0.487	1.462	0.868	0.021
UNT – M3	0.790	12.31	0.957	0.004	0.476	1.304	0.835	0.03
UNT – M4	0.408	10.42	0.982	0.001	0.406	1.133	0.776	0.049
UNT – M5	0.349	11.29	0.975	0.002	0.379	1.218	0.752	0.057
UNT – M6	0.279	9.67	0.834	0.03	0.309	1.031	0.851	0.026
Real time – M1	0.818	18.14	0.978	0.001	0.648	2.348	0.760	0.054
Real time – M2	0.766	14.50	0.946	0.005	0.580	1.627	0.854	0.025
Real time – M3	0.869	19.23	0.992	0.001	0.814	2.430	0.829	0.032
Real time – M4	0.568	18.26	0.989	0.001	0.792	2.535	0.749	0.058
Real time – M5	0.509	16.15	0.795	0.042	0.667	2.059	0.749	0.058
Real time – M6	0.266	8.97	0.946	0.005	0.227	0.850	0.894	0.015
Accelerated – M1	0.771	13.82	0.991	0.001	0.689	2.255	0.804	0.039
Accelerated – M2	0.811	13.69	0.920	0.01	0.607	2.115	0.871	0.02
Accelerated – M3	0.736	13.87	0.980	0.001	0.675	2.215	0.844	0.028
Accelerated – M4	0.819	14.18	0.995	0.001	0.828	2.326	0.819	0.035
Accelerated – M5	0.512	12.37	0.895	0.015	0.529	1.794	0.834	0.03
Accelerated – M6	0.606	12.54	0.981	0.001	0.548	1.755	0.769	0.051
UNT – M1	0.666	14.73	0.998	0.001	0.709	1.960	0.846	0.027
UNT – M2	0.834	15.27	0.986	0.001	0.589	1.960	0.750	0.058
UNT – M3	0.720	14.70	0.984	0.001	0.600	1.896	0.826	0.033
UNT – M4	0.865	14.66	0.986	0.001	0.501	1.628	0.850	0.026
UNT – M5	0.818	12.65	0.998	0.001	0.592	1.594	0.788	0.045
UNT – M6	0.660	13.51	0.992	0.001	0.533	1.566	0.848	0.026
3% H_2O_2 – M1	0.527	16.44	0.946	0.005	0.610	1.955	0.868	0.021
3% H_2O_2 – M2	0.714	17.02	0.987	0.001	0.805	2.170	0.828	0.032
3% H_2O_2 – M3	0.432	16.16	0.881	0.018	0.678	1.903	0.846	0.027
3% H_2O_2 – M4	0.892	17.02	0.881	0.018	0.676	1.906	0.810	0.037
3% H_2O_2 – M5	0.512	16.87	0.973	0.002	0.592	1.834	0.823	0.033
3% H_2O_2 – M6	0.501	16.18	0.939	0.006	0.778	2.151	0.699	0.078
$H_2O_2/CoCl_2$ – M1	0.502	12.78	0.965	0.003	0.407	1.358	0.885	0.017
$H_2O_2/CoCl_2$ – M2	0.517	12.83	0.975	0.002	0.382	1.389	0.737	0.063
$H_2O_2/CoCl_2$ – M3	0.690	12.27	0.919	0.01	0.527	1.491	0.764	0.053
$H_2O_2/CoCl_2$ – M4	0.582	12.57	0.996	0.001	0.405	1.455	0.810	0.038
$H_2O_2/CoCl_2$ – M5	0.588	12.62	0.974	0.002	0.462	1.449	0.805	0.039
$H_2O_2/CoCl_2$ – M6	0.570	12.51	0.983	0.001	0.535	1.591	0.750	0.058

Table 8-2: Storage stiffness (equation 4.1) and loss stiffness (equation 4.2) regression analyses of Bionate II 80A.

	k'				k''			
Specimen ID	A	B	R^2	P Value	C	D	R^2	P Value
UNT – M1	0.973	18.84	0.990	0.001	0.994	2.666	0.797	0.041
UNT – M2	0.609	17.06	0.974	0.002	0.751	2.150	0.869	0.021
UNT – M3	0.652	17.23	0.932	0.008	0.851	2.293	0.872	0.02
UNT – M4	0.676	16.94	0.946	0.005	0.920	2.279	0.803	0.04
UNT – M5	0.823	17.04	0.985	0.001	0.845	2.237	0.888	0.017
UNT – M6	0.463	16.61	0.815	0.036	0.727	2.047	0.819	0.035
Real time – M1	1.543	34.05	0.937	0.007	3.170	7.020	0.693	0.08
Real time – M2	1.196	32.91	0.676	0.087	2.428	6.141	0.799	0.041
Real time – M3	1.487	31.95	0.908	0.012	2.503	6.106	0.760	0.054
Real time – M4	1.524	34.12	0.985	0.001	2.517	6.391	0.765	0.052
Real time – M5	2.197	36.40	0.982	0.001	3.293	7.762	0.758	0.055
Real time – M6	2.285	31.54	0.979	0.001	2.381	5.799	0.768	0.051
Accelerated – M1	0.720	15.78	0.922	0.009	0.675	2.012	0.812	0.037
Accelerated – M2	2.107	29.95	0.941	0.006	2.051	5.653	0.858	0.024
Accelerated – M3	1.828	29.77	0.995	0.001	1.983	5.818	0.818	0.035
Accelerated – M4	1.645	28.20	0.997	0.001	2.100	5.366	0.807	0.038
Accelerated – M5	2.030	29.59	0.972	0.002	2.364	6.165	0.779	0.047
Accelerated – M6	1.106	22.81	0.949	0.005	1.107	3.834	0.717	0.07
UNT – M1	0.737	24.53	0.548	0.153	1.468	4.197	0.740	0.061
UNT – M2	0.622	25.41	0.676	0.088	1.748	4.541	0.805	0.039
UNT – M3	1.182	26.08	0.977	0.001	1.842	4.656	0.803	0.039
UNT – M4	1.470	25.80	0.991	0.001	1.623	4.418	0.852	0.025
UNT – M5	0.393	25.73	0.184	0.472	1.202	3.913	0.946	0.005
UNT – M6	1.665	24.46	0.969	0.002	1.802	4.292	0.811	0.037
3% H_2O_2 – M1	0.152	22.11	0.080	0.644	0.605	2.831	0.704	0.076
3% H_2O_2 – M2	0.098	21.31	0.026	0.795	0.901	2.993	0.665	0.092
3% H_2O_2 – M3	-0.168	22.24	0.058	0.697	0.791	3.072	0.725	0.067
3% H_2O_2 – M4	-0.181	21.38	0.067	0.674	0.800	2.926	0.742	0.061
3% H_2O_2 – M5	0.425	20.84	0.432	0.228	0.640	2.545	0.769	0.051
3% H_2O_2 – M6	0.198	21.61	0.104	0.596	0.688	2.767	0.896	0.015
$H_2O_2/CoCl_2$ – M1	1.345	23.49	0.896	0.015	1.340	3.694	0.847	0.027
$H_2O_2/CoCl_2$ – M2	1.578	22.92	0.980	0.001	1.417	3.569	0.844	0.028
$H_2O_2/CoCl_2$ – M3	1.383	25.56	0.939	0.006	1.619	4.388	0.754	0.056
$H_2O_2/CoCl_2$ – M4	1.624	25.78	0.999	0.001	1.698	4.448	0.817	0.035
$H_2O_2/CoCl_2$ – M5	1.466	23.56	0.970	0.002	1.422	3.719	0.777	0.048
$H_2O_2/CoCl_2$ – M6	1.060	23.07	0.991	0.001	1.275	3.693	0.828	0.032

Table 8-3: Storage stiffness (equation 4.1) and loss stiffness (equation 4.2) regression analyses of Quadrathane ARC 80A.

	k'				k''			
Specimen ID	A	B	R^2	P Value	C	D	R^2	P Value
UNT – M1	0.449	10.80	0.888	0.016	0.436	1.215	0.760	0.054
UNT – M2	0.157	11.88	0.821	0.034	0.343	1.164	0.902	0.013
UNT – M3	0.523	13.04	0.944	0.006	0.511	1.519	0.788	0.044
UNT – M4	0.256	12.55	0.916	0.011	0.418	1.378	0.766	0.052
UNT – M5	0.297	12.81	0.827	0.032	0.346	1.231	0.781	0.047
UNT – M6	0.528	13.56	0.981	0.001	0.407	1.425	0.808	0.038
Real time – M1	0.551	15.56	0.966	0.003	0.717	1.817	0.784	0.046
Real time – M2	0.563	15.92	0.887	0.017	0.664	1.792	0.839	0.029
Real time – M3	0.505	10.89	0.983	0.001	0.297	0.986	0.892	0.016
Real time – M4	0.332	8.22	0.973	0.002	0.347	0.853	0.763	0.053
Real time – M5	0.477	12.55	0.918	0.01	0.418	1.214	0.939	0.006
Real time – M6	0.465	10.23	0.988	0.001	0.364	1.037	0.896	0.015
Accelerated – M1	0.789	12.10	0.993	0.001	0.427	1.657	0.874	0.02
Accelerated – M2	0.927	11.12	0.997	0.001	0.433	1.485	0.864	0.022
Accelerated – M3	0.901	11.12	0.994	0.001	0.460	1.511	0.807	0.038
Accelerated – M4	0.759	12.05	0.969	0.002	0.548	1.731	0.814	0.036
Accelerated – M5	0.696	12.38	0.976	0.002	0.533	1.650	0.841	0.028
Accelerated – M6	1.015	13.48	0.990	0.001	0.588	1.969	0.899	0.014
UNT – M1	0.331	10.26	0.432	0.228	0.582	1.524	0.876	0.019
UNT – M2	0.667	12.06	0.985	0.001	0.595	1.565	0.902	0.013
UNT – M3	0.435	14.13	0.444	0.22	0.736	1.942	0.855	0.025
UNT – M4	0.968	15.95	0.937	0.007	0.844	2.309	0.942	0.006
UNT – M5	0.973	16.17	0.960	0.003	1.145	2.651	0.806	0.039
UNT – M6	0.704	15.42	0.931	0.008	0.998	2.396	0.837	0.029
3% H_2O_2 – M1	0.560	12.63	0.963	0.003	0.613	1.611	0.876	0.019
3% H_2O_2 – M2	0.414	12.02	0.911	0.012	0.585	1.395	0.929	0.008
3% H_2O_2 – M3	0.575	13.20	0.932	0.008	0.642	1.520	0.828	0.012
3% H_2O_2 – M4	0.503	11.94	0.863	0.023	0.468	1.298	0.903	0.013
3% H_2O_2 – M5	0.615	12.95	0.958	0.004	0.666	1.666	0.836	0.03
3% H_2O_2 – M6	0.656	13.12	0.931	0.008	0.740	1.863	0.889	0.016
$H_2O_2/CoCl_2$ – M1	0.519	11.12	0.938	0.007	0.452	1.348	0.860	0.023
$H_2O_2/CoCl_2$ – M2	0.881	16.25	0.981	0.001	0.816	2.144	0.944	0.006
$H_2O_2/CoCl_2$ – M3	0.474	11.70	0.929	0.008	0.514	1.374	0.848	0.027
$H_2O_2/CoCl_2$ – M4	0.548	13.79	0.976	0.002	0.795	2.004	0.816	0.036
$H_2O_2/CoCl_2$ – M5	0.616	13.43	0.987	0.001	0.609	1.804	0.853	0.025
$H_2O_2/CoCl_2$ – M6	0.623	14.63	0.959	0.004	0.848	2.149	0.895	0.015

Table 8-4: Storage stiffness (equation 4.1) and loss stiffness (equation 4.2) regression analyses of ChronoFlex C 80A.

	k'				k''			
Specimen ID	A	B	R^2	P Value	C	D	R^2	P Value
UNT – M1	1.017	20.03	0.983	0.001	1.320	3.434	0.880	0.018
UNT – M2	1.162	20.39	0.940	0.006	1.255	3.418	0.841	0.028
UNT – M3	1.361	20.36	0.962	0.003	1.621	3.892	0.840	0.029
UNT – M4	1.048	20.92	0.989	0.001	1.362	3.503	0.866	0.022
UNT – M5	1.119	20.29	0.936	0.007	1.367	3.546	0.848	0.026
UNT – M6	1.166	20.07	0.936	0.007	1.369	3.390	0.843	0.028
Real time – M1	0.975	18.93	0.957	0.004	1.102	2.894	0.885	0.017
Real time – M2	0.741	17.91	0.952	0.004	1.036	2.735	0.872	0.02
Real time – M3	0.954	18.20	0.972	0.002	0.998	2.673	0.909	0.012
Real time – M4	0.947	18.07	0.958	0.004	1.081	2.801	0.860	0.023
Real time – M5	0.814	17.72	0.988	0.001	1.226	2.807	0.823	0.034
Real time – M6	0.965	18.08	0.999	0.001	1.061	2.593	0.854	0.025
Accelerated – M1	0.959	15.45	0.977	0.002	0.953	2.461	0.881	0.018
Accelerated – M2	1.002	15.99	0.992	0.001	0.854	2.518	0.902	0.013
Accelerated – M3	0.909	15.62	0.988	0.001	0.866	2.474	0.885	0.017
Accelerated – M4	0.875	15.61	0.997	0.001	0.848	2.477	0.892	0.016
Accelerated – M5	1.378	17.54	0.994	0.001	1.100	3.040	0.870	0.021
Accelerated – M6	0.855	15.91	0.985	0.001	0.969	2.713	0.845	0.027
UNT – M1	1.279	22.82	0.996	0.001	1.704	4.088	0.828	0.032
UNT – M2	0.887	19.80	0.902	0.014	1.305	3.232	0.771	0.05
UNT – M3	0.854	18.93	0.728	0.066	1.188	3.191	0.773	0.05
UNT – M4	0.809	19.21	0.787	0.045	0.893	2.852	0.865	0.022
UNT – M5	0.964	18.95	0.871	0.02	1.200	2.933	0.840	0.029
UNT – M6	0.393	19.64	0.821	0.034	1.072	3.109	0.869	0.021
3% H_2O_2 – M1	0.867	18.07	0.991	0.001	1.066	2.652	0.859	0.023
3% H_2O_2 – M2	1.002	18.82	0.967	0.003	1.250	2.856	0.822	0.034
3% H_2O_2 – M3	0.865	18.60	0.999	0.001	0.954	2.565	0.852	0.025
3% H_2O_2 – M4	0.962	18.65	0.987	0.001	1.069	2.617	0.852	0.025
3% H_2O_2 – M5	0.989	18.29	0.994	0.001	1.045	2.654	0.844	0.027
3% H_2O_2 – M6	0.741	17.79	0.909	0.012	1.004	2.511	0.815	0.036
$H_2O_2/CoCl_2$ – M1	0.502	17.78	0.733	0.064	0.867	2.628	0.807	0.038
$H_2O_2/CoCl_2$ – M2	0.863	18.45	0.946	0.005	1.027	2.706	0.853	0.025
$H_2O_2/CoCl_2$ – M3	1.454	23.53	0.951	0.005	1.437	3.881	0.792	0.043
$H_2O_2/CoCl_2$ – M4	1.231	22.06	0.954	0.004	1.377	3.746	0.843	0.028
$H_2O_2/CoCl_2$ – M5	0.968	22.13	0.981	0.001	1.277	3.534	0.887	0.017
$H_2O_2/CoCl_2$ – M6	1.069	19.88	0.949	0.005	1.097	2.936	0.872	0.02

Table 8-5: Storage stiffness (equation 4.1) and loss stiffness (equation 4.2) regression analyses of Chronosil 5% 80A.

	k'				k''			
Specimen ID	A	B	R^2	P Value	C	D	R^2	P Value
UNT – M1	1.065	10.79	1.000	0.001	0.663	2.340	0.916	0.011
UNT – M2	1.766	13.81	0.991	0.001	1.349	3.446	0.869	0.021
UNT – M3	1.536	16.07	0.978	0.001	1.406	3.941	0.853	0.025
UNT – M4	1.102	10.74	1.000	0.001	0.715	2.183	0.889	0.016
UNT – M5	0.897	9.90	0.989	0.001	0.662	2.083	0.828	0.032
UNT – M6	0.937	11.47	0.983	0.001	0.704	2.374	0.863	0.022
Real time – M1	1.490	15.22	0.999	0.001	1.329	3.620	0.920	0.01
Real time – M2	1.237	14.24	0.982	0.001	1.074	3.197	0.896	0.015
Real time – M3	1.292	12.46	0.984	0.001	0.959	2.719	0.876	0.019
Real time – M4	1.352	12.46	0.978	0.001	0.914	2.664	0.961	0.003
Real time – M5	1.105	12.22	0.923	0.009	0.718	2.357	0.875	0.02
Real time – M6	1.219	13.45	0.959	0.004	1.004	2.917	0.866	0.022
Accelerated – M1	0.953	10.95	0.924	0.009	0.670	2.210	0.895	0.015
Accelerated – M2	1.083	12.06	0.991	0.001	0.820	2.608	0.883	0.018
Accelerated – M3	1.417	13.32	0.977	0.002	1.020	3.102	0.886	0.017
Accelerated – M4	1.233	12.23	0.917	0.01	0.773	2.675	0.848	0.026
Accelerated – M5	0.809	10.32	0.979	0.001	0.625	2.065	0.798	0.041
Accelerated – M6	0.867	7.135	0.999	0.001	0.470	1.360	0.916	0.011
UNT – M1	1.133	11.46	0.959	0.004	0.867	2.558	0.885	0.017
UNT – M2	0.649	10.38	0.792	0.043	0.609	2.092	0.899	0.014
UNT – M3	0.531	11.22	0.684	0.084	0.666	2.336	0.868	0.021
UNT – M4	0.846	11.09	0.873	0.02	0.787	2.364	0.887	0.017
UNT – M5	0.859	9.990	0.997	0.001	0.681	2.076	0.895	0.015
UNT – M6	1.249	12.25	0.949	0.005	1.042	3.042	0.920	0.01
3% H_2O_2 – M1	0.966	12.09	0.917	0.01	0.814	2.395	0.917	0.01
3% H_2O_2 – M2	1.090	11.73	0.991	0.001	0.770	2.441	0.931	0.008
3% H_2O_2 – M3	0.901	13.75	0.964	0.003	1.103	2.947	0.883	0.018
3% H_2O_2 – M4	0.715	9.155	0.942	0.006	0.658	1.790	0.865	0.022
3% H_2O_2 – M5	1.259	14.44	0.954	0.004	1.147	3.129	0.802	0.04
3% H_2O_2 – M6	1.032	13.51	0.967	0.003	1.048	2.919	0.859	0.024
$H_2O_2/CoCl_2$ – M1	1.094	12.29	0.976	0.002	1.013	2.877	0.861	0.023
$H_2O_2/CoCl_2$ – M2	0.747	8.717	0.962	0.003	0.537	1.742	0.905	0.013
$H_2O_2/CoCl_2$ – M3	1.038	11.91	0.960	0.003	0.923	2.771	0.881	0.018
$H_2O_2/CoCl_2$ – M4	1.446	17.02	0.976	0.002	1.556	4.379	0.816	0.036
$H_2O_2/CoCl_2$ – M5	0.876	11.21	0.977	0.001	0.684	2.114	0.878	0.019
$H_2O_2/CoCl_2$ – M6	1.005	11.09	0.990	0.001	0.728	2.300	0.853	0.025

8.6 Appendix F – Regression (DMA)

Table 8-6: Storage stiffness (equation 4.1) and loss stiffness (equation 4.2) regression analyses of Quadrathane ARC 80A B20.

	k'				k''			
Specimen ID	A	B	R^2	P Value	C	D	R^2	P Value
UNT – M1	0.588	11.53	0.962	0.001	0.169	1.036	0.918	0.001
UNT – M2	0.599	11.79	0.968	0.001	0.169	1.064	0.934	0.001
UNT – M3	0.599	11.79	0.949	0.001	0.178	1.072	0.916	0.001
Real time – M1	0.538	11.63	0.797	0.001	0.208	1.142	0.669	0.001
Real time – M2	0.616	12.21	0.960	0.001	0.167	1.086	0.928	0.001
Real time – M3	0.639	12.25	0.968	0.001	0.179	1.125	0.924	0.001
Accelerated – M1	0.601	8.540	0.964	0.001	0.155	1.024	0.941	0.001
Accelerated – M2	0.588	8.620	0.957	0.001	0.151	1.028	0.948	0.001
Accelerated – M3	0.607	8.670	0.967	0.001	0.154	1.039	0.945	0.001
UNT – M1	0.567	10.96	0.945	0.001	0.166	0.984	0.916	0.001
UNT – M2	0.535	11.13	0.905	0.001	0.199	1.066	0.622	0.001
UNT – M3	0.508	10.98	0.774	0.001	0.181	1.041	0.915	0.001
UNT – M4	0.557	11.11	0.951	0.001	0.183	1.036	0.822	0.001
UNT – M5	0.513	10.37	0.966	0.001	0.148	0.922	0.922	0.001
3% H_2O_2 – M1	0.610	12.17	0.963	0.001	0.168	1.073	0.926	0.001
3% H_2O_2 – M2	0.527	11.28	0.927	0.001	0.172	1.037	0.866	0.001
3% H_2O_2 – M3	0.544	11.18	0.967	0.001	0.155	0.985	0.915	0.001
3% H_2O_2 – M4	0.562	11.39	0.963	0.001	0.160	1.022	0.926	0.001
3% H_2O_2 – M5	0.561	11.42	0.970	0.001	0.160	1.017	0.924	0.001
$H_2O_2/CoCl_2$ – M1	0.559	10.93	0.954	0.001	0.178	1.018	0.910	0.001
$H_2O_2/CoCl_2$ – M2	0.525	10.67	0.969	0.001	0.157	0.951	0.923	0.001
$H_2O_2/CoCl_2$ – M3	0.551	10.74	0.965	0.001	0.172	0.991	0.896	0.001
$H_2O_2/CoCl_2$ – M4	0.553	11.22	0.855	0.001	0.199	1.092	0.858	0.001
$H_2O_2/CoCl_2$ – M5	0.568	10.74	0.933	0.001	0.191	1.039	0.853	0.001

Table 8-7: Storage stiffness (equation 4.1) and loss stiffness (equation 4.2) regression analyses of Bionate II 80A.

	k'				k''			
Specimen ID	A	B	R^2	P Value	C	D	R^2	P Value
UNT – M1	0.752	16.01	0.944	0.001	0.301	1.480	0.888	0.001
UNT – M2	0.870	17.18	0.954	0.001	0.349	1.670	0.897	0.001
UNT – M3	0.838	17.04	0.957	0.001	0.334	1.639	0.901	0.001
Real time – M1	0.948	18.06	0.889	0.001	0.445	1.957	0.880	0.001
Real time – M2	0.754	16.73	0.687	0.001	0.409	1.762	0.792	0.001
Real time – M3	0.962	18.71	0.946	0.001	0.393	1.832	0.890	0.001
Accelerated – M1	0.864	14.64	0.945	0.001	0.320	1.663	0.869	0.001
Accelerated – M2	0.796	13.49	0.940	0.001	0.288	1.497	0.797	0.001
Accelerated – M3	0.901	15.18	0.956	0.001	0.312	1.656	0.863	0.001
UNT – M1	0.957	17.73	0.945	0.001	0.389	1.825	0.898	0.001
UNT – M2	0.866	17.56	0.957	0.001	0.346	1.695	0.897	0.001
UNT – M3	1.064	17.90	0.919	0.001	0.484	2.049	0.832	0.001
UNT – M4	0.975	17.52	0.950	0.001	0.421	1.907	0.887	0.001
UNT – M5	1.004	17.76	0.949	0.001	0.429	1.958	0.897	0.001
3% H_2O_2 – M1	1.015	18.10	0.943	0.001	0.425	1.947	0.892	0.001
3% H_2O_2 – M2	0.841	18.32	0.626	0.001	0.448	1.986	0.812	0.001
3% H_2O_2 – M3	0.981	18.90	0.950	0.001	0.388	1.865	0.889	0.001
3% H_2O_2 – M4	0.966	18.24	0.941	0.001	0.384	1.797	0.881	0.001
3% H_2O_2 – M5	0.815	18.48	0.462	0.001	0.441	1.980	0.822	0.001
$H_2O_2/CoCl_2$ – M1	0.978	18.29	0.952	0.001	0.384	1.847	0.906	0.001
$H_2O_2/CoCl_2$ – M2	0.936	17.72	0.958	0.001	0.370	1.794	0.906	0.001
$H_2O_2/CoCl_2$ – M3	0.972	18.08	0.953	0.001	0.386	1.832	0.901	0.001
$H_2O_2/CoCl_2$ – M4	0.933	17.38	0.943	0.001	0.385	1.800	0.895	0.001
$H_2O_2/CoCl_2$ – M5	0.917	17.40	0.949	0.001	0.387	1.803	0.888	0.001

Table 8-8: Storage stiffness (equation 4.1) and loss stiffness (equation 4.2) regression analyses of Quadrathane ARC 80A.

	k'				k''			
Specimen ID	A	B	R^2	P Value	C	D	R^2	P Value
UNT – M1	0.406	9.370	0.961	0.001	0.130	0.744	0.899	0.001
UNT – M2	0.405	9.325	0.962	0.001	0.119	0.718	0.919	0.001
UNT – M3	0.407	9.175	0.959	0.001	0.126	0.725	0.918	0.001
Real time – M1	0.418	9.644	0.962	0.001	0.124	0.754	0.929	0.001
Real time – M2	0.412	9.698	0.966	0.001	0.120	0.738	0.926	0.001
Real time – M3	0.385	9.665	0.867	0.001	0.131	0.763	0.881	0.001
Accelerated – M1	0.463	7.137	0.953	0.001	0.126	0.795	0.949	0.001
Accelerated – M2	0.512	7.506	0.959	0.001	0.136	0.839	0.943	0.001
Accelerated – M3	0.494	7.304	0.964	0.001	0.134	0.825	0.944	0.001
UNT – M1	0.405	9.212	0.963	0.001	0.126	0.723	0.913	0.001
UNT – M2	0.396	9.213	0.901	0.001	0.139	0.749	0.871	0.001
UNT – M3	0.370	9.303	0.750	0.001	0.137	0.771	0.895	0.001
UNT – M4	0.407	9.358	0.964	0.001	0.141	0.778	0.833	0.001
UNT – M5	0.377	9.297	0.796	0.001	0.138	0.772	0.902	0.001
3% H_2O_2 – M1	0.403	9.529	0.958	0.001	0.127	0.757	0.922	0.001
3% H_2O_2 – M2	0.440	9.613	0.958	0.001	0.137	0.771	0.911	0.001
3% H_2O_2 – M3	0.428	9.686	0.963	0.001	0.136	0.786	0.911	0.001
3% H_2O_2 – M4	0.438	9.846	0.968	0.001	0.143	0.809	0.922	0.001
3% H_2O_2 – M5	0.429	9.625	0.960	0.001	0.136	0.767	0.900	0.001
$H_2O_2/CoCl_2$ – M1	0.373	9.331	0.721	0.001	0.129	0.753	0.928	0.001
$H_2O_2/CoCl_2$ – M2	0.374	9.113	0.946	0.001	0.116	0.703	0.928	0.001
$H_2O_2/CoCl_2$ – M3	0.404	9.355	0.967	0.001	0.119	0.717	0.930	0.001
$H_2O_2/CoCl_2$ – M4	0.418	9.196	0.964	0.001	0.130	0.745	0.916	0.001
$H_2O_2/CoCl_2$ – M5	0.386	8.876	0.965	0.001	0.119	0.691	0.918	0.001

Table 8-9: Storage stiffness (equation 4.1) and loss stiffness (equation 4.2) regression analyses of ChronoFlex C 80A.

	k'				k''			
Specimen ID	A	B	R^2	P Value	C	D	R^2	P Value
UNT – M1	0.854	15.25	0.946	0.001	0.311	1.562	0.897	0.001
UNT – M2	0.788	14.87	0.962	0.001	0.282	1.470	0.907	0.001
UNT – M3	0.800	15.14	0.959	0.001	0.291	1.514	0.904	0.001
Real time – M1	0.853	16.36	0.955	0.001	0.302	1.565	0.910	0.001
Real time – M2	0.861	16.25	0.955	0.001	0.315	1.599	0.906	0.001
Real time – M3	0.854	16.14	0.957	0.001	0.318	1.594	0.903	0.001
Accelerated – M1	0.745	12.20	0.951	0.001	0.244	1.381	0.908	0.001
Accelerated – M2	0.612	11.72	0.736	0.001	0.224	1.319	0.908	0.001
Accelerated – M3	0.827	12.85	0.960	0.001	0.269	1.494	0.924	0.001
UNT – M1	0.865	15.64	0.960	0.001	0.318	1.633	0.912	0.001
UNT – M2	0.839	15.20	0.935	0.001	0.339	1.611	0.832	0.001
UNT – M3	0.857	15.91	0.963	0.001	0.302	1.578	0.912	0.001
UNT – M4	0.873	16.02	0.957	0.001	0.310	1.611	0.906	0.001
UNT – M5	0.831	15.58	0.955	0.001	0.305	1.566	0.893	0.001
3% H_2O_2 – M1	0.960	17.07	0.944	0.001	0.341	1.720	0.900	0.001
3% H_2O_2 – M2	0.888	16.34	0.945	0.001	0.314	1.606	0.910	0.001
3% H_2O_2 – M3	0.803	15.83	0.940	0.001	0.320	1.584	0.846	0.001
3% H_2O_2 – M4	0.768	16.42	0.683	0.001	0.342	1.690	0.834	0.001
3% H_2O_2 – M5	0.952	16.95	0.958	0.001	0.354	1.765	0.907	0.001
$H_2O_2/CoCl_2$ – M1	0.900	15.05	0.913	0.001	0.345	1.616	0.858	0.001
$H_2O_2/CoCl_2$ – M2	0.892	15.64	0.951	0.001	0.321	1.602	0.897	0.001
$H_2O_2/CoCl_2$ – M3	0.960	15.93	0.928	0.001	0.358	1.712	0.889	0.001
$H_2O_2/CoCl_2$ – M4	0.855	15.84	0.955	0.001	0.318	1.612	0.878	0.001
$H_2O_2/CoCl_2$ – M5	0.808	15.08	0.960	0.001	0.281	1.466	0.907	0.001

Table 8-10: Storage stiffness (equation 4.1) and loss stiffness (equation 4.2) regression analyses of Chronosil 5% 80A.

	k'				k''			
Specimen ID	A	B	R^2	P Value	C	D	R^2	P Value
UNT – M1	0.759	7.952	0.945	0.001	0.313	1.569	0.957	0.001
UNT – M2	0.814	8.347	0.963	0.001	0.330	1.680	0.960	0.001
UNT – M3	1.095	9.469	0.949	0.001	0.443	2.033	0.945	0.001
Real time – M1	0.632	7.916	0.944	0.001	0.272	1.327	0.951	0.001
Real time – M2	0.690	8.191	0.953	0.001	0.290	1.406	0.951	0.001
Real time – M3	0.606	7.806	0.960	0.001	0.255	1.271	0.955	0.001
Accelerated – M1	0.566	7.324	0.962	0.001	0.214	1.120	0.946	0.001
Accelerated – M2	0.572	7.164	0.954	0.001	0.218	1.141	0.954	0.001
Accelerated – M3	0.529	6.940	0.953	0.001	0.200	1.047	0.949	0.001
UNT – M1	0.802	8.412	0.957	0.001	0.334	1.643	0.950	0.001
UNT – M2	0.973	9.175	0.954	0.001	0.394	1.881	0.950	0.001
UNT – M3	0.728	7.843	0.953	0.001	0.296	1.481	0.949	0.001
UNT – M4	0.687	7.798	0.665	0.001	0.305	1.515	0.922	0.001
UNT – M5	0.797	8.178	0.960	0.001	0.324	1.608	0.956	0.001
3% H_2O_2 – M1	0.611	7..836	0.954	0.001	0.252	1.234	0.946	0.001
3% H_2O_2 – M2	0.798	8.717	0.948	0.001	0.333	1.557	0.941	0.001
3% H_2O_2 – M3	0.850	8.898	0.869	0.001	0.364	1.630	0.913	0.001
3% H_2O_2 – M4	0.717	8.583	0.956	0.001	0.296	1.440	0.951	0.001
3% H_2O_2 – M5	0.763	8.610	0.948	0.001	0.318	1.504	0.939	0.001
$H_2O_2/CoCl_2$ – M1	0.668	7.790	0.960	0.001	0.282	1.396	0.952	0.001
$H_2O_2/CoCl_2$ – M2	0.664	7.385	0.926	0.001	0.278	1.320	0.938	0.001
$H_2O_2/CoCl_2$ – M3	0.688	7.830	0.959	0.001	0.288	1.414	0.954	0.001
$H_2O_2/CoCl_2$ – M4	0.797	8.160	0.882	0.001	0.362	1.578	0.901	0.001
$H_2O_2/CoCl_2$ – M5	0.810	8.321	0.817	0.001	0.388	1.676	0.902	0.001

8.7 Appendix G – Savitzky Golay – *in vitro* biomaterial degradation

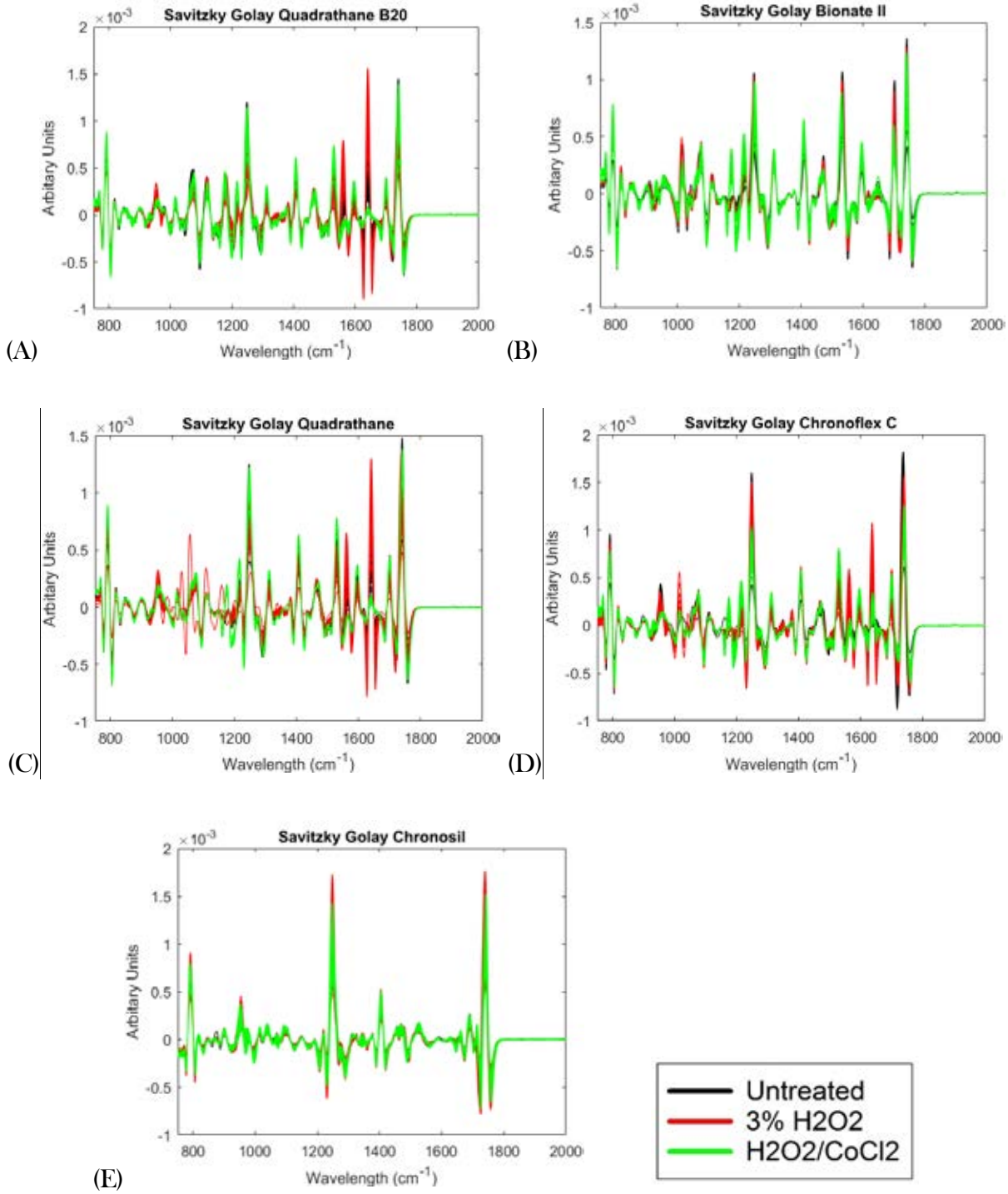

Figure 8-14: Savitzky Golay plots of untreated and *in vitro* oxidative degraded five biomaterials; (A) Quadrathane ARC 80A B20, (B) Bionate II 80A, (C) Quadrathane ARC 80A, (D) ChronoFlex C 80A and (E) ChronoSil 80A 5%. (Black plot) Untreated, (red plot) 3% H_2O_2 and (green plot) $H_2O_2/CoCl_2$ oxidative degraded method

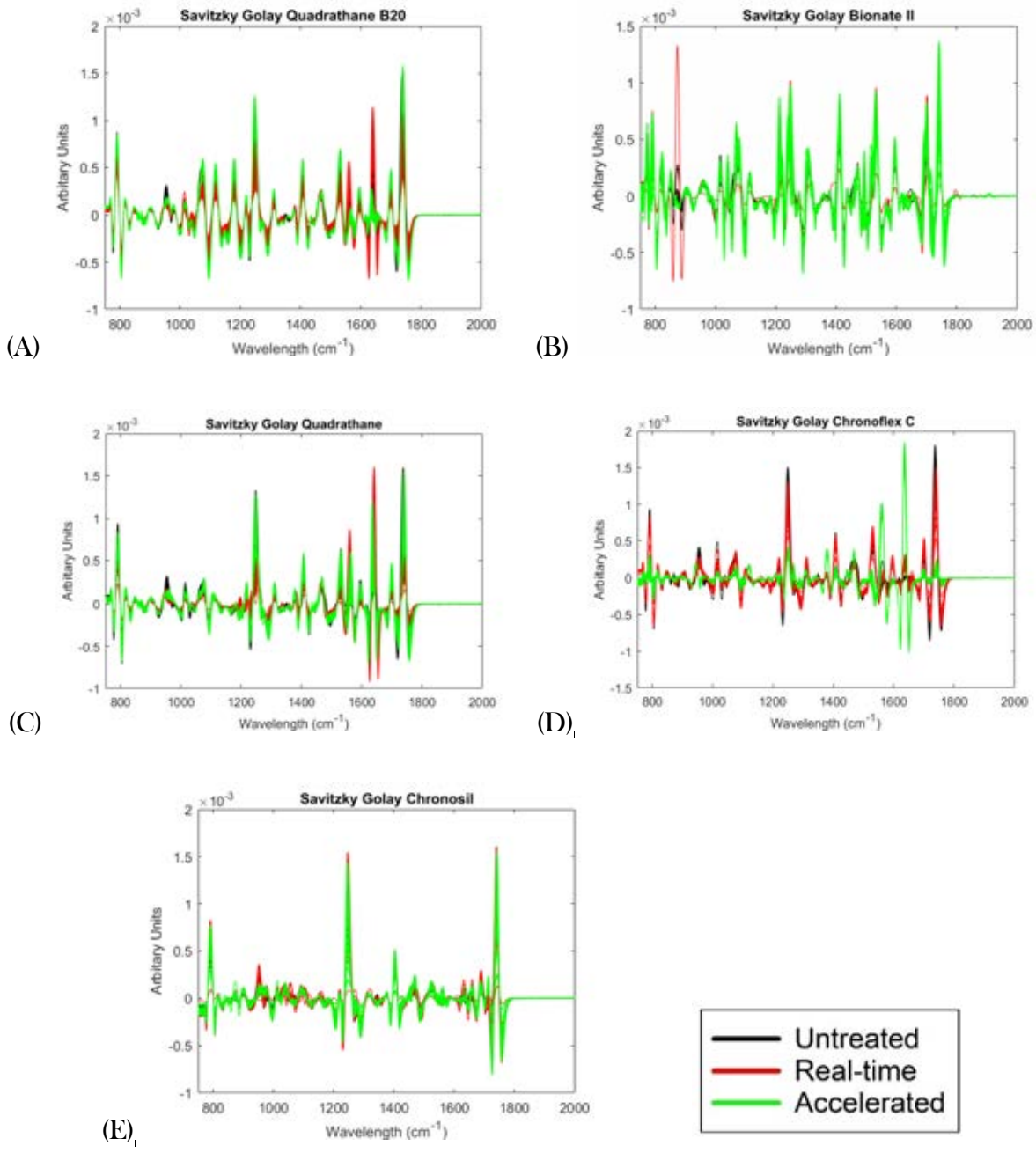

Figure 8-15: Savitzky Golay plots of untreated and *in vitro* hydroltic degraded five biomaterials; (A) Quadrathane ARC 80A B20, (B) Bionate II 80A, (C) Quadrathane ARC 80A, (D) ChronoFlex C 80A and (E) ChronoSil 80A 5%. (Black plot) Untreated, (red plot) real-time hydrolytic degraded and (green plot) accelerated hydrolytic degraded method

8.8 Appendix H – Matlab script to calculate viscoelastic properties

```
%Viscoelastic Properties MATLAB File-Compression Cylinders

%If you use this code or a section of this code for your own
research, please cite this thesis as the source of where you
got the code – thank you.

%Authors: Mr. Bernard Michael Lawless, Dr. Spencer C.
Barnes, Dr. David G. Eckold

%Description: This script calculates the viscoelastic
properties of a viscoelastic material. This material must
have been evaluated on a BOSE (TA Instruments) 3200 DMA
machine

%%
clc;
clear all;

%% Please define the following parameters
% Definition of Cylindrical Parameters
dcyl = 8; % Please state the diameter of the cylinder (in
mm)
hcyl = 1; % Please state the height of the cylinder (in
mm)
Wordbook = 'cartSub3 03162018 041643 v4.xlsx'; % state
wordbook name and file eg.'Test1.xlsx'
% Please ensure that in the spreadsheet; Time is in Column
1, Displacement is in Column 2 and Load in Column 3.

%% Importing of Excel File
T = xlsread(Wordbook); % Read Wordbook (Excel File)
Time = T(:,1); % Time Data in Column 1
DisplacementData = T(:,2); % Displacement Data in Column 2
LoadData = T(:,3); % Load Data in Column 3
NumberOfRows = length(DisplacementData); % Count number of
rows
MeanDisplacement = mean(DisplacementData); % Calculate
mean of displacement
MeanLoad = mean(LoadData);% Calculate mean of load
Blank ='  ';
ResultsDivider = '-------------------------------------';
```

```
%% FFT of Data
% Creation of Fourier transforms of data
nfft = 2^nextpow2(length(LoadData)); % Setting Data to the
next power of 2
dx = abs(Time(find(diff(Time),1)+1)-Time(1)); % Measuring
the Time Step
Fs = 1/dx; % Sampling Frequency
f = Fs/2*linspace(0,1,nfft/2+1);

fftDisp = fft(DisplacementData); % FFT of Disp Data
fftLoad = fft(LoadData); % FFT of Load Data

subplot(1,2,1), plot(f(2:end),2*abs(fftDisp(2:nfft/2+1))),
ylabel('Amplitude'), xlabel('Freq'), title('Disp') % Plot
of FFT Disp
subplot(1,2,2), plot(f(2:end),2*abs(fftLoad(2:nfft/2+1))),
ylabel('Amplitude'), xlabel('Freq'), title('Load') % Plot
of FFT Load

[MaxLoad, idx1]=max(abs(fftLoad(2:end))); % Finding the
position of the peak of the fft of load
[MaxDisp, idx2]=max(abs(fftDisp(2:end))); % Finding the
position of the peak of the fft of disp

r = abs(angle(fftLoad(idx1+1))-angle(fftDisp(idx2+1))); %
Measure of phase angle in radians
deg = r*180/pi; % Converting the phase angle to degrees

disp(ResultsDivider)
disp(Wordbook)

if deg > 90 % If the phase angle is greater that 90 degree
    disp(Blank)
    disp('WARNING: THE PHASE ANGLE IS GREATER THAT 90
DEGREES!')
    disp(Blank)
    disp('WARNING: THE DISPLACEMENT IS LEADING THE LOAD -
CHECK THE NATURAL FREQUENCY OF THE MATERIAL')
    degr=180-deg;
else % if the phase angle is less than 90 degree
    disp(Blank)
    disp('THE LOAD IS LEADING THE DISPLACEMENT - NORMAL')
    degr= deg;
end

ActualFrequency = f(idx1+1); % Measure of actual frequency
from FFT
```

```
phaseangle=(-0.0667*ActualFrequency)+degr; % Calculation
of actual phase angle with correction factor (see BOSE
manual pg.14-10 for more information about the correction
factor)
phaseradians = (phaseangle*pi)/180; % Converting phase
angle from deg to radians
LossFactor = tan(phaseradians); % Loss Factor Calculation

X1 = ['Actual Frequency (Hz):          ',
num2str(ActualFrequency)];
X2 = ['Phase Angle (deg):              ',
num2str(phaseangle)];
X3 = ['Loss Factor                     ',
num2str(LossFactor)];
X4 = ['Time Step (s):                  ', num2str(dx)];
X5 = ['Max Load and Disp Index:        ', num2str(idx1), ',
' , num2str(idx2)];
disp(Blank)
disp(X1)
disp(Blank)
disp(X2)
disp(Blank)
disp(X3)
disp(Blank)
disp(X4)
disp(Blank)
disp(X5)
disp(Blank)

%% Calculation of Cylinder Cross Sectional Area (CSA) and
Shape Factor
CylinderCSA = (pi*dcyl^2)/4; % Cylinder CSA
ShapeFactor = (pi/hcyl)*((dcyl/2)^2); % Cylinder Shape
Factor

%% Calculation of angular velocity
omega = 2*pi*ActualFrequency; % Angular velocity
calculation
Radian = omega*Time; % Radians (w*t)
RadianLength = length(Radian);

%% Calculation of X, F, Strain, Stress
X = DisplacementData-MeanDisplacement; % Displacement
around zero
F = LoadData-MeanLoad; % Load around zero
```

```
Strain = X/hcyl; %Strain Calculation
StrainLength = length(Strain);
Stress = F/CylinderCSA; %Stress Calculation
StressLength = length(Stress);

XMax = max(X); % Maximum Displacement
FMax = max(F); % Maximum Load
StressMax = max(Stress); % Maximum Stress
StrainMax = max(Strain); % Maximum Strain

%% Graphs of Stress and Strain
% Plot of time (s) vs Load (N) and Disp (mm)
figure
plotyy(Time,LoadData,Time,DisplacementData);
xlabel('Time (s)');
ylabel('Load(N)');
title(Wordbook);
legend('Load','Disp');
% Plot of time (s) vs Stress (MPa) and Strain
figure
plotyy(Time,Stress,Time,Strain);
xlabel('Time (s)');
ylabel('Stress(MPa)');
title('Time (s) vs Stress/Strain');
legend('Stress','Strain');
% Plot of time (rads) vs Stress (MPa) and Strain
figure
plotyy(Radian,Stress,Radian,Strain);
xlabel('Radians');
ylabel('Stress(MPa)');
title('Radians vs Stress/Strain');
legend('Stress','Strain');

%% Complex Stiffness (K*), Storage Stiffness (K') and Loss
Stiffness (K'')
ComplexStiffness = MaxLoad/MaxDisp; % Calculation of
Complex Stiffness
StorageStiffness = ComplexStiffness*cos(phaseradians); %
Calculation of Storage Stiffness
LossStiffness = ComplexStiffness*sin(phaseradians); %
Calculation of Loss Stiffness

StiffnessResult1 = ['Complex Stiffness (N/mm):      ',
num2str(ComplexStiffness)];
StiffnessResult2 = ['Storage Stiffness (N/mm):      ',
num2str(StorageStiffness)];
```

```
StiffnessResult3 = ['Loss Stiffness (N/mm):          ',
num2str(LossStiffness)];
disp(StiffnessResult1)
disp(StiffnessResult2)
disp(StiffnessResult3)
disp(Blank)

%% Complex Modulus (E*), Storage Modulus (E') and Loss
Modulus (E'')

ComplexModulusMPa = ComplexStiffness/ShapeFactor;
%Calculation of Complex Modulus
StorageModulusMPa = StorageStiffness/ShapeFactor;
%Calculation of Storage Modulus
LossModulusMPa = LossStiffness/ShapeFactor; %Calculation
of Loss Modulus

ModulusResult1 = ['Complex Modulus (MPa):          ',
num2str(ComplexModulusMPa)];
ModulusResult2 = ['Storage Modulus (MPa):          ',
num2str(StorageModulusMPa)];
ModulusResult3 = ['Loss Modulus (MPa):             ',
num2str(LossModulusMPa)];
disp(ModulusResult1)
disp(ModulusResult2)
disp(ModulusResult3)
disp(Blank)
disp(Blank)
disp('END OF RESULTS')
disp(Blank)
disp(ResultsDivider)

%END
```

8.9 Appendix I – Savitzky Golay – Explanted BDyn components

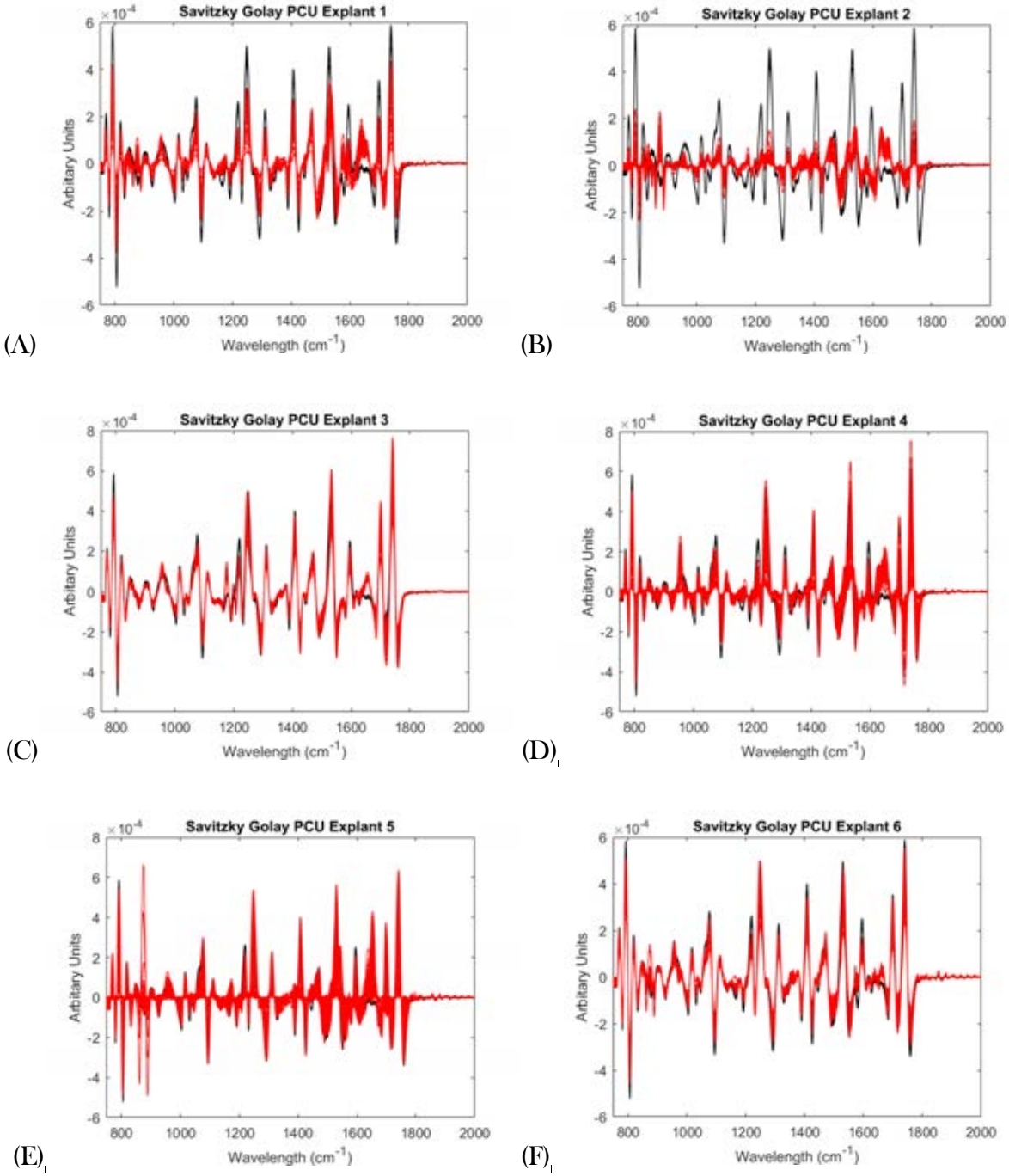

Figure 8-16: Savitzky Golay plots of untreated and explanted six PCU rings; (A) Explant 1, (B) Explant 2, (C) Explant 3, (D) Explant 4, (E) Explant 5 and (F) Explant 6. (Black plot) Untreated, (red plot) explanted component.

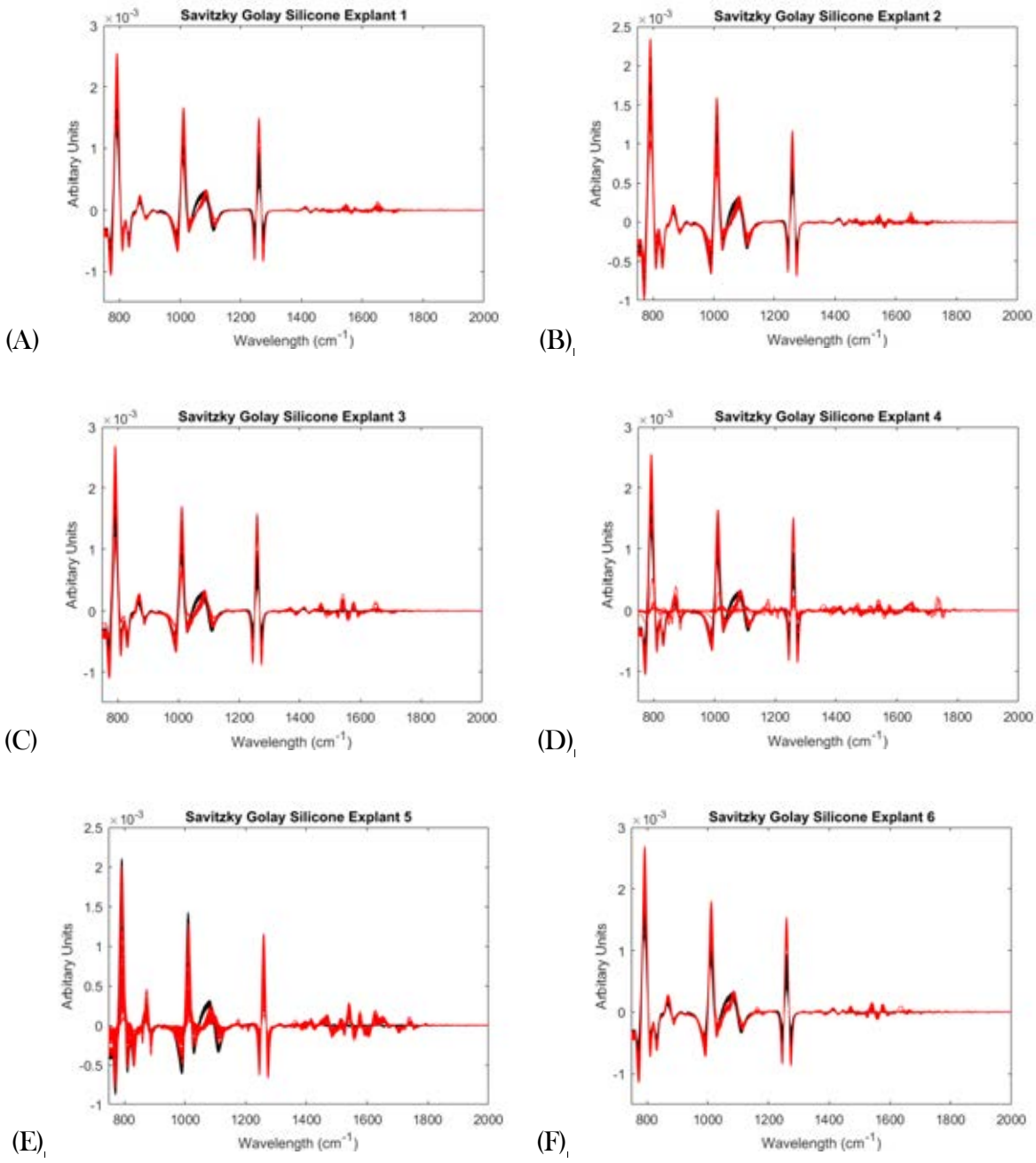

Figure 8-17: Savitzky Golay plots of untreated and explanted six silicone cushions; (A) Explant 1, (B) Explant 2, (C) Explant 3, (D) Explant 4, (E) Explant 5 and (F) Explant 6. (Black plot) Untreated, (red plot) explanted component.

8.10 Appendix J – Preliminary tests

8.10.1 Force vs displacement graph of five PCU biomaterials (tension)

8.10.1.1 Introduction

Preliminary study to quantify the tensile force versus displacement response of the five long-term implantable PCU biomaterials (section 3.1).

8.10.1.2 Materials and methods

The force versus displacement tension tests of the five PCU biomaterials were measured using a Bose ElectroForce 3300 testing machine running WinTest 4.1 DMA software (Bose Corporation, Electroforce Systems Group, Minnesota, USA; now, TA Instruments, New Castle, DE, USA). ASTM D1708 shaped specimens were used to keep consistency with the oxidation and hydrolysis studies. A displacement rate of 0.02 mm/s was applied to each tested specimen up to a displacement limit of 4 mm. All specimens were tested at room temperature and the sample size, of each biomaterial, was three (n = 3). The order of specimen testing was randomised by using the Excel Random Function (Microsoft, Redmond, Washington, USA).

8.10.1.3 Results

Figure 8-18 illustrates the force versus displacement curves for the five PCU biomaterials.

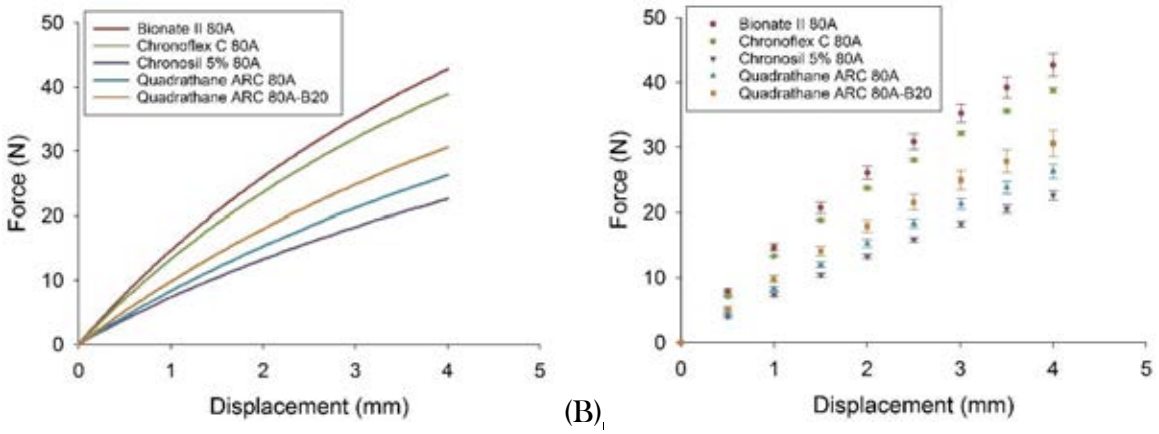

Figure 8-18: Force versus displacement of the five PCU biomaterials, (A) mean of the five PCUs and (B) mean ± standard deviation, at 0.5 mm intervals, of five PCUs

8.10.1.4 Conclusion

This preliminary study quantified the tensile mechanical behaviour (force versus displacement) of the five PCU biomaterials.

8.10.2 Force vs displacement graph of five PCU biomaterials (compression)

8.10.2.1 Introduction

Preliminary study to quantify the compressive force versus displacement response of the five long-term implantable PCU biomaterials (section 3.1).

8.10.2.2 Materials and methods

The force versus displacement compression tests of the five PCU biomaterials were measured using a Bose ElectroForce 3300 testing machine running WinTest 4.1 DMA software (Bose Corporation, Electroforce Systems Group, Minnesota, USA; now, TA Instruments, New Castle, DE, USA). Cylindrical disc shaped specimens with a height of 3 mm and a diameter of 8 mm were used. A displacement rate of 0.02 mm/s was applied to each tested specimen up to a displacement limit of 1 mm. All specimens were tested at room temperature and the sample size, of each biomaterial, was six (n = 6). The order of specimen testing was randomised by using the Excel Random Function (Microsoft, Redmond, Washington, USA).

8.10.2.3 Results

Figure 8-19 illustrates the force versus displacement curves for the five PCU biomaterials.

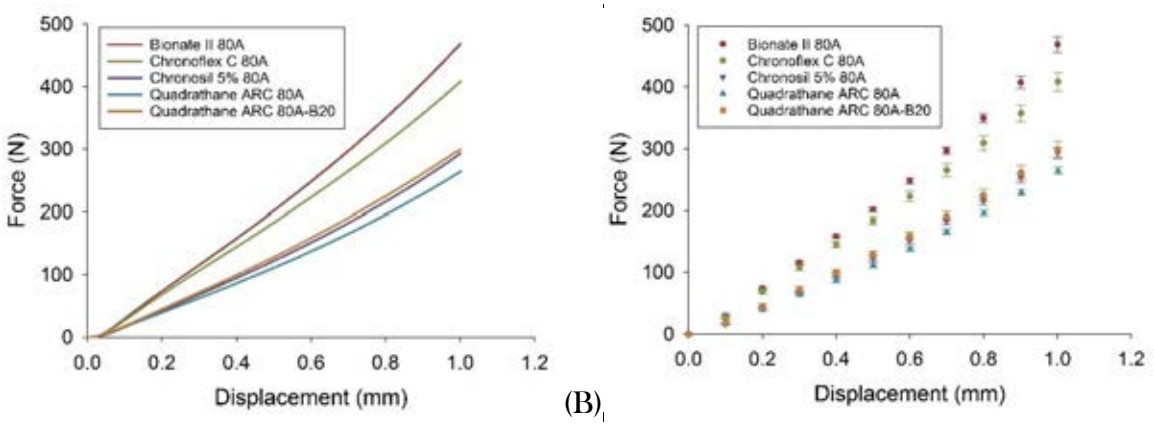

Figure 8-19: Force versus displacement of the five PCU biomaterials, (A) mean of the five PCUs and (B) mean ± standard deviation, at 0.5 mm intervals, of five PCUs

8.10.2.4 Conclusion

This preliminary study quantified the compressive mechanical behaviour (force versus displacement) of the five PCU biomaterials.

8.10.3 Force vs displacement graph of the BDyn device

8.10.3.1 Introduction

Preliminary study to quantify the force versus displacement response of the BDyn Implant.

8.10.3.2 Materials and methods

The force versus displacement of three BDyn 1 level devices (n = 3) were measured using the MTS Landmark Servo-Hydraulic testing machine running MTS Multi-Purpose Testware (MPT) on FlexTest 40 Station Manager Version 5.3B software (MTS Corporation, Eden Prairie, MN, USA). MTS 647 hydraulic wedge grips and MTS 647.02B jaws were used to clamp the mobile and fixed rods of the BDyn device (Figure 2-15).

A custom testing procedure was created on the MTS MPT software. Firstly, a compressive displacement rate of 0.02 mm/s was applied to the silicone cushion of the BDyn device (see Figure 2-15 and Figure 8-20 (B)) until a load of -1250 N was recorded. Next, the hydraulic actuator moved at a displacement rate of 0.5 mm/s to -1 mm displacement position. Then, a tensile displacement rate of 0.02 mm/s was applied to the device until a tensile load of 1750 N was recorded (Figure 8-20 (C)); this device tensile load is a compressive load to the PCU ring in the BDyn device Titanium Alloy housing (see Figure 2-15). Once 1750 N was recorded, the hydraulic actuator moved at a displacement rate of 0.5 mm/s to 0 mm (the starting position) and the test ended.

(A) 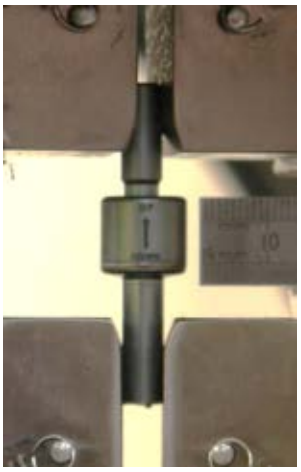 (B)  (C) 

Figure 8-20: Testing of the BDyn device in the MTS Landmark Servo-Hydraulic Test System; (A) at 0 N, (B) at -1250 N [compression of silicone cushion] and (C) at 1750 N [compression of PCU ring]

All specimens were tested at room temperature.

8.10.3.3 Results

Figure 8-21 illustrates the force versus displacement of (A) a BDyn device tested by the MTS MPT custom test procedure, (B) compression of the BDyn device (compression of the silicone cushion) and (C) tension of the BDyn device (compression of the PCU ring). The plots illustrated in Figure 8-21 (B) and (C) are mean average with standard deviation error bars. In tension, all three BDyn devices reached 1750 N while in compression, all three BDyn devices reached -1250 N.

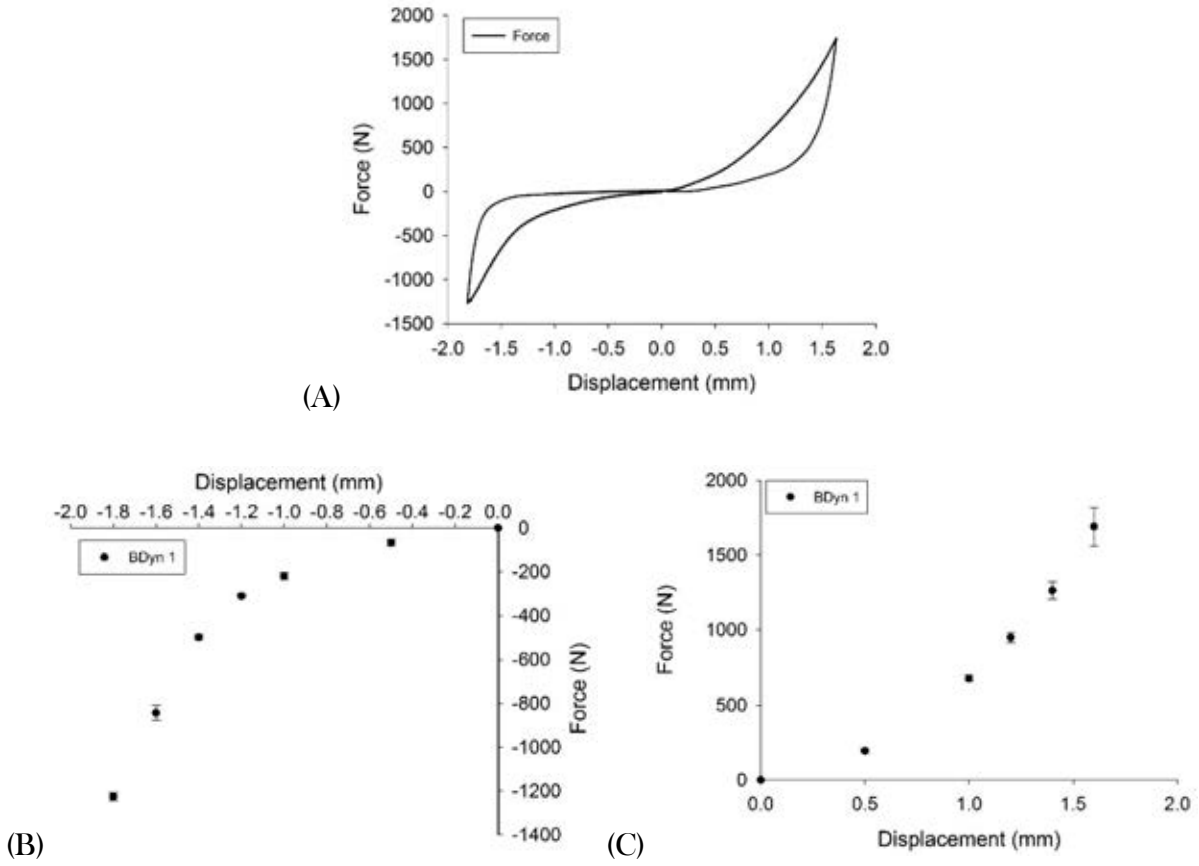

Figure 8-21: Force versus displacement of (A) a BDyn device tested by the MTS MPT custom test procedure, (B) compression of the BDyn device (compression of the silicone cushion) and (C) tension of the BDyn device (compression of the PCU ring).

8.10.3.4 Conclusion

This preliminary study quantified the compressive and tensile force versus displacement curves of the BDyn device. All three BDyn devices reached -1250 N in compression and 1750 N in tension.

8.10.4 Effect of ion treatment on the viscoelastic properties

8.10.4.1 Introduction

Preliminary study to investigate the effect of ion treatment on the viscoelastic response of the PCU ring and silicone cushion of the BDyn device.

8.10.4.2 Materials and methods

Twelve silicone and twelve polycarbonate urethane (PCU) components (Figure 5-1) were obtained from S14 Implants (Pessac, France). Six of these silicone cushions and six PCU rings were treated with a "full" ion treatment while the other six silicone cushions and six PCU rings were treated with a "weak" ion treatment; unfortunately, no specific parameters in relation to the ion treatment are known.

The experimental methods such as applied sinusoidal load, investigated frequencies, machine fixtures used, etc. were kept consistent as the evaluation of the control, *in vitro* and *in vivo* degraded BDyn components (section 5.2.3).

Wilcoxon rank sum tests were performed to compare the viscoelastic properties of the "full" and "weak" ion treated PCU rings and silicone cushions.

8.10.4.3 Results

Figure 8-22 and Figure 8-23 demonstrate the viscoelastic properties of the ion treated PCU ring and silicone cushion, respectively.

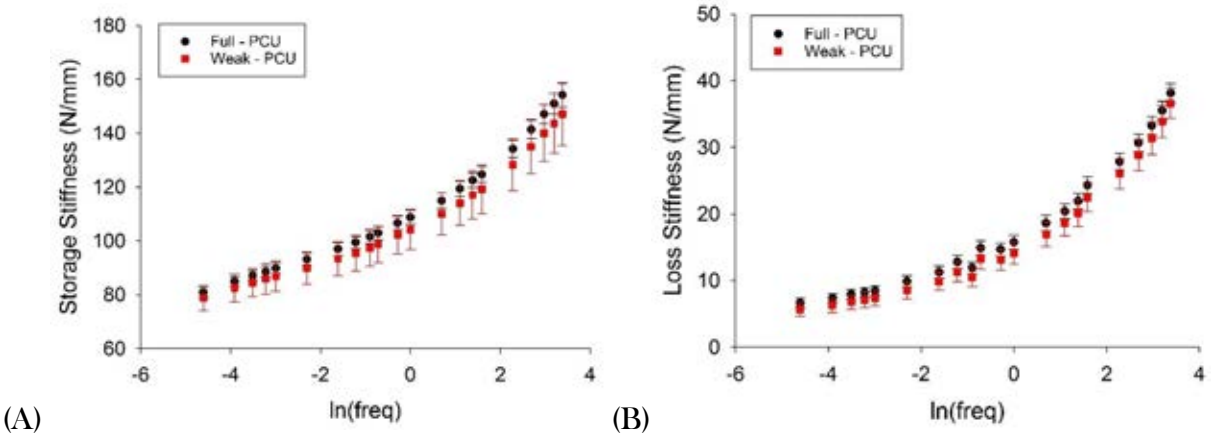

(A) (B)

Figure 8-22: (A) Storage stiffness and (B) loss stiffness of the ion treated (full and weak) PCU ring

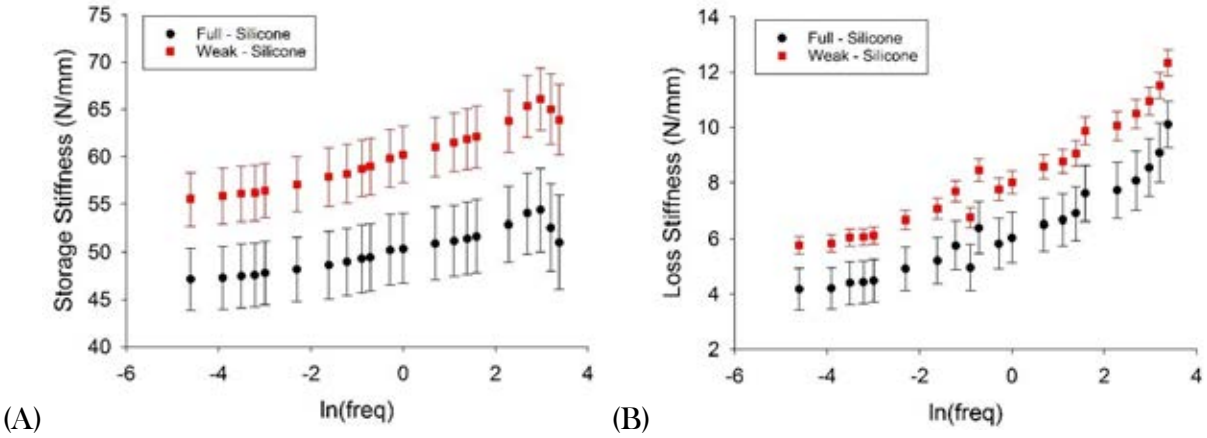

Figure 8-23: (A) Storage stiffness and (B) loss stiffness of the ion treated (full and weak) silicone cushion

The storage and loss stiffness of the full and weak ion treated silicone components were significantly different for all frequencies range tested ($p < 0.05$) while the PCU component storage and loss stiffness were not significantly different for all frequencies tested ($p > 0.05$).

8.10.4.4 Conclusion

The silicone cushion viscoelastic properties are affected by the level of ion treatment while the PCU ring viscoelastic properties remain unchanged due to the level of ion treatment.